Accepted papers (original version)

for ICPST-39

日本語シンポジウム

- The accepted papers are published in Journal of Photopolymer Science and Technology Vol. 35, No. 1-5 (2022).
- Publication work on journal of Photopolymer Science and Technology, Vol. 35, No. 1-5 (2022) has been delayed. We sincerely apologize for any inconvenience.
- Please be careful when handling the file.

Contact:
Dr. Hiroyuki Mayama, Editor-in-Chief of Journal of Photopolymer Science and Technology
e-mail: mayama@asahikawa-med.ac.jp

Low Temperature Curable Low Dk & Df Polyimide for Redistribution Layer

Masaya Jukei[1*], Hitoshi Araki[1], Hisashi Ogasawara[1], Akira Shimada[1], Takenori Fujiwara[1], and Masao Tomikawa[1]

[1] Department of Electronic & Imaging Materials Res. Labs., Toray Industries Inc., 1-2, Sonoyama 3-Chome, Otsu, Shiga 520-0842, Japan
**masaya.jukei.n6@mail.toray*

In this paper, we report low temperature curable (around 200~250℃), low Dk (2.7) and low Df (0.007) negative tone type photo-definable polyimides. Those materials, which were in states of liquid or B-stage sheet, were able to be patterned by photolithography process. Our novel polyimides showed excellent dielectric and mechanical properties, and good results on reliability tests. Our developed polyimides kept enough insulating performance after a biased HAST (High Accelerated Stress Test). Finally, in collaboration with IME, a test package which mounted our novel polyimide as redistribution layers was fabricated.
Keywords: Photo-definable Polyimide, Low Dk & Df, High frequency, Patterning, Low transmission loss, Low temperature cure, Antenna in Package

1. Introduction

In the 5G communication and millimeter-wave radar for automobiles, 28~80 GHz bands millimeter-waves will be used. It will be expected to be applied to various services such as high performance video streaming and AR/VR gaming by high speed wireless communication.[1] Especially, around 78 GHz bands millimeter-wave radar is important for collision avoidance system of automobiles.[2] In such a high frequency device, transmission loss energies will become larger than these of below-millimeter-wave device. Dielectric constant (Dk) and dissipation factor (Df) of insulation materials are related to loss energies of high frequency device. Therefore many companies and research institutions have efforted to develop low Dk and Df materials.

Polytetrafluoroethylenes (PTFE) and liquid crystal polymers (LCP) are known as typical examples of low Dk and low Df materials. However, it is difficult for those materials to adhere to substrates and create patterning. On the other hand, polyimides can fulfill these properties, thus low Dk and low Df polyimide materials is desired.

At the same time, fun-out wafer level package has attracted attention as the semiconductor package that decrease package size and manufacturing cost.[3] Especially, antenna in package with fun-out technologies is the most important factor for device on high frequency bands.[4, 5, 6] Redistribution layers will need to be low Dk and low Df insulation.

We have previously developed low Dk and low Df polyimide under concept of restriction of molecular dynamics and reduction of polarity.[7, 8]

In this paper, we developed negative photo-definable low Dk and low Df polyimides. A test device using the developed polyimides showed good results on reliability tests.

Received April 1, 2022
Accepted June 24, 2022

2. Experimental Section

2.1. Preparation of polyimides

Polyimide resins were synthesized by polycondensation of tetracarboxylic dianhydrides with diamines. The prescribed amount of diamines was poured into a 4 neck flask with a mechanical stirrer, a thermometer and an inlet pipe for nitrogen flow. N-methyl-2-pyrrolidone (NMP, Mitsubishi Chem.) was added into the 4 neck flask. Under nitrogen flow, the flask was heated to 60 ℃. The prescribed amount of tetracarboxylic dianhydrides was added into the flask with NMP. The mixture in the flask was stirred for 1hr at 60 ℃, followed by polycondensation was performed for 4 hr at 180 ℃.

2.2. Preparation of polyimide solution and B-stage sheet

A Polyimide solution was obtained by following procedure. 10 g of polyimide was dissolved by γ-butyrolactone (GBL, Mitsubishi Chem.) to prepare polyimide solution at concentration of 35 wt%. Then, 10~40 wt% crosslinker and 1~10 wt% photoinitiator were added to those solution. B-stage sheet was produced by the following procedure: Polyimide solution was coated on polyethylene terephthalate (PET) film by die coater and dried in oven at 80 ℃ for 10 min.

2.3. Measurement of dielectric properties

Polyimide solution was coated at about 10 μm thickness on 6 inch wafer by spin coating. Coated wafer was softly baked by hot plate at 120 ℃ for 3 min. The softly baked wafer was exposed to 1500 mJ/cm^2 UV (i-line energy) without photomask, then the exposed wafer was softly baked by hot plate at 130 ℃ for 5 min. The baked wafer was cured under N_2 flow at 220 ℃ for 1 hr. Polyimide film was obtained from the cured wafer soaked in HF solution at room temperature for 2 min.
Obtained polyimide film was dried in oven at 50 ℃ for 1 hr. Dielectric property of polyimide film at 20 GHz was measured by TMR-1A (Keycom, Cavity resonation method).

2.4. Patterning process

After photolithography patterning, a B-stage sheet was laminated at about 20 μm thick on 6 inch Si wafer by roll laminator. PET substrate film was removed from laminated wafer. Laminate conditions were as follows; temperature = 120 ℃, pressure = 0.3 MPa, lamination speed = 0.2 m/min. In patterning process, 1500 mJ/cm^2 UV (i-line energy) was exposed through photomask with via holes, lines and spaces. After exposed wafer was post-baked at 130 ℃ for 5 min by hot plate, post-baked wafer was developed by propylene glycol monomethyl ether acetate (PGMEA). Patterned polyimide film on wafer was cured under N_2 flow at 220 ℃ for 1hr.

2.5. Measurement of mechanical properties

Polyimide film of thickness 10 μm was obtained as in Section 2.3. The coefficient of thermal expansion (CTE) and glass translation temperature (Tg) were measured by TMA equipment (SEIKO, TMA/SS6000) at heating rate 5 ℃/min under N_2 flow. Young's module, elongation and strength were measured by Universal testing machine (Orientech, TENSILON RTM-100) at rate of 5 mm/min.

2.6. Chemical resistance

The cured polyimide on wafer was immersed in various chemicals under specific conditions. Then, the treated polyimide on wafer was observed by microscope to check cracks and measured those thickness by STM-802 (Dainippon-screen).

2.7. Reliability tests

Patterned cylinder Cu pads were fabricated on 8 inch wafer by sputtering, electroplating and photolithography process.

B-stage sheet was laminated, patterned and baked at about 20 μm thickness on the wafer as in Section 2.4. We observed the baked wafer and counted cracks on the Cu pads by microscope before and after thermal cycle test. Reliability was evaluated by rate of crack occurrence on Cu pads.

The polyimide solution was coated at 10 μm thickness on TEG substrate as shown in Fig 1. The dimensions of line, space and height of copper were 5 mm, 5 mm and 3 mm, respectively. Then biased HAST was carried out at 130 ℃ for 96 hr with 5 V in 85 %RH. The TEG substrate was fabricated as in Fig. 2.

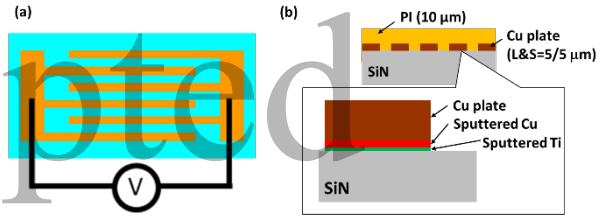

Fig. 1. (a) Top of view of test vehicle. (b) Cross section of test vehicle.

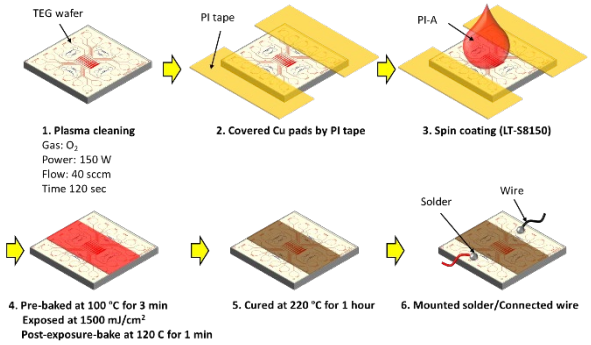

Fig. 2. Procedure of test vehicle fabrication for biased HAST.

2.8. Fabrication of test package

We collaborated with IME to fabricate a test package mounted redistribution layers (RDL) consisting of b-stage polyimide sheets and patterned Cu layers.

3. Results & Discussion

3.1. Properties of low Dk and low Df polyimide

materials

Previously, we reported that it was important to suppress molecular motion at low temperature around -100 ℃ for Df reduction at high frequency. In addition, decreasing polarity in the polyimide was another point to achieve low Dk and Df polyimide. In terms of dielectric material for semiconductor package, it is important not only Dk & Df value but also mechanical property, thermal stability and chemical resistivity.

Properties of developed polyimide materials are summarized in Table 1. PI-A and PI-B contain photoinitiator and crosslinker to obtain photolithographic property. PI-A and PI-B could be patterned by conventional photolithographic tools (Discussed in Section 3.2). PI-A is a liquid type photo-definable polyimide and PI-B is a b-stage sheet material. In addition, PI-B is a higher Tg type material.

Table 1. Properties of PI-A and PI-B

	PI-A	PI-B
Material type	Liquid	B-stage sheet
Photo-definable type	Nega. type	Nega. Type
Dk(20GHz)	2.7	2.7
Df(20GHz)	0.007	0.008
Tg	120℃	150℃
CTE	90ppm	75ppm
Young's Modules	2.0GPa	1.8GPa
Tensile strength	70MPa	70MPa
Elongation	50%	10%
Moisture uptake	0.6%	0.5%
Cure Temp.	200℃	230℃

In addition, PI-A showed good chemical resistance. The chemical resistance test of PI-A was performed in several chemicals and conditions as shown in Table 2. We observed no change in appearance even after treatment to various chemicals (organic solvent, aqueous acid and base).

Table 2. Chemical resistance of PI-A

Chemicals	Conditions	Thickness change
NMP	40℃/10min	No change
PGMEA	rt/30min	No change
Acetone	rt/30min	No change
2.38%TMAH	rt/30min	No change
10%KOH	rt/30min	No change
10%H_2SO_3	rt/30min	No change
8%HNO_3	rt/30min	No change
1%HF	rt/30min	No change

3.2. Patterning result

Typical procedure and patterning results are shown in Fig.3. PI-B is solvent-development-type, negative-tone, photo-definable material. PGMEA, which is one of common developer for negative tone resist, could be used as a developer. The developer is PGMEA that is one of common developer for negative-tone resist. PI-B offered fine pattern of 20 μm via and 10/20 μm line and space by broadband exposure. The advantage of PI-B is that conventional photolithographic tools are compatible to this material. Pattern resolution of PI-B was fine enough to RDL of AiP. PI-A, which is a liquid type material, can be also patterned by similar procedure.

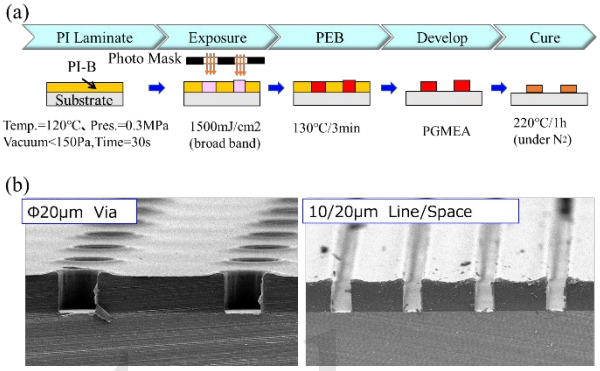

Fig. 3. (a) Process flow and conditions of photolithography process using PI-B. (b) SEM image of 20 μm via and 10 μm /20 μm L/S from cross section view.

3.3. Reliability test results of PI-A

PI-A showed a good insulation reliability by biased HAST. As shown in Fig. 4, no short and open failure were observed at 130 ℃ for 96 hr with 5 V in 85 %RH.

This result indicated that PI-A and PI-B have enough insulating performance as RDL even after the reliability test.

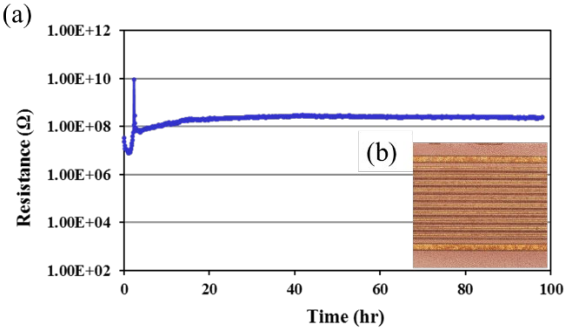

Fig. 4. (a) Resistivity of PI-A cured for 220 ℃ for 1 hr during the treatment at a condition of 130 ℃, 85 RH%, and 5 V bias for 96 hrs. (b) Image of test vehicle after biased HAST test.

3.4. Evaluation of RDL in a package

Collaborated with IME, we fabricated RDL structure on mold wafer including RFIC dice using PI-B. The number of layers of Cu and polyimide was 2 and 2, respectively. Top and cross section view of the RDL are shown in Fig. 5. A thickness step of Cu wire derived from die and mold resin was almost flat by b-stage sheet lamination. The flatness of Cu wire influences signal loss in case of AiP.

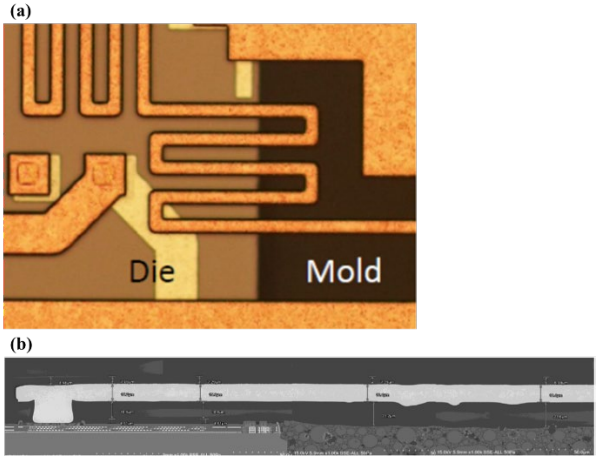

Fig. 5. (a) top view of RDL of the test vehicle. (b) SEM image of cross section of RDL.

We evaluated the reliability of the package by thermal cycle (TC) tests. TC test was carried out from -55 ℃ to 150 ℃. TCOB (Thermal Cycle on Board) test was carried out from -40℃ to 125 ℃ on organic substrate. Results were summarized at Table 3. No failure was observed on the specimen up to 1000 cycles.

Table. 3. Crack occurrence rate of PI-B for thermal cycle tests.

	Number of thermal cycles			
tests	250	500	750	1000
TC	0/13	0/13	0/13	0/13
TCOB	0/11	0/11	0/11	0/11

4. Conclusion

High frequency electronic device for 5G telecommunication and millimeter wave radars require low Dk (2.7) and Df (0.007) material to decrease signal loss. We developed negative tone photo-definable polyimide with low Dk & Df, in combination with photo-initiator and cross-linker. It showed good several properties, patterning abilities and reliabilities (chemical resistance, biased HAST, TC, TCOB).

Our novel low Dk and Df polyimides are suitable for insulator of RDL applied for AiP, interposer and other RF microelectronics whose applications are 5G communication and millimeter-wave radar for automobiles.

5. Acknowledgement

Authors are grateful to the Institute of Microelectronics (IME) for RDL fabrication and reliability tests.

6. References

[1] Y. Kishiyama, A. Benjebbour, S. Nagata, Y. Okumura, and T. Nakamura, NTT Docomo Tech. J., 23_4 (2014) 6.
[2] T. Yamawaki and S. Yamano, “60-GHz Millimeter-Wave Automotive Radar”, Fujitsu Ten Tech. J. 11 (1998) 3.
[3] S.W. Yoon, J.A. Caparas, Y. Lin, and P.C. Marimuthu, Electronic Components and Technology Conference (ECTC) 2012, 1250.
[4] C. T. Wang, T. C. Tang, C.W. Lin, C.W. Hsu, J.S. Hsieh, C.H. Tsai, K.C. Wu, H.P. Pu, and Douglas C. H. Yu, Electronic Components and Technology Conference (ECTC) 2018, 202.
[5] S.W. Ho, S.S. Boon, L.B. Long, H. H. Yao, C.S. Choong, S.L.P. Siang, L.T. Guan and C.T. Chong, Electronics Packaging Technology Conference (EPTC) 2020.
[6] S.P.S. Lim, S.C. Chong, D.H.S. Wee, W.W. Seit, J.J. Soh and T.C. Chai, Electronics Packaging Technology Conference (EPTC) 2021.
[7] H. Araki, Y. Kiuchi, A. Shimada, H. Ogasawara, M. Jukei and M. Tomikawa, Electronic Components and Technology Conference
(ECTC) 2020, 635.
[8] T. Fujiwara, Y. Tatsuta, K. Matsumura, D. Kanamori, H. Araki, A. Shimada and M. Tomikawa, International Wafer Level Packaging Conference (IWLPC) 2020.

Synthesis and Higher-order Structural Characterization of Polyimides Containing Chain-length-controlled Polysiloxanes

Erina Yoshida[1], Yuta Nabae[1], and Teruaki Hayakawa[1*]

[1] Department of Materials Science and Engineering, School of Materials and Chemical Technology Tokyo Institute of Technology, 2-12-1-S8-36, Ookayama, Meguro-ku, Tokyo, 152-8552, Japan
**hayakawa.t.ac@m.titech.ac.jp*

The synthesis of polyimides (PIs) containing polydimethylsiloxane (PDMS) with controlled chain length and the formation of higher-order structures were studied. Polycondensation was carried out using diphenyl-3,3',4,4'-tetracarboxylic dianhydride (BPDA) and diamine oligomers having amino groups on both ends of PDMS. The obtained poly(amic acid) (PAA) and PI showed good solubility in several common polar solvents while less soluble in non-protic amide polar solvents. The obtained bulk films of PI suggested forming a microphase-separated structure with domains based on PDMS and other aromatic moieties.

Keywords: Polysiloxane, Chain-length-control, Polyimide, Micro-phase separated nanostructure, Self-assembly

1. Introduction

Polyimide (PI), featuring excellent heat resistance, good mechanical strength, and appropriate dielectric constant, has been widely considered for applications in insulating layers, buffer coatings, and passivation layers in microchip technology [1-4]. In particular, communication technology using high frequencies has been promoted in recent years to realize high-speed and large-capacity communication. The development of insulating polyimides with low dielectric constant and low dielectric dissipation factor as rewiring layers for high-frequency applications is desired.

One of the most effective approaches to achieving a low dielectric constant is the introduction of bulky molecular chains, and oligo or polysiloxane-containing PIs have attracted attention [5]. On the other hand, controlling the segment length of polysiloxane in oligo or polysiloxane-containing PIs is vital because it is closely related to other essential properties required of PIs, such as film formability and heat resistance. However, there have been no detailed

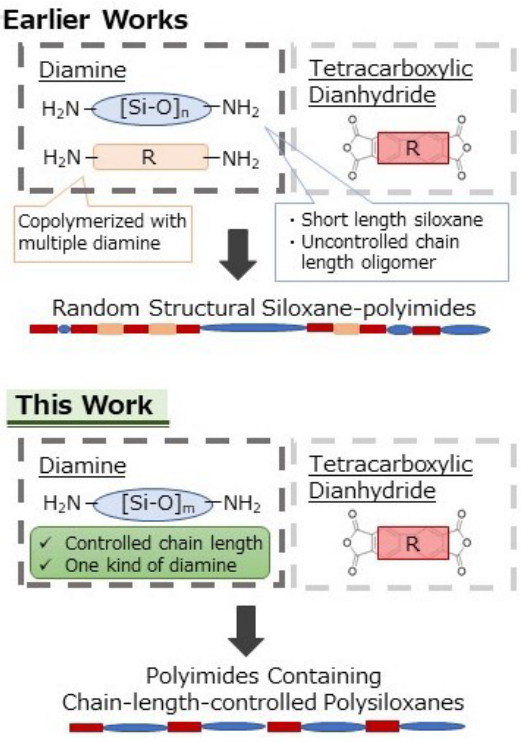

Fig. 1. Concept of this study

Received March 31, 2022
Accepted June 20, 2022

studies on the synthesis of polysiloxane chain-length-controlled PI and the structure-property relationship of the resulting polymers. The degree of polymerization of oligosiloxanes (*n* in Fig. 1) in previous studies is mainly limited to 2-10 [6-17]. There are only a few synthetic examples concerning molecular weight-controlled polysiloxanes in the PIs with relatively high molecular weights with degrees of polymerization more significant than 10. As the molecular weight of the polysiloxane increases, the repulsive interactions with other segments, including the imide moieties in the polymer chain, also increase significantly. The resulting PIs are expected to form higher-order structures due to microphase separation, which may help incorporate other required properties such as low dielectric dissipation factor into material design.

This study reports on the synthesis, properties, and higher-order structure of PI containing chain-length-controlled polysiloxane. The chain-length-controlled polysiloxanes were prepared by ring-opening living anionic polymerization with water as an initiator, as reported by Fuchise and G. G. Lohmeijer et al. [18-19]. The subsequent reactions were conducted as shown in Schemes 1 and 2 [20-21], and the higher-order structure of the resulting polymers was characterized by wide-angle X-ray diffraction (WAXD) and small-angle X-ray scattering (SAXS).

2. Experimental

2.1. Materials

Hexamethylcyclotrisiloxane (D_3) was purchased from Tokyo Chemical Industry (TCI), and purified by sublimation at 55 °C. Diphenyl-3,3',4,4'-tetracarboxylic dianhydride (BPDA) was purchased from TCI, and recrystallized from acetic anhydride. Tetrahydrofuran (THF, dehydrated and stabilizer free) was distilled prior to use over a small amount of *Sec*-butyllithium (*sec*-BuLi, in cyclohexane n-hexane). H_2O was prepared by Direct-Q UV. Chlorodimethylsilane (Me_2HSiCl), 1,5,7-triazabicyclo[4.4.0]dec-5-ene (TBD),

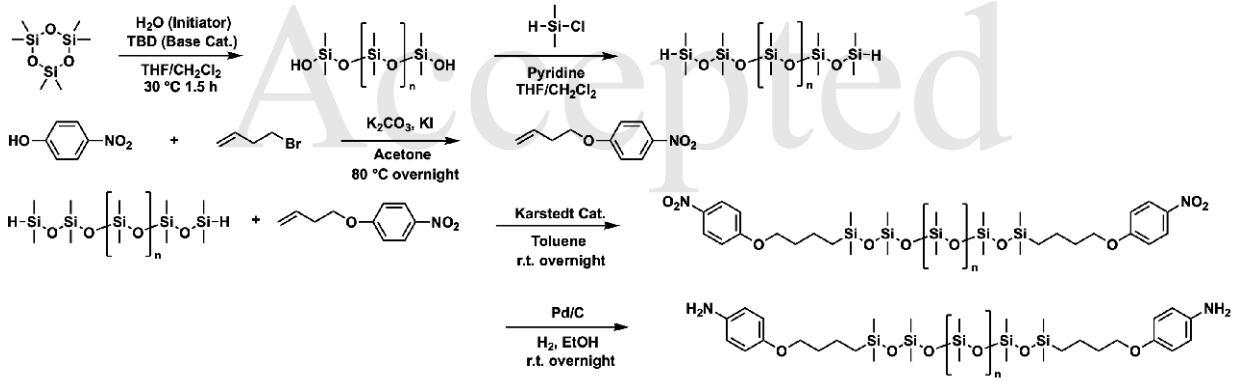

Scheme 1. Synthesis of Polysiloxane-containing Diamine

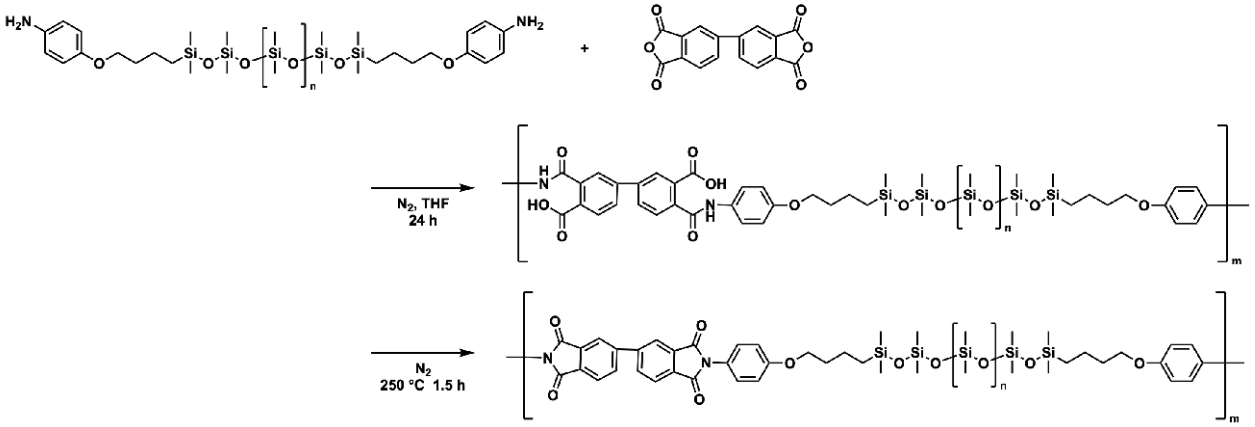

Scheme 2. Synthesis of Polysiloxane-containing Polyimides

palladium 10% on carbon, wetted with ca. 55% water (Pd/C), platinum(0)-1,3-divinyl-1,1,3,3-tetramethyl disiloxane in xylene, Pt ~2 % (Karstedt cat.) and all the other chemicals were reagent grade and used as received, unless otherwise stated.

2.2. Measurements

Nuclear magnetic resonance (NMR) was acquired on a JEOL JNM-ECS 400 spectrometer (JEOL, Tokyo, Japan) at 400 MHz for ^{1}H, 100MHz for ^{13}C and 60MHz for ^{29}Si. The number-average molecular weight (M_n) and polydispersity (M_w/M_n) were determined by the size exclusion chromatography (SEC) using a Shodex GPC-101 system with a Shodex LF-804 column and THF eluent. FT-IR was measured with a JASCO FT/IR-4100 plus spectrophotometer by the NaCl plate method. Thermogravimetric analysis (TGA) was performed with an EXSTAR TG/DTA 7300 (Seiko Instrument Inc., Tokyo, Japan) at a heating rate of 10 °C min^{-1}. Differential scanning calorimetry (DSC) was performed with an EXSTAR DSC 7020 system (Seiko Instrument Inc., Tokyo, Japan). Polarized optical microscopy (POM) was conducted using a BH-2 microscope (Olympus, Tokyo, Japan) equipped with a Mettler FP82HT hot-stage system. WAXD was measured with Discover D8 (Bruker AXSK.K., Kanagawa, Japan). SAXS was measured with Bruker NanoSTAR (Bruker AXSK.K., Kanagawa, Japan) (50 kV per 50 mA).

2.3. Synthesis of diamine

2.3.1 PDMS

PDMS was synthesized via living anionic ring-opening polymerization. D_3 (667 mg, 3.00 mmol), dichloromethane (CH_2Cl_2) (2.3 mL), a solution of TBD (0.0188 mol/L), and H_2O (0.176 mol/L) in dry THF (1.7 mL) were added to a flask equipped with a needle-bulb under an argon atmosphere at 30 °C. After 90 min of stirring, Me_2HSiCl (0.20 mL, 1.8 mmol) and pyridine (0.20 mL, 2.4 mmol) were added as an end-capping agent and an acid scavenger, respectively. The end-capping reaction was continued at 30 °C for 15 min. After THF and CH_2Cl_2 were removed in vacuo, the residue was washed with acetonitrile four times and dried in vacuo to obtain PDMS (PDMS-($OSiMe_2H)_2$) (648 mg, 76% yield, $M_{n,NMR}$ = 3000 g/mol, $M_{n,SEC}$ = 2800 g/mol, $Đ$ = 1.06). ^{1}H NMR (400 MHz, $CDCl_3$, δ, ppm): 0.03-0.09 (m, 216H, -Si-*Me*$_2$), 0.17-0.19 (m, 12H, -SiH-*Me*$_2$), 4.68-4.72 (m, 2H, -$SiMe_2$-*H*). ^{13}C NMR (100 MHz, $CDCl_3$, δ, ppm): 0.51-1.60. ^{29}Si NMR (60 MHz, $CDCl_3$, δ, ppm): -5.15, -7.76, -19.37, -21.44.

2.3.2 1-(but-3-en-1-yloxy)-4-nitrobenzene (**a**)

1-(but-3-en-1-yloxy)-4-nitrobenzene was synthesized via the Williamson ether synthesis. To a solution of *p*-nitrophenol (1.40 g, 10.1 mmol), K_2CO_3 (4.15 g, 30.0 mmol) and KI (87.5 mg, 0.527 mmol) in acetone (35 mL), 4-bromo-1-butene (6.76 g, 50.1 mmol) was added, and the mixture was refluxed overnight. The solution was filtered, and the filtrate was concentrated under reduced pressure. The residue was chromatographed on silica gel using n-hexane/CH_2Cl_2 (=3/1, v/v) as the eluent to obtain a pale yellowish oil by evacuation. (1.66 g, 87% yield). ^{1}H NMR (400 MHz, $CDCl_3$, δ, ppm): 2.56-2.61 (m, 2H, -C*H*$_2$-), 4.11 (t, *J*=6.64, 2H, -O-C*H*$_2$), 5.13-5.22 (m, 2H, -CH=C*H*$_2$), 5.84-5.94 (m, 1H, CH_2=C*H*-), 6.95 (d, *J*=9.16, 2H, Ar*H*), 8.20 (d, *J*=9.16, 2H, Ar*H*).^{13}C NMR (100 MHz, $CDCl_3$, δ, ppm): 33.0, 67.7, 114.2, 117.2, 125.5,133.5, 141.0, 163.8. IR (NaCl, *v*, cm^{-1}): 3083, 2941, 1643, 1607, 1594, 1513, 1497, 1469, 1342, 1262, 1173, 1112, 1024, 921, 846, 752, 690, 654.

2.3.3 PDMS-dinitrobenzene (**b**)

Polymer **b** was synthesized via the hydrosilylation of PDMS. To a solution of **a** (373 mg, 1.94 mmol) and PDMS (1.45 g, $M_{n,NMR}$ = 3000 g/mol, 0.483 mmol), in toluene (2.0 mL), Karstedt's catalyst (4 drops, 10 μL) (2 wt% of platinum divinyltetramethyldisiloxane complex in xylene) was added. The reaction mixture was refluxed under argon for 24 h, and then toluene was removed by evaporation. The residue was chromatographed on silica gel using *n*-hexane/CH_2Cl_2 (= 5/1, v/v) as the eluent. The compound **b**, (1.59 g, $M_{n,NMR}$ = 3400 g/mol, 91% yield) was then isolated by evaporation as a pale yellow oil. ^{1}H NMR (400 MHz, $CDCl_3$, δ, ppm): 0.04-0.10 (m, 136H, -Si-*Me*$_2$), 0.58-0.62 (m, 4H, -Si-C*H*$_2$), 1.48-1.56 (m, 4H, -C*H*$_2$-), 1.81-1.88 (m, 4H, -C*H*$_2$-), 4.05 (t, *J*=6.41, 4H, -O-C*H*$_2$), 6.93 (d, *J*=9.16, 4H, Ar*H*), 8.19 (d, *J*=9.16, 4H, Ar*H*).^{13}C NMR(100 MHz, $CDCl_3$, δ, ppm): 0.29-1.55, 18.0, 19.8, 32.6, 68.6, 114.5, 126.0, 141.4, 164.4. IR (NaCl, *v*, cm^{-1}): 2962, 1608, 1594, 1519, 1499, 1469, 1342, 1261, 1092, 1021, 799, 661. $M_{n,SEC}$: 2400 kg/mol, $Đ$: 1.08.

Table 1. Solubility of PAA(BPDA) and PI (BPDA)

	Solubility[a]									
	NMP	DMAc	DMF	THF	Acetone	$CHCl_3$	Hexane	Toluene	MeOH	EtOAc
PAA	±	+h	--	+	+	--	--	±	--	±
PI	--	--	--	+	+h	+	--	+h	--	+

[a] +: soluble at room temperature; +h: soluble on heating; ±: partially soluble or swelling on heating; and --: insoluble even on heating.

2.3.4 PDMS-diamine

PDMS-diamine was synthesized via hydrogenation of polymer **b**. A mixture of **b** (1.25 g, $M_{n,NMR}$ = 3400 g/mol, 0.367 mmol) and Pd/C (12.5 mg, 10 wt %) in EtOH (25 mL) was stirred at room temperature overnight under a hydrogen atmosphere with a balloon. The solution was filtered through celite, and the filtrate was concentrated in vacuo. The residue was chromatographed on silica gel using a *n*-hexane/CH_2Cl_2 (=2/1, v/v) eluent to obtain diamine **c** (1.20 g, $M_{n,NMR}$ = 3300 g/mol, 99% yield) as a brown oil. ^{1}H NMR (400 MHz, THF-d_8, δ, ppm): 0.07-0.15 (m, 162H, -Si-Me_2), 0.60-0.64 (m, 4H, -Si-CH_2), 1.48-1.56 (m, 4H, -CH_2-), 1.72-1.77 (m, 4H, -CH_2-), 3.81 (t, *J*=5.95, 4H, -O-CH_2), 3.98 (s, 4H, -NH_2), 6.46 (d, *J*=8.70, 4H, Ar*H*), 6.59 (d, *J*=8.70, 4H, Ar*H*). ^{13}C NMR (100 MHz, THF-d_8, δ, ppm): 0.37-1.85, 18.6, 20.6, 33.9, 68.43, 114.9, 115.9, 142.5, 152.1. IR (NaCl, *v*, cm^{-1}): 3371, 2962, 1512, 1261, 1238, 1092, 1023, 800, 703, 663, 513. $M_{n,SEC}$: 2400 g/mol, *Đ*: 1.08.

2.4. Synthesis of PDMS-PAA/PI

2.4.1 PDMS-PAA

PDMS-PAA was synthesized via the polyaddition of tetracarboxylic dianhydride and diamine. BPDA (37.6 mg, 0.13 mmol) was added to a solution of the PDMS-diamine **c** (294.6 mg, $M_{n,NMR}$ = 3000 g/mol 0.098 mmol) in THF, and the solution was stirred at room temperature for 24 h. The mixture was precipitated into an excessive amount of MeOH, and then filtered. The residue was dried in vacuo overnight to obtain PDMS-PAA (206.3 mg, 62% yield) as a brown solid.^{1}H NMR(400 MHz, THF-d_8, δ, ppm): 0.07-0.14 (m, 216H, -Si-Me_2), 0.64-0.68 (m, 4H, -Si-CH_2), 1.49-1.61 (m, 4H, -CH_2-), 1.77-1.84 (m, 4H, -CH_2-), 3.95 (t, *J*=6.40, 4H, -O-CH_2), 6.47 (d, J=8.69, Ar*H*), 6.60 (d, *J*=8.69, Ar*H*), 6.81-6.84 (m, Ar*H*), 7.59-7.66 (m, Ar*H*), 7.83-8.03 (m, Ar*H*), 8.23-8.27 (m, Ar*H*), 9.34-9.36 (m, Ar*H*), 10.86 (m, NH_2). IR(NaCl, *v*, cm^{-1}): 3274, 3066, 2962, 1698, 1651, 1602, 1540, 1512, 1473, 1414, 1260, 1091, 1021, 862, 799, 702. $M_{n,SEC}$: 47100, *Đ*: 1.99

2.4.1 PDMS-PI

PDMS-PI was synthesized via thermal imidization. PDMS-PAA was held at 250 ° C for 1.5 h under nitrogen atmosphere to obtain the brown solid. ^{1}H NMR(400 MHz, THF-d_8, δ, ppm): 0.07-0.15 (m, 180H, -Si-Me_2), 0.66-0.70 (m, 4H, -Si-CH_2), 1.53-1.63 (m, 4H, -CH_2-), 1.81-1.88 (m, 4H, -CH_2-), 4.03 (t, *J*=6.40, 4H, -O-CH_2), 6.47 (d, *J*=8.69, Ar*H*), 6.60 (d, *J*=8.69, Ar*H*), 7.00 (d, *J*=9.15, 4H, Ar*H*), 7.37 (d, *J*=9.15, 4H, Ar*H*), 8.05 (d, *J*=7.78, 2H, Ar*H*), 8.30 (d, *J*=7.78, 2H, Ar*H*), 8.39 (s, 2H, Ar*H*), 10.85 (s, -NH_2). IR(NaCl, *v*, cm^{-1}): 2962, 2360, 1768, 1719, 1514, 1416, 1384, 1299, 1260, 1094, 1021, 862, 799, 697. $M_{n,SEC}$: 59200, *Đ*: 2.29

3. Results and discussion

3.1. Solubility and Thermal Properties of PAA/PI

The obtained PAAs and PIs were insoluble in aprotic amide-based polar solvents such as NMP, DMAc, and DMF but soluble in ordinary polar solvents such as acetone and THF (Table1). This peculiar solubility may be attributed to the PDMS segments being much longer than the aromatic segments.

TGA measurement was performed on PDMS-PAA, and the result is shown in Fig. 2. A

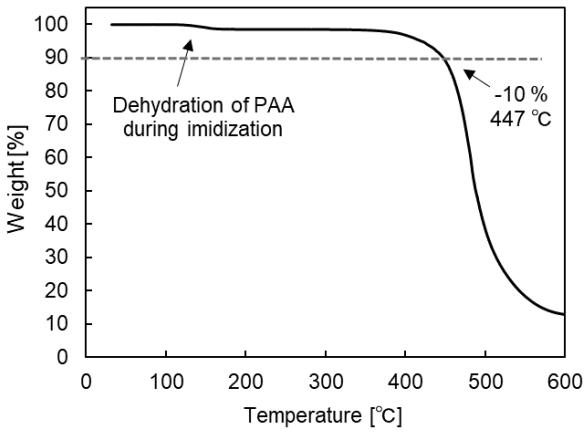

Fig. 2. TGA profile of PDMS-PAA

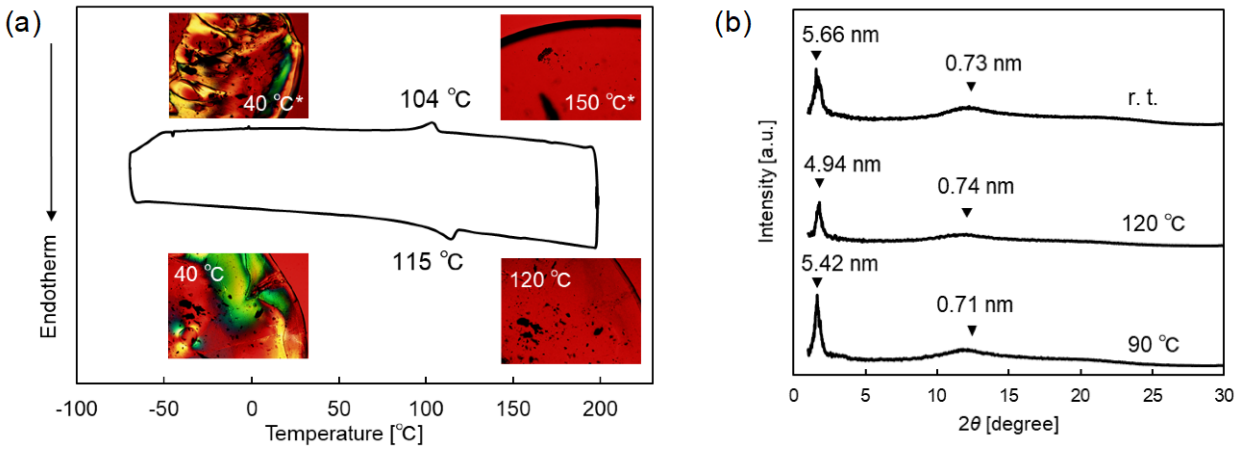

Fig. 3. (a) DSC curve and POM images of PDMS-PI (b) WAXD profiles of PDMS-PI at room temperature and 120 °C in heating process and 90 °C in cooling process

weight loss due to dehydration corresponding to 1.23 wt% was observed at 145 °C. This weight loss is in close agreement with the calculated value of 1.10 wt%. The resulting PI was stable up to 447 °C, where a weight loss of 10 wt% was observed.

3.2. Higher-order structural characterization of PI

Fig. 3 (a) shows the DSC curve and POM images of PDMS-PI. The DSC curve suggests that the phase transition occurred at 115 °C during the heating and 104 °C during the cooling processes, respectively. In the POM images, an optical texture was observed at 40 °C, but disappeared when the temperature exceeded 115 °C during the heating process. Subsequently, the optical structure was observed during the cooling process, although with supercooling behavior. These experimental results suggest that this sample has thermotropic liquid crystalline properties.

WAXD and SAXS profiles at room temperature are shown in Fig. 3 (b) and Fig. 4,

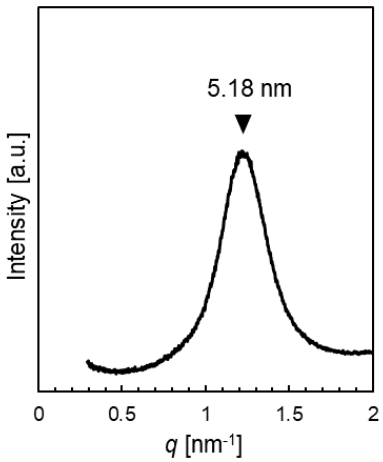

Fig. 4. SAXS profile of PDMS-PI at room temperature

respectively. In the WAXD profile, a strong peak based on d= 5.66 nm and a broadening peak based on d= 0.73 nm were observed at room temperature. In the SAXS profile, a peak at 2θ= 1.7° (d= 5.18 nm) was also observed. This peak is considered to be consistent with the strong peak at 2θ= 1.6° (d= 5.66 nm) in the WAXD profile. These results suggest that the peaks appearing in the small-angle region in WAXD and SAXS profiles are based on the repeat units of the domains formed by the polysiloxane segment and other aromatic segments in the polymer chain, respectively.

On the other hand, the wide-angle peak in the WAXD profile based on d= 0.73 nm is considered to be based on the polysiloxane interchain length. The WAXD profile also shows a weak peak around 2θ= 20° at room temperature, which disappears at 120 °C in the heating process. Then, upon cooling, this peak can be seen again at 90 °C. This suggests that the broadening peak at 2θ= 12° (d= 0.73 nm) and the weaker broadening peak at 2θ= 20° (d= 0.4-0.5 nm) originates from the intermolecular chain length of PDMS and the aromatic imide segment in PDMS-PI, respectively. DSC, POM, and WAXD analyses suggest that the higher-order structure of the obtained polymer is based on a microphase-separated structure formed by repulsive interactions between the aromatic imide segments and polysiloxane segments in the PDMS-PI.

4. Conclusion

Polyimides containing chain-length-controlled polysiloxanes were synthesized by the polymerization of BPDA and newly synthesized PDMS-diamine. The solubility of prepared PI was found to be more strongly derived from the PDMS segment than from the aromatic segment. The

higher-order structure was formed by the microphase separation of PDMS and PI domains and the stacking of PDMS-PI chains due to the weak interactions between them. These structures are considered to change with heat, and this PDMS-PI also has thermotropic liquid crystalline properties.

Acknowledgement

Part of this work was financially supported by JST-CREST (JPMJCR19I3, Prof. Junko Morikawa) and JSPS KAKENHI Grant 20H02785 and 21K04828.

References

1. Ghosh, K. M., and K. L. Mittal, *Polyimides Fundamentals and Applications* (ed, Marcel Decker, New York, 1996)
2. M. Ding, *Prog. Polym. Sci*., **32** (2007) 623.
3. D. Liaw, K.-L. Wang, Y.-C. Huang, K.-R. Lee, J. Lai, and C. Ha, *Prog. Polym. Sci.*, **37** (2012) 907.
4. M. Hasegawa, and K. Horie, *Prog. Polym. Sci.,* **26** (2001) 259.
5. H. Araki, Y. Kikuchi, A. Shimada, H. Ogasawara, M. Jukei, and M.Tomikawa, *J. Photopolym. Sci. Technol.*, **33** (2020) 165.
6. V. J. Eddy, and J. E. Hallgren, U.S. Patent 4 542 226 (1985).
7. V. J. Eddy, J. E. Hallgren, and R. E. Colborn, *J. Polym. Sci.*, *Part A*, *Polym. Chem*., **28** (1990) 2417.
8. L. Xiong, X. Wang, H. Qi, and F. Liu, *J. Appl. Polym. Sci.*, 127 (2013) 1493.
9. C. M. Mahoney, J. A. Gardella, and J. C. Rosenfeld, *Macromolecules*, **35** (2002) 5256.
10. M. E. Rogers, T. E. Glass, S. J. Mecham, D. Rodrigues, G. L. Wilkes, and J. E. McGrath, *J. Polym. Sci*., *Part A*, *Polym. Chem.* **32** (1994) 2663.
11. S. Rimdusit, W. Benjapan, S. Assabumrungrat, T. Takeichi, and R. Yokota, *Polym. Eng. Sci*., **47** (2007) 489.
12. W.-C. Liaw, and K.-P. Chen, *J. Appl. Polym. Sci*., **105** (2007) 809.
13. W.-C. Liaw, and K.-P. Chen, *J. Polym. Res.*, **14** (2007) 5.
14. A. Ghosh, and S. Banerjee, *Polym. Adv. Technol.*, **19** (2008) 1486.
15. M. B. H. Othman, M. R. Ramli, L. Y. Tyng, Z. Ahmad, and H. M. Akil, *Mater. Des.*, **32** (2011) 3173.
16. X. Pei, G. Chen, J. Liu, and X. Fang, *Polymer*, **56** (2015) 229.
17. H. Qi, X. Wang, T. Zhu, J. Li, L. Xiong, F. Liu, *ACS Omega*, **4** (2019) 22143.
18. K. Fuchise, M. Igarashi, K. Sato, and S. Shimada, *Chem. Sci.*, **9** (2018) 2879.
19. G. G. Lohmeijer, G. Dubois, F. Leibfarth, R. C. Pratt, F. Nederberg, A. Nelson, R. M. Waymouth, C. Wade, and J. L. Hedrick, *ORGANIC LETTERS*, Vol.8 No.21 (2006) 4683.
20. Y. Shoji, R. Ishige, T. Higashihara, S. Kawauchi, J. Watanabe, and M. Ueda, *Macromolecules*, **43** (2010) 8950.
21. C. A. Arnold, J. D. Summer, and J. E. Mcgrath, *Polym. Eng. Sci*., **29** (1989) 1413.

Fabrication of Polyimide Nano-Particles by Precipitation Polymerization

Satoshi Kuretani[1], Yuta Nabae[1]* and Teruaki Hayakawa[1]

[1] Department of Materials Science and Engineering, School of Materials and Chemical Technology, Tokyo Institute of Technology, 2-12-1 S8-26 Ookayama, Meguro-ku, Tokyo 152-8552, Japan
**nabae.y.aa@m.titech.ac.jp*

Polyimides have been widely used as high-performance polymers, but controlling their morphology is still challenging. This study focuses on fabricating spherical polyimide particles by the precipitation polymerization of diamine and tetracarboxylic dianhydride monomers. Polyimide particles were prepared by changing the concentration and structure of the monomers in the presence of a dispersant, and the effect of these conditions on the size and distribution of the particles are discussed. The effect of crosslinking by a triamine monomer is also described.

Keywords: Polyimide, Nano-particles, Particle size, Dispersant

1. Introduction

Polyimide has excellent thermal stability, chemical stability, mechanical toughness and electrical insulation properties, and has been applied in various fields [1-4]. In terms of expanding the application of polyimides, controlling the morphology of polyimides is meaningful [5-13]. Our research group is especially interested in spherical polyimides [6, 14].

Spherical particles of polyimide have been typically fabricated by reprecipitation, suspension polymerization, and precipitation polymerization. The precipitation polymerization is especially suitable for a large-scale synthesis of small nano-particles below 500 nm [15-19]. Indeed, our research group has demonstrated the fabrication of polyimide nano-particles with 50-60 nm of diameters [20], which can be used as a good precursor for catalytically active nano-carbons in fuel cells [14].

In this context, we are motivated to fabricate an even smaller particle size of polyimide. In the preparation of polyimide particles by the precipitation polymerization, stabilizing the polymer/solvent interface is important to control the particle size, and dispersants such as *N,N*-dimethyldodecylamine are quite effective [20, 21]. The concentration of monomers is also an important parameter [6]. Furthermore, crosslinking of the polymer could affect the particle size, because it will enhance the precipitation of polymer droplets during the polymerization. To the best our knowledge, 50-60 nm of polyimide nano-particles are the smallest in the reported studies, and we have been interested in even smaller particle sizes of polyimides.

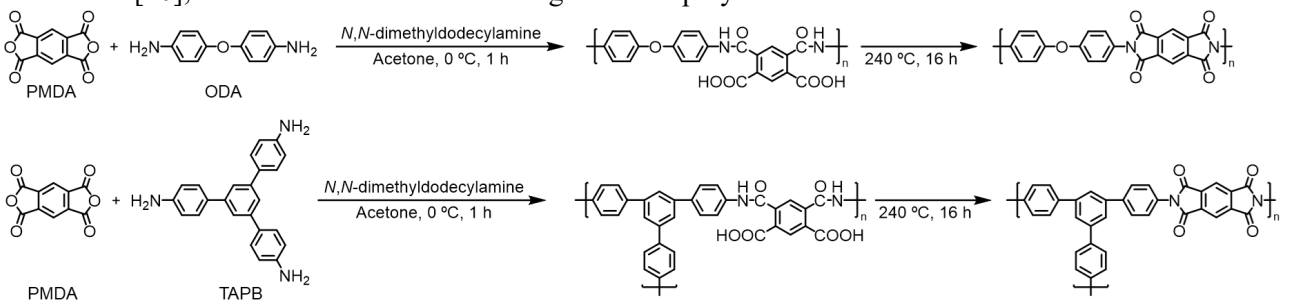

Scheme 1. Synthesis of polyimide nano-particle by precipitation polymerization.

Received	April 1, 2022
Accepted	June 20, 2022

The purpose of this study is to clarify the polymerization conditions to obtain sub-50 nm of polyimides. As shown in Scheme 1, the precipitation polymerization of pyromellitic dianhydride (PMDA) and 4,4'-oxydianiline (ODA) was studied as the polymerization of the most common monomers. Furthermore, 1,3,5-tris(4-aminophenyl)benzene (TAPB) was also studied to investigate the effect of crosslinking. The effect of the concentration of monomers and addition of dispersant were carefully investigated.

2. Experimental

2.1. Materials

PMDA and ODA were purchased from Tokyo Chemical Industry and purified by sublimation before use. TAPB, purchased from Tokyo Chemical Industry, was used as purchased. All the other chemicals were reagent grade and used as received, unless otherwise stated.

2.2. Precipitation polymerization of PMDA and ODA .

A solution of PMDA (0.09 mol L^{-1}) and *N,N*-dimethyldodecylamine (1.85×10^{-3} mol L^{-1}) in acetone (50 ml) and a solution of ODA (0.09 mol L^{-1}) in acetone (50 ml) were each stirred at 0°C for 20 min. The solution of ODA was added to the solution of PMDA and *N,N*-dimethyldodecylamine, and the mixture was stirred at 0℃ for 60 min. After removing the solvent with a rotary evaporator, thermal imidization was performed at 240℃ under vacuum for 16 h. The obtained polyimide samples was denoted as PMDA-ODA(0.09) with dispersant. Yield: 99 %. The polymers with other concentrations were prepared by changing the concentration of monomer but retaining the monomer ratio, and denoted as PMDA-ODA(*x*) with dispersant, where *x* (0.005-0.09) represents the molar concentration of PMDA. The polymers without dispersant were also prepared in a similar manner and denoted as PMDA-ODA(*x*) without dispersant.

2.3. Precipitation polymerization of PMDA and TAPB

A solution of PMDA (0.09 mol L^{-1}) and *N,N*-dimethyldodecylamine (1.85×10^{-3} mol L^{-1}) in acetone (50 ml) and a solution of TAPB (0.06 mol L^{-1}) in acetone (50 ml) were each stirred at 0°C for 20 min. The solution of TAPB was added to the solution of PMDA and *N,N*-dimethyldodecylamine, and the mixture was stirred at 0℃ for 60 min. After removing the solvent with a rotary evaporator, thermal imidization was performed at 240℃ under vacuum for 16 h. The obtained polyimide samples were denoted as PMDA-TAPB(0.09) with dispersant. Yield: 99 %. The polymers with other concentrations were prepared by changing the concentration of monomer but retaining the monomer ratio, and denoted as PMDA-TAPB(*x*) with dispersant, where *x* (0.005-0.09) represents the molar concentration of PMDA. The polymers without dispersant were also prepared in a similar manner and denoted as PMDA-TAPB(*x*) without dispersant.

2.4. Measurements

Field emission scanning electron microscopy (FE-SEM) was conducted using an S-5500 microscope (Hitachi-hightech) at 1.0-3.0 kV. Fourier transform infrared (FT-IR) spectra of the poly(amic acid) and polyimide were obtained using a JASCO FT-IR 4100 spectrometer by the KBr pellet method.

3. Results and discussion

3.1. Synthesis of polyimide nano-particles

The polyimide nano-particles prepared with and without the dispersant were prepared by the synthetic route shown in Schemes 1, and characterized by FT-IR. Fig. 1 shows the FT-IR spectra of the poly(amic acid) and polyimide synthesized with 0.03 mol L^{-1} of PMDA and ODA. Absorption peaks due to amide groups are observed at 1670 cm^{-1} (C=O stretch) and 1550 cm^{-1} (C-N-H stretch) in the spectra (a) and (b), but not observed after the thermal imidization (c and d). In addition, absorption peaks due imide groups are observed at 1780 cm^{-1} (C=O stretch) and 1375 cm^{-1} (C-N-C stretch), suggesting that the imidization has fully progressed. The polyimide nano-particles from PMDA and TAPB were also prepared in a similar manner, and their FT-IR spectra were shown in Fig. 2, suggesting that the imidization has fully progressed.

3.2. Polymerization without dispersant

The polyimide nano-particles were prepared under various polymerization conditions, and the results of FE-SEM are summarized in Fig. 3, Table 1 and Fig. 4. The PMDA-ODA(*x*) without dispersant showed relatively large sizes of polyimide particles over 200 nm of diameters. The uniformity of the particles is fairly good, yielding

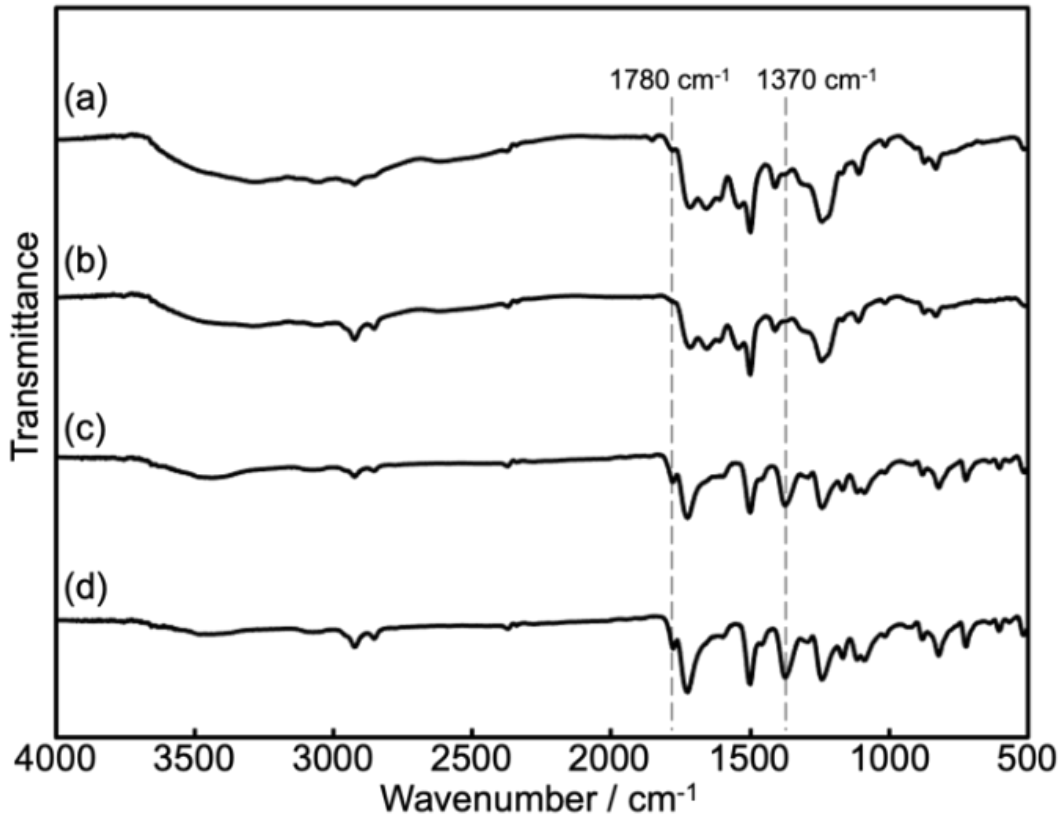

Fig. 1. FT-IR spectra of the poly(amic acid)s from PMDA and ODA (a) without and (b) with dispersant, and the polyimides (c) without and (d) with dispersant.

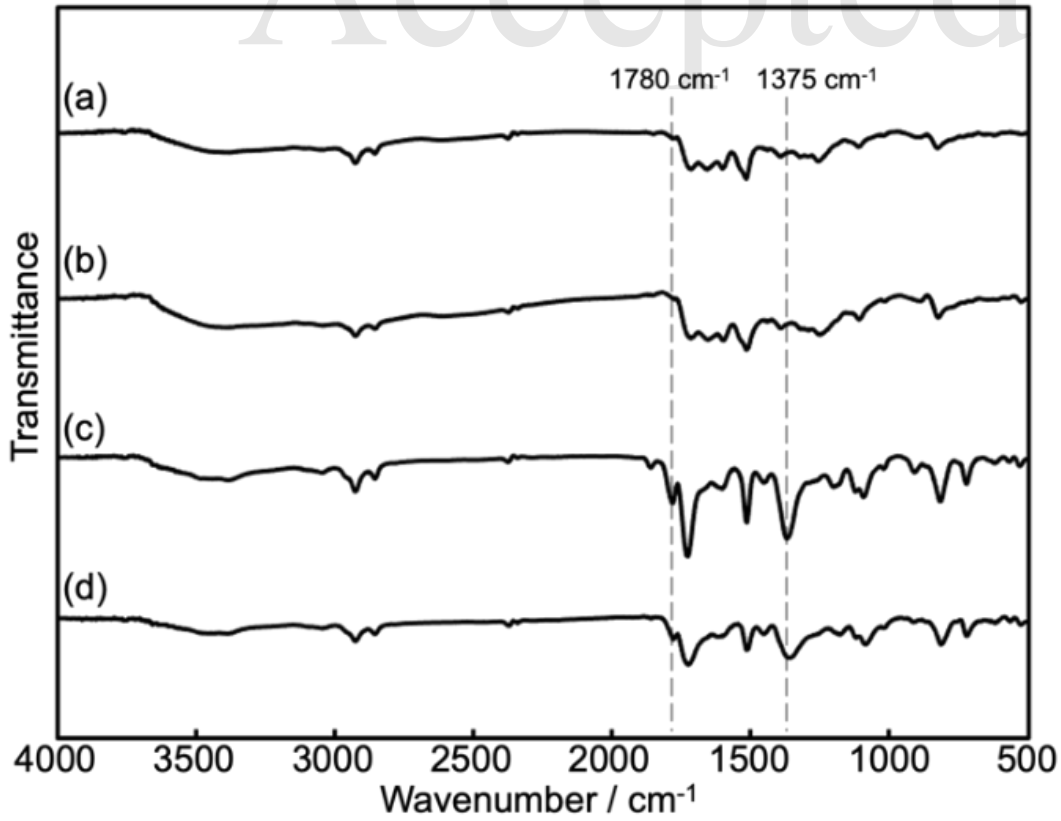

Fig. 2. FT-IR spectra of the poly(amic acid)s from PMDA and TAPB (a) without and (b) with dispersant, and the polyimides (c) without and (d) with dispersant.

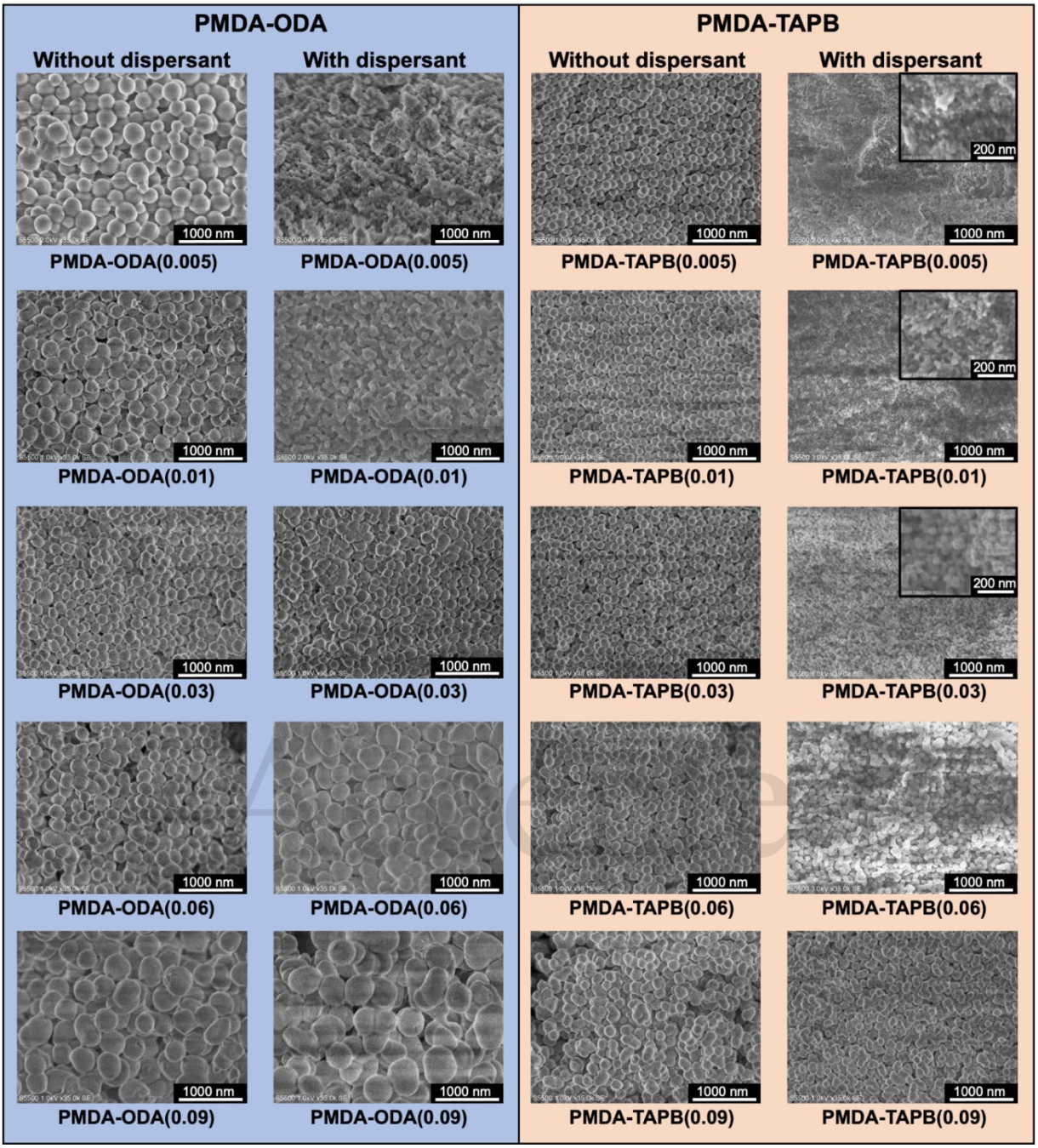

Fig. 3. FE-SEM images of PMDA-ODA(x) and PMDA-TAPB(x) prepared by the precipitation polymerization.

Table.1. Particle size and standard deviation of PMDA-ODA(x) and PMDA-TAPB(x).

x [a] (mol L^{-1})	PMDA-ODA				PMDA-TAPB			
	Without dispersant		With dispersant		Without dispersant		With dispersant	
	Particle size[b] / nm	σ[b]/ nm	Particle size[b] / nm	σ[b]/ nm	Particle size[b] / nm	σ[b]/ nm	Particle size[b] / nm	σ[b]/ nm
0.005	280	44	72	5	162	10	21	2
0.01	250	33	112	13	137	11	29	2
0.03	166	15	157	13	127	13	43	4
0.06	208	16	289	18	148	11	75	5
0.09	363	44	466	35	169	13	119	16

[a] PMDA concentrations for the synthesis (PMDA:ODA = 1:1, PMDA:TAPB = 1.5:1).
[b] Standard deviation calculated from the FE-SEM images.

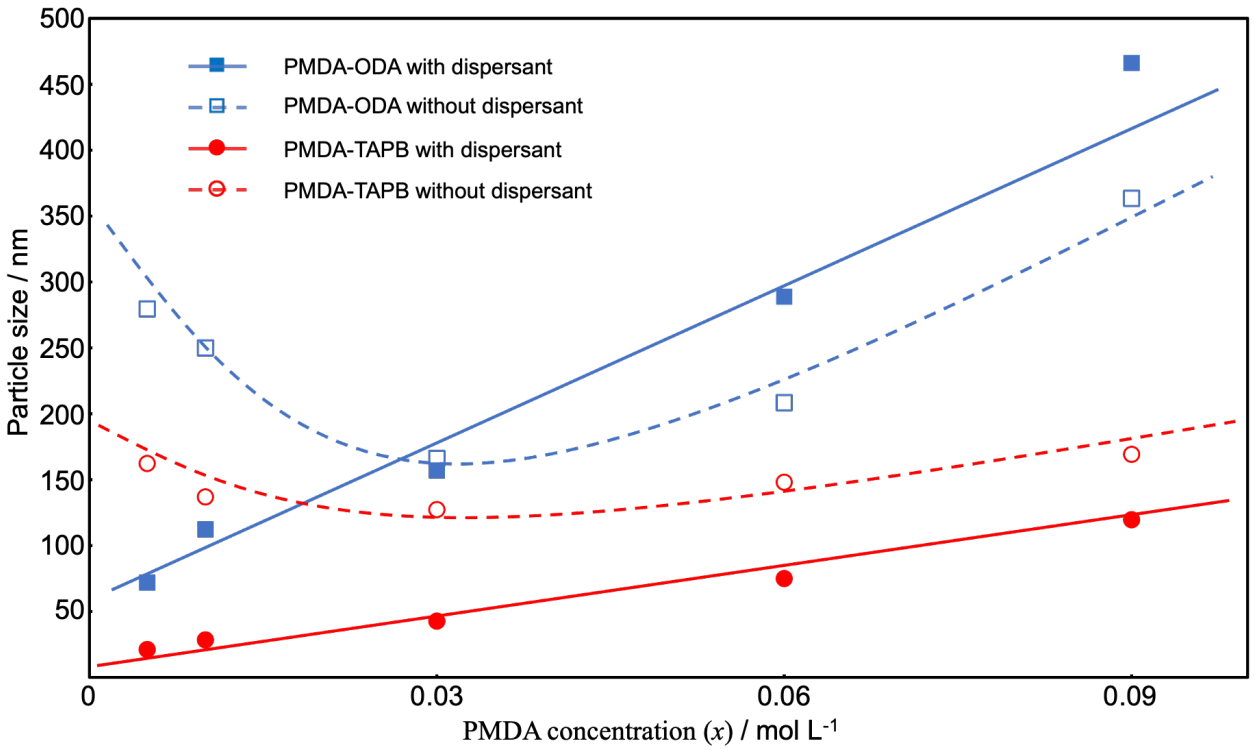

Fig. 4. Monomer concentration dependency of PMDA-ODA(x) and PMDA-TAPB(x).

standard deviations below 50 nm. The PMDA-TAPB(x) without dispersant showed smaller particle sizes around 150 nm, accompanied by standard deviations below 15 nm. The monomer concentration dependency showed U-shaped curves for PMDA-ODA(x) and PMDA-TAPB(x). This trend is probably derived from the solubility of the polymers during the polymerization. If the concentration of monomer is low, the concentration of the resulting polymer will be also low, and relatively long polymer chains can dissolve in the solvent. On the contrary, if the monomer concentration is extremely high, the polymer chains can grow rapidly before precipitation, resulting in relatively large particle sizes.

3.3. Polymerization with dispersant

The tendency observed for the polymerization with the dispersant was quite different from that without dispersant. As shown in Fig 4, in both cases of PMDA-ODA(x) and PMDA-TAPB(x), the particle sizes increased as the monomer concentration increased. This tendency could be relevant to the dispersant/monomer ratio. In the presence of the dispersant, the dispersant will form a micelle structure surrounding the poly(amic acid) droplet, to stabilize the polymer/solvent interface. A high dispersant/monomer ratio will contribute to the formation of a small droplet, and probably result in a small size of poly(amic acid).

3.4 Effect of crosslinking

As shown in Fig. 4, in both cases of the polymerizations with and without the dispersant, TAPB provided smaller particle sizes of polyimides than ODA. This is probably derived from the crosslinking of the polymers. The crosslinked polymer would probably form small and insoluble polymer droplets at a quite early stage of polymerization, and it would work as a nucleus of precipitate. It should be noted that PMDA-TAPB(0.005) with dispersant provided 21 nm of diameter. This is a much smaller particle size than previously reported ones [10,16]; therefore, is probably the smallest size for polyimide nano-particles in the world.

4. Conclusion

Polyimide nano-particles with diameters of about 20 nm were successfully prepared by precipitation polymerization. By investigating the effect of the monomer concentration, it was found that the particle size of polyimide particles with the dispersant linearly increases as the monomer concentration increases. It was also found that the crosslinking of the polymer contributes to forming

small nano-particles. Since the present findings have clarified the tendency for controlling the particle size of polyimides, various functional polyimide nano-particles are expected to be developed for a wide range of applications.

Acknowledgement

This study was supported by the New Energy and Industrial Technology Development Organization (NEDO) and JSPS KAKENHI (21K04828). The FE-SEM measurements were supported by a project for promoting public utilization of advanced research infrastructure by MEXT (JPMXS0420900521).

References

1. C. E. Sroog, *J. Polym. Sci. Macromolecular Reviews*, **11** (1976) 161.
2. M. Suwa, Y. Fujita, T. Yuba, S. Yoshida and M. Tomikawa, *J. Photopolym. Sci. Technol*., **16** (2003) 221.
3. T. Komamura, K. Okuhara, S. Horiuchi, Y. Nabae and T. Hayakawa, *ACS Appl. Polym. Mater*., **1** (2019) 1209.
4. H. Yabu, M. Tanaka, K. Ijiro and M. Shimomura, *Langmuir,* **19** (2003) 6297.
5. Y. Nabae, S. Nagata, K. Ohnishi, Y. Liu, L. Sheng, X. Wang, and T. Hayakawa, *J. Polym. Sci. Part A: Polym. Chem*., **55** (2017) 464.
6. Y. Nabae, Y. Kuang, M. Chokai, T. Ichihara, A. Isoda, T. Hayakawa, and T. Aoki, *J. Mater. Chem. A*, **2** (2014) 11561.
7. L. Gao, A. Chandra, Y. Nabae, and T. Hayakawa, *Polym. J*., **50** (2018) 389.
8. T. Komamura, K. Okuhara, S. Horiuchi, Y. Nabae, and T. Hayakawa, *ACS Appl. Polym. Mater*., **1** (2019) 1209.
9. Y. Liu, K. Ohnishi, S. Sugimoto, K. Okuhara, R. Maeda, Y. Nabae, M. Kakimoto, X. Wang, and T. Hayakawa, *Polym. Chem*., **5** (2014) 6452.
10. M. Chokai, Y. Nabae, S. Kuroki, T. Hayakawa, M. Kakimoto and S. Miyata, *J. Photopolym. Sci. Technol*., **24** (2011) 241.
11. Y. Nabae, S. Nagata, K. Kusaba, T. Aoki, T. Hayakawa, H. Tanida, H. Imai, K. Hori, Y. Yamamoto, S. Arai and J. Ohyama, *Catal. Sci. Technol*., **10** (2020) 493.
12. Y. Nabae and S. Nagata, *J. Photopolym. Sci. Technol*., **29** (2016) 255.
13. Y. Nabae, *Catalysts*, **8** (2018) 324.
14. Y. Nabae, S. Nagata, T. Hayakawa, H. Niwa, Y. Harada, M. Oshima, A. Isoda, A. Matsunaga, K. Tanaka and T. Aoki, *Sci. Rep*., **6** (2016) 1.
15. T. Lin, K. W. Stickney, M. Rogers, J. S. Riffle, J. E. McGrath and H. Marand, *Polymer*, **34** (1993) 772.
16. J. Y. Xiong, X. Y. Liu, S. B. Chen and T. S. Chung, *J. Phys. Chem. B*, **109** (2005) 13877.
17. K. Asao, *J. Photopolym. Sci. Technol*., **27** (2014)181.
18. L. Wang, J. Lu, M. Liu, Li. Lin and J. Li, *Particuology*, **14** (2014) 63.
19. Y. Nabae, M. Mikumi, T. Hayakawa and M. Kakimoto, *J. Photopolym. Sci. Technol*., **27** (2014) 139.
20. K. Hori, S. Nagata, Y. Nabae, and T. Hayakawa, *J. Photopolym. Sci. Technol*., **33** (2020) 327.
21. S. Watanabe, K. Okamoto, T. Namikoshi, Y. Kohari and M. Murata, *Polym. J*., **51** (2019) 405.

Synthesis and Properties of Polyguanamines Containing *N*-Phenylmelamine Units

Tadashi Tsukamoto[1], Yuji Shibasaki[1], and Yoshiyuki Oishi[*1]

[1] *Department of Chemistry & Biological Science, Faculty of Science & Engineering, Iwate University, 4-3-5 Ueda, Morioka, Iwate 020-8551, Japan*
**yoshiyu@iwate-u.ac.jp*

The polyguanamines were prepared by the polymerization of bis[*N*-(2-anilino-4-chloro-1,3,5-triazine)yl]-4,4'-oxydianiline (**Bis(ACT)**) with α,ω-alkylene diamines such as 1,12-diaminododecane, 1,10-diaminodecane and 1,8-diaminooctane. The NMR analysis of **Bis(ACT)** and the resulting polyguanamines showed that the hydrogen bonds cause between triazine and adjacent anilino units. The resulting polyguanamines have good solubility in typical organic solvent. Temperatures where 5% weight losses of the polyguanamines occur under N_2 flow are in the rage of 435-449°C. The glass transition temperatures (T_g) are in the range of 133-156°C. Almost colorless and flexible films were successfully prepared by a solution casting method. The optical transmittance of films was high as 80% at 400 nm. Furthermore, the films exhibited high reflective index around 1.67.

Keywords: Polyguanamine, Polycondensation, Thermal stability, High reflective index

1. Introduction

Dichlorotriazine compounds are easily polymerized *via* nucleophilic substitution polycondensation with di-functional nucleophiles such as diamines, diols and dithiols to afford the corresponding polyguanamines, polycyanurates and polythiocyanurates [1-20], respectively. These polymers exhibit good thermal stability and optical property derived from the triazine skeleton, which is a six-membered heterocyclic aromatic ring. Polyguanamines particularly draw much attentions because the polymers have unique hydrogen bond networks with the films. While, wholly aromatic polyguanamines show poor solubility due to the hydrogen-bonded networks, aliphatic polyguanamines have better solubility. However, they sometimes crystalize, and thus deteriorate not only solubility but also thermal and optical properties [14]. In this work, we have developed polyguanamines from a triazine-based hard segment, which was prepared by the condensation of two equiv. 2-nilino-4,6-dichloro-1,3,5-triazine (**AnDCT**) with 4,4'-oxydianiline (**ODA**), with α,ω–alkylene diamines as solvent processable optical polymers.

Received	March 30, 2022
Accepted	June 24, 2022

2. Experimental

2.1 Materials

AnDCT was prepared by nucleophilic substitution reaction of cyanuric chloride with aniline in the presence of Na_2CO_3, according to our previous report [10]. All solvents were distilled or dried before use according to the general purification procedure. Commercially available reagents including cyanuric chloride, aniline, **ODA**, triethylamine (Et_3N), 1,12-diaminododecane, 1,10-diaminodecane, 1,8-diaminooctane, (Tokyo Chemical Industry Co., Ltd.), sodium carbonate (Na_2CO_3) and sodium hydrogen carbonate ($NaHCO_3$) (FUJIFILM Wako Chemicals Co., Ltd.) were used without further purification unless otherwise noted.

2.2 Measurement

The ^1H and ^{13}C NMR spectra were measured on a BRUKER Biospin AVANCE III HD 500 spectrometer at 500 and 125 MHz, respectively. ^1H NMR shifts were expressed in parts per million relatives to the internal standard $(CH_3)_2SO$ (δ, 2.49). ^{13}C NMR shifts were referenced to the solvent of DMSO-d_6 (δ, 39.5). FT-IR spectra were measured

on a JASCO FT-IR 4200. High resolution mass spectra (HR-MS) were measured on a JEOL JMS-700 mass spectrometer using fast atom bombardment (FAB) method. Elemental analyses were performed on a YANAKO CHN CORDER MT-6. The M_n, M_w and M_w / M_n values were determined using a Tosoh HLC-8220 gel permeation chromatograph (GPC) equipped with a RI detector and a consecutive polystyrene gel column (TSK-gel α-M x 2) at 40°C and eluted with NMP containing 0.01 mol / L LiBr at a flow rate of 1.0 mL/min. UV-vis spectra were measured on a Shimadzu UV-1800. Thermogravimetric analysis (TGA) was performed on a Hitachi TG/DTA7220 at a heating rate of 10°C/min. Differential scanning calorimetry (DSC) was performed on a Hitachi DSC7000 at a heating rate of 20°C/min. In-plane (n_{TE}) and out-of-plane (n_{TM}) refractive indexes of polymer films measured out using a Metricon Prism Coupler Model 2010/M.

2.3 Film preparation

The polymer samples were dissolved in THF (10 wt%), and the homogeneous solution was drop-cast onto a glass plate. After drying in desiccator at room temperature for 12 h, the film was dried at temperatures of 60°C for 3 h.

2.3 Synthesis of **Bis(ACT)**

The solution of **AnDCT** (4.82 g, 20 mmol) in NMP (30 mL) was stirred at r.t., and the solution of **ODA** (2.00 g, 10 mmol) in NMP (20 mL) was added. After stirred at r.t. for 5 min, NEt_3 (2.02 g, 20 mmol) was added, and then stirred at r.t. for 1 h. The reaction mixture was poured into brine in a beaker and extracted with THF three times. The combined extracts were dried over anhydrous Na_2SO_4. After removal of the drying reagent, THF was removed under reduced pressure. The crude product was purified using column chromatography (THF:Hexane=3:1) to give pure **Bis(ACT)** as a white powder in 75% yield (4.56 g). ^{1}H NMR (500 MHz, DMSO-d_6, 80°C) δ: 9.93 (br, 4H), 7.71-7.58 (m, 8H), 7.30 (t, 4H, J=5 Hz), 7.07 (t, 2H, J=5 Hz), 6.99 (d, 4H, J=10 Hz) ppm. ^{13}C NMR (125 MHz, DMSO-d_6, 80°C) δ: 168.8, 164.5, 164.4, 153.6, 138.9, 134.3, 128.9, 124.0, 123.5, 121.6, 119.0 ppm. FT-IR ν (KBr): 3388 (N-H), 3262 (N-H), 1576 (C=C), 1493 (C=N), 1216 (C-N), 985 (C-Cl) cm^{-1}. HRMS (FAB-MS, positive) (*m/z*) for C30H23Cl2N10O ([M+H]$^+$): Calculated 609.1433; Found 609.1433. Anal. Calcd. For C30H22Cl2N10O: C 59.21; H 3.64; N 22.98, Found: C 58.88; H 3.78; N 22.92.

2.4 Synthesis of **PG1**

All glass vessels were heated *in vacuo* before use. In a three-necked flask equipped with a three-way stopcock, a reflux condenser, and a mechanical stirrer, $NaHCO_3$ (168 mg, 2.0 mmol) and 1,12-diaminododecane (200 mg, 1.0 mmol) were dissolved in dry NMP (2.0 mL) at r.t.. To this solution, **Bis(ACT)** (609 mg, 1.0 mmol) and distilled water (1.0 mL) were added in that order. The mixture was stirred for 10 min and then the polymerization was performed at 100°C for 24 h. The polymerization solution was cooled to r.t. and then poured into an excess amount of methanol. The precipitate was dried at r.t. for 12 h, washed with hot methanol, and dried at 100°C for 12 h under reduced pressure. **PG1** was obtained in 98% yield (722 mg). ^{1}H NMR (500 MHz, DMSO-d_6, 80°C) δ: 8.71 (br, 4H), 7.82-7.69 (m, 8H), 7.21 (t, 4H, J=5 Hz), 6.96-6.86 (m, 6H), 6.73 (br, 2H), 3.29 (q, 4H, J=5, 15 Hz), 1.60-1.49 (m, 4H), 1.38-1.14 (m, 16H) ppm. ^{13}C NMR (125 MHz, DMSO-d_6, r.t.) δ: 166.1, 164.6, 164.4, 152.2, 140.9, 136.3, 128.7, 121.9, 120.3, 118.7, 40.6, 29.8, 29.6, 29.4, 27.1 ppm. FT-IR ν (KBr): 3413 (N-H), 3278 (N-H), 2925 (Aromatic C-H), 2852 (Alkyl C-H), 1580 (C=C), 1494 (C=N), 1216 (C-N) cm^{-1}. Anal. Calcd. For C42H48N12O: C 68.45; H 6.57; N 22.81, Found: C 68.36; H 6.64; N 22.71.

2.4 Synthesis of **PG2**

A similar procedure described above was used except for using 1,10-diaminodecane (172 mg, 1.0 mmol) instead of 1,12-diaminododecane. The yield was 89%. (631 mg). ^{1}H NMR (500 MHz, DMSO-d_6, 80°C) δ: 8.68 (br, 4H), 7.83-7.66 (m, 8H), 7.21 (t, 4H, J=5 Hz), 6.96-6.86 (m, 6H), 6.70 (br, 2H), 3.35-3.25 (m, 4H), 1.60-1.49 (m, 4H), 1.38-1.18 (m, 12H) ppm. ^{13}C NMR (125 MHz, DMSO-d_6, r.t.) δ: 166.1, 164.6, 164.4, 152.2, 140.9, 136.2, 128.7, 121.9, 120.3, 118.7, 40.7, 29.8, 29.6, 29.4, 27.1 ppm. FT-IR ν (KBr): 3413 (N-H), 3278 (N-H), 2925 (Aromatic C-H), 2853 (Alkyl C-H), 1578 (C=C), 1497 (C=N), 1218 (C-N) cm^{-1}. Anal. Calcd. For C40H44N12O: C 67.77; H 6.26; N 23.71, Found: C 67.49; H 6.30; N 23.55.

2.4 Synthesis of **PG3**

A similar procedure described above was used except for using 1,8-diaminooctane (144 mg, 1.0 mmol) instead of 1,12-diaminododecane. The yield was 64% (436 mg). ^{1}H NMR (500 MHz, DMSO-d_6, r.t.) δ:9.14-8.80 (m, 4H), 7.85-7.53 (m, 8H), 7.21 (t, 4H, J=5 Hz), 7.10-6.80 (m, 6H), 3.40-3.15 (m, 4H), 1.62-1.42 (m, 4H), 1.39-1.07 (m, 8H) ppm. ^{13}C NMR (125 MHz, DMSO-d_6, r.t.) δ: 166.1, 164.6, 164.4, 152.2, 140.9, 136.2, 128.7, 121.9, 121.9, 120.3, 118.7, 40.7, 29.8, 29.5, 27.1 ppm. FT-IR ν (KBr): 3409 (N-H), 3272 (N-H), 2925 (Aromatic C-H), 2853 (Alkyl C-H), 1578 (C=C), 1507 (C=N),

1225 (C-N) cm^{-1}. Anal. Calcd. For C38H40N12O: C 67.04; H 5.92; N 24.69, Found: C 63.81; H 5.70; N 23.33.

3. Results and discussion

3.1. Monomer preparation and structure analysis

Firstly, preparation of **Bis(ACT)** was conducted under the various reaction conditions (Table 1).

Table 1. Synthesis of **Bis(ACT)** monomer

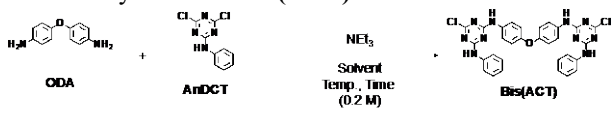

Run	Solvent	Base	Temp.	Time / h	Yield / %
1	Acetone	Na_2CO_3	r.t.	12	20
2	Acetone	Na_2CO_3	reflux	12	14
3	NMP	Na_2CO_3	r.t.	12	65
4	NMP	NEt_3	r.t.	12	73
5	NMP	NEt_3	r.t.	1	75

When the similar conditions to the synthesis of **AnDCT**, which was nucleophilic substitution reaction with Na_2CO_3 in acetone / H_2O at room temperature, was employed, heterogeneous reaction proceeded to give **Bis(ACT)** in 20% yield (Run 1). However, a large amount of unreacted **AnDCT** and a biproduct were recovered. Then, the reaction temperature was changed to reflux, but the yield of the **Bis(ACT)** decreased and the biproducts increased (Run 2). When the solvent was replaced to NMP in order to keep a homogeneous reaction system, the yield of **Bis(ACT)** product increased. By using NEt_3 as the base, **AnDCT** was consumed and the reaction was completed in 1 h to obtain **Bis(ACT)** in 75% yield.

The structure of **Bis(ACT)** was characterized by one-dimensional (1D) and two-dimensional (2D) NMR spectroscopy, FT-IR, FAB-high-resolution mass spectrometry (FAB-HR-MS) and elemental analysis. Fig. 1 shows the variable temperature (VT)-NMR experiments of **Bis(ACT)**. As the measurement temperature was raised from 30-80°C, the signals of guanamine N-H ($H_{d,\ e}$) and aromatic protons became gradually sharp. The result exhibits that the protons at 30°C fixed by intramolecular hydrogen bonds between the triazine and the adjacent anilino units moved as the temperature increased.

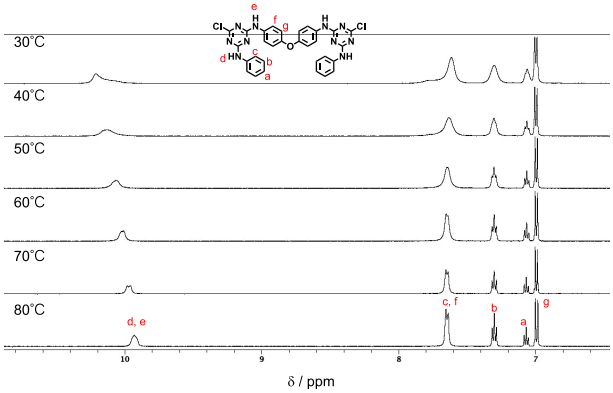

Fig. 1. VT-NMR spectra of **Bis(ACT)** (500 MHz, DMSO-d_6).

3.2. Synthesis and structure analysis of polyguanamines (**PG1-3**)

Polymerization of **Bis(ACT)** with 1,12-diaminododecane/1,10-diaminodecane/1,8-diaminooctane was performed in the presence of $NaHCO_3$ in NMP/H_2O at 100°C for 24 h (Table 2).

Table 2. Synthesis of **PG1-3**

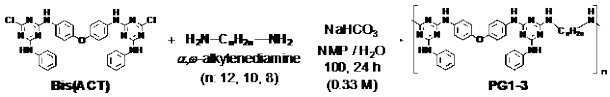

Run	n	Polyguanamine	Yield / %	M_n / $10^{4\ a)}$	M_w / $10^{4\ a)}$	M_w / M_n a)
1	12	**PG1**	98	3.69	15.23	4.13
2	10	**PG2**	89	3.49	12.49	3.58
3	8	**PG3**	64	1.01	6.42	6.38

a) Determined by GPC (eluent: NMP / LiBr) detected RI.

The resulting **PG1-3** were obtained in 98, 89 and 64% yields, and the M_ns were measured to be 36900, 34900 and 10100, respectively. The structures of **PG1-3** were characterized by NMR, FT-IR, elemental analysis and GPC. Fig. 2 shows VT-NMR spectra of **PG1**. Similar to the **Bis(ACT)**, the signals of aromatic and aliphatic protons became sharp from broad by raising the temperature of 30-80°C. On the other side, the protons of guanamine ($H_{d,e}$) were divided into multiple parts at 30°C, but it changed to one broad signal with the up field shift as the temperature raise. The result suggests that the intramolecular hydrogen bond acts strongly not only monomer **Bis(ACT)** but also **PG**s. Similar changes were observed with **PG2** and **PG3**.

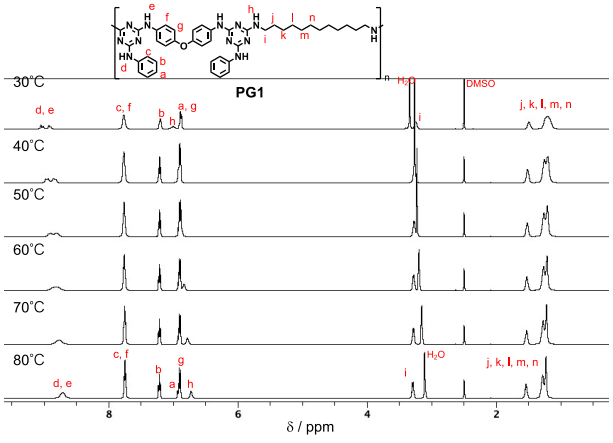

Fig. 2. VT-NMR spectra of **PG1** (500 MHz, DMSO-d_6)

Fig. 3 shows the FT-IR spectra of **PG1-3** and **Bis(ACT)** for comparison. N-H absorption was observed at 3400-3200 cm^{-1}, along with absorptions assignable to C-H at 2925, 2852 cm^{-1} and aromatic C=C and C=N at 1580 and 1494 cm^{-1}, respectively.

Fig. 3. FT-IR spectra of **Bis(ACT)** and **PG1-3**.

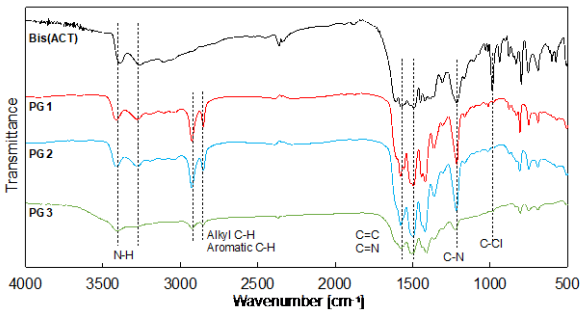

The solubilities of **PG1-3** are summarized in Table 3. All of the polymers were soluble in typical organic solvent such as NMP, DMF, DMSO and THF at r.t., however insoluble in chloroform. It is noteworthy that **PG1-3** dissolves in cyclohexanone, a relatively less polar solvent. In addition, the resulting **PG1-3** were more soluble in a wider range of solvents than the previously reported ones [14].

Table 3. Solubility of **PG1-3**[a)]

	NMP	DMF	DMSO	THF	*c*-hexanone[b)]	Chloroform
PG1	++	++	++	++	++	–
PG2	++	++	++	++	++	–
PG3	++	++	++	++	+	–

a) Polymer 2 mg / Solvent 1 mL, ++, soluble at r.t.; +, partially insoluble; –, insoluble.
b) Cyclohexanone.

3.3. Thermal properties

Thermogravimetric analysis of the **PG1-3** disclosed excellent thermal stability under N_2. No loss of weight in the temperature which rage up to 400°C was observed about **PG1** and **PG2**. On the other hand, T_{d5} value of **PG3** is about 10°C lower than the other two, it may decompose from a lower molecular weight, which may be due to the slightly lower molecular weight of **PG3**. DSC measurement revealed that all of **PG**s are amorphous. Glass transition temperatures (T_g) of **PG**s are in 133-156°C, which is higher than that of the previously reported **PG**s prepared *via* polycondensation of **AnDCT** and 1,12-diaminododecane / 1,10-diaminodecane / 1,8-diaminooctane [14]. The increase in T_g is thought to be due to the replacement of the mono(*N*-phenylmelamine) unit with bis(*N*-phenylmelamine) units in the polyguanamines. Possibly, not only intramolecular hydrogen bonds but also intermolecular hydrogen bonds may act more strongly in the solid state.

Table 4. Thermal properties of **PG1-3**.

	T_{d5} / °C[a)]	T_g / °C[a)]
PG1	449	133
PG2	447	144
PG3	435	156

a) Determined by TGA and DSC in N_2 at a heating rate of 10°C / min.

3.4. Optical properties

The optical properties of **PG1-3** films with thickness of 12-9 μm were analyzed using a UV-vis spectrometer and prism coupler, as summarized in Fig. 4 and Table 5. A all of the **PG** films obtained an almost colorless and flexible film. The cutoff wavelengths (λ_{cutoff}) of the **PG1-3** films ranged of 313-320 nm, and the transmittance was as high as 80% at around 500 nm. The films of **PG1-3** show high n_d values around 1.66-1.67 despite having the alkylene main chain, because of the tight packing caused by both the intramolecular and intermolecular interactions and the high molecular refraction of the triazine units.

Table 5. Optical properties of **PG1-3**.

	d[a)] / ∝m	λ_{cutoff}[b)] / nm	T_{500}[c)] / %	Mode[d)]	n_F[e)]	n_d[e)]	n_C[e)]	n_{dav}[e)]	ν_d[f)]
				TE	1.6897	1.6732	1.6550	1.6688	19.4
PG1	12	313	83	TM	1.6765	1.6601	1.6440		20.3
				(Δn[g)])	0.0132	0.0131	0.0110		
				TE	1.6909	1.6706	1.6510	1.6645	16.8
PG2	10	320	82	TM	1.6698	1.6522	1.6302		16.5
				(Δn[g)])	0.0211	0.0184	0.0208		
				TE	1.6986	1.6810	1.6615	1.6765	18.4
PG3	9	319	85	TM	1.6837	1.6676	1.6492		19.4
				(Δn[g)])	0.0149	0.0134	0.0123		

a) Film thickness. b) Cutoff wavelength . c) Trancemittance at 500 nm. d) TE, in-plane; TM, out-of-plane.
e) Refractive index by a prism coupler: F-line, 486 nm; d-line, 589 nm; C-line, 656 nm: $n_{dav}=[(2n_{dTE}^2+n_{dTM}^2)/3]^{1/2}$.
f) Abbe's number: $n_d = (n_d-1)/(n_F-n_C)$. g) Birefringence: $\Delta n=n_{TE}-n_{TM}$.

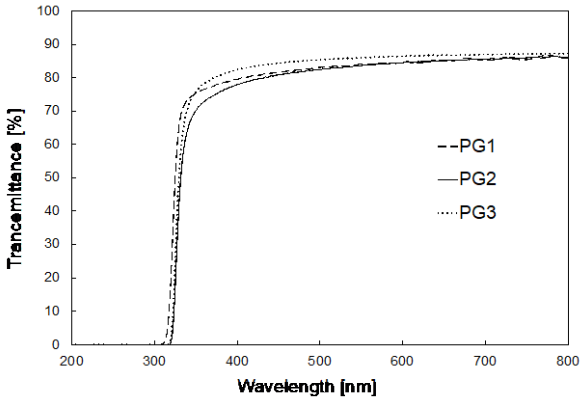

Fig. 4 UV-vis spectra of **PG1-3** films.

4. Conclusion

In this study, we have synthesized **Bis(ACT)**, which prepared *via* condensation of 2 eq. of 2-anilino-dichlorotriazine (**AnDCT**) and 4,4'-oxydianiline (**ODA**) and have developed a series of **PG**s through nucleophilic substitution polymerization of **Bis(ACT)** with α,ω-alkylene diamines. The VT-NMR analysis of the resulting **Bis(ACT)** and **PG**s revealed that intramolecular hydrogen bonds are strongly formed at room temperature in solution. The **PG**s have a high thermal property even though the main chain contained a flexible alkylene chain. The refractive indexes show around 1.66-1.67 with high transparency. The Abbe numbers were in the rage of 16-20, as much as the reported triazine polymers [10, 14, 15, 20]. In particular, **PG3** has comparable T_g with polycarbonate, which is a condensation-based optical material, and exhibits a higher refractive index. In addition, by replacing the anilino site of the side chain or the oxydianilino skeleton that connects the triazine unit in the **Bis(ACT)**, better optical properties will be expected.

References

1. H.K. Reimschuessel, A.M. Lovelace, and E.M. Hagermann, *J. Polym. Sci.*, **40** (1959) 270.
2. G.F. Ehlers, and J.D. Ray, *J. Polym. Sci.*, *Part A-1*, **4** (1966) 1645.
3. D.W. Wang, and M.M. Fisher, *J. Polym. Sci., Polym. Chem. Ed.*, **21** (1983) 671.
4. J.A. Mikroyannidis, *J. Polym. Sci., Polym. Chem. Ed.*, **26** (1988) 583.
5. D. Braun, and T. Ziser, *Angew. Makromol. Chem.*, **219** (1994) 27.
6. D. Braun, and T. Ziser, *Angew. Makromol. Chem.*, **221** (1994) 187.
7. D. Braun, R. Ghahary, and T. Ziser, *Angew. Makromol. Chem.*, **233** (1995) 121.
8. D. Braun, R. Ghahary, and H. Pasch, *Polymer*, **37** (1996) 777.
9. N. Irles, J. Puiggalí, and J.A. Subirana, *Macromol. Chem. Phys.*, **202** (2001) 3316.
10. T. Kotaki, N. Nishimura, M. Ozawa, A. Fujimori, H. Muraoka, S. Ogawa, T. Korenaga, E. Suzuki, Y. Oishi, and Y. Shibasaki, *Polym. Chem.*, **7** (2016) 1297.
11. Y. Shibasaki, T. Koizumi, N. Nishimura, and Y. Oishi, *Chem. Lett.*, **40** (2011) 1132.
12. K. Saito, N. Nishimura, S. Sasaki, Y. Oishi, and Y. Shibasaki, *React. Funct. Polym.*, **73** (2013) 756.
13. S. Miura, Y. Shidara, T. Yunoki, M.A.A. Mamun, Y. Shibasaki, and A. Fujimori, *Macromol. Chem. Phys.*, **218** (2017) 1600520.
14. Y. Shibasaki, T. Kotaki, T. Bito, R. Sasahara, N. Idutsu, A. Fujimori, S. Miura, Y. Shidara, N. Nishimura, and Y. Oishi, *Polymer*, **146** (2018) 12.
15. H. Sasaki, T. Kotaki, A. Fujimori, T. Tsukamoto, E. Suzuki, Y. Oishi, and Y. Shibasaki, *RSC Adv.*, **10** (2020) 1361.
16. Y. Shibasaki, R. Sasahara, Y. Hoshino, T. Tsukamoto, E. Suzuki, and Y. Oishi, *Mater. Today Commun.*, **24** (2020) 101043.
17. R. Shibata, T. Ishihara, T. Tsukamoto, Y. Oishi, Yoshiyuki A. Fujimori, and Y. Shibasaki, *Eur. Polym. J.*, **162** (2022) 110890.
18. Y. Oishi, J. J. Kim, M. Nakamura, H. Hirahara, and K. Mori, *Macromol. Rapid Commun.*, **20** (1999) 294.
19. N.H. You, T. Higashihara, Y. Oishi, S. Ando, and M. Ueda, *Macromolecules*, **43** (2010) 4613.
20. S. Shi, Y. Onodera, T. Tsukamoto, Y. Shibasaki, and Y. Oishi, *J. Photopolym. Sci. Technol.*, **34** (2021) 251.

Fabrication of SiO:CH Particle-agglomerated Films by PECVD with Vinyl-group Organosilicon Reactants

Yuki Nakaizumi[1], K. Hasegawa[1], Yasushi Inoue[1*], Osamu Takai[2],

[1] Department of Advanced Materials Science and Engineering, Graduate School of Engineering, Chiba Institute of Technology, 2-17-1 Tsudanuma, Narashino, Chiba 275-0016, Japan
[2] Materials and Surface Engineering Research Institute, Kanto-gakuin University, 1162-2 Ogikubo, Odawara, Kanagawa 250-0042, Japan
**inoue.yasushi@it-chiba.ac.jp*

Particle-agglomerated films exhibit rough surfaces, which can be suitable for realization of ultra hydrophobicity. We fabricated particles and their deposits of silica with organic functional groups (SiO:CH) by plasma polymerization of organosilicon reactants including methyl and vinyl functional groups. The trimethyl(vinyl)silane reactant showed a uniform deposition of the plasma-polymerized SiO:CH particles in a large area, while the trimethyl (vinyloxy)silane exhibited a localized particle deposition.
Keywords: Plasma-enhanced chemical vapor deposition, Organosilicon reactant, Particle agglomeration, Hydrophobicity

1. Introduction

Silica-based materials with organic constituents (SiO:CH) have attracted much attention because of their interesting features such as water repellency [1-4], low dielectric constants [5-8], and a gas-barrier ability [9-12] based on surface hydrophobic organic groups, low physical densities, and flexible chemical bonding states, respectively, in addition to the characteristics of pure silica such as optical transparency in the visible range, high electrical insulation properties, and chemical inertness. We have studied on hydrophobicity of SiO:CH films fabricated by plasma-enhanced chemical vapor deposition (PECVD) processes with organosilicon reactants, and achieved ultra hydrophobicity with the water contact angle over 150° by simultaneous realization of fabrication of the hydrophobic particles in the plasma and deposition of these particles resulting in a large surface roughness [13-15]. However, the ultra hydrophobic particle-deposited area has been remained to be localized and uncontrollable on the substrates [16-17]. We presume that one of the origin of the nonuniform deposition of the SiO:CH particles is positional fluctuation of the plasma temperature and/or density which result in the localized particle generation. Therefore, application of the reactant molecules with lower activation energies for electron-impact radicalization in the plasmas must be effective for homogenization of the SiO:CH particle deposition.

In this paper, we report on a successful uniform deposition of the SiO:CH particles on the entire area of the substrate surfaces by using vinyl-based organosilicon precursors. Surface morphologies and chemical bonding states of the deposited films were characterized, and reaction mechanisms are discussed.

2. Experimental

The SiO:CH films were deposited by using a capacitively-coupled radio frequency (RF) PECVD system which consists of a chamber, a rotary pump, parallel-plate stainless steel electrodes with the diameter of 200 mm, and a RF power generator (SEREN, R301MK II, frequency : 13.56 MHz). We used p-type Si (100) plates as substrates, which were placed on the center of both the upper grounded and the lower powered electrodes. The distance between these two electrodes were fixed

Received April 4, 2022
Accepted June 20, 2022

at 15 mm. We used trimethyl(vinyloxy)silane (TMVOS : $(CH_3)_3SiOCH=CH_2$) and trimethyl (vinyl)silane (TMVS : $(CH_3)_3SiCH=CH_2$) as the reactant organosilicon materials. Trimethyl-methoxysilane (TMMOS : $(CH_3)_3SiOCH_3$) was also used for comparison to the previous works [16-17]. Figure 1 illustrates a schematic diagram of the capacitively-coupled PECVD system and structures of the reactant molecules. After the chamber was evacuated, Ar, O_2, and one of the reactant organosilicon gases were mixed and introduced into the chamber through a dispersion ring located around the lower electrode. The gas pressures were fixed at Ar : O_2 : the organosilicon = 50 Pa : 40 Pa : 60 Pa (total 150 Pa). Then a glow discharge was generated by applying a RF power of 100 W to the lower electrode. The deposition period was 20 min.

During deposition, the optical emission spectra of the plasmas were measured by a multi-channel spectrometer (Ocean Optics, USB2000+). The microstructures and chemical bonding states of the deposited SiO:CH films were characterized by using a scanning electron microscope (SEM, Hitatchi, S-3000N) and a Fourier-transform infrared spectrometer (IR, JASCO, FT/IR-4000), respectively.

3. Results and discussion

3.1. Optical Emission Spectra

Figure 2 shows the optical emission spectra

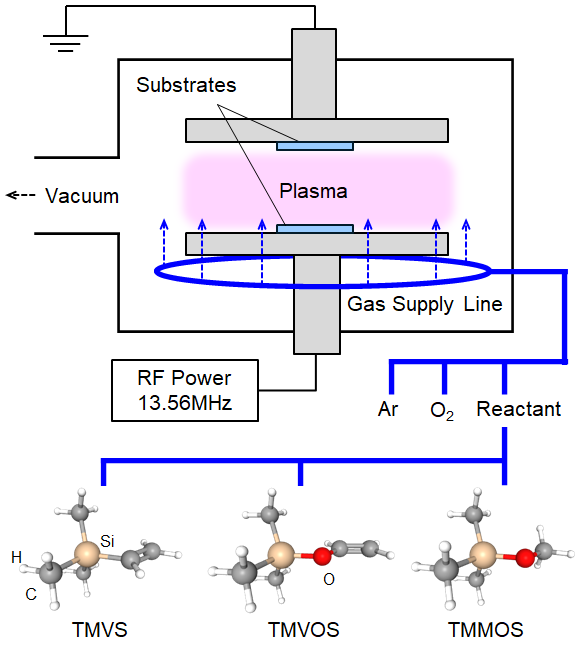

Fig. 1. Schematic illustrations of the PECVD system and reactant molecules used in this study.

Table 1. The emissive species in the plasmas.

Label	Species	Transition
A	OH	$A^2\Sigma^+ - X^2\Pi$
B	CO	$b^3\Sigma - a^3\Pi$ (Third positive system)
C	Ar	5p - 4s
D	CH	$A^2\Delta - X^2\Pi$
E	CO	$B^1\Sigma - A^1\Pi$ (Ångström system)

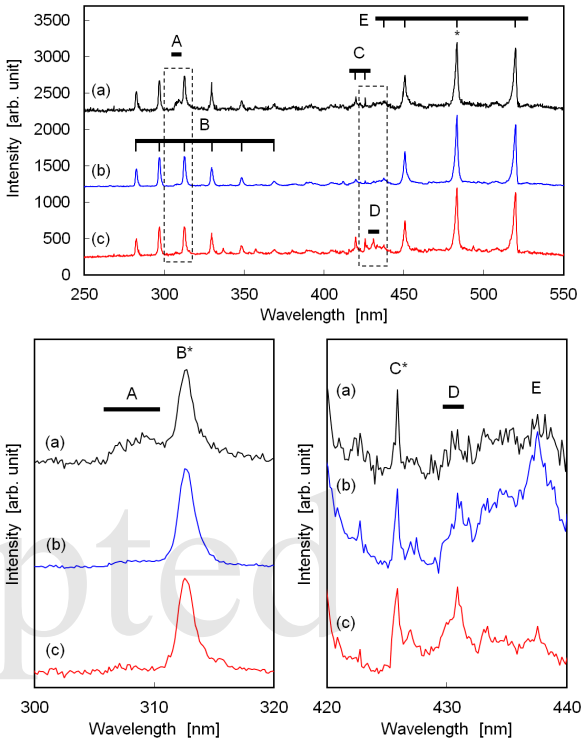

Fig. 2. Optical emission spectra measured for the plasmas of (a) TMMOS, (b) TMVOS, (c) TMVS with Ar and O_2 gases. Each asterisk (*) label indicate the standard band or line for normalization of the vertical axis. Bands and lines A~E are listed in Table 1.

measured in the plasmas using the three types of reactants. The region over 550 nm is omitted due to a lot of strong Ar lines. The emission bands and lines are identified as listed in Table 1 [18-19]. The existences of OH and CH radicals indicate that oxidation of hydrogen and fragmentation of the methyl groups occur in the plasmas, respectively. It is interesting that Balmer lines of hydrogen atoms (Hα at 656.3 nm, Hβ at 486.1 nm, etc.) and C_2 Swan bands (the main peak at 516.5 nm), which are often observed in low-temperature plasmas with organosilicon reactants [20-22], are not detected in this study. These results show that the mixing ratio of O_2 and organosilicon gases in this study makes the plasmas oxidizing atmospheres.

Both the higher emission intensity of OH in the TMMOS plasma and that of CH in the TMVOS and TMVS plasmas are due to the difference of number of carbon atoms in the reactant molecules.

3.2. Macro Images

Figure 3 shows the macro images of the electrodes after deposition. The SiO:CH particle-deposited areas look white because of the light scattering induced by the quite rough surface morphologies. A continuous SiO:CH film is deposited on the area with interference fringes. In the cases of TMMOS and TMVOS reactants, we can see clearly the inhomogeneous deposition of the SiO:CH particles. On the other hand, most of the electrode surfaces were successfully covered with the SiO:CH particles by using TMVS.

3.3. SEM Images

The SEM images observed around the center of the substrates placed on the upper grounded electrode are shown in Fig, 4. The SiO:CH particles are agglomerated in 3D chain-like configurations with partly coalescent shapes similar to sintered objects. From the spherical shape of the particles, we suppose that the particles are formed via homogeneous nucleation reactions in each plasma phase. The coalescent feature in the aggregates indicates that the particles grow after linking together, that is to say, formation of the particles, their agglomeration, and growth of continuous SiO:CH layers take place simultaneously in the PECVD processes. The average size of the particles formed in the TMMOS, TMVOS, and

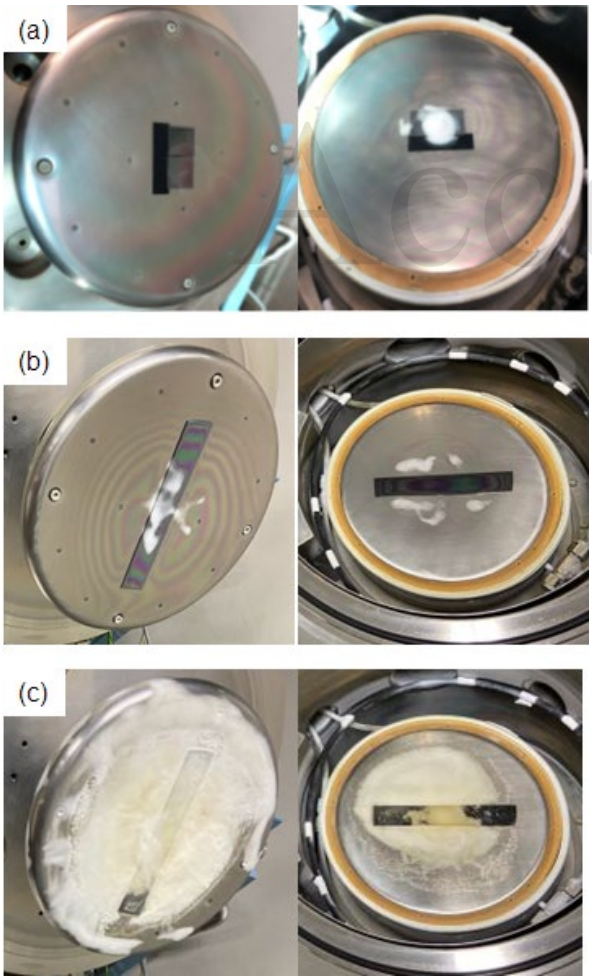

Fig. 3. Macro images of the electrode surfaces (left : upper grounded, right : lower powered) after deposition using the plasmas of (a) TMMOS, (b) TMVOS, (c) TMVS with Ar and O_2 gases.

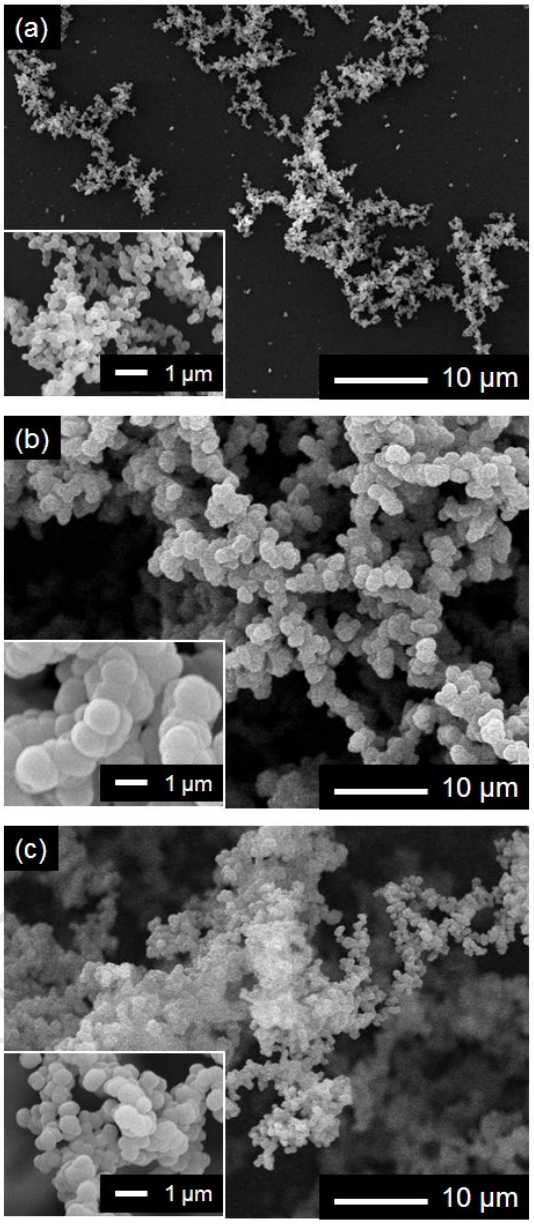

Fig. 4. SEM images of the samples deposited on the substrates located on the upper grounded electrode by using the plasmas of (a) TMMOS, (b) TMVOS, (c) TMVS with Ar and O_2 gases.

TMVS plasma was 0.2 μm, 1.4 μm, 0.7 μm, respectively. We defined a simple geometric parameter *R* in order to quantify the coalescence degree of the particles as shown in Fig. 5. The value *R* is zero when the particles are not coalescent and linked at a point, and the maximum value is unity. Several pairs of the particles flatly lying down in the SEM imaging planes were selected and estimated their *R* values. The averaged value of *R* was found to be 0.24, 0.48, and 0.41 for the samples deposited by using TMMOS, TMVOS, and TMVS, respectively. Both the smaller size of the particles formed in the TMMOS plasma with the lower coalescence degree and their area density compared to those of the other two plasmas denote much lower radical generation rate for SiO:CH deposition due to the higher activation energy for electron-impact radicalization of the TMMOS molecules. Since a TMMOS molecule consist of σ bonds of Si-C, C-H, Si-O and O-C, any of them must be dissociated for polymerization. Yun et al. reported that the bond-dissociation energies for TMMOS are 3~4 eV [23]. Therefore, the TMMOS molecules must be impacted by electrons which have higher energy than these values. On the other hand, the C=C double bond in TMVOS and TMVS molecules can initiate polymerization without full dissociation. Ouchi et al. reported the activation energy of vinyl polymerization as 0.75 eV [24], which is much lower than the bond-dissociation energies. In the case of TMVOS, however, the particle deposition was still localized as shown in the macro images in Fig. 3(b), although the SiO:CH growth rate must be sufficiently high and the particle-deposited area is spread compared to the case of TMMOS. It may due to the resonance effect of the O-C=C bond of the vinyloxy group, which resonate with O=C-C due to the unshared electron pair of the oxygen atom, then the activation energy of polymerization increases.

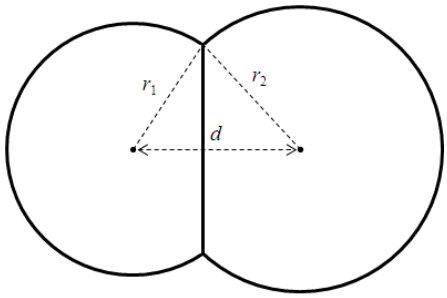

coalescing degree : $R = \dfrac{r_1 + r_2 - d}{r_1 + r_2}$

r_1 : radius of particle 1
r_2 : radius of particle 2
d : distance of center

Fig. 5. Definition of the coalescing degree.

3.4. IR Spectra

Figure 6 shows IR spectra of the samples deposited by using TMMOS, TMVOS, and TMVS as reactants. The absorption bands are identified as listed in Table 2 [25]. In common, the bonding states of the deposits are Si-X-Si (X=O, CH_n) siloxane-like networks with a plenty of $-CH_3$ terminal groups. Since the -OH terminations are not detected, the sample surfaces are expected to be hydrophobic. Focusing on the bands B1~B4, the intensities of the absorption bands due to $-CH_2-$ (B2 and B4) become higher, and the band shapes broaden in the cases of TMVOS and TMVS, which indicate that the $-CH_2-$ bonds have various bonding states due to the diverseness of the surrounding atoms. Furthermore, the bands D and F are distinguishing in polyethylene [26]. These results indicate the occurrence of polymerization reactions via the cleavage of the C=C bonds in the vinyl and vinyloxy groups. Especially these characteristics are prominent in the case of TMVS. From the fact that the main backbone structure is Si-X-Si, the polyethylene-like $-CH_2-$ chains may mixed in the Si-X-Si frameworks.

4. Conclusion

We successfully fabricated particles and their deposits of SiO:CH by PECVD using TMMOS, TMVOS and TMVS as reactants. The TMVS reactant resulted in a homogeneous deposition of the SiO:CH particles within the size of the PECVD electrodes. Applying these results of this study, formation of the ultra water- repellent surfaces will be realized in a large area.

References

1. O. Takai, A. Hozumi, N. Sugimoto, *J. Non-Crystal. Solids*, **218** (1997) 280.
2. A. Hozumi, O. Takai, *Thin Solid Films*, **303** (1997) 222.
3. J. H. Kim. V. R.-Santiago, A. A. Williams, T. Gougousi, D. D. Papas, J. K. Hirvonen, *Surf. Coat. Technol.*, **234** (2013) 21.
4. N. E. Blanchard, B. Hanselmann, J. Drosten, M. Heuberger and D. Hegemann, *Plasma Proc. Polymers*, **12** (2015) 32.
5. A. Grill and V. Oatel, *Appl. Phys. Lett.*, **79** (2001) 803.
6. H. Shimizu, N. Tajima, T. Kada, S. Nagano, Y. Shimogaki, *Jpn. J. Appl. Phys.*, **50** (2011)

Table 2. List of IR absorption bands detected.

Label	Chemical Bondings	Vibration
A	-OH	O-H str.
B1	$-CH_3$	C-H asym. str.
B2	$-CH_2-$	C-H asym. str.
B3	$-CH_3$	C-H sym. str.
B4	$-CH_2-$	C-H sym. str.
C	$-SiH_x-$	Si-H str.
D	$-(CH_2)_n-$	H-C-H def.
E	$Si-CH_3$	$-CH_3$ asym. def.
F	$C-CH_3$	C-H def. vib.
G	$Si-CH_3$	$-CH_3$ sym. def.
H	Si-X-Si (X=O, CH_n)	Si-X-Si asym. str.
I	$Si(CH_3)_n$	Si-C str.
J	$Si(CH_3)_n$	$Si-CH_3$ rocking

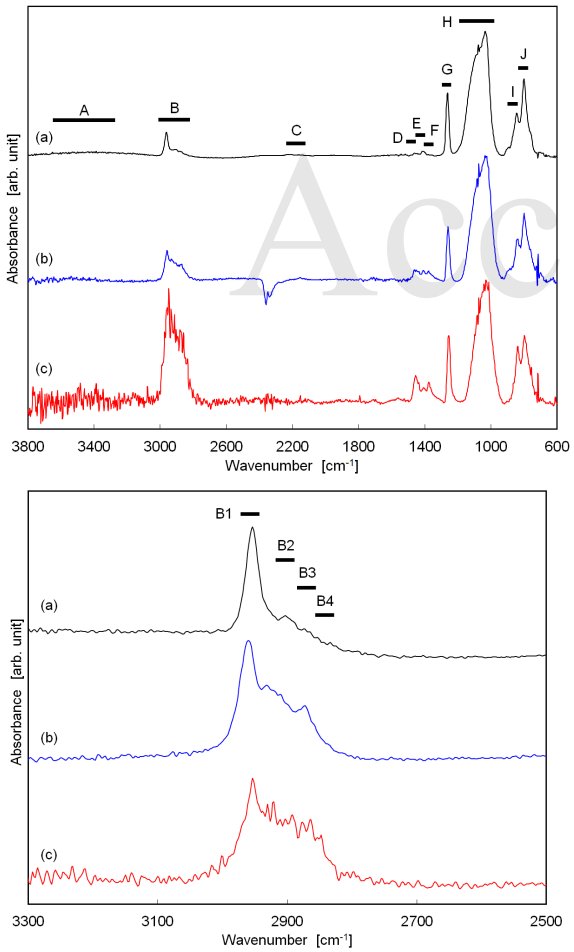

Fig. 6. Transmission IR spectra of the samples deposited by using the plasmas of (a) TMMOS, (b) TMVOS, (c) TMVS with Ar and O_2 gases. Absorption bands A~H are listed in Table 2.

05EB01.
7. M. R. Baklanov, J-F. de Marneffe, D. Shamiryan, A. M. Urbanowicz, H. Shi, T. V. Rakhimova, H. Huang and P. S. Ho, *J. Appl. Phys.*, **113** (2013) 041101.
8. Y. Lee, W. Ban, S. Jang, D. Jung, *J. Nanosci. Nanotechnol.*, **21** (2021) 2139.
9. N. Inagaki, S. Tasaka, M. Makino, *J. Appl. Polymer*, **64** (1997) 1031.
10. K. Teshima, H. Sugimura, Y. Inoue and O. Takai, *Langmuir*, **19** (2003) 8331.
11. R. Charifou, E. Espuche, F. Gouanve, L. Dubost, B. Monaco, *J. Membrane Sci.*, **500** (2016) 245.
12. M. Nakaya, K. Motomura, T. Maeda, A. Hotta, *Quart. Phys. Rev.*, **4** (2018) 1.
13. Y. Y. Wu, M. Kuroda, H. Sugimura, Y. Inoue, O. Takai, *Surf. Coat. Technol.*, **174** (2003) 867.
14. Y. Y. Wu, M. Bekke, Y. Inoue, H. Sugimura, H. Kitauchi, C. S. Liu, O. Takai, *Thin Solid Films*, **457** (2004) 122.
15. Y. S. Yun, T. Yoshida, N. Shimizu, N. Nanba, Y. Inoue, N. Saito and O. Takai, *J. Surf. Finish. Soc. Jpn.*, **58** (2007) 307.
16. Y. Inoue, H. Koike, O. Takai, *J. Photopolym. Sci. Technol.*, **29** (2016) 419.
17. Y. Inoue, H. Koike, T. Aihara, O. Takai, *J. Photopolym. Sci. Technol.*, **30** (2017) 337.
18. R. W. B. Pearse and A. G. Gaydon, "*The Identification of Molecular Spectra*", Wiley (1976).
19. A. Kramida, Yu. Ralchenko, J. Reader, and NIST ASD Team, "*NIST Atomic Spectra Database (ver. 5.9)*" (2021) [Online].
20. Y. S. Yun, *J. Korean Soc. Marine Eng.*, **35** (2011) 323.
21. Yu. M. Rumyantsev, M. N. Chagin, V. R. Shayapov, I. V. Yushina, V. N. Kichai, and M. L. Kosinova, *Glass Phys. Chem.*, **44** (2018) 174.
22. J. Ropcke, D. Loffhagen, E. von Wahl, A. S.C. Nave, S. Hamann, J.P. H. van Helden, N. Lang, and H. Kersten, *Eur. Phys. J. D*, **72** (2018) 87.
23. Y. S. Yun, M. H. Lee, Y. Inoue, N. Saito, O. Takai, *J. Nanosci. Nanotechnol.*, **14** (2014) 9653.
24. T. Ouchi, N. Beika, and M. Imoto, *Polymer J.*, **14** (1982) 155.
25. G. Scrates, "*Infrared and Raman Characteristic Group Frequencies*", Wiley (2001).
26 S. Krimm, C. Y. Liang, G. B. B. M. Sutherland, J. Chem. Phys., 25 (1955) 549.

Biomimetic Diamond-like Carbon Coating on a Lumen of Small-diameter Long-sized Tube Modified Surface Uniformly with Carboxyl Group using Oxygen Plasma

Yuichi Imai[1,2]*, Hiroyuki Fukue[2], Tatsuyuki Nakatani[2], Shinsuke Kunitsugu[3], Kazuhiro Kanda[4], Tsuneo Suzuki[5], Shogo Watari[6], Yasuhiro Fujii[7], Daiki Ousaka[8], Susumu Oozawa[8], Tomio Uchi[1]**

[1] STRAWB Inc., [2] Okayama Univ. of Science,
[3] Industrial Technology Center of Okayama Prefecture, [4] Univ. of Hyogo,
[5] Nagaoka Univ. of Technology, [6] Okayama Medical Center, [7]
Japan Agency for Medical Research and Development, [8] Okayama Univ.
**imai_y@strawb.jp, **nakatani@ous.ac.jp*

Silicone tubing is used in small-diameter long-sized tubes for medical applications, such as urinary catheters. However, bacteria in urine adhere to the catheters, forming colonies and biofilms and resulting in blockages and urinary tract infections. Therefore, we have reported a method of AC high-voltage plasma chemical vapor deposition to prevent bacterial adhesion by depositing diamond-like carbon (DLC) on a lumen of a silicone catheter and smoothing the surface. However, the sp^3/sp^2 structure of DLC on the lumen surface is unresolved, and biomimetic DLC with a functionalized surface has not been investigated. Therefore, we analyzed a flexible membrane structure that can deform as the resin tube deforms. In addition, we developed a lumen surface-modification method using an AC high-voltage burst oxygen plasma processing to bring the DLC surface closer to the *in vivo* environment. We succeeded in creating biomimetic DLC and introducing carboxyl groups. Using this technology, the surface functionalization of medical tube materials is biocompatible with various protein-adsorption properties.

Keywords: Plasma, DLC, Tube, Biomimetic, NEXAFS, Catheter

1. Introduction

Medical plastic tubing, such as artificial vascular grafts, and catheters are produced using expanded polytetrafluoroethylene (ePTFE), silicone, and polyurethane. Mostly the tubing dimensions are 1 to 8 mm in inner diameter, 1 mm in wall thickness, and 100 to 1500 mm in length. The tubes are flexible and can be rolled into a cylindrical shape. These tubes have the issue of stenosis and occlusion due to organic matter adhesion. For example, artificial vascular grafts have been used in clinical application for 60 years, first reported by Voorhees [1] and DeBarkey [2]. Recently, polyester has been used in vessel disease (>6 mm), whereas ePTFE is applied in middle or small vessel disease (<6 mm) [3, 4]. However, ePTFE surgical patency for 5 years in below-knee bypass is 31% [5], indicating a need to improve patency, especially for vascular grafts with small diameters. In addition, urinary catheters have small diameters with an inner diameter of about 1–2 mm. In urology, urethral catheters are used globally [6]. However, in 30 days after the insertion of a urinary catheter, almost 100% of people became infected with bacteria [7]. Bacteria in urine adhere to the catheter surface, forming a biofilm, followed by catheter occlusion and symptomatic urinary tract infection [8]. Catheters with hydrophilic properties and various materials have been developed [9-13]; however, their results are insufficient. Thus, silicone catheters are used for long-term indwelling [6].

Diamond-like carbon (DLC) is an amorphous

Received March 29, 2022
Accepted June 19, 2022

thin film composed of carbon allotropes. The DLC coatings deposited using radio frequency plasma chemical vapor deposition (CVD) systems are hydrogenated amorphous carbon (a-C:H), containing composite carbon–carbon bonds of sp^3 (sp^3 C–C) and sp^2 (sp^2 C=C) [14]. In addition to biocompatibility, DLC coatings have useful properties, such as low friction, smoothness, wear resistance, and low cost, making them suitable for application in medical devices [15, 16]. Recently, biocompatible DLC membranes have been commercialized for coronary stents [17, 18], and their application to medical implants, such as artificial tooth roots, is considered [19, 20]. DLC deposition on polyurethane films reduced bacterial adhesion [21]. Despite these promising reports, DLC coating has not been applied on urinary catheters. This is due to the technical limitations associated with applying DLC coatings to the lumen of small-diameter long tubing. DLC coatings have been demonstrated on flat surfaces using conventional methods. However, in 2018, we developed the technology to apply DLC coating to the luminal surface of thin tubes. Based on DLC-coating technology for the inner surface of small metal tubes, the plasma-based ion implantation (PBII) [22, 23] and microwave sheath-voltage combination plasma (MVP) [24, 25] methods have been proposed. However, few reports on DLC deposition technology on the inner wall of small-diameter long tubes made of resin are available. We observed the formation of a thin a-C:H film on the lumen by Raman analysis using methane as the source gas. An aspect ratio of 750 at an inner diameter of 2 mm was achieved, and an overall length of 1,500 mm of the glow discharge inside the silicon tube was achieved. This is the length required for the tube to be used *in vivo* [26]. By the experiment, the glow discharge was confirmed at an inner wall of 1 mm and an overall length of 400 mm using a silicone tube. This satisfied the requirement for use as urethral catheters. Bacterial biofilms were formed on the lumen more than on the outer surface of tubular medical devices [27]; thus, coatings that exhibit antibacterial and antibiofilm effects should be applied to the lumen. Recently, we confirmed that the ureteral catheter, Pseudomonas aeruginosa adhesion inhibition, and biofilm formation were inhibited [28].

However, there is biomimetic DLC, which increases biocompatibility. This is because biocompatibility increases when amino and carboxyl groups imitating amino acids are used to control the surface potential [29]. According to the reference, introducing functional groups is easier when sp^3 C–C is more abundant than sp^2 C=C. The functional group introduction depends on the sp^3 C–C ratio because the binding energies of the sp^3 C–C bond are lower than those of the sp^2 C=C bond [30]. Therefore, to discuss the biomimetic DLC, it is necessary to examine the structural analysis of sp^3 and sp^2. For luminal DLC films, Raman structural analysis has been reported [26]; however, the sp^3/sp^2 ratio has not been elucidated. In addition, the biomimetic DLC of the luminal surface has not been investigated.

Therefore, this study clarifies the structure of sp^3 and sp^2, identifies the DLC film types, and investigates the possibility of the biomimetic DLC of the luminal surface using a carboxyl group, which is a component of the biomimetic surface. The surface zeta potential can be controlled to be negatively charged [31]. Therefore, we propose a new method of oxygen plasma surface modification of the tube lumen surface using AC high-voltage burst plasma processing.

2. Experimental Method

2.1. Structural analysis of thin film

Figure 1 shows a schematic of the experimental equipment. The equipment was set up by adding O_2 and NH_3 to modify the surface amino and carboxyl groups. The details of the system configuration of the DLC deposition equipment using the developed AC high-voltage methane plasma-CVD method are described in reference [26]. The discharge conditions for DLC film formation and oxygen plasma treatment are 5 kV AC voltage, 2 kV offset voltage, 10 kHz frequency, 10 pps pulse frequency, and 39 Pa combined pressure, and methane and oxygen gases were introduced as the source material

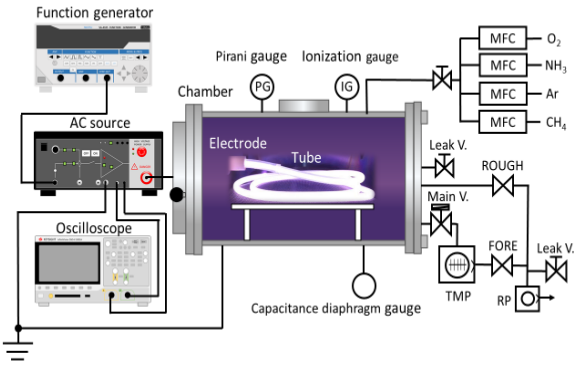

Fig. 1. Schematic of the experimental equipment.

gases at 96 sccm. In the experiment, the DLC was deposited for 20 min, and the oxygen plasma was treated for 1–5 s after the film formation. The sample size had an inner diameter and length of 4 and 350 mm, respectively.

The sp^3/sp^2 ratio was evaluated using the carbon *K*-edge near-edge X-ray absorption fine-structure (NEXAFS) spectroscopy, in total electron yield (TEY) mode, to determine the ease of introducing carboxyl groups on a lumen of small-diameter long-sized silicone tube using oxygen plasma treatment after DLC deposition. However, measuring the insulator using the NEXAFS in TEY mode is difficult. Thus, a piece of the silicon wafer was placed 3 mm from the exit of the tube, irradiated the plasma at 90° angle, and evaluated the film deposited on the silicon wafer. The tube length was 300 mm, and the deposition time was 2.5 min. The NEXAFS measurements were conducted at Beamline 09A (BL09A) of NewSUBARU. The electron energy of the NewSUBARU ring, which is a synchrotron radiation facility in this experiment, was 1.5 GeV. The BL09A equipment was described in detail in reference [32]. Synchrotron radiation provided by an 11 m undulator was extracted using varied-line spacing-plane gratings of 1200 lines/mm. It was irradiated on the sample film at 54.7° (magic angle) to the surface of samples. The energy axis was calibrated using the position of the π-peak of highly oriented pyrolytic graphite (HOPG) as the literature value (258.38 eV [33]) and the HOPG spectrum closest to the sample measurement as the reference. The NEXAFS spectrum of carbon *K*-edge absorption was measured according to the description by Kanda *et al*. [34-36].

Resin tubes are soft material. DLC softness depends on the hydrogen content. Therefore, we evaluated hydrogen content using the observation of Rutherford backscattering spectrometry (RBS)/elastic recoil detection analysis (ERDA). DLC classification is determined by sp^3 ratio and hydrogen content. The atomic fraction of H in the sample is determined by measuring RBS and ERDA spectra with MeV-He^+ irradiation using an electrostatic accelerator (High Voltage Engineering Europe, Tandetron Accelerator System 4117MC+) located at the Extreme Energy Density Research Institute, Nagaoka University of Technology. The details of RBS and ERDA measurements are described in references [37, 38]. The He_2^+ accelerated to 2.5 MeV was used as an incident beam at 72° to the normal surface of samples. The He_2^+ beam current was maintained at 6 nA. In the RBS measurement, a small fraction, less than 0.1%, of high-energy He_2^+ scattered elastically because the sample was captured using a solid-state detector (SSD) arranged at 12° to the normal surface of samples toward the incident beam [34].

The mechanical properties of the films were evaluated using a nanoindentation system (Hsyitron Inc.; Triboindentor TI-950) and a nanoindentation method (ISO14577 [39]). The hardness (H_{IT}) values and reduced elastic modulus (E_r) were calculated from the load–displacement curve using Berkovich-type diamond indenter. The hardness and elastic modulus of the films were determined using the average values among contact depth (h_c) regions without the efficiency Si substrate hardness.

2.2. Surface analysis of thin film

To evaluate the uniformity of the oxygen treatment, the contact angles of the pure water drop on the DLC-coated silicone sheet inserted on a lumen were measured. The measurements were conducted using the Kyowa Interface Science Dropmaster. The average value was calculated using several accumulations, that is, more than five times.

X-ray photoelectron spectroscopy (XPS; JEOL JPS-9200S) was used to evaluate the chemical structure at the bonding state of the DLC film and the silicone lumen surface after oxygen plasma treatment. The X-ray source was non-monochromatized Mg (1253.6 eV). The X-ray gun was operated at 10 kV, and the anode power was 100 W. A pass energy of 10.0 eV was chosen for high-resolution spectrum acquisition (C1s). For all measurements, the photoelectron take-off angle (TOA) was 90° (about 7 nm of the sampling depth).

The ELSZ-1000 of Otsuka Electronics Co., Ltd., was used to measure the zeta potential of the DLC-coated silicone sheet inserted on a lumen. The zeta potential of the surface of a solid sample was determined by measuring the electric mobility at different points in a flat cell and analyzing the electroosmotic flow using the Mori–Okamoto equation. A flat cell silicone sheet was used to measure the zeta potential of the solid surface of a flat or film sample. A measurement sample of 25 mm × 7 mm × 3 mm was set in the plating cell, and 100 mL distilled water and 500 μL monitoring particles (Otsuka Electronics Co., Ltd.) were adjusted for measurement. The oxygen-plasma-treated DLC plate was attached to a chamber, and the chamber was filled with a 10 mM NaCl solution, in which monitoring particles were suspended.

Electrophoresis of the particles was conducted, and the apparent velocity distribution in the chamber was determined. The electrophoresis conditions were as follows: mean electric field intensity, 17.33 V/cm, and average current, 1.02 mA.

2.3. *in vitro* evaluation

Anti-bacterial-adhesion and anti-biofilm properties of DLC coating, deposited on the inner surface of a thin silicon catheter, were evaluated in vitro model. A 400 mm length of silicone tube with an inner diameter of 2 mm was coated with DLC followed by treating with oxygen plasma. It was cut into 100-mm length of pieces while connected to a continuous-flow system. *Pseudomonas aeruginosa* strains transfected using green fluorescent protein (GFP) plasmid were used to fill the lumen of the silicone tube and clamped for 2 h. After the clamp was released, artificial urine was refluxed at a rate of 20 ml/h. The samples were observed using the confocal laser-scanning microscope model LSM780 (ZEISS). For the biofilm evaluation, the photographs taken using LSM780 were analyzed using Comstat version 2. The antibiofilm properties of oxygen DLC silicone were compared to those of an uncoated silicone catheter or plain DLC silicone.

3. Results and Discussion

3.1. Structural analysis of thin film

Figure 2 shows the NEXAFS spectrum of thin film. Three measurements were performed on the same sample, and the reproducibility was high. In addition, no location dependence was found. The thickness of this film varied; however, the film quality was uniform. The sharp peak at 285 eV indicates the transition from 1*s* orbital to the π vacancy level. The broadband in blue brackets around 290–310 eV indicates the transition from 1*s* orbital to the σ vacancy level. The spectral shape shows a structure in the σ region, and deep valley between the π region and σ region was characteristic of soft films. The $sp^3/(sp^3+sp^2)$ was calculated by comparing it with that of HOPG. The $sp^3/(sp^3+sp^2)$ carbon atoms in this film were 43.9% according to the analysis of the NEXAFS of the *K*-edge of carbon atoms. The evaluation method of the $sp^3/(sp^3+sp^2)$ ratio of DLC films is enough to introduce a carboxyl group on a lumen, according to ISO20523:2017.

Figure 3 shows the RBS spectrum of thin film. The peak on the horizontal axis of the spectrum rising from 1000 is a silicon substrate, and the peaks between 300 and 450 are carbon. Since there are no other peaks, it can be considered that there were almost no impurities in the thin film. From the simulation results, the areal density is from 2100 to 2200 $\times 10^{15}$ atoms/cm^2. Figure 4 shows the ERDA spectrum of thin film. The spectrum was incompletely fitted owing to the nonuniformity of the film thickness. The rise of the red (areal density 2200 H = 35) and blue (areal density 2100 H = 36) spectra from the simulation results do not agree with the simulation results (left figure), indicating that the film thickness is nonuniform. Considering the RBS results and nonuniformity of the film thickness,

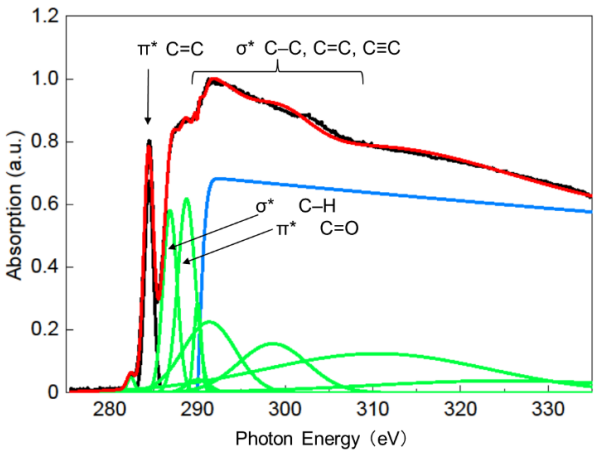

Fig. 2. NEXAFS spectrum of thin film.

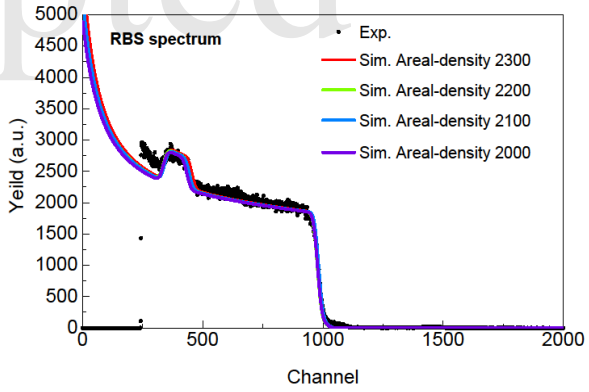

Fig. 3. RBS spectrum of thin film.

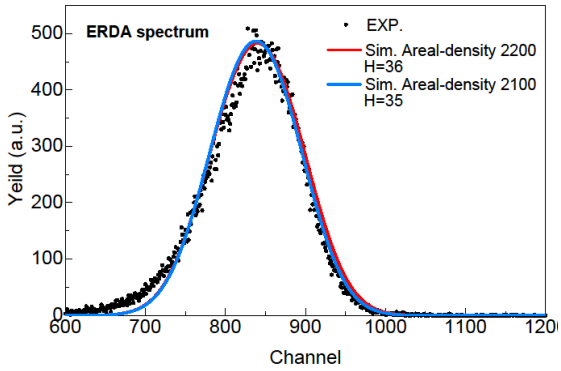

Fig. 4. ERDA spectrum of thin film.

the hydrogen and film thickness were adjusted and fitted. Thus, the assumed areal density is from 2100 to 2200 $\times 10^{15}$ atoms/cm^2, and the amount of hydrogen is from 35 to 36 at.%. The films were classified as a-C:H film, which belongs to the DLC category, not polymer-like carbon according to ISO20523:2017.

Figure 5 show the mechanical properties obtained using the nanoindentation method. The film's hardness (H_{IT}) and reduced elastic modulus (E_r) were 0.79 and 8.51 GPa, respectively. The film is a polymer-like carbon, which is a flexible membrane. Since resin tubes are deformable, DLC with a small elastic modulus is required to prevent delamination of the film. Ohtake *et al.* reported that the DLC is more than 9 GPa [40]. However, the DLC deposited on the lumen surface is soft, suggesting that it is a promising durable DLC for medical use. In addition, the structure of the deposited thin film is that of a-C:H film, which is DLC; however, its hardness is positioned as a polymer-like material. Therefore, in the classification of carbon films according to ISO 20523:2017, the corresponding thin films show no DLC, suggesting the possibility of a new type of DLC.

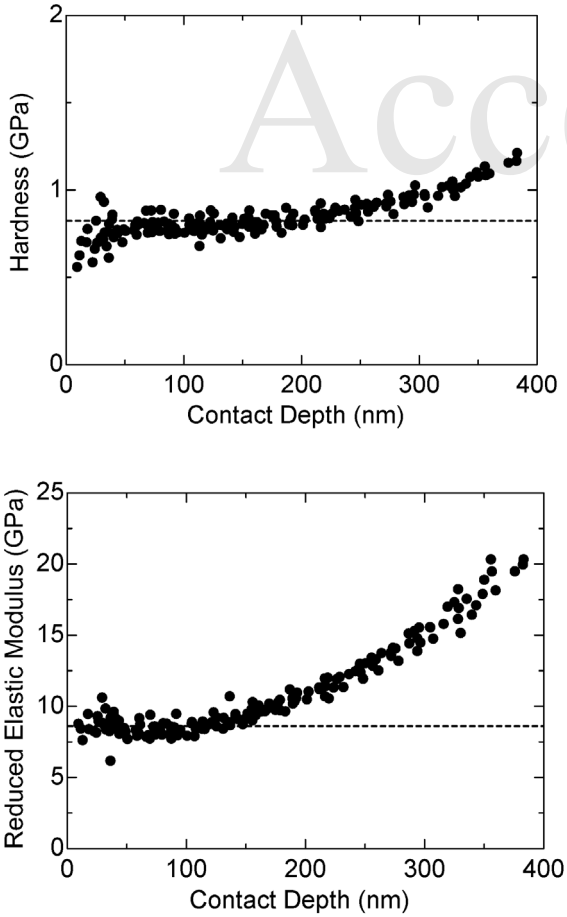

Fig. 5. The mechanical properties obtained by nanoindentation method. Hardness (H_{IT}) and Reduced elastic modulus (E_r) of the film.

3.2. Surface analysis of thin film

Figure 6 shows the contact angles. The contact angle of the normal silicone tube was 119.5° ± 1.8% (average of 8 times); that of the DLC-coated silicone tube film deposited for 20 min was 104.4° ± 2.3% (average of 9 times); that of the DLC-coated silicone tube treated for 1 s using oxygen plasma, after film deposition for 20 min, was 99.2 °±2.7% (average of 10 times); that of the DLC-coated silicone tube treated for 2 s using oxygen plasma, after film deposition for 20 min, was 90.6 ° ± 5.4% (average of 7 times); and that of the DLC-coated silicone tube treated for 5 s using oxygen plasma, after film deposition for 20 min, was 95.1 ° ± 6.6% (average of 10 times). The contact angle variation increases with oxygen plasma treatment time, indicating that etching progresses [41]. However, the hydrophilic functional groups increased in the tube lumen. In addition, the sampling frequency is the maximum number of measurements on a cut specimen.

Figure 7 shows the existence ratios of O–C=O, C–O, sp^3 C–C, C–H, and sp^2 C=C bonds in relation to binding energy and normalized intensity for blank, 20 min DLC deposition, and 20 min DLC deposition plus 2 s of oxygen plasma, respectively, in the lumen at 150 mm tube length. The XPS spectrum was fitted using the pseudo-Voigt function (Gaussian 70% and Lorentzian 30%). This Gaussian and Lorentzian component ratio of the pseudo-Voigt function had the lowest error in the preliminary fitting. The C1s spectrum of the DLC film was deconvoluted into four peaks with the positions at 284.7 eV (sp^2 C=C) [42, 43], 285.4 eV (sp^3 C–C, C–H) [44-47], 286.5 eV (C–O) [44-46, 48-50], and 288.3 eV (O–C=O) [42, 44-47]. C=O was excluded from the evaluation because it is roughly one tenth of C–O. The positions of these peaks were fixed, and their respective area ratios were determined

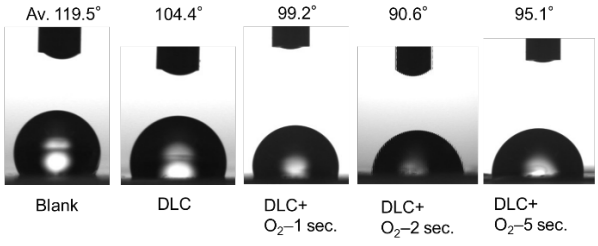

Fig. 6. The contact angles. Each photograph is close to the mean.

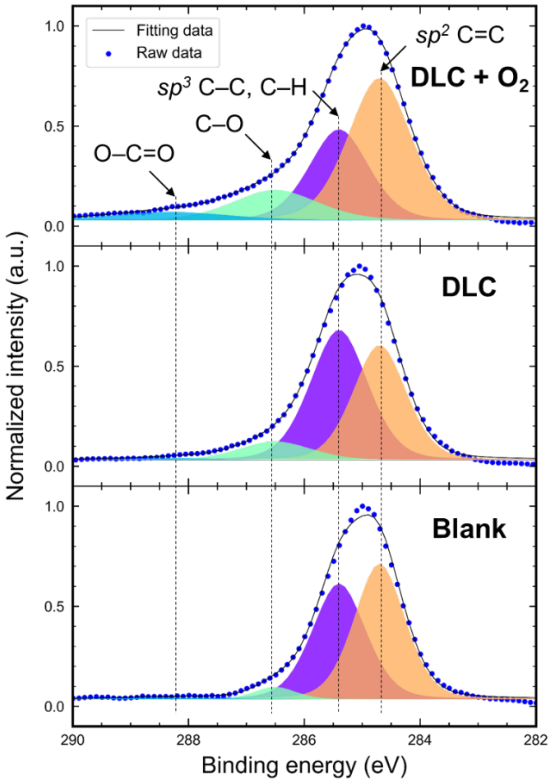

Fig. 7. The existence ratios of O–C=O, C–O, sp^3 C–C, C–H, and sp^2 C=C bonds in relation to binding energy and normalized intensity for blank, 20 min DLC deposition, and 20 min DLC deposition plus 2 s of oxygen plasma, respectively, in the lumen at 150 mm tube length.

according to references [42-50]. This C1s spectrum was subtracted from the background by the Shirley method before fitting [51]. The fitting of C1s spectrum was conducted using the nonlinear least-squares method using the Levenberg–Marquardt algorithm [52, 53]. In addition, the ratios of peak area are shown in Table 1 (unit: percent). Compared to DLC, sp^2 C=C increased from 40.40% to 49.94%, whereas sp^3 C–C and C–H decreased from 49.44% to 30.29% in the DLC deposition, followed by oxygen plasma treatment. C–O and O–C=O increased from 9.04% to 14.40% and from 1.13% to 5.38%, respectively. This may be due to the decrease in the percentage of sp^3 C–C and C–H due to the sp^3 C–C bond cleavage, surface oxidation, and C–O and O–C=O introduction [30].

The change in surface zeta potential using oxygen plasma treatment time is shown in Figure 8. The surface zeta potential of the blank silicone tube resulted in a negative charge. However, the zeta potential of the DLC film is positively charged. In contrast, the zeta potential of the DLC film was negatively charged using oxygen plasma treatment. After 1.0 s, the zeta potential was −15.9 mV. The zeta potential turned positive at treatment times longer than 1 s. We inferred that oxygen plasma irradiation etches DLC by oxygen radicals [41]. Therefore, we inferred that a longer irradiation time would have reduced the film area due to etching, decreasing the efficiency of the introduced functional group. The decrease in zeta potential is due to the introduction of carboxyl groups on the DLC surface using the oxygen plasma treatment of the lumen surface, which is negatively charged by the divergence of protons in the liquid. This suggests that introducing functional groups to the sample surface, which has been reported, was applied to the tube lumen surface [31]. Therefore, the proposed AC high-voltage burst oxygen plasma processing creates biomimetic DLC on tube lumen surfaces.

Table1. The ratios of peak area.

	sp^2 C=C [%]	sp^3 C-C, C-H [%]	C-O [%]	O-C=O [%]
DLC + O_2	49.94	30.29	14.40	5.38
DLC	40.40	49.44	9.04	1.13
Blank	50.16	45.06	3.69	1.09

Figure 9 shows a variation of oxygen binding ratio of oxygen-plasma-treated DLC with tube position. The ratio of O–C=O, C–O, sp^2 C=C, sp^3 C–C, and C–H was calculated from the waveform separation results of the narrow scan spectrum, and the results are shown in the figure. The O–C=O, C–O bonds averaged 19.5 ± 1.3 at.% of carbon in the 5 to 30 cm tube length region, indicating that the modification was almost uniform. Preliminary experiments have confirmed that the plasma bullets

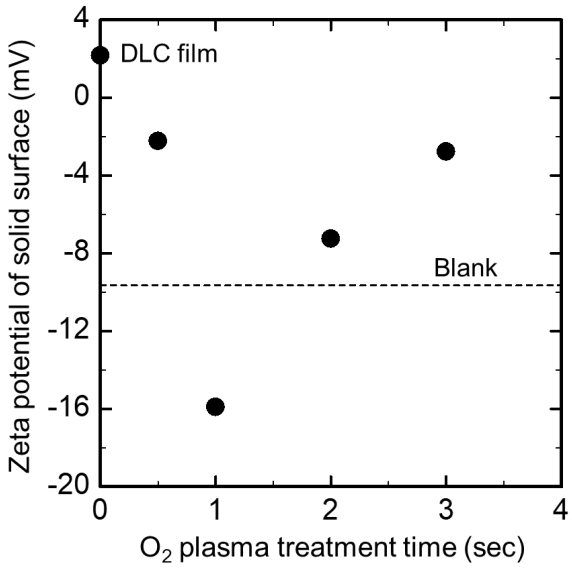

Fig. 8. The change in surface zeta potential using oxygen plasma treatment time.

at the electrode side are transported toward the open end of the tube when the plasma was observed using a high-speed video camera. Figure 10 shows the plasma bullets captured by an ultra-fast camera (Hyper Vision HPV-X2, SHIMADZU) at 10 million frames per second. We inferred that uniform oxygen plasma surface modification implies uniform plasma generation through stable plasma bullet transport.

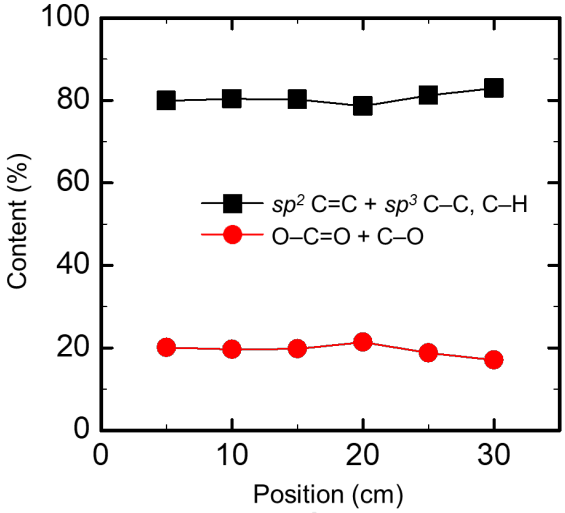

Fig. 9. Variation of oxygen binding ratio of oxygen plasma treated DLC with tube position.

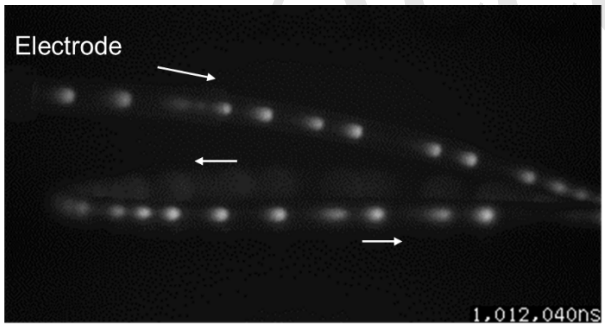

Fig. 10. The plasma bullets captured by an ultra-fast camera (Hyper Vision HPV-X2, SHIMADZU) at 10 million frames per second.

3.3. *in vitro* evaluation

Figure 11 shows the GFP-labeled *Pseudomonas aeruginosa* adhering to the oxygen-plasma-treated DLC. In the observed image, the green-colored areas are where GFP is attached, and the other black-colored areas are where GFP is not attached. A decreasing trend of GFP can be seen with DLC deposition and oxygen plasma treatment. Figure 12 shows the change in the total biomass and biofilm thickness for no DLC deposition, 20 min of DLC deposition, and 1 and 5 s of oxygen plasma treatment after DLC deposition, respectively. The results suggested that optimizing the oxygen plasma treatment, perhaps for 5 s, can improve the property that inhibits *Pseudomonas aeruginosa* adhesion and biofilm formation better than the property of plain DLC. For the zeta potential, the minimum value is obtained using an oxygen plasma treatment time of 1 s; there may be an optimum value for zeta potential. This experiment showed a difference in biomass and biofilm thickness compared to DLC at an oxygen plasma treatment time of 5 s, suggesting that there may be other optimum values. Watari *et al*. reported that surface roughness might affect Pseudomonas aeruginosa adhesion [28]. Therefore, the importance of controlling morphology and zeta potential is an element to be considered. However, the proposed AC high-voltage burst-plasma processing is expected to be an effective surface modification of the lumens of medical materials.

4. Conclusion

This study proposed a new method for oxygen plasma surface modification of the lumen surface of small-diameter long tubes using an AC high-voltage burst-plasma CVD method. It was clarified that a-C:H (hydrogenated amorphous carbon) with a typical amorphous structure of DLC on a lumen of small-diameter long-sized silicone tube. The film

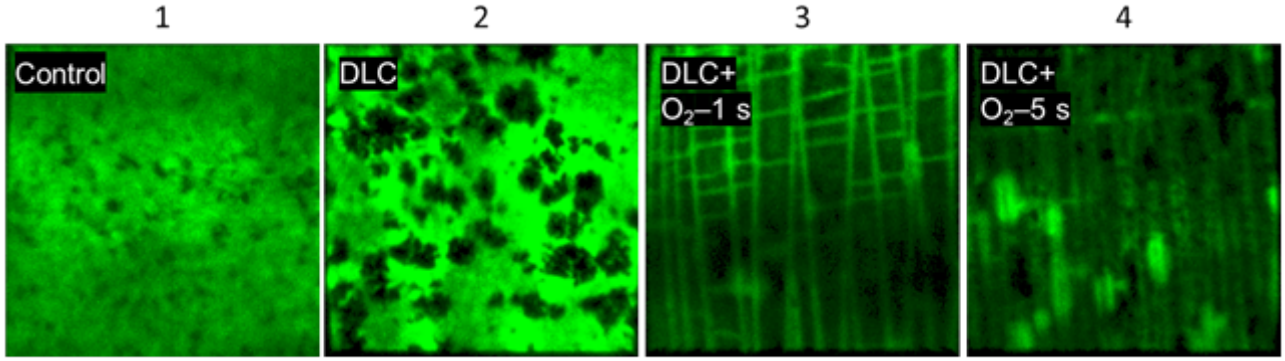

Fig.11. The GFP-labeled *Pseudomonas aeruginosa* adhering to the oxygen-plasma-treated DLC 72 hours after unclamping.

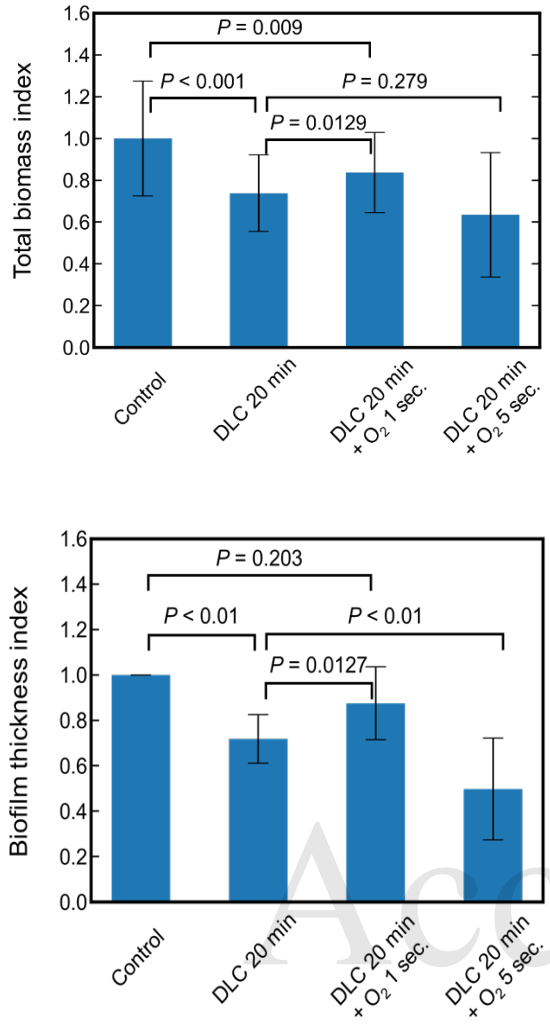

Fig. 12. The change in the total biomass and biofilm thickness for no DLC deposition, 20 min of DLC deposition, and 1 and 5 s of oxygen plasma treatment after DLC deposition, respectively.

quality was suggested to be an unparalleled soft DLC. Using oxygen plasma treatment, the surface-modified using hydrophilic functional group, i.e., carboxyl group, is a biomimetic factor. After DLC deposition and oxygen plasma treatment of the lumen of the silicone tube, C–O and O–C=O bonds were observed, suggesting that plasma processing can be used to control the uniformity of the biomaterial.

The surface functionalization of the developed small-diameter long-tube lumen for medical use is biocompatible with the adsorption characteristics of various proteins.

References

1. A. B. Voorhees Jr, J. Alfred III and A. H. Blakemore, *Annals of Surgery*, **135** (1952) 332.
2. M. E. D. Bakey and D. A. Cooley, *J. Am. Med. Assoc.*, **155** (1954) 1398.
3. H. Takagi, S. Goto, M. Matsui, H. Manabe and T. Umemoto, *J. Vasc. Surg.*, **52** (2010) 232.
4. J. M. W. Donker, G. H. Ho, A. T. Slaa, H. G. W. D. Groot, J. C. H. V. D. Waal, E. J. Veen and L. V. D. Laan, *Vasc. Endovasc. Surg.*, **45** (2011) 598.
5. M. Albers, V. M. Battistella, M. Romiti, A. A. E. Rodrigues and C. A. B. Pereira, *J. Vasc, Surg.*, **37** (2003) 1263.
6. N. Venkatesan, S. Shroff, K. Jayachandran, and M. Doble, *J. Endourol.*, **24** (2010) 191.
7. S. H. Paick, H. K. Park, S. J. Oh and H. H. Kim, *Urology*, **62** (2003) 214.
8. P. Vergidis and R. Patel, *Infect. Dis. Clin. North. Am.*, **26** (2012) 173.
9. A. J. Shepherd, W. G. Mackay and S. Hagen, *Cochrane Database Syst. Rev.*, (2017) 3.
10. X. Bonfill, D. Rigau, M. E. Fuertes, J. M. B. Chacón, M. L. J. Abrisqueta, S. Salvador, C. M. Alemán, A. Borau, M. B. Muñoz, B. Hidalgo, M. J. Andrade, J. R. Espinosa, M. J. M. Zapata, E. Cánovas, N. Zazo, I. Gich, M. Bea, M. Garran, M. P. Herrero, M. Morcillo, E. Bárbara, M. L. Jáuregui, M. Cuadrado, N. C. Sánchez, I. L. Mendieta, M. E. Ferreiro, S. Moraleda, B. Méndez, M. J. Zarco, I. García, M. Esteban, M. Florencio, J. I. D. Miguel, C. M. Lanzillotti, J. Navarro, D. Soares, Y. Akkoc, O. Senocak, N. N. Vásquez, V. Orrego, M. Courbis and M. Seguel, *The Spine Journal*, **17** (2017) 1650.
11. C. E. M. Probst, A. Fernandez and J. D. Denstedt, *Curr. Urol. Rep.*, **11** (2010) 67.
12. E. Dayyoub, M. Frant, S. R. Pinnapireddy, K. Liefeith and U. Bakowsky, *Int. J. Pharm.*, **531** (2017) 205.
13. D. M. Rocca, V. Aiassa, A. Zoppi, J. S. Compagnucci and M. C. Becerra, *J. Endourol.*, **34** (2020) 345.
14. A. Grill and B. S. Meyerson, "Synthetic Diamond: Emerging CVD Science and Technology", K. E. Spear and J. P. Dismukes, Eds., Wiley, New York (1994) pp. 91-141.
15. D. P. Monaghan, K. C. Laing and P. A. Logan, *Mater. World*, **1** (1993) 347.
16. S. J. Bull, *Diam. Relat. Mater.*, **4** (1995) 827.
17. S. Kesavan, J. W. Strange, T. W. Johnson, S. F. Roese and A. Baumbach, *EuroIntervention*, **8** (2013) 1012.
18. T. Nakatani, K. Okamoto, I. Omura and S. Yamashita, *J. Photopolym. Sci. Technol.*, **20** (2007) 221.

19. Y. Mine, T. Nakatani, K. Okamoto, S. Hara, K. Takagi and H. Nikawa, *J. Photopolym. Sci. Technol.*, **27** (2014) 373.
20. T. Shuto, T. Nakatani, K. Okamoto, N. Saizaki, S. Mimura, S. Kunitsugu and H. Nikawa, *J. Photopolym. Sci. Technol.*, **29** (2016) 413.
21. D. S. Jones, C. P. Garvin, D. Dowling, K. Donnelly and S. P. Gorman, *J. Biomed. Mater. Res. B Appl. Biomater.*, **78** (2006) 230.
22. K. Baba, R. Hatada, S. Flege and W. Ensinger, *Appl. Surf. Sci.*, **310** (2014) 262.
23. K. Baba and R. Hatada, *J. Surf. Finish. Soc. Jpn.*, **52** (2001) 449 (in Japanese).
24. H. Kousaka and N. Umehara, *Vacuum*, **80** (2006) 806.
25. H. Kousaka, *J. Plasma Fusion Res.*, **90** (2014) 76 (in Japanese).
26. T. Nakatani, Y. Imai, Y. Fujii, T. Goyama and S. Ozawa, *J. Photopolym. Sci. Technol.*, **31** (2018) 373.
27. J. C. Wang, P. L. Tran, R. Hanes, J. Cordero, J. Marchbanks, T. W. Reid, J. A. C. Hamood and A. N. Hamood, *Otolaryngol. Head Neck Surg.*, **139** (2013) 1009.
28. S. Watari, K. Wada, M. Araki, T. Sadahira, D. Ousaka, S. Oozawa, T. Nakatani, Y. Imai, J. Kato, R. Koriyama, T. Watanabe and Y. Nasu, *Int. J. Urol.*, **28** (2021) 1282.
29. A. Mochizuki, T. Ogawa, K. Okamoto, T. Nakatani and Y. Nitta, *Mater. Sci. Eng. C*, **31** (2011) 567.
30. Y. Nitta, K. Okamoto, T. Nakatani and M. Shinohara, *IEEE Trans. Plasma Sci.*, **40** (2012) 2073.
31. Y. Nitta, K. Okamoto, T. Nakatani, H. Hoshi, A. Honma, E. Tatsumi and Y. Taenaka, *Diam. Relat. Mat.*, **17** (2008) 1972.
32. M. Niibe, M. Mukai, S. Miyamoto, Y. Shoji, S. Hashimoto, A. Ando, T. Tanaka, M. Miyai and H. Kitamura, *AIP Conf. Proc.*, **705** (2004) 576.
33. P. E. Batson, *Phys. Rev. B*, **48** (1993) 2608.
34. K. Kanda, M. Okada, Y. Kang, M. Niibe, A. Wada, H. Ito, T. Suzuki and S. Matsui, *Jpn. J. Appl. Phys.*, **49** (2010) 06GH06.
35. J. Igaki, A. Saikubo, R. Kometani, K. Kanda, T. Suzuki, K. Niihara and S. Matsui, *Jpn. J. Appl. Phys.*, **46** (2007) 8003.
36. K. Kanda, R. Imai, S. Tanaka, S. Suzuki, M. Niibe, T. Hasegawa, T. Suzuki and H. Akasaka, *Materials*, **14** (2021) 924.
37. Y. Ohkawara, S. Ohshio, T. Suzuki, H. Ito, K. Yatsui, and H. Saitoh, *Jpn. J. Appl. Phys.*, **40** (2001) 7007.
38. Y. Ohkawara, S. Ohshio, T. Suzuki, H. Ito, K. Yatsui, and H. Saitoh, *Jpn. J. Appl. Phys.*, **40** (2001) 3359.
39. Metallic materials — Instrumented indentation test for hardness and materials parameters — Part 1: Test method: ISO 14577-1: 2015; The International Organization for Standardization; Vernier: Geneva, Switzerland, 2015.
40. N. Ohtake, M. Hiratsuka, K. Kanda, H. Akasaka, M. Tsujioka, K. Hirakuri, A. Hirata, T. Ohana, H. Inaba, M. Kano and H. Saitoh, *Materials*, **14** (2021) 315.
41. T. Aizawa and T. Fukuda, *Surf. Coat. Technol.*, **215** (2013) 364.
42. S. Zhang, Y. Fu, H. Du, X. T. Zeng and Y. C. Liu, *Surf. Coat. Technol.*, **162** (2003) 42.
43. S. Wan, H. Hu, G. Chen and J. Zhang, *Electrochem. Commun.*, **10** (2008) 461.
44. G. A. Abbas, P. Papakonstantinou, T. I. T. Okpalugo, J. A. McLaughlin, J. Filik and E. H. Jones, *Thin Sol. Fil.*, **482** (2005) 201.
45. P. Patsalas, M. Handrea, S. Logothetidis, M. Gioti, S. Kennou and W. Kautek, *Diam. Relat. Mat.*, **10** (2001) 960.
46. L. Li, H. Zhang, Y. Zhang, P. K. Chu, X. Tian, L. Xia and X. Ma, *Mater. Sci. Eng. B*, **94** (2002) 95.
47. H. S. Zhang, J. L. Endrino and A. Anders, *Appl. Surf. Sci.*, **255** (2008) 2551.
48. J. Y. Jao, S. Han, L. S. Chang, C. L. Chang, Y. C. Liu and H. C. Shih, *Appl. Surf. Sci.*, **256** (2010) 7490.
49. I. Gerhards, C. Ronning, H. Hofsäss, M. Seibt and H. Gibhardt, *J. Appl. Phys.*, **93** (2003) 1203.
50. B. B. Fabre, G. Lazar, D. Ballutaud, C. Godet and K. Zellama, *Diam. Relat. Mat.*, **17** (2008) 700.
51. D. A. Shirley, *Phys. Rev., B,* **5** (1972) 4709.
52. D. W. Marquardt, *J. Soc. Ind. Appl. Math.*, **11** (1963) 431.
53. F. Rose, N. Wang, R. Smith, Q. F. Xiao, H. Inaba, T. Matsumura, Y. Saito, H. Matsumoto, Q. Dai, B. Marchon, F. Mangolini and R. W. Carpick, *J. Appl. Phys.*, **116** (2014) 123516.

Adhesion Improvement Mechanism of Polytetrafluoroethylene by Heat-assisted Atmospheric Pressure Glow Plasma Treatment

Kunihito Tanaka[1*], Koya Sato[1], Kazuo Takahashi[1] and Masuhiro Kogoma[1]

[1] Department of Materials and Life Sciences, Faculty of Science and Technology, Sophia University, 7-1 Kioicho, Chiyoda-ku, Tokyo 102-8554, japan
**tanaka@sophia.ac.jp*

The adhesive strength of polytetrafluoroethylene (PTFE) film increased drastically by heat-assisted plasma treatment and PTFE indicated cohesive failure inside the PTFE. By increasing the temperature, defluorination progressed. The PTFE treated with H_2/He had significantly lower adhesive strength than the PTFE treated with only He. The peak assigned to stretching vibration of -CH_2- could be observed only in the film treated with H_2/He plasma. From above, we concluded the improvement of the adhesive strength requires the formation of dangling bonds and a crosslinked structure on the PTFE surface.
Keywords: Heat-assisted atmospheric pressure glow plasma, Polytetrafluoroethylene, Adhesive strength.

1. Introduction

Polytetrafluoroethylene (PTFE) has various excellent properties such as non-adhesiveness, heat resistance and insulation properties. Thus, PTFE is applied in various products such as automobile parts, semiconductor manufacturing equipment, and cookware.

However, since the use of PTFE is limited because of its low adhesiveness, the surface modification of PTFE is often performed by wet treatment with metallic sodium or treatment with low-pressure Ar plasma. However, each treatment has its own disadvantages: wetting with metallic sodium requires the treatment of liquid waste and low-pressure Ar plasma lacks production efficiency. Hence, discovering a novel drying process which could compensate these issues is necessary.

Atmospheric pressure glow plasma has attracted attention as the most effective drying method because of the high density of excited species, low temperature and uniform surface treatment [1-3]. Atmospheric pressure glow plasma treatment has been expected to improve the adhesion of PTFE by removing fluorine. In a previous study [4,5], a plasma treatment containing boron effectively removed fluorine on the surface of PTFE, resulting

Received March 23, 2022
Accepted June 20, 2022

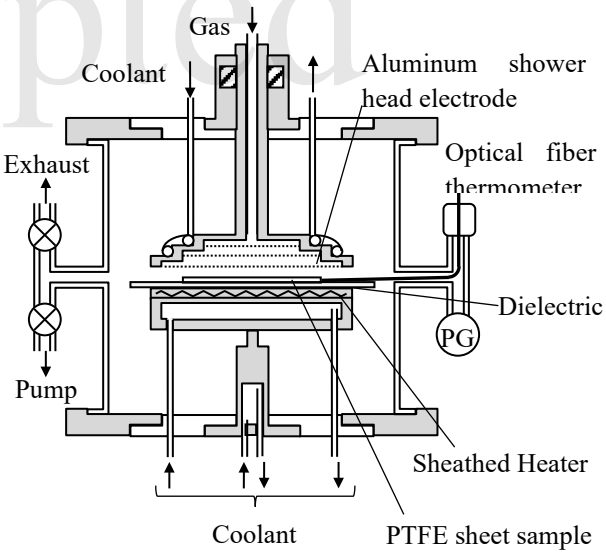

Fig. 1 Schematic diagram of the discharge chamber.

Table 1 The plasma treatment conditions.

Discharge frequency	13.56 MHz
Discharge power	100 ~ 200 W
Discharge gap	3 mm
Treatment time	0 ~ 30 min
He flow rate	2 slm
Treatment temperature	110 ~ 270 °C

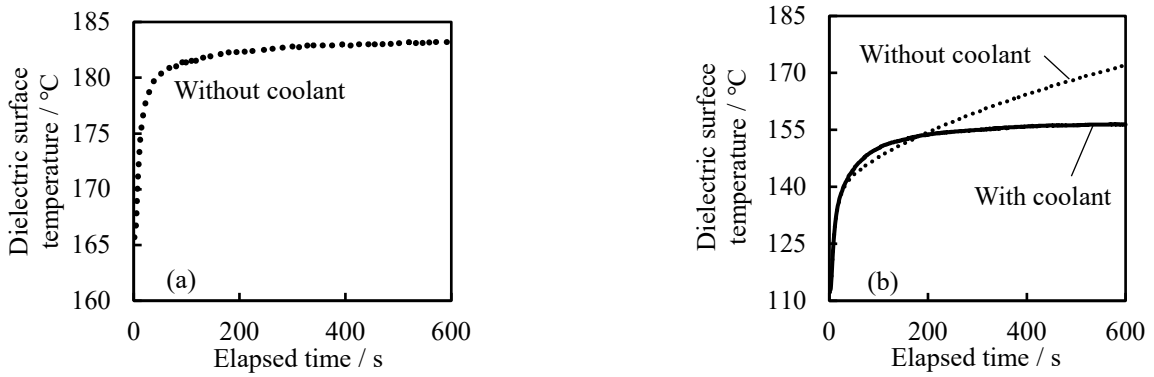

Fig. 2 The relationship between elapsed time and the dielectric surface temperature discharged at (a) 100 W, (b) 200 W. Coolant flow rate was 100 ml min^{-1}.

in a high adhesive strength. However, a higher adhesive strength is required industrially.

Recently, Ohkubo et al. reported a method of significant improving adhesive strength of PTFE, named "heat-assisted plasma" [6], while the effects of temperature and discharge power on the improvement of the adhesive strength have not been independently evaluated. Therefore, in this study, we prepared a new discharge chamber, and investigated these effects and adhesive mechanism.

2. Experimental

Fig. 1 shows the standard dielectric barrier discharge chamber with the shower head electrode. The chamber was first vacuumed with a rotary pump, and then the pressure was restored with gas to atmospheric pressure. The plasma was generated with a 13.56 MHz power supply. Table 1 shows the plasma treatment conditions.

The dielectric surface temperature was measured by an optical fiber thermometer. This temperature was increasing during discharge. Thus, a heater and cooling system were included in the lower electrode. Typical electrode temperature profiles discharged at 100 and 200 W are shown in Fig. 2. Surface temperature of the dielectric reached a constant value after 30 s discharge when coolants were not used for 100 W and when coolant used with a flow rate of 100 ml min^{-1} for the 200 W measurements.

The dimension of PTFE sheet was 25 mm × 130 mm × 0.2 mm, and was washed with trichloroethylene and deionized water in an ultrasonic cleaner before each treatment.

The samples for the peel test were prepared as follows: first, a treated PTFE sheet was glued on a stainless plate with an epoxy glue (Alaldite, NICHIBAN Inc.), and was leaved alone for 24 hours. Second, adhesive strength was measured by a 180° peel test at 30 mm min^{-1} peel speed.

The chemical state was measured with the XPS (Versa Probe II, ULVAC-Phi). The binding energies of XPS spectra were corrected with the C_{1s} peak position (C-C, 284.6 eV) [7].

The chemical bonding state of the PTFE surface was measured with FTIR-ATR (FT/IR-4100, Jasco).

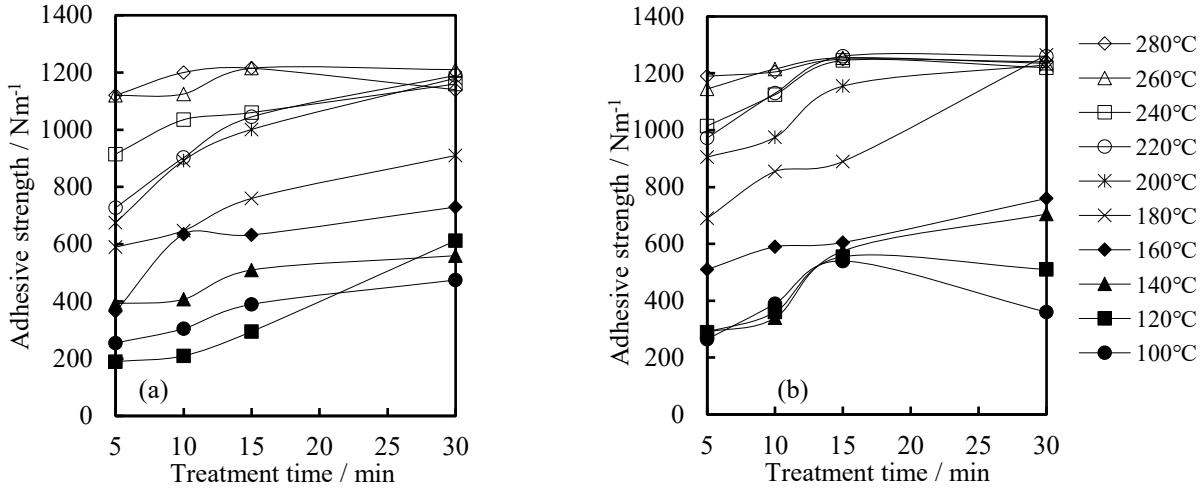

Fig. 3 Relationship between processing time and adhesive strength for each the dielectric surface temperature discharged at (a) 100 W, (b) 200 W.

3. Results and discussion

Fig. 3 shows the relationship between treatment time and adhesive strength for each the dielectric surface temperature at a discharge power of 100 W and 200 W. Longer treatment time and higher discharge power contributed to the increase of adhesive strength, as longer treatment times increase the effect of treatment and increased power fasten the treatment speed. An increase in the dielectric surface temperature has resulted in a significant increase in adhesive strength. At a certain surface temperature (200 °C or higher at 100 W, 180 °C or higher at 200 W) and treatment time, the adhesive strength converged to about 1250 Nm^{-1}. This is considered due to the cohesive failure occurred inside PTFE.

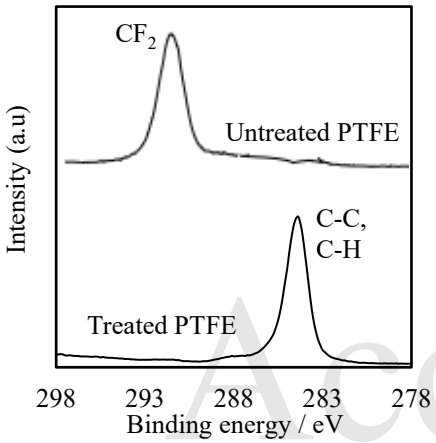

Fig. 4 C_{1s} spectrum of untreated PTFE and PTFE treated at 200 W discharge power and 240 ℃ dielectric surface temperature for 15 min.

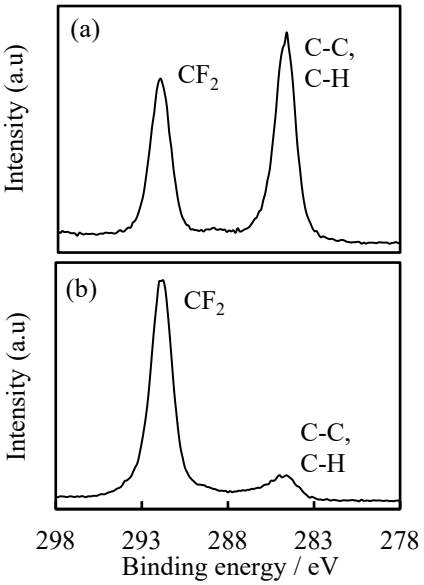

Fig. 5 C_{1s} spectra of (a) treated PTFE-peeled epoxy glue surface, (b) PTFE surface peeled off from epoxy glue. Peeled-PTFE was treated at a discharge power of 200 W and 240 ℃ dielectric temperature for 15 min.

The surface element composition changes of the plasma-treated PTFE were measured by XPS (Fig. 4). The peak assigned to CF_2 was dramatically reduced and a new peak assigned to C-C, C-H was generated. Therefore, the defluorination of the PTFE surface by the plasma treatment might affected the adhesive strength.

In order to verify the aforementioned cohesive failure, a peel resistance test was performed on PTFE, which is assumed to have occurred cohesive failure. The plasma-treated C_{1s} spectra of the peel interface between the epoxy glue surface (Fig. 5 (a)) and PTFE surface (Fig. 5 (b)) are shown. The peak assigned to -CF_2- appeared in the epoxy glue surface, a peak similar to untreated PTFE was observed at the peeled PTFE surface; we concluded that cohesive failure was observed on the treated PTFE and that the mechanical strength has reached to that of the material itself.

In order to investigate the effect of treatment time and dielectric surface temperature on the defluorination of PTFE, the ratio of fluorine and carbon (F/C) contained in the PTFE surface was investigated by changing the treatment time and dielectric surface temperature (Fig. 6) The F/C ratio

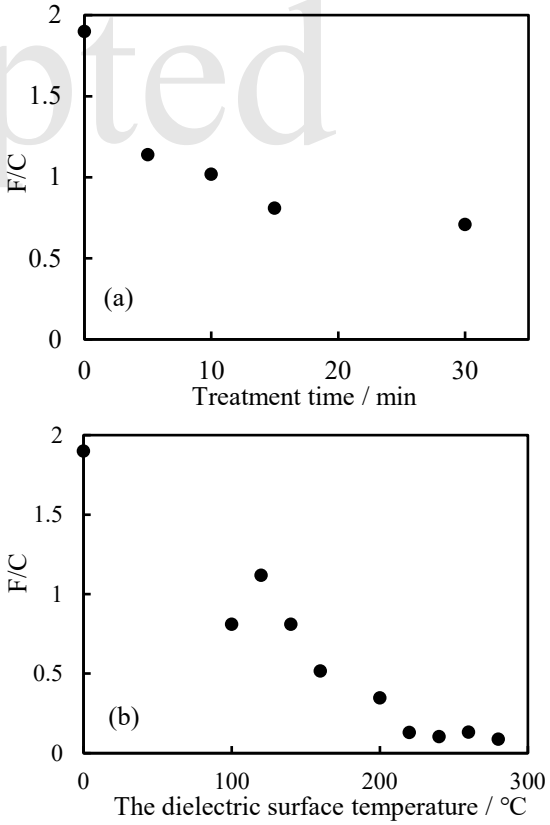

Fig. 6 Relationship between F/C and (a) treatment time. Discharge power was 200 W and the dielectric temperature was 100 ℃, (b) the dielectric surface temperature. Discharge power was 200 W and treatment time was 15 min.

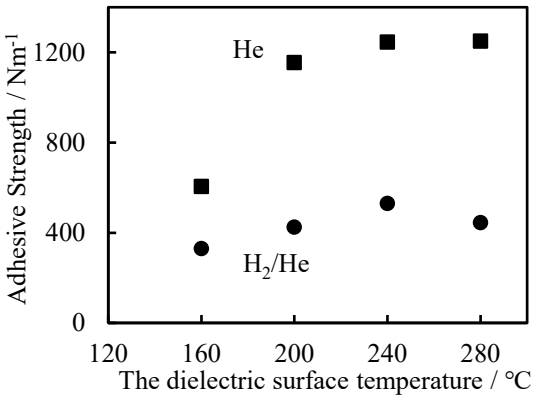

Fig. 7 Adhesive strength of PTFE treated with each gas at 200 W for 15 min.

of the untreated PTFE was 1.93. F/C ratio has decreased at longer treatment times (Fig 6 (a)) and at higher dielectric surface temperature (Fig. 6 (b)). F/C ratio has decreased to 0.05 by 240 °C. This may be due to the increase in fluidity of the molecular chains of PTFE as the dielectric surface temperature increased. We also speculated that the formation of dangling bonds on the PTFE surface and the bonding of them resulted in the formation of a crosslinked structure, which led to a significant increase in adhesive strength.

To verify this assumption, the sample gas was changed to H_2/He mixture, and the relationship between the dielectric surface temperature and adhesive strength is shown in Fig. 7. In addition, the surface chemical bonding state of untreated PTFE, He plasma treated PTFE, and H_2/He plasma treated PTFE was investigated (Fig. 8). The PTFE treated with H_2/He had significantly lower adhesive strength than the PTFE treated with only He. The peak assigned to stretching vibration of -CH_2- (near 2915 cm^{-1}) and a peak assigned to bending vibration of -CH_2- (near 1480 cm^{-1}) could be observed only in the film treated with H_2/He plasma. Therefore, the adhesive strength might be reduced, since the addition of hydrogen eliminated dangling bond to suppress cross-linking. Further, in Fig. 8 (c), a slight peak was observed around 1630 cm^{-1}, which assigned to the wavelength near the stretching vibration of C=C. The high adhesive strength of He treated PTFE may be caused from the C=C bond on the PTFE surface, which may have chemically bonded to the epoxy glue.

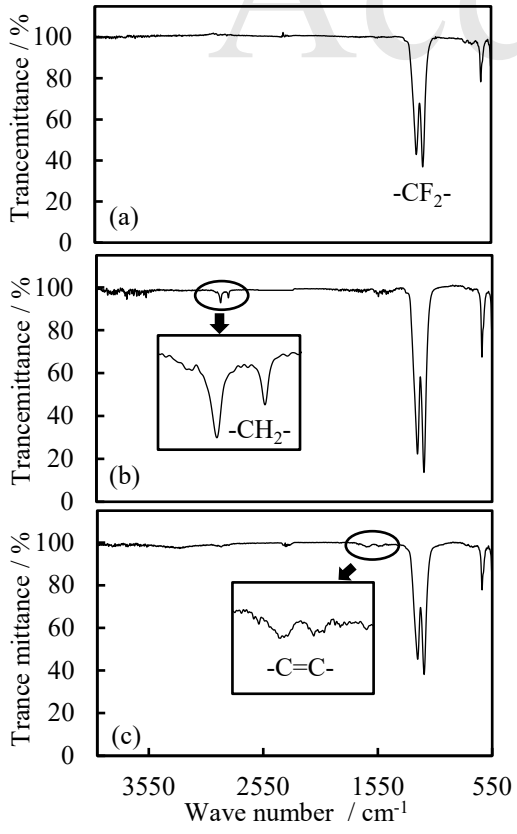

Fig. 8 ATR spectra of PTFE: (a) untreated PTFE, (b) treated with H_2/He, (c) treated with He.

4. Conclusion

By treating PTFE at a certain dielectric surface temperature and treatment time, the bonding strength was greatly increased to the level at which cohesive failure occurred. The fluidity of molecular chains on the PTFE surface was increased by the dielectric surface temperature, so that fluorine in the PTFE bulk could be removed.

In addition, the adhesion strength of PTFE treated with H_2/He plasma is significantly lower than that of PTFE treated with He, and -CH_2- is formed on the surface of PTFE treated with H_2/He plasma. It is considered that the improvement of the adhesive strength requires the formation of dangling bonds and a crosslinked structure.

References

1. S. Kanazawa, M. Kogoma, T. Moriwaki and S. Okazaki, J. Phys. D, **21** (1988) 838.
2. T. Yokoyama, M. Kogoma, T. Moriwaki and S. Okazaki, J. Phys. D, **23** (1990) 1125.
3. T. Yokoyama, M. Kogoma, S. Kanazawa, T. Moriwaki and S. Okazaki, J. Phys. D, **23** (1990) 374.
4. K. Tanaka, K. Takahashi, M. Kogoma, J. Photopolymer Sci. Tech., **23**, 4 (2010) 549.
5. K. Tanaka, K. Takahashi, M. Kogoma, J. Photopolymer Sci. Tech., **24**, 4 (2011) 441.
6. Y. Ohkubo, K. Ishihara, H. Sato, K. Endo, K. Yamamura, J, Surface Finishing Society of Japan, **67**, 10 (2016) 551.
7. U. Gelius, P. F. Heden, J. Hedman. B. J. Lindberg, R. Manne, R. Nordberg, C. Nordling and K. Siegbahn, Phys. Scr., **2** (1970) 70.

Surface Functionalization of Diamond-like Carbon Film with Biocompatible Polymer Brushes

Yasushi Sasai[1*], Daiki Ousaka[2], Yasuhiro Fujii[3], Aoi Isono[1]
Yukinori Yamauchi[4], Shin-ichi Kondo[5] and Tatsuyuki Nakatiani[6]

[1] Department of Pharmacy, Gifu University of Medical Science,
4-3-3 Nijigaoka, Kani, Gifu 509-0293, Japan
[2] Department of Pharmacology, Okayama University Graduate School of Medicine,
Density and Pharmaceutical Science, Okayama, 700-8558, Japan
[3] Division of Strategic Planning and Evaluation, Department of Innovative Drug
Discovery and Development, Japan Agency for Medical Research and Development,
1-7-1, Otemachi, Chiyoda-ku, Tokyo 100-0004, Japan
[4] Department of Pharmaceutical Physical Chemistry, College of Pharmaceutical Sciences,
Matsuyama University, 4-2 Bunkyo-cho, Matsuyama, Ehime 790-8578, Japan
[5] Laboratory of Pharmaceutical Physical Chemistry, Gifu Pharmaceutical University,
1-25-4 Daigaku-Nishi, Gifu 501-1196, Japan
[6] Institute of Frontier Science and Technology, Okayama University of Science,
1-1 Ridaicho, Kita-ku, Okayama 700-0005, Japan
**ysasai@u-gifu-ms.ac.jp*

Biocompatible polymer brushes were successfully synthesized on diamond-like carbon (DLC) films via surface-initiated atom transfer radical polymerization (SI-ATRP) of 2-mtharyloyloxyethyl phosphorylcholine (MPC). The DLC film with a water contact angle (WCA) of approximately 71.9° was modified into a highly hydrophilic surface with a WCA of approximately 15.0° after MPC polymer brush modification. Protein adsorption tests using a quartz crystal microbalance showed that the MPC polymer brush modification dramatically decreased the physical adsorption of bovine albumin and fibrinogen when compared with the DLC film. This indicated an improvement in the surface biocompatibility. Considering that DLC coatings can be applied to various materials such as metals, polymers, and ceramics, MPC polymer brush modification of DLC films would be a versatile technology for improving the surface biocompatibility of a variety of biomedical devices.

Keywords: Polymer brushes, Diamond-like carbon, 2-Methacryloyloxyethyl phosphorylcholine, Atom-transfer radical polymerization, Protein adsorption

1. Introduction

Various materials including metals, polymers, and ceramics have been used in medical devices and artificial organs [1-5]. The most important requirement for such biomaterials is their stability and biocompatibility in the physiological environment to prevent significant adverse biological responses such as inflammation and thrombus formation. When biomaterials are implanted into the body, most reactions occur on the surface of the material. Thus, the surface of these biomaterials must be chemically and biologically inert to their physiological surroundings, except for biomaterials designed to specifically interact with a ligand in the body [6]. However, many biomaterials do not have sufficient surface biocompatibility despite having good bulk properties. Hence, they require some surface modifications to improve their surface biocompatibility. Various methods have been investigated and applied to improve the surface biocompatibility of commercial products, including physical and/or chemical modifications such as polymer grafting, polymer coating, chemical etching, plasma surface treatment, plasma polymerization, micro or nano-patterning,

Received April 1, 2022
Accepted May 20, 2022

and bioactive molecule immobilization [7-11].

Diamond-like carbon (DLC) film coatings have been commonly used as biomaterials owing to their good biocompatibility, low friction coefficient, chemical inertness, and physical stability [12-14]. Another advantage of DLC films is that they can be used to coat substrates with complex shapes. Nakatani *et al.* developed a DLC film coating method on a coronary stent, which has been clinically proven to be effective for use in the treatment of coronary artery disease [15]. Moreover, a technique for homogeneous DLC film coating on the inner surface of a small-diameter tube (inner diameters of less than 6 mm for expanded polytetrafluoroethylene (ePTFE) tubes and 2 mm for silicon tubes) has been reported recently [16, 17]. Although DLC films have many advantages in biomedical applications, it is difficult to modify their surface for active functionalization, as achieved by polymer modification, because it is chemically inert.

Polymer brush modification is achieved by covalently tethering one end of each polymer chain with a dense grafting density on a substrate. This method has been widely used in biomedical fields for surface functionalization of materials to obtain blood-compatible materials, lubricant surfaces, functional substrate/cell interfaces, and biosensing platforms with resistance against non-specific adsorption from biological samples [18]. However, some researchers have reported the instability of polymer brushes fabricated on inorganic substrates in aqueous solutions and humid air [19-21].

Surface biocompatibility is required for various medical devices, and DLC film coatings can be applied to biomaterials with complex shapes. Thus, methods to fabricate polymer brushes on DLC films would be very useful for active functionalization of the surface, which cannot be achieved by DLC film coatings alone. In this study, we investigated a 2-methacryloyloxyethyl phosphorylcholine (MPC) polymer brush modification of a DLC film and its protein adsorption properties. The MPC polymer (Fig. 1) is a well-known hydrophilic methacrylate polymer with excellent biocompatibility and antifouling activities. Some MPC polymer-coated implantable medical devices have also been approved by the Food and Drug Administration (FDA) and are in use [22].

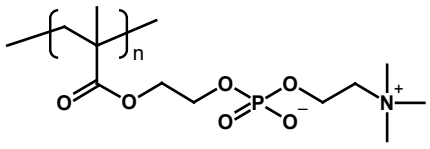

Fig. 1. Structure of the MPC polymer.

2. Experimental

2.1. Materials

2-methacryloyloxyethyl phosphorylcholine (MPC) was purchased from Sigma-Aldrich and used after removing the inhibitor. 3-Aminopropyltrimethoxysilane (APTMOS), 2-bromoisobutyryl bromide (BIBB), CuBr, and $CuBr_2$ were obtained from Sigma-Aldrich and used as without any modifications. 2,2-bipyridyl (bpy), bovine albumin, and bovine fibrinogen were obtained from FUJIFILM Wako Pure Chemical Corp. and used without any modifications. The atom transfer radical polymerization (ATRP) initiator, 3-(2-bromoisobutyramido)propyl(trimethoxy)silane (BrTMOS), was synthesized by a reaction of APTMOS and BIBB according to literature [23]. An 8.0 mm × 10 mm silicon wafer and Au-coated QCM chip (AT-cut, 9 MHz), used as substrates for DLC coating, were obtained from AS One Corp. and SEIKO EG&G Co., Ltd., respectively.

2.2. DLC coating

The DLC film was coated on the substrates using the plasma-enhanced chemical vapor deposition (PECVD) method with a parallel type 13.56 MHz radio frequency (RF) PECVD apparatus [24]. Before DLC coating, the substrate surfaces were cleaned by Ar ion bombardment. The apparatus for this was the same as PECVD. The Ar gas flow rate was maintained at 10 sccm. Subsequently, the Ar gas in the chamber was exhausted, and CH_4, the source gas for the DLC coating, was introduced into the chamber at the rate of 10 sccm. For the silicon wafer sample, Ar ion bombardment was performed for 60 min at an RF power of 20 W, and PECVD was performed for 10 min at an RF power of 70 W. For the QCM chip, Ar ion bombardment was performed for 15 min at an RF power of 20 W, and PECVD was performed for 5 min at an RF power of 70 W. During both the processes, the operational pressure in the chamber was maintained at 5 Pa.

2.3 MPC polymer brush modification of DLC coated substrates

Before the ATRP initiator modification, the

substrates were exposed to oxygen plasma for 30 s in the reaction chamber to introduce hydroxyl groups on the DLC film. The oxygen plasma state was generated by an RF inductively coupled discharge at 13.56 MHz with a supplied power of 50 W , and O_2 gas flow rate of 50 mL/min and pressure of 66.6 Pa [25].

The surfaces of the oxygen plasma-irradiated substrates were modified by the ATRP initiator via a chemical vapor adsorption method, as reported by Kobayashi et al. [26]. The MPC polymer brushes were prepared by surface-initiated atom transfer radical polymerization (SI-ATRP) of the MPC from the ATRP initiator-functionalized substrates in a degassed solution consisting of [MPC]/[CuBr]/[$CuBr_2$]/[bpy] with a feed ratio of 50 (0.75 M):1:0.2:2 in a mixture of methanol and water (1:4 (v/v)) at 40 °C (Fig. 2). The SI-ATRP time was 6 h. After the reaction, the substrates were removed from the ATRP solution, rinsed with methanol, and dried in vacuum.

2.4. Analytical method

2.4.1. X-ray photoelectron spectroscopy (XPS)

XPS measurements were performed to determine the surface chemical compositions of the polymer brushes using a PHI Quantera SXM instrument (ULVAC-PHI) with AlKα as the X-ray radiation source operating at 10 mA and 20 kV.

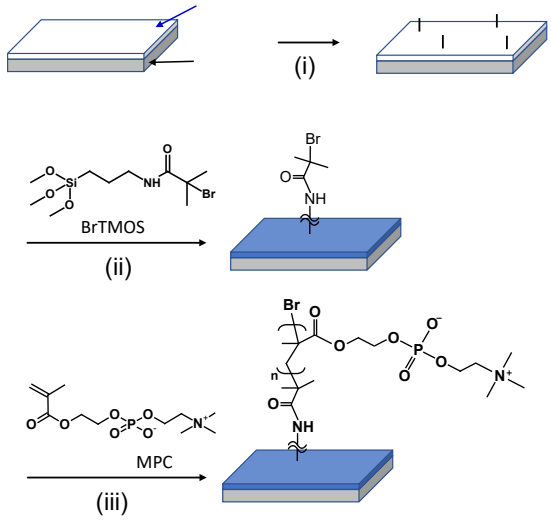

Fig. 2. Preparation of MPC polymer brushes on the DLC film. (i) Oxygen plasma irradiation (13.56 MHz RF ICP, O_2 50mL/min, 66.6 Pa, 30W, 30s) (ii) ATRP initiator modification via a chemical vaper adsorption of BrTMOS (iii) Polymer brush modification via SI-ATRP of MPC.

2.4.2. Water contact angle (WCA) measurement

The static WCA was measured to evaluate the surface wettability of the substrates using an SImage Auto 100 system (Excimer. Inc.). The WCAs were automatically obtained immediately after a drop (5 μL) of deionized water was applied from a syringe to the sample surface. All reported WCAs represented the average ± SD of the three measurements.

2.4.3. Atomic force microscopy (AFM)

AFM images were obtained to determine the polymer brush thickness using an AFM-5300E (Hitachi High-Tech Corp.) in the dynamic force mode and an SI-DF3P2 cantilever (Hitachi High-Tech Corp.). For sample preparation, the ATRP-functionalized silicon wafer was UV-irradiated for 6 min through a very fine thin bar grid (1500 mesh, EM Japan, Co., Ltd.) placed 3 cm from the substrates using a spot UV irradiation apparatus (Spot Cure SP-9, Ushio Inc.) (Fig. 3). Next, the MPC polymer brushes were prepared from an ATRP initiator-patterned surface.

2.4.4. Quartz Crystal Microbalance (QCM) measurement

A QCM measurement system with a flow cell (QCA922, SEIKO EG&G Co., Ltd.) was used to evaluate protein adsorption onto the DLC film and polymer brushes. 5.0 mg/mL bovine albumin in phosphate buffer saline (PBS, pH 7.4) and 0.5

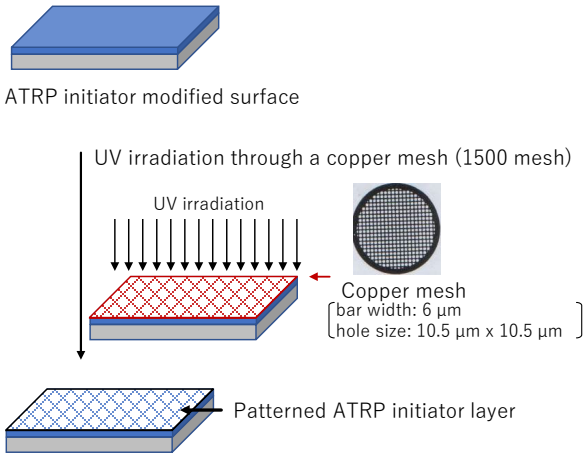

Fig. 3. Preparation of patterned ATRP initiator layer.

mg/mL bovine fibrinogen in PBS were used as model protein solutions. The DLC film-coated QCM chip, with or without MPC polymer brushes, was mounted on the flow cell, and the PBS was flowed into the cell. After the baseline of the oscillating frequency stabilized, the PBS in the cell was replaced with the protein solution. Once the oscillating frequency reached a plateau, the protein solution in the cell was replaced with PBS to wash out the weakly adsorbed protein molecules on the sample surface. The amount of protein on the substrate was determined from the frequency shift between the baseline frequency and the post-washout process frequency using the Sauerbrey equation [27].

3. Results and discussion

3.1. Fabrication of MPC polymer brushes on DLC film

We synthesized MPC polymer brushes via the SI-ATRP of MPC from DLC film-coated substrates. SI-ATRP is a highly versatile approach for the fabrication of densely grafted polymer brush layers [28]. ATRP initiator modification is an important step in the synthesis of polymer brushes via SI-ATRP. Kobayashi et al. reported the modification of the DLC film surface by chemical vapor adsorption of a triethoxy-silane-type ATRP initiator [26]. Based on this method, we modified the DLC film surface with the trimethoxy-type ATRP initiator, BrTMOS.

Figure 4 and Table 1 show the results of the WCA measurements at each step from the DLC-coated surface to the MPC polymer brush modified surface. The WCA of the oxygen plasma irradiated surface increased from 26.6 ± 1.2° to 79.8 ± 2.8°, indicating that the DLC surface was successfully modified with the hydrophobic ATRP initiator, BrTMOS, through a chemical vapor adsorption method. Moreover, after MPC polymer brush modification, the surface wettability was dramatically changed to a hydrophilic nature with a WCA of 15.0 ± 2.5°. These results show that our method is effective for the MPC polymer modification of DLC films. The XPS also demonstrated the MPC polymer brush modification of the DLC film because the atomic % on the MPC polymer brush modified surface was similar to the theoretical value (Fig. 5 and Table 2).

The thickness of the MPC polymer brushes were determined by AFM analysis. Figure 6A shows the optical microscope image of the patterned polymer brush surfaces. When the

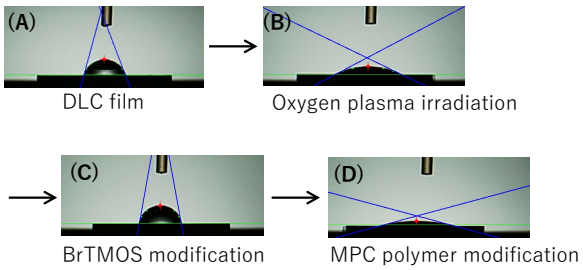

Fig. 4. Photographs of water droplets on each sample surface.

Table 1 The water contact angle of each sample surface.

Sample	WCA (°)
DLC film on Silicon wafer	71.9 ± 2.2
Oxygen plasma irradiated DLC film	26.6 ± 1.2
BrTMOS modified surface	79.8 ± 2.8
MPC polymer brush modified surface	15.0 ± 2.5

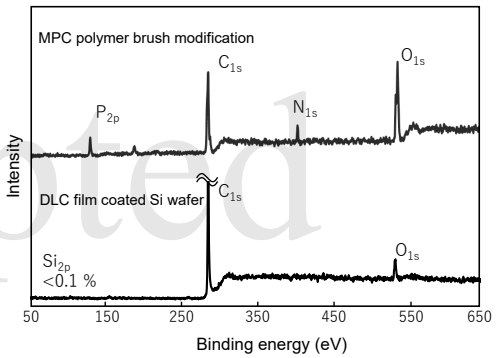

Fig. 5. Wide scan spectra of XPS for the DLC film and the MPC polymer brush modified DLC film.

Table 2 Surface atomic % determined by XPS.

	Atomic %			
	C	O	N	P
Theoretical atomic % of MPC polymer	57.9	31.6	5.3	5.3
DLC film on silicon wafer	94.8	5.21	—	—
MPC polymer brush modified surface	59.9	29.0	5.9	5.0

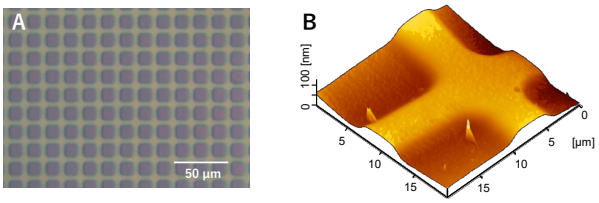

Fig. 6. Patterned MPC polymer brushes: (A) Optical and (B) AFM images.

sample was prepared, the BrTMOS surface was treated by UV irradiation through a metal mesh. The BrTMOS on the surface was deactivated at the area exposed to the UV radiation. which passed through the holes of the mesh. The patterned BrTMOS surface was used for the MPC polymer brush modification. As shown in Fig. 6A, the metal mesh pattern was clearly printed as a pattern of MPC polymer brushes. Moreover, the results indicate that the MPC polymer brush with homogeneous thickness and grafting density was fabricated using the present ATRP initiator modification and SI-ATRP conditions. Figure 6B shows an AFM image visualizing the difference in the height of the DLC film and the top of the polymer brushes. From the cross-sectional profile of the AFM images at three different points on the patterned surface, the brush thickness was calculated to be 44.3 ± 4.2 nm.

3.2. Protein adsorption properties

The non-specific protein adsorption on the materials in the body often causes adverse reactions, resulting in the failure of many biomaterials, such as medical implants [29]. In this study, the protein adsorption properties of MPC polymer brush-modified surfaces were compared with those of DLC films. Figure 7 shows the changes in the amounts of adsorbed albumin and fibrinogen on the sample surface monitored by the QCM system. The first and second spikes in the graph were points where the protein solution was introduced into the flow cell and the protein solution was replaced by PBS to remove weakly adsorbed proteins, respectively. On the DLC film, the amount of protein adsorbed after removing the weakly bound proteins is 622.7 ng/cm^2 for albumin and 1292 ng/cm^2 for fibrinogen. On the MPC polymer brushes fabricated with the DLC film, the adsorption was negligible for albumin and 41.52 ng/cm^2 for fibrinogen. As seen in Figure 7, the MPC polymer brush modification dramatically decreased the adsorption of albumin and fibrinogen onto the surface. These results suggest that DLC films might be a good interfacial layer for introducing polymer brushes on various biomaterials.

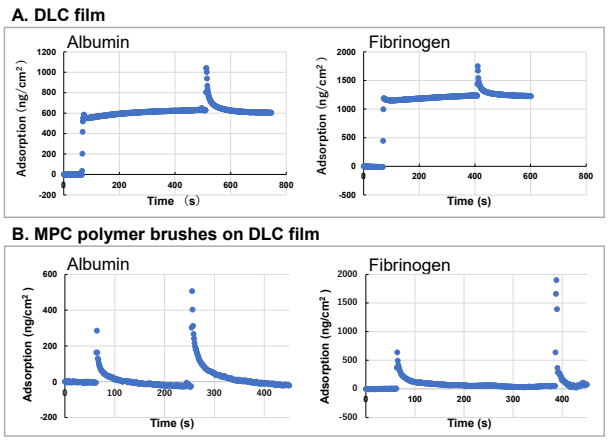

Fig. 7 Protein adsorption on the sample surfaces measured by the QCM system.

4. Conclusions

The biocompatible MPC polymer brush modification on a chemically inert DLC film was successfully achieved via SI-ATRP method. The protein adsorption experiments demonstrated the function of MPC polymer brushes on DLC film. Based on the results, the polymer brush modification can be applied to even an unsuitable material surface using a DLC film as an interfacial layer between polymer brushes and materials.

Acknowledgement

This work was supported by JSPS KAKENHI (grant number 19K09270).

References

1. H. Qu, H. Fu, Z. Han, Y. Sun, *RSC Adv.*, **9** (2019) 26252.
2. A.J. Festas, A. Ramos, J.P. Davim, *Proc. Inst. Mech. Eng. L: J. Materials: Design and Applications*, **234** (2020) 218.
3. N. Angelova, D. Hunkeler, *Trends Biotechnol.*, **17** (1999) 409.
4. A. J. T. Teo, A. Mishra, I. Park, Y.-J. Kim, W.-T. Park, Y.-J. Yoon, *ACS Biomater. Sci. Eng.*, **2** (2016) 454.
5. K. Prasad, O. Bazaka, M. Chua, M. Rochford, L. Fedrick, J. Spoor, R. Symes, M. Tieppo, C. Collins, A. Cao, D. Markwell, K. Ostrikov, K. Bazaka, *Materials*, **10** (2017) 884.
6. E. Gibon, L.A. Córdova, L. Lu, T.-H. Lin, Z. Yao, M. Hamadouche, S. B. Goodman, *J. Biomed. Mater. Res. Part B Appl. Biomater.*, **105** (2017) 1685.
7. A. A. John, A. P. Subramanian, M. V. Vellayappan, A. Balaji, S. K. Jaganathan, H. Mohandas, T. Paramalinggam, E. Supriyanto, M. Yusof, *RSC Adv.*, **5** (2015) 39232.
8. W. Sun, W. Liu, Z. Wu,H. Chen, *Macromol. Rapid Commun.*, **41** (2020) 1900430.

9. T. Desmet, R. Morent, N. D. Geyter, C. Leys, E. Schacht, P. Dubruel *Biomacromolecules*, **10** (2009) 2351.
10. S. Bose, S. F. Robertson, A. Bandyopadhyay. *Acta Biomater*., **66** (2018) 6.
11. A. Sultana, M. Zare, H. Luo, S. Ramakrishna, *Int. J. Mol. Sci.*, **22** (2021) 11788.
12. M. Allen, B. Myer, N. Rushton, *J. Biomed. Mater. Res.*, **58** (2001) 319.
13. R. K. Roy, K. R. Lee, *J. Biomed. Mater. Res. B Appl. Biomater.*, **83** (2007) 72.
14. M. Rahmati, M. Mozafari, *Front. Bioeng. Biotechnol.*, **7** (2019) doi: 10.3389/fbioe.2019.00004.
15. T. Nakatani, K. Okamoto, I. Omura, S. Yamashita, *J. Photopolym. Sci. Technol.*, **20** (2007) 221.
16. T. Nakatani, Y. Imai, Y. Fujii, T. Goyama, S. Ozawa, *J. Photopolym. Sci. Technol.*, **31** (2018) 373.
17. S. Watari, K. Wada, M. Araki, T. Sadahira, D. Ousaka, S. Oozawa, T. Nakatani, Y. Imai, J. Kato, R. Kariyama, T. Watanabe, Y. Nasu. *Int. J. Urol.*, **28** (2021) 1282.
18. M. Krishnamoorthy, S. Hakobyan, M. Ramstedt, J. E. Gautrot, *Chem. Rev.* **114** (2014) 10976.
19. H.-A. Klok, J. Genzer, *ACS Macro Lett.*, **4** (2015) 636.
20. K. A. Melzak, K. Yu, D. Bo, J. N. Kizhakkedathu, J. L. Toca-Herrera, *Langmuir*, **31** (2015) 6463.
21. M. B. Pérez, M. Cirelli, S. de Beer, *ACS Appl. Polym. Mater*., **2** (2020) 3039.
22. K. Ishihara, *J. Biomed. Mater. Res. A*, **107** (2019) 933.
23. S. Tugulu, A. Arnold, I. Sielaff, K. Johnsson, H.-A. Klok, *Biomacromolecules*, **6** (2005) 1602.
24. T. Nakatani, H. Takeuchi, A. Wada, S. Yamashita, *J. Photopolym. Sci. Technol.*, **32** (2019) 511.
25. Y. Sasai, N. Doi, Y. Yamauchi, M. Kuzuya, S. Kondo, *J. Photopolym. Sci. Technol.*, **32** (2019) 529.
26. M. Kobayashi, M. Kaido, A. Suzuki, A. Takahara, *Polymer*, **89** (2016) 128.
27. G. Sauerbrey, Z. Phys., **155** (1959) 206
28. R. Barbey, L. Lavanant, D. Paripovic, N. Schüwer, C. Sugnaux, S. Tugulu, H.-A. Klok, *Chem. Rev.* , **109** (2009) 5437.
29. C. Blaszykowski, S. Sheikh and M. Thompson, *Chem. Soc. Rev.*, **41** (2012) 5599.

Immobilization of CYP1A2 and CYP Reductase onto Self-assembled Phospholipid Layer and Evaluation of their Activity

Shin-ichi Kondo[1*], Ayano Ishii[1], Naoki Doi[1], Yasushi Sasai[2], Yukinori Yamauchi[3], and Masayuki Kuzuya[1]

[1] Laboratory of Pharmaceutical Physical Chemistry, Gifu Pharmaceutical University, 1-25-4 Daigaku-Nishi, Gifu 501-1196, Japan
[2] Faculty of Pharmacy, Gifu University of Medical Science, 4-3-3 Nijigaoka, Kani-shi, Gifu 509-0293, Japan
[3] Department of Pharmaceutical Physical Chemistry, College of Pharmaceutical Sciences, Matsuyama University, 4-2 Bunkyo-cho, Matsuyama, Ehime 790-8578, Japan
**skondo@gifu-pu.ac.jp*

We had immobilized cytochrome P450 (CYP) 1A2 and CYP reductase (CPR) onto a self-assembled phospholipid layer containing stearic acid (LDPE-StA-PC-SA) to confirm the functional interaction between CYP 1A2 and CPR. The formation of resorufin from 7-ethoxy resorufin was observed by use of the film immobilizing CYP 1A2 and CPR onto LDPE-StA-PC-SA. It was clarified that the fluidity of LDPE-StA-PC-SA was very important. The actual activity of CYP 1A2 did not depend on the density of CYP 1A2 on LDPE-StA-PC-SA, although its specific activity was affected on its density. The activity of immobilized CYP 1A2 depended on a temperature. It was assumed that the optimal temperature was about 45 ºC.

Keywords: Self-assembled phospholipid layer, Plasma irradiation, Cytochrome P450 (CYP), CYP reductase

1. Introduction

Considerable interest has been focused on the immobilization of functional molecules, such as DNA, enzyme and protein, onto a water-insoluble material, which has been used as a biochip or biosensor [1-3]. There are three major methods for immobilizing biomolecules: encapsulation[4, 5], adsorption[6-8] and covalent bonding. Covalent bonding method to immobilize proteins onto a material has several advantages and disadvantages [9-11]. It is usually thought to be the stable method to prevent the elution of protein from the material. On the other hand, it is relatively expensive and complicated in procedures involved. Activity yields may be low due to the exposure of the proteins to harsh environments or toxic reagent and the modification of active site. It is also considered that the interaction between material surface and immobilized proteins might make their activities lower.

Received March 31, 2022
Accepted June 20, 2022

NADPH-supported catalysis of cytochrome P450 (CYP) monooxygenase reactions requires a functional interaction between CYP and NADPH-cytochrome P450 reductase (CPR). This means that CYP and CPR must approach each other to undergo monooxygenase reactions.

On the other hand, we have developed the method to introduce a durable surface wettability on several hydrophobic polymers by plasma-assisted method [12-16], and to fabricate a self-assembled phospholipid (phosphatidyl choline (PC)) layer containing stearic acid (StA) (LDPE-StA-PC-SA) on it [17]. It was confirmed that LDPE-StA-PC-SA possessed fluidity resembling to cellular membrane. We also reported the immobilization of antibody and enzyme onto LDPE-StA-PC-SA, and the evaluation of their activities [18, 19]. As described above, it is necessary for CYP and CPR to approach each other to interact functionally. Therefore, it was considered that CYP and CPR

must be immobilized on the movable type surface, such as LDPE-StA-PC-SA.

In this paper, we had immobilized CYP 1A2 and CPR onto LDPE-StA-PC-SA to confirm the functional interaction between them (Fig. 1). The activity of immobilized CYP 1A2 was estimated by the reaction of 7-ethoxyresorufin (7-ER) to resorufin. The activity of immobilized CYP 1A2 was also examined against its density and temperature.

2. Experimental

2.1. Materials

Cytochrome P450 1A2 overexpression lysate and cytochrome P450 1A2 human were purchased from Novus Biologicals and SIGMA-Aldrich, respectively. NADPH regenerating system (NADPH) was obtained from SEKISUI MEDICAL CO., LTD. P450 Oxidoreductase, Human Liver, Purified (CYP450-GP) was purchased from Funakoshi Co., Ltd. 7-ER was obtained from Cayman Chemical.

2.2. Immobilization of CYP 1A2 and CPR onto the LDPE-StA-PC-SA

According to the literatures, the LDPE-StA-PC-SA film (1 x 3 cm) was fabricated[17, 18]. To 10 mL of phosphate buffer (pH 4.0) was added 200 µL of 0.047 µmol/ml 1-ethyl-3-(3-dimethylamino-propyl) carbodiimide hydrochloride (EDC-HCl) water solution, and then LDPE-StA-PC-SA film was immersed into the solution. This solution was kept at 4 ºC for 2 h. The LDPE-StA-PC-SA film was taken off from the solution and washed with water. This film was soaked into 10 mL of pH 7.4 phosphate buffer saline (PBS) containing various concentration of CYP1A2 and CPR (molar ratio 1:1) at 4 ºC for 24 h. This film was washed with PBS to obtain the LDPE-StA-PC-SA film immobilizing CYP 1A2 and CPR.

2.3. Estimation of activity of immobilized CYP 1A2 [20]

To 138.2 mL of dimethyl sulfoxide was dissolved 0.1 mg of 7-ER to obtain 7-ER solution (3 µM). NADPH solution (1 mM) was prepared by the dissolution of 0.3 mL of NADPH into 0.7 mL of MilliQ. The film immobilizing CYP 1A2 and CPR was immersed into the mixture of 7-ER solution, PBS and NADPH solution. Enzyme reaction was carried out at 37 ºC for a prescribed period. The fluorescence intensity of this solution was measured at excitation wave length 525 nm and fluorescence wave length 620 nm.

2.4 Activity of immobilized CYP 1A2 against temperature

The activity of immobilized CYP 1A2 was measured at various temperatures (37-55 ºC) according to the above-mentioned method. The fluorescence measurement was performed after cooling this solution to room temperature.

3. Results and Discussion

3.1. Activity of CYP 1A2 immobilized onto LDPE-StA- PC-SA

CYP 1A2 and CPR were immobilized onto LDPE-StA-PC-SA. The total amount of CYP 1A2 and CPR immobilized onto LDPE-StA- PC-SA was 1.67 pmol/cm^2 by Bradford method. As the radio of unreacted CYP 1A2 and CPR was almost 1:1 by capillary electrophoresis, it was assumed that the ratio of CYP 1A2 and CPR on LDPE-StA-PC-SA might be 1:1. As a comparison, we prepared the LDPE-StA-PC-SA film immobilizing only CYP 1A2 or CPR. Figure 2 shows the progressive changes in produced resorufin with 3 types of films immobilizing CYP 1A2. Resorufin was not observed with the film immobilizing only CYP 1A2. It was also shown that resorufin was hardly detected with the films separately immobilizing CYP 1A2 and CPR. When CYP 1A2 and CPR was immobilized onto the same film, resorufin was produced. This result suggested that CYP 1A2 and CPR could approach to each other to proceed the functional interaction.

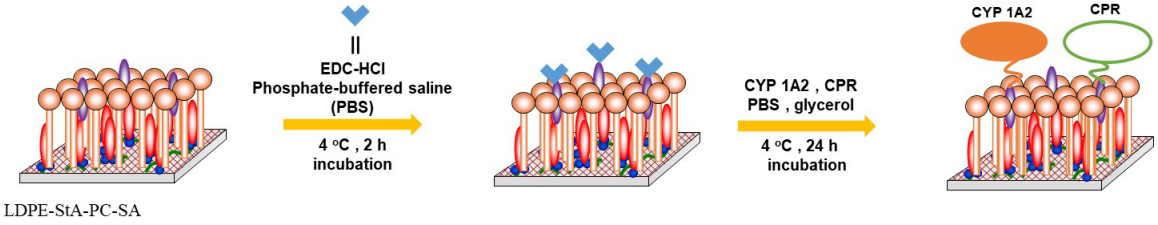

Fig. 1. Schematic illustration of the immobilization of CYP 1A2 and CPR onto LDPE-StA-PC-SA.

3.2. Specific activity of immobilized CYP 1A2 against its density

Figure 3 shows the specific activity of immobilized CYP 1A2 against its density.

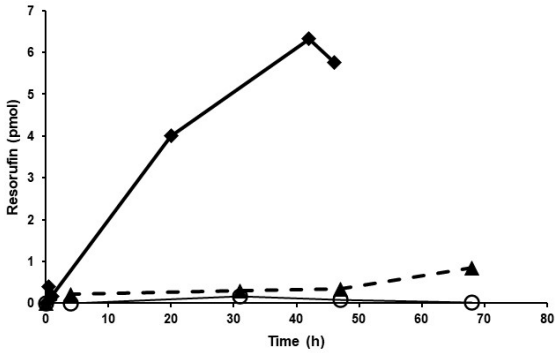

Fig. 2. Progressive changes in produced resorufin with 3 types of films immobilizing CYP 1A2.
○ : only CYP 1A2 was immobilized, ▲ ; CYP 1A2 and CPR were immobilized on separate sheets, ◆ ; CYP 1A2 and CPR were immobilized on the same sheet.

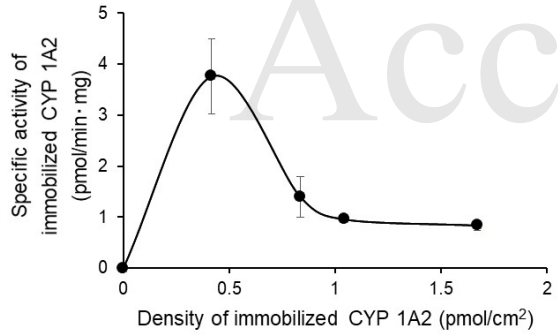

Fig. 3. Specific activity of immobilized CYP 1A2 against its density.

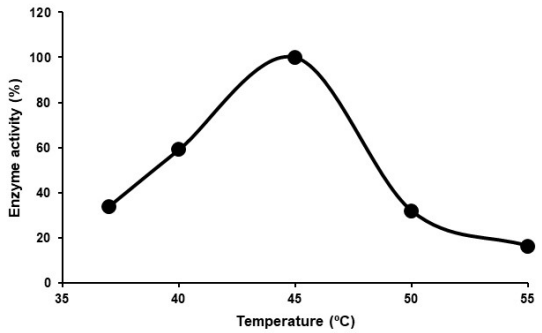

Fig. 4. Changes in activity of immobilized CYP 1A2 against temperature

When the density of immobilized CYP 1A2 was 0.4 pmol/cm^2, the specific activity showed the maximum value. After the maximum value, the specific activity steeply decreased toward to the limiting value. It was considered that the specific activity might be higher in lower density due to the ease to move, but lower in higher density due to the hard to move. It was assumed that actual activity of enzyme could depend on the specific activity and density of enzyme, and represent the product of specific activity and density. In comparison with 0.4 and 1.7 pmol/cm^2, there is no significant difference between their actual activities.

3.3 Changes in activity of immobilized CYP 1A2 against temperature

We studied the changes in activity of immobilized CYP 1A2, whose density was 1.6 pmol/cm^2, against temperature (Fig. 4). As shown in Fig. 4, enzyme activity increased from 30 ºC to 45 ºC. After then, enzyme activity rapidly decreased. It was suggested that CYP 1A2 was denatured over 45 ºC, and that the optimal temperature was about 45 ºC.

4. Conclusion

The conclusions drawn from the present study can be summarized as follows.

The formation of resorufin was observed by use of the film immobilizing CYP 1A2 and CPR onto the self-assembled phospholipid layer possessing fluidity (LDPE-StA-PC-SA). It was clarified that the fluidity of LDPE-StA-PC-SA was very important. The actual activity, which was denoted the product of specific activity and density, of CYP 1A2 did not depend on the density of CYP 1A2 on LDPE-StA-PC-SA. The activity of immobilized CYP 1A2 depended on a temperature. It was assumed that the optimal temperature was about 45 ºC.

We are now actively elaborating the chemical reaction using the film immobilizing CYP and CPR.

References

1. R. J. Lipshutz, S. P. A. Fodor, T. R. Gingeras, and D. J. Lockhart, *Nature Genet. Suppl.* **21** (1991) 20.
2. M. Nouaimi, K. Möschel, and H. Bisswanger, *Enzyme Microb. Technol.* **29** (2001) 567.
3. F. Poncin-Epaillard, and G. Legeay, *J. Biomate. Sci. Polymer Edn.* **14** (2003) 1005.
4. M. F. Canbolat, H. B. Savas, and F. Gultekin, *J. Appl. Polym. Sci.*, **134** (2017) 44404.
5. M. D. A. Porto, J. P. dos Santos, H. Hackbart, G. P. Bruni, L. M. Fonseca, E. da Rosa Zavareze, and A. R. G. Dias, *Int. J. Biol. Macromol.*, **126** (2019) 834.

6. S. Smith, M. Delaney, and M. Frey, *Polymers*, **12** (2020) 1117.
7. E. Vonasek, P. Lu, Y.-L. Hsieh, and N. Nitin, *Cellulose*, **24** (2017) 4581.
8. J. Zdartaa, M. Staszaka, K. Jankowskaa, K. Kaźmierczaka, O. Degórskaa, L. N. Nguyenb, E. Kijeńska-Gawrońskacd, M. Pineloe, and T. Jesionowskia, *Int. J. Biol. Macromol.*, **165** (2020) 2049.
9. M. A. Mitz and R. J. Schlueter, *J. Am. Chem. Soc.* **81** (1959) 4024.
10. A. Kumar and M. N. Gupta, *J. Mol. Cata. B: Enzymatic* **5** (1998) 289.
11. X. Chen, J. Jia, and S. Dong, *Electroanalysis.* **15** (2003) 608.
12. M. Kuzuya and T. Yamashiro, *J. Photopolym. Sci. Technol.,* **8** (1995) 381.
13. M. Kuzuya, Y. Matsuno, T. Yamashiro, and M. Tuiki, *Plasmas Polym.,* **2** (1997) 79.
14. M. Kuzuya, T. Yamashiro, S. Kondo, and M. Tuiki, *Plasmas Polym.,* **2** (1997) 133.
15. M. Kuzuya, T. Sawa, T. Yamashiro, S. Kondo, and O. Takai, *J. Photopolym. Sci. Technol.,* **14** (2001) 87.
16. S. Kondo, Y. Sasai, and M. Kuzuya, *Thin Solid Films,* **515** (2007) 4136.
17. S. Kondo, Y. Sasai, Y. Yamauchi, and M. Kuzuya, *J. Photopolym. Sci. Technol.,* **22** (2009) 477.
18. S. Kondo, Y. Sasai, Y. Yamauchi, and M. Kuzuya, *J. Photopolym. Sci. Technol.,* **23** (2010) 567.
19. S. Kondo, Y. Sasai, Y. Yamauchi, and M. Kuzuya, *J. Photopolym. Sci. Technol.,* **24** (2011) 467.
20. P. Quantin, E. Colaco, K. E. Kirat, C. Egles, and H. Ficheux, *ACS Omega,* **3** (2018) 12535.

Development of low-residual-stress photosensitive adhesive materials for wafer-scale microfluidic device fabrication

Takashi Doi,* Isao Nishimura, Masahiro Kaneko, and Tsutomu Shimokawa

Yokkaichi Research Center, JSR Corporation
100 Kawajiri-cho, Yokkaichi, Mie 510-8552, Japan
**Takashi_Doi@jsr.co.jp*

We have previously developed a photosensitive adhesive material that enables microfluidic channel structure formation and subsequent bonding to a cover with the aim of simplifying the process of wafer-scale microfluidic device fabrication. However, the bonding process and a subsequent curing process required heat treatment at 200 °C and 180 °C, respectively, resulting in the generation of relatively high residual thermal stress. This may lead to delamination, warping, and cracking depending on the application environment. Therefore, in the present study, we designed a new material platform in which the patterning, bonding, and curing processes are based on ultraviolet (UV) reaction of polyfunctional acrylate, tackiness of epoxy resin, and UV/thermal reaction of epoxy resin in order to achieve low residual stress through low-temperature processing. Proof of concept was conducted through the evaluation of various physical properties of the system and found that the new type of photosensitive adhesive material, which bonded to a cover and cured at lower temperatures of 100 °C and 120 °C, respectively, had a low residual stress of 10 MPa and good insulation reliability. This is a promising material for applications such as cooling devices for semiconductor chips, where long-term reliability is required.

Keywords: Photosensitive adhesive materials, Microfluidic channels, Low residual stress, Dual crosslinking, Tackiness

1. Introduction

In recent years, there has been a growing need for smaller, thinner, and more integrated semiconductor chips and packages in order to realize even higher speeds, larger capacities, and lower power consumption in electronic devices. However, these should be accompanied by an increase in power density and the generation of the large amount of heat, which adversely affects the reliability and performance of semiconductor devices. As one of the solutions, cooling technology using microfluidic channels is attracting attention [1-14]. Microfluidic channels with a width/height of a few microns to a few thousand microns have a large surface area per unit volume (specific surface area), which increases the heat exchange efficiency of the liquid flowing in the channel and enables rapid cooling [15]. In microfluidic devices, if there is not enough insulation between a water flow route for cooling and an electric current flow route for driving, it is known that the electrode reaction is caused by the potential difference and the cooling water and the accompanying formation of metal oxides can lead to failures such as clogging, corrosion, and short circuit. Therefore, it is necessary to provide insulation reliability between the water flow route and the electric current flow route by utilizing the suitable device structure and materials. As an example, Wang *et al.* had reported that good reliability is shown by using aluminum nitride internal ceramic layers coated with thin copper layers as insulation layers above and below the water flow route [1].

We had previously developed two photosensitive materials that are expected to be candidates for microfluidic channel formation materials. One is a photo-patternable and adhesive (PA) material that

Received April 6, 2022
Accepted June 19, 2022

requires a developing process [16] and the other is a nonreversible surface relief formation compound that does not require it [17]. In the former case, the microfluidic channel was able to be directly fabricated using the PA applied on silicon wafers and can also be directly bonded to a cover such as a cover glass with no use of other adhesives, thus simplifying the fabrication of microfluidic devices. In addition, we have also confirmed good cytotoxicity of the PA, making it suitable for biosensor applications. However, the bonding process required thermal fusion at 200 °C in order for the developed pattern to interact well with the cover, and a subsequent curing process required heat treatment at 180 °C above the temperature for the patterning process (110 °C) because patterning and curing based on the reactions of the same epoxy resin should have been separated by adopting different temperatures. Due to this manufacturing process, the PA showed a residual stress of 16 MPa.

Semiconductor packages have essentially a multi-layered structure consisting of a complex combination of inorganic components, such as silicon-based semiconductor chips and copper wiring, and organic components, such as insulating layers and mold resin. Therefore, thermal stress generated during the heat treatment process becomes residual stress after cooling, which can lead to delamination, warpage, cracks, and other degradation of reliability. This means that low residual stresses are required for organic materials used in semiconductor applications. Since thermal stress is generally governed by the product of Young's modulus, a coefficient of thermal expansion (CTE) difference between two materials, and a temperature difference [18,19], we conceived the idea of realizing low residual stress through low-temperature processing from the viewpoint of reducing energy consumption and environmental impact.

The concept of the material platform designed for low-temperature processing in this study is shown in Table 1 along with that of the previous PA. The idea is to use inherent tackiness of epoxy resin for lowing the temperature of the bonding process (to the cover) and different crosslinking reactions for the patterning process and the curing process to lower the temperature of the curing process. Specifically, regarding the crosslinking reaction, ultraviolet (UV) reaction of polyfunctional acrylate [20] and UV/thermal reaction of epoxy resin [21] are used for the patterning process and the curing process, respectively. Since epoxy resins may also undergo UV reaction at the same time during the patterning process, a basic organic compound is added to delay it as shown in Figure 1. In this paper, we focus on the validation of such material design through the evaluation of physical properties to develop a new photosensitive adhesive material with low residual stress and good insulation reliability.

2. Experimental

2.1. Preparation of resin compositions

Four kinds of resin compositions (samples **1**, **2**, **3**, and **4**) were prepared by dissolving a base polymer with alkaline-dissolving units, polyfunctional acrylate **A** (viscosity: 7,500 mPa·s) or **B** (viscosity: 150 mPa·s), epoxy resin **a** (viscosity: 2,000 mPa·s) or **b** (viscosity: 150 mPa·s), photo-radical initiator, photochemical acid generator, basic organic compound, and surfactant in propylene glycol monomethyl ether acetate (PGMEA). The

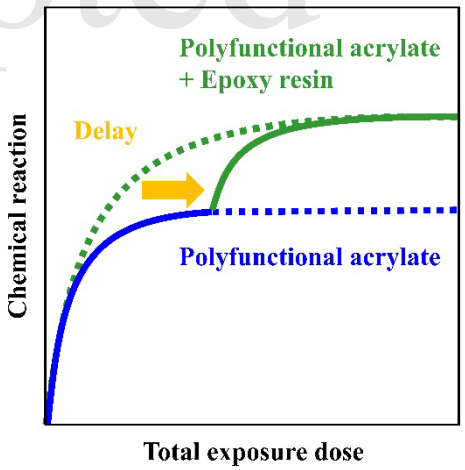

Fig. 1. A graphical image of reactivity against total UV exposure dose for the designed material platform.

Table 1. The concept of material platform.

	Patterning	Bonding	Curing
Previous photo-patternable and adhesive PA	UV/thermal reactions of epoxy resin (110 °C)	Thermal fusion (200 °C)	Thermal reaction of epoxy resin (180 °C)
PA developed in this work	UV reaction of polyfunctional acrylate	Adhesion based on tackiness of epoxy resin	UV/thermal reactions of epoxy resin

combination of polyfunctional acrylate **A**/**B** and epoxy resin **a**/**b** are shown in Table 2 in the section 3.1.

2.2. Tackiness measurement

Each of samples **1**, **2**, **3**, and **4** was spin-coated using 1H-360S (MIKASA Co., Ltd.) on a 4-inch silicon wafer and baked at 110 °C for 3 min to form a thin film with a thickness of 18 μm. Then, the whole films on silicon wafers were exposed to UV light at 300 mJ·cm^{-2} using a mask aligner MA-200 (SÜSS MicroTec SE). After that, paddle development was performed for each film with 2.38% tetramethylammonium hydroxide aqueous solution (PD523, Tama Chemicals Co., Ltd.) for 60 s using a developing apparatus AD-3000 (TAKIZAWA SANGYO K.K.), and the films were rinsed with ultrapure water for 60 s and spin-dried at 1,500 rpm for 30 s. The tackiness of the films was measured using a tack tester TAC1000 (RHESCA Co., Ltd.) at room temperature with a pressing speed of 0.5 mm·s^{-1}, a pressing load of 100 gf for 10 s, and a pulling speed of 10 mm·s^{-1}. This measurement was repeated five times and the maximum values obtained from each measurement were used to calculate an average value for each sample.

2.3. Evaluation of bonding strength

The same procedure to prepare a thin coated film on a silicon wafer with that described above (in the section 2.2.) was carried out for sample **1**, except for the use of a photomask with a micropattern based on 120 μm-holes when the exposure using MA-200. A glass wafer die with a size of 8 mm × 8 mm was attached onto the obtained dot patterns using a die bonder FTD-1940 (SHIBAURA MECHATRONICS Corp.) with a load of 2.1 MPa for 10 s at 30 °C or 100 °C for adhesion. After that, the whole film was exposed to UV light using MA-200 at 1,000 mJ·cm^{-2} through the transparent glass chip and then thermally treated with an oven VF-1000 (KOYO THERMO SYSTEMS Co., Ltd.) under a nitrogen atmosphere by raising the temperature from 23 °C to 120 °C at 10 °C·min^{-1} and maintaining it at 120 °C for 60 min. The bonding strength of the thin film with the dot patterns against the glass chip was measured using a bond tester 4000 (NORDSON Corp.) as shown in Figure 2. An averaged value over five measurements was used as the bonding strength value.

2.4. Evaluation of physical properties of the cured film

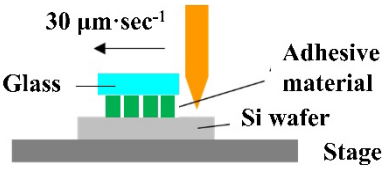

Fig. 2. Overview of the setup for bonding strength measurement.

Sample **1** was coated onto three 4-inch silicon wafers using 1H-360S and baked at 110 °C for 3 min to obtain resist films with a thickness of 18 μm. Then, the whole films were exposed to UV light with MA-200 at 1,300 mJ·cm^{-2} and thermally treated with VF-1000 under a nitrogen atmosphere at 120 °C for 60 min. After cooling the film-coated wafers at 23 °C for 12 h, residual stress was measured along three axes with a thin films' stress measurement apparatus FLX-320S (KLA-Tencor Corp.) to obtain an averaged value. After that, to evaluate chemical resistance, the silicon wafer with the cured film was broken into some parts, which were immersed in propylene glycol monomethyl ether (PGME)/PGMEA, *N*-methyl pyrrolidone (NMP), dimethyl sulfoxide (DMSO), or isopropyl alcohol (IPA) at 23 °C for 10 min. They were rinsed with ultrapure water for 30 s. Surface water was gently wiped off, followed by air-drying of the film-coated wafers at 23 °C for 5 s. The film thickness was measured with a stylus profiler P-16+ (KLA-Tencor Corp.) at three locations on the film before and after the immersion to calculate an average value of the change in film thickness (%).

Cured films were prepared through the same procedure with that described above, except for the use of three 6-inch silicon wafers. After placed the wafers at 23 °C and 50% relative humidity (RH) for 24 h, they were immersed in ultrapure water for 24 h. Then, remained water on the top surface and the bottom surface was gently wiped off, followed by air-drying of the wafers at 23 °C for 5 s. The three film-coated wafers were weighed before and after the immersion to calculate an average value of the change in weight, which was used as the water absorption rate (%).

Sample **1** was spin-coated using 1H-360S on a polyethylene terephthalate (PET) sheet-attached 6-inch silicon wafer and dried in an oven at 110 °C for 10 min to form a thin film with a thickness of 18 μm on the PET sheet. Then, the whole coated film was exposed to UV light using MA-200 at 1,300 mJ·cm^{-2} and thermally treated in VF-1000 under a nitrogen atmosphere at 120 °C for 60 min. A part of the cured film peeled off from the PET sheet was cut into

3 mm-wide pieces, which were used for viscoelasticity measurement using DMS6100 (Seiko Instruments Inc.) at a frequency of 1 Hz, a nitrogen gas flow at 200 mL·min^{-1}, and a heating rate of 10 °C·min^{-1} to measure the glass transition temperature (T_g). Another part of the cured film was cut into 5 mm-wide pieces, which were used for tensile tests using a tensile tester AGS-500NX (SHIMADZU Corp.) at room temperature with a distance of 10 mm between grips and a tensile speed of 5 mm·min^{-1} to measure tensile strength at break, elongation at break, and Young's modulus. The tensile test was performed for ten 5 mm-wide pieces to calculate average values. The remaining part of the cured film was cut into small pieces which were used for the measurement of 5% weight loss temperature (T_{d5}) using a thermogravimetric apparatus TG209 F1 Lira (NETZSCH GmbH & Co. KG) and an aluminum pan by heating from 23 °C to 600 °C at a heating rate of 10 °C·min^{-1} under a nitrogen flow of 200 mL·min^{-1}.

2.5. Pattern formation via photolithography

Sample **1** was applied to a 6-inch silicon wafer using a photoresist coater/developer CLEAN TRACK Mark 8 (Tokyo Electron Ltd.), and then baked at 110 °C for 3 min to form a coating film with a thickness of 30 µm. The film-coated wafer was exposed to i-line light through a 15/15 and 20/20 µm/µm line/space (L/S) photomask using an i-line exposure system NSR-2205i12D (NIKON Corp.) with an exposure dose of 300 mJ·cm^{-2}, a depth of focus of 0 µm, and numerical aperture of 0.63. Then, using CLEAN TRACK Mark 8, a resist pattern was formed by paddle development with PD523 for 60 s, rinsed with ultrapure water for 60 s, and spin-dried at 1,500 rpm for 30 s. A scanning electron microscope (SEM) SU8220 (Hitachi High-Tech Corp.) was used to observe the resist patterns.

2.6. Highly accelerated stress test (HAST)

On a test element group (TEG) chip with 20 µm/20 µm L/S comb-shaped copper wiring and its pad area covered with tape, sample **1** was applied using 1H-360S and then baked at 110 °C for 3 min to form a thin film with a thickness of 18 µm. After the tape was peeled off, the whole surface of the coated thin film was exposed to UV light using MA-200 at 1,300 mJ·cm^{-2} and then thermally treated at 120 °C for 60 min under a nitrogen atmosphere in VF-1000. The change in resistance was tracked using an ion migration evaluation system AMI-025-P (ESPEC Corporation) under the conditions of 121 °C, 85% RH, 5 V, and 120 h.

3. Results and Discussion

3.1. Proof of concept for the material design

Based on the concept of the material design shown in Table 1, samples **1**, **2**, **3**, and **4** were prepared using the combination of the crosslinkers, polyfunctional acrylate **A** (viscosity: 7,500 mPa·s) or **B** (viscosity: 150 mPa·s) and epoxy resin **a** (viscosity: 2,000 mPa·s) or **b** (viscosity: 150 mPa·s) as shown in Table 2. To verify that reactions proceed in the samples in accordance with the concept, we first compared tackiness of the resin compositions after the patterning process. After the UV exposure and paddle development for the thin films of these resin compositions coated on silicon wafers, which was assumed as a patterning process, tackiness of the films was measured. The results of the tackiness measurement are shown in Figure 3. The tackiness values of samples **1** and **3** prepared using epoxy resin **a** were 53 gf and 46 gf, respectively, which were

Table 2. Crosslinker compositions of samples **1**, **2**, **3**, and **4**.

Sample	Polyfunctional acrylate (viscosity[a])/mPa·s)	Epoxy resin (viscosity[a])/mPa·s)
1	**A** (7,500)	**a** (2,000)
2	**A** (7,500)	**b** (150)
3	**B** (150)	**a** (2,000)
4	**B** (150)	**b** (150)

a) Catalog data at 25 °C.

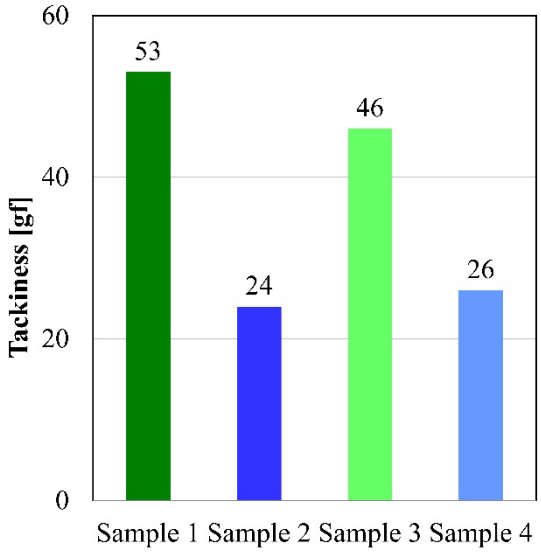

Fig. 3. Tackiness of samples **1**, **2**, **3**, and **4** at room temperature after the UV exposure (exposure dose: 300 mJ·cm^{-2}) and alkaline development (developing time: 60 s).

higher than those of samples **2** and **4** prepared using epoxy resin **b** (24 gf and 26 gf, respectively). Tackiness was hardly affected by the viscosity of the polyfunctional acrylates. This strongly indicates that the polyfunctional acrylate mainly contributed to the formation of a three-dimensional crosslinked structure during the UV exposure and its tackiness (inherent to unreacted polyfunctional acrylates) was disappeared, and also that the UV reaction of the epoxy resin was effectively suppressed by the basic organic compound during the UV exposure, as expected, resulting in the plenty amount of remaining unreacted epoxy resin.

Next, dot patterns with a dot diameter of 120 μm was formed on the thin film of sample **1** on the silicon wafer and bonded to a glass wafer die at 30 °C or 100 °C. It was observed that the patterned film did not bond well to the glass wafer die at 30 °C but bonded well to it at 100 °C (data not shown). This is presumably because of a lower surface viscosity of the patterned film at the higher temperature (due to higher molecular mobility of unreacted epoxy resin), resulting in sufficient interaction to the glass wafer die. The subsequent curing process using additional UV exposure at 1,000 mJ·cm^{-2} and heat treatment at 120 °C for 60 min resulted in good bonding strength of 10 MPa (listed in Table 4 in the section below). These results suggest that the tackiness and the crosslinking based on UV/thermal reaction of the epoxy resin are the main contributors to the bonding process and the curing process, respectively. It was confirmed that the reactions proceed for sample **1** according well to the concept shown in Table 1.

3.2. Evaluation of physical properties of the cured film

In sample **1** after the curing process, the formation of a sufficient three-dimensional crosslinked structure was confirmed by the chemical resistance test. The rate of change in film thickness after immersion in PGME/PGMEA, NMP, DMSO, or IPA process chemicals is summarized in Table 3.

Table 3. Chemical resistance of sample **1**[a)] (exposed to UV at 1,300 mJ·cm^{-2} and thermally treated at 120 °C for 60 min)

Chemicals	Change in film thickness (%)
PGME/PGMEA	100
NMP	101
DMSO	101
IPA	100

a) Measured after the immersion at 23 °C for 10 min.

Although each of the chemicals basically dissolves the base polymer, the polyfunctional acrylate, and the epoxy resin, the rate of change in film thickness was all 100% or 101%, which means swelling was 1% or less, indicating a sufficient crosslinked structure formation and resulting good chemical resistance of the thin film.

The residual stress, water absorption, thermal and mechanical properties of sample **1** after the curing process are shown in Table 4. Despite the formation of a sufficient three-dimensional crosslinked structure, the residual stress was 10 MPa, which was lower, as expected, than the 16 MPa of the previous grade PA. The lower residual stress can be attributed to lower thermal stresses left in the material derived from the lower-temperature processing in this study. The water absorption rate was low at 0.9%. The T_g and T_{d5} values were 184 °C and 291 °C, respectively, indicating high heat resistance. Tensile test data indicate mechanical robustness of the formed film. The water absorption, T_g, T_{d5}, and tensile test data imply the sufficient crosslinked structure formation in the thin film.

3.3. Evaluation of the photolithography patterns

The thin film of sample **1** (thickness: 30 μm) formed on a silicon wafer was used for the pattern formation by the i-line exposure through a 15/15 and 20/20 μm/μm L/S photomask and alkaline development. As shown in Figure 4, the formation of a negative-type rectangular pattern was confirmed. This feature is suitable for microfluidic channels.

3.4. Evaluation of resistance to the HAST

Finally, the insulation reliability of sample **1** was evaluated by the resistance to HAST. The cured film of sample **1** was formed on a TEG chip with 20 μm/20 μm L/S comb-shaped copper wiring, and the change in resistance under 121 °C, 85% RH, 5 V, and

Table 4. Cured film properties of sample **1** (exposed at 1,300 mJ·cm^{-2} and thermally treated at 120 °C for 60 min)

Items	Sample **1**
Bonding strength	10 MPa
Residual stress	10 MPa
Water absorption	0.9%
T_g	184 °C
T_{d5}	291 °C
Tensile strength at break	31 MPa
Elongation at break	3.2%
Young's modulus	1.6 GPa

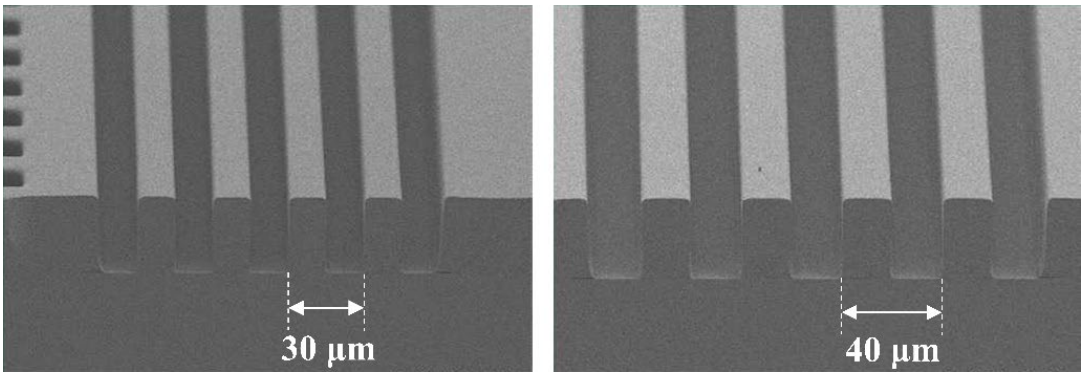

Fig. 4. SEM photographs of negative-type patterns of sample **1** formed after UV exposure (exposure dose: 300 mJ·cm^{-2}) and the development (developing time: 60 s).

120 h was tracked. As shown in Figure 5, no short circuit was observed even after 120 h. Ion migration, which causes short-circuits, is a phenomenon that occurs through a series of chemical reactions: (i) ionization of copper and electrolysis of water at the anode, (ii) precipitation of copper hydroxide due to the association of copper ions and hydroxide ions, (iii) re-generation of copper ions from a portion of copper hydroxide, and (iv) migration and precipitation of copper ions to the cathode due to the Coulombic force [22]. We speculate that the low water absorbency (0.9%) shown in Table 4 reduced the electrolysis of water (i) in the material and the higher T_g (184 °C) than the HAST condition (121 °C) inhibited the migration of copper ions (iv). The resistance evaluation based on HAST indicates that the film has good insulation reliability.

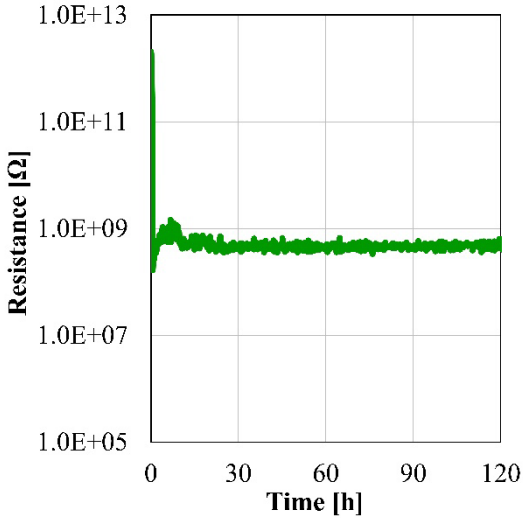

Fig. 5. Change in resistance of cured film of sample **1** (exposed at 1,300 mJ·cm^{-2} and thermally treated at 120 °C for 60 min) in the HAST (121 °C, 85% RH, 5 V, 120 h)

4. Conclusion

In this paper, for the purpose of achieving low residual stress of photosensitive adhesive materials through low-temperature processing, we designed a material platform that uses the UV reaction of polyfunctional acrylate for the patterning process and the tackiness of epoxy resin for the bonding process. We confirmed that the reactions proceed in the materials in accordance with the concept designed in this study. The new photosensitive adhesive material developed in this study does not only exhibit low residual stress of 10 MPa but also shows good chemical resistance and insulation reliability owing to the relatively low process temperatures (100 °C for the bonding process and 120 °C for curing), compared with those for the previously reported photo-patternable and adhesive PA [16]. The new photosensitive adhesive material is expected to be used for microfluidic materials for cooling semiconductor chips.

References

1. B. Wang, Y. Jia, H. Zhang, S. Jia, J. Liu, W. Wang, X. Liu, *Proc. SPIE 10513, Components and Packaging for Laser Systems IV,* (2018) 105130Q.
2. E. G. Colgan, B. Furman, M. Gaynes, N. LaBianca, J. Magerlein, R. Polastre, R. J. Benzama, R. Choudhary, K. Marston, H. Toy, J. A. Wakil, R. Schmidt, *HVAC&R Research*, **12**, (2006) 1031.
3. R. v. Erp, R. Soleimanzadeh, L. Nela, G. Kampitsis, E. Matioli, *Nature*, **585** (2020) 211.
4. R. v. Erp, G. Kampitsis, E. Matioli, *2019 IEEE Applied Power Electronics Conference and Exposition (APEC)*, (2019) 1383.
5. R. v. Erp, G. Kampitsis, L. Nela, R. S. Ardebili, E. Matioli, *2020 19th IEEE Intersociety Conference on Thermal and Thermomechanical*

Phenomena in Electronic Systems (ITherm), (2020) 53.
6. L. Nela, R. v. Erp, N. Perera, A. Jafari, C. Erine, E. Matioli, in *IEEE Electron Device Letters*, **42** (2021) 1642.
7. T. Wei, *Nature*, **585** (2020) 188.
8. S. Wang, Y. Yin, C. Hu, P. Rezai, *Micromachines, **9** (2018) 287.*
9. H. Y. Zhang, D. Pinjala, T. N. Wong, K. C. Toh, Y. K. Joshi, *Appl. Therm. Eng.*, **25** (2005) 1472.
10. B. Ramos-Alvarado, B. Feng, G. P. Peterson, *Appl. Therm. Eng.*, **59** (2013) 648.
11. A. Sakanova, C. C. Keian, J. Zhao, *Int. J. Heat Mass Transf.,* **89** (2015) 59.
12. P. Y. Paik, V. K. Pamula, K. Chakrabarty, in *IEEE Transactions on Very Large Scale Integration (VLSI) Systems*, **16** (2008) 432.
13. E. G. Colgan, B. Furman, A. Gaynes, W. Graham, N. LaBianca, J. H. Magerlein, R. J. Polastre, M. B. Rothwell, R. J. Bezama, R. Choudhary, K. Marston, H. Toy, J. Wakil, J. Zitz, *Semiconductor Thermal Measurement and Management IEEE Twenty First Annual IEEE Symposium, 2005.*, (2005) 1.
14. P. Selvakumar, S. Suresh, in *IEEE Transactions on Components, Packaging and Manufacturing Technology*, **2** (2012) 1600.
15. G. Karniadakis, A. Beskok, N. Aluru, *Microflows and Nanoflows; Fundamentals and Simulation,* Springer, New York, USA (2005).
16. H. Kubo, T. Doi, I. Nishimura, E. Hayashi, K. Hieda, S. Peters, R. Vanroosbroeck, *J. Photopolym. Sci. Technol.,* **28** (2015) 411.
17. T. Doi, I. Rozhanskii, T. Nakamura, T. Shimokawa, *J. Appl. Polym. Sci*., **139** (2022) 52173.
18. W. D. Callister Jr., D. G. Rethwisch, *Materials Science and Engineering: An Introduction, 8th ed.*, John Wiley & Sons, New Jersey, USA (2010).
19. G. F. Carter, D. E. Paul, *Materials science & engineering,* ASM International, Ohio, USA (1991).
20. U. Poth, R. Baumstark, *Acrylic Resins*, Vincentz Network, Hannover, Germany (2014).
21. B. Ellis, *Chemistry and Technology of Epoxy Resins,* Springer, Dordrecht, Netherlands (1993).
22. C. Tang, K. Mitobe, N. Yoshimura, *IEEJ Trans. FM*, **123** (2003) 651 (in Japanese).

Characterization of Hydrogel Films with Reflective Colors Templated by Colloidal Crystals

Katsumasa Takayama[1], Naoto Iwata[2,3], and Seiichi Furumi[2,3]*

[1] Department of Chemistry, Faculty of Science
[2] Department of Applied Chemistry, Faculty of Science,
[3] Department of Chemistry, Graduate School of Science,
Tokyo University of Science, 1-3 Kagurazaka, Shinjuku, Tokyo 162-8601, Japan
**furumi@rs.tus.ac.jp*

In this report, we successfully fabricated the temperature-responsive porous gel film by templating the colloidal crystal (CC) film of silica microparticles embedded in a hydrogel matrix of poly(*N*-isopropylacrylamide) (NIPA). As elevating the temperature from 25 °C, this porous gel film showed the color changes of Bragg reflection from red to blue, arising from the geometric decrease in the lattice spacing of pores caused by the shrinkage of NIPA gel matrix upon heating process. Such reflection color changes of the porous gel film were found to be fully reversible in the temperature range between 26 °C and 33 °C. Moreover, Fourier transform infrared (FT-IR) spectroscopy and thermal gravimetric analysis (TGA) measurements suggested that the silica microparticles of CC film are thoroughly removed after treatment with hydrofluoric acid, thereby resulting in the formation of porous NIPA gel film without the silica component. This report provides a promising protocol to check the residual silica microparticles in porous gel films by both FT-IR and TGA measurements.
Keywords: Colloidal crystal, Porous, Poly(*N*-isopropylacrylamide), Hydrogel, Thermal gravimetric analysis, Bragg reflection

1. Introduction

Colloidal crystals (CCs) are the well-ordered 3D periodic arrays of monodisperse colloidal particles of silica, polymers, and so on [1-6]. The CCs are also regarded as one of the 3D photonic crystals, which show the photonic band-gaps in the visible wavelength range due to the spatially periodic modulation in refractive indices of dielectric materials [5,7-9]. The CCs have attracted a great deal of technological attention for their wide range of photonic applications in sensors, displays, lasers, and so forth.

In this context, the porous gel films are polymer hydrogel films by templating the close-packed CCs of colloidal particles. For instance, they can be prepared by the selective removal of internal colloidal particles embedded in CCs stabilized with hydrogel matrices [10-15]. Therefore, monodisperse pores are periodically ordered in the porous gel films. In other words, the porous structures are referred to as the inversed CCs. One of the unique optical properties of porous gel films is their capability to show visible Bragg reflection, arising from the spatial periodicity in refractive indices of the ordered pores and the surrounding hydrogel matrix. The reflection peak wavelength (λ) of porous gel film is quantitatively determined by physical parameters including the effective refractive index of porous gel films (n), the lattice spacing (d), and the Bragg angle (θ) according to the following equation [16].

$$\lambda = 2nd \sin \theta \qquad (1)$$

Especially, the temperature-responsive porous gel films are quite attractive for detecting and visualizing the water temperature through the changes in Bragg reflection colors [10,14]. This is because the reflection peak wavelength of porous gel films can be ascribed to the geometric change in lattice spacing of the pores by the thermally-induced volume change of hydrogel matrices [10,17].

Received March 29, 2022
Accepted June 19, 2022

So far, there have been a few reports on the fabrication of temperature-responsive porous gel films using poly(*N*-isopropylacrylamide) (NIPA), as shown in Figure 1, for the sensor applications [10,14,18]. The NIPA hydrogel has an intrinsic capability to dynamically shrink and swell by expelling and absorbing large amounts of water in response to temperature, respectively [19]. As reported in the precedents, the porous gel films were prepared by the following procedure. First, the close-packed CC as the template was prepared by a solvent evaporation method using suspensions of colloidal silica microparticles. After that, the CC was immobilized in a hydrogel matrix of NIPA to obtain the CC gel film. Finally, the porous gel film with ordered pores was obtained by treatment with a solution of hydrofluoric acid or sodium hydroxide to remove silica microparticles from the CC gel film. Since the NIPA gel has both hydrophilic and hydrophobic groups in its basic skeleton, this film exhibits the temperature-responsive volume changes [17]. Eventually, the reflection wavelength of porous gel film can be tuned by changing the water temperature [10,14,18]. However, no report had been made to provide clear-cut evidence for the complete removal of silica microparticles from the CC template. Considering the possibility to apply porous gel films as temperature sensors, it is quite important to establish the analytical methods for the porous gel films.

In this report, we successfully demonstrated the Bragg reflection color changes of temperature-responsive porous gel film templated by CC of silica microparticles. We also confirmed that no silica microparticle remains in the porous NIPA gel by Fourier transform infrared (FT-IR) spectroscopy and thermal gravimetric analysis (TGA) measurements. The present report indicates that both FT-IR and TGA measurements can be used as effective analytical tools to confirm the presence or absence of residual silica microparticles inside porous gel films.

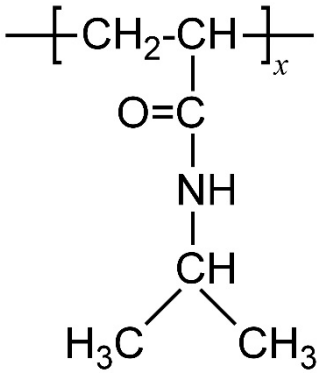

Fig. 1. Chemical structure of temperature-responsive hydrogel of poly(*N*-isopropylacrylamide) (NIPA).

2. Experimental

2.1. Materials

As a monomer, *N*-isopropylacrylamide was purchased from FUJIFILM Wako Pure Chemical Co., and was purified by 5 cycles of recrystallization from a mixture of toluene and hexane. After that, the recrystallized *N*-isopropylacrylamide was used after drying under vacuum. We adopted *N,N'*-methylenebis(acrylamide) (BIS) as a crosslinking agent and dimethyl sulfoxide (DMSO) as a polymerization solvent, which were obtained from FUJIFILM Wako Pure Chemical Co. A thermal radical initiator of 2,2'-azobis(isobutyronitrile) (AIBN) was obtained from Tokyo Chemical Industry Co. Ltd. Hydrofluoric acid (HF) was purchased from FUJIFILM Wako Pure Chemical Co. These materials were used as received.

A 20 wt% aqueous suspension of monodisperse silica microparticles with a diameter of ~220 nm was obtained from Nippon Shokubai Co. Ltd. In a preliminary experiment on the silica microparticles, the coefficient of variation in the diameter was found to be 5.8% by the observation with scanning electron microscopy (JSM-7001F, JEOL). Ultrapure water was obtained using a water purification system (Direct-Q UV 5, Merck Millipore).

2.2. Fabrication of bulk NIPA gel film

A mixture of 1.70 g of *N*-isopropylacrylamide (15.0 mmol) and 46.3 mg of BIS (300 μmol) was dissolved in 7.50 mL of DMSO. After degassing with nitrogen gas for 10 min, 5.0 mg of AIBN (30.4 μmol) was added into the solution to prepare the precursor solution of NIPA gel. After this precursor solution was injected into a pair of glass substrates with a gap of 400 μm, heating treatment at 60 °C for 6 h gave rise to the thermal polymerization of precursor (bulk NIPA gel). Finally, the bulk NIPA gel was purified by washing in ultrapure water to remove unreacted components of monomer and BIS or decomposed components of AIBN.

2.3. Fabrication of CC NIPA gel film and porous NIPA gel film

A close-packed CC film was fabricated on a hydrophilic glass substrate by dropping the aqueous

suspension of silica microparticles with a diameter of ~220 nm, followed by heating at 65 °C for 24 h to evaporate the dispersion medium of water in a gradual manner. Then, the precursor solution of NIPA gel was carefully injected into the close-packed CC film on the glass substrate, and another glass substrate was covered with a gap of 400 µm. The CC film stabilized with NIPA gel (CC NIPA gel) was obtained after heating at 60 °C for 6 h and washing in ultrapure water. Afterward, the CC NIPA gel was immersed into a 5 wt% HF aqueous solution for 2 days to remove silica microparticles of CC film. Lastly, the porous NIPA gel film (porous NIPA gel) was obtained after washing with ultrapure water for 3 days.

2.4. Measurement of the reflection spectra

Reflection spectra of porous NIPA gel were measured using a CCD spectrometer (USB2000+, Ocean Optics) equipped with a halogen light source (HL-2000, Ocean Optics) and an optical fiber with reflection probe (R200-7-UV-VIS, Ocean Optics). The porous NIPA gel was cut into a disk-shaped film with a diameter of ~4 mm, and was subsequently immersed in excess ultrapure water to maintain the swelling state of NIPA matrix with water. The temperature of porous NIPA gel, enclosed between two glass substrates, was precisely controlled using a hot stage system (HS1 and HS82, Mettler-Toledo).

2.5. Measurement of the volume phase transition temperature of porous NIPA gel

After the porous NIPA gel was cut into a disk-shaped film with a diameter of ~5 mm, its diameter was measured using a conventional ruler upon changing the temperature from 26 °C to 33 °C.

2.6. Characterization of the porous NIPA gel

FT-IR spectra of the CC NIPA gel and porous NIPA gel were measured using an FT-IR spectrometer (FT-IR4700, JASCO) equipped with an attenuated total reflection (ATR) unit with a diamond prism (ATR PRO ONE, JASCO). TGA curves of silica microparticles, bulk NIPA gel, CC NIPA gel, and porous NIPA gel were measured using a thermogravimetric analyzer (TGA 2010SA, NETZSCH) in the temperature range from 25 °C to 450 °C at the heating rate of 10 °C/min under nitrogen flow. All samples were freeze-dried and powdered before each measurement.

3. Results and discussion

3.1. Temperature response of reflection properties of porous NIPA gel

The Bragg reflection wavelength of porous NIPA gel could be tuned by changing the temperature. Figure 2A shows the changes in the reflection spectrum of the porous NIPA gel in the temperature range from 26 °C to 33 °C at the interval of 1 °C. At 26 °C, the initial reflection peak of porous NIPA gel appeared at 639 nm, whose color was observed as red. When the temperature was gradually increased from 26 °C to 33 °C, the reflection peak was continuously blue-shifted from 639 nm to 489 nm. At 33 °C, the porous NIPA gel exhibited blue reflection color. Furthermore, we confirmed that the full widths at half maxima of the reflection peaks are approximately 20 nm, which are comparable to that reported in the previous report [10]. However, as the porous NIPA gel was heated above 34 °C, the reflection peak abruptly disappeared, concurrently resulting in the color appearance alteration to white turbidity. This can be ascribed to the light scattering caused by the aggregation of polymer networks induced by the shrinkage of porous NIPA gel. Such aggregation of NIPA happens from the hydrophobic interaction of NIPA gel by heating treatment. Notably, this volume phase transition temperature of porous

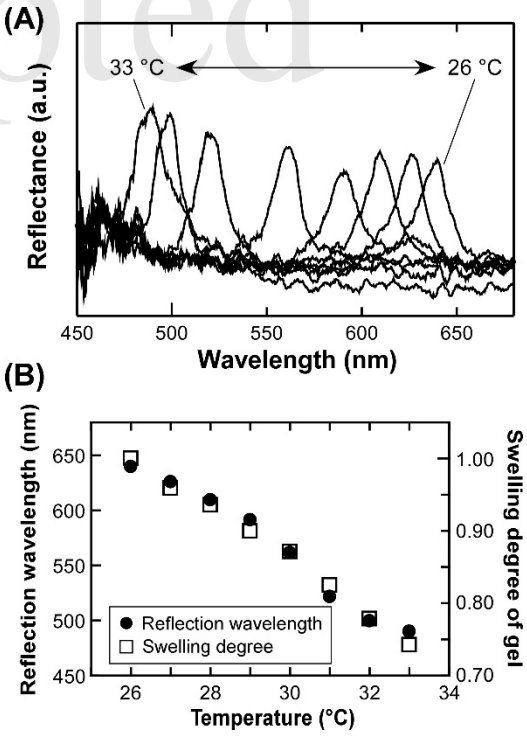

Fig. 2. (A) Reflection spectra of the porous NIPA gel in the temperature range between 26 °C and 33 °C. (B) Changes in reflection wavelength and swelling degree of the porous NIPA gel as a function of temperature between 26 °C and 33 °C.

NIPA gel was comparable to that reported in the previous report, corresponding to ~32 °C [10]. Moreover, the reflection peak could be returned to the initial wavelength of 639 nm in a reversible manner by cooling from 34 °C to 26 °C.

In order to elucidate the reflection wavelength shift behavior by the temperature change, we measured the film diameter of porous NIPA gel in the temperature range between 26 °C and 33 °C. Figure 2B shows the changes in both reflection wavelength and swelling degree of the porous NIPA gel as a function of temperature. Here, the swelling degree was defined as the ratio of a diameter of porous NIPA gel at elevated temperatures to that at 26 °C. As expected, the swelling degree declined from 1.00 to 0.74 by changing the temperature from 26 °C to 33 °C. The shrinkage of porous NIPA hydrogel upon the heating process is also explained by the hydrophobic interactions of NIPA gel. In general, the NIPA gel can retain a large amount of water to be the swelling state below the volume phase transition temperature. However, as heating over the volume phase transition temperature, the hydrophobic interactions of NIPA became dominant, and its hydrogel gradually changed from hydrophilic to hydrophobic. As a result, the aggregation of polymer networks and shrinkage of NIPA gel are induced by hydrophobic interactions. From this process, the shift in the Bragg reflection wavelength was affected by the changes in the swelling degree of porous NIPA gel. Based on these results, a blue-shift in reflection peak wavelength of porous NIPA gel upon heating can be ascribed to the decrease in lattice spacing of the pores caused by the shrinkage of porous NIPA gel triggered by heating. Furthermore, it is known that the shift of reflection wavelength upon temperature change can be controlled by the mixing ratio of *N*-isopropylacrylamide monomer and BIS crosslinking reagent because the swelling degree of NIPA gel at each temperature varies [10].

3.2. Comparison of FT-IR spectra between CC NIPA gel and porous NIPA gel

The removal of silica microparticles by the treatment of CC NIPA gel with HF was confirmed by FT-IR spectral measurements. Figure 3 shows the comparison of FT-IR spectra of CC NIPA gel (dashed curve) and porous NIPA gel (solid curve). The FT-IR spectrum of CC NIPA gel showed a sharp peak around the fingerprint region of 1100 cm^{-1}, which was assigned to the stretching vibrations of Si-O-Si bonds [20]. The emergence of this peak is reasonable since CC NIPA gel is comprising silica microparticles. On the other hand, this peak disappeared in the FT-IR spectrum of porous NIPA gel, which was prepared by the treatment of CC NIPA gel with HF. These experimental results implied that the close-packed silica microparticles are readily dissolved and removed from the CC NIPA gel by the treatment with HF due to the interconnecting structure of colloidal particles.

In addition, the FT-IR spectrum of porous NIPA gel exhibited two characteristic peaks at around 1630 cm^{-1} and 1560 cm^{-1}, which were assigned to the C=O stretching vibrations and N-H deformation vibration of the amide groups in NIPA, respectively [21]. Since these peaks of amide groups were also confirmed in the FT-IR spectrum of bulk NIPA gel, the fact indicated that the NIPA component in porous NIPA gel is not decomposed even after treatment with HF.

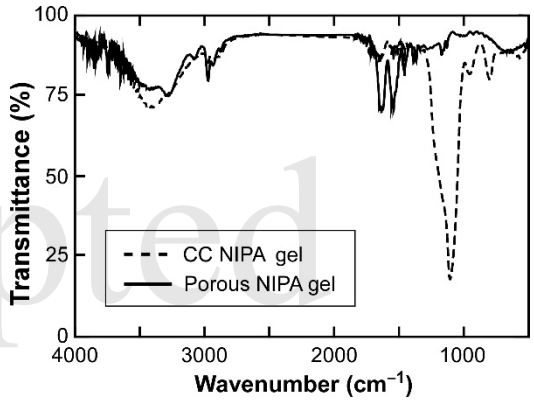

Fig. 3. FT-IR spectra of CC NIPA gel and porous NIPA gel.

3.3. Characterization of porous NIPA gel

TGA measurements provide invaluable information on the relative weight changes of silica microparticles, bulk NIPA gel, CC NIPA gel, and porous NIPA gel, thereby enabling the experimental confirmation for the residual silica microparticles in porous NIPA gel. Figure 4 shows the TGA curves for each sample in the temperature range from 25 °C to 450 °C. Also, as summarized in Table 1, the relative weight loss values for samples at 430 °C were estimated from the TGA results.

First, we discussed the results of silica microparticles. The relative weight loss reached 6.5%, probably corresponding to the surface-adsorbed water on silica microparticles. Taking account of the fact that silica is heat resistant inorganic material, it is reasonable that thermal decomposition of silica microparticles hardly

occurs after heating up to 450 °C [22,23].

On the contrary, the bulk NIPA gel showed the relative weight loss of 93.9%, indicative of the thermal decomposition of NIPA matrix. However, the weight loss of bulk NIPA gel was less than 100%. This phenomenon can be ascribed to the carbonization of NIPA by heating treatment. It is anticipated that thermal decomposition and carbonization occur when the carbon-based materials are heated under anoxic conditions. If the TGA measurement of bulk NIPA gel is conducted under nitrogen flow, the relative weight loss of bulk NIPA gel would be close to 100% because the complete thermal decomposition of NIPA is prevented by the partial carbonization. This can be also supported by the experimental fact that a small amount of black powder remained after the TGA measurements.

With regard to the result of CC NIPA gel, the relative weight loss was 39.8%. This weight loss is attributed to the NIPA component in the CC NIPA gel. Because the NIPA can be assumed to be completely decomposed by heating treatment at 450 °C. Consequently, the remaining component after TGA measurement can be considered as the silica microparticles in CC NIPA gel.

Finally, the relative weight loss of the porous NIPA gel attained a relatively high value of 95.8%. This weight loss was much larger than that of CC NIPA gel (39.8%). In addition, this weight loss was comparable to that of bulk NIPA gel (93.9%). These results strongly inferred that porous NIPA gel consists of only a hydrogel matrix of NIPA. As another evidence, there were black powders left behind after the TGA measurement. Considering the fact that the black powders remain after TGA measurements of bulk NIPA gel, as mentioned above, it turned out that the residual black powders after TGA measurement of porous NIPA gel are considered as not silica microparticles but carbonized NIPA components. The overall results highlighted that no silica microparticles remain in the porous NIPA gel and that silica microparticles are completely dissolved and removed from the CC NIPA gel by the treatment with HF. To the best of our knowledge, although a few studies have hitherto shown the fabrication and photonic properties of porous films of NIPA hydrogel, we believe that both FT-IR and TGA results presented here are the first evidence to confirm the porous structures fabricated by templating the close-packed CC structures.

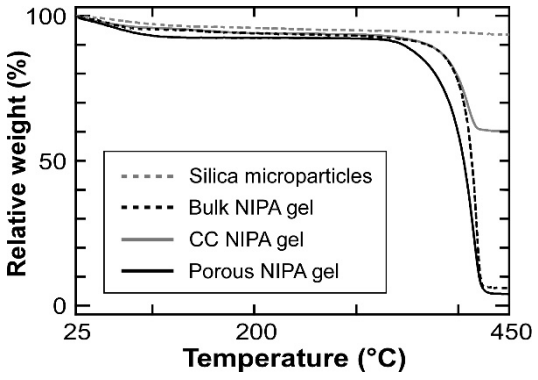

Fig. 4. TGA curves for silica microparticles, bulk NIPA gel, CC NIPA gel, and porous NIPA gel.

Table 1. The relative weight loss rate of silica microparticles, bulk NIPA gel, CC NIPA gel, and porous NIPA gel.

Sample name	Relative weight loss (%)
Silica microparticles	6.5
Bulk NIPA gel	93.9
CC NIPA gel	39.8
Porous NIPA gel	95.8

4. Conclusion

In this report, we successfully fabricated the temperature-responsive porous gel films with NIPA hydrogel by the selective removal of the silica microparticles from CC NIPA gel. The porous NIPA gel film showed the change in Bragg reflection color from red to blue upon heating process. Such a reflection color change was triggered by the decrease in the lattice spacing of the pores embedded in the NIPA hydrogel matrix by the thermally-induced shrinkage of NIPA hydrogel. Subsequently, the reflection color returned to the initial state after the cooling process. Therefore, the reflection color changes of porous NIPA gel were fully reversible between heating and cooling processes. Furthermore, the residual silica microparticles in porous NIPA gel were characterized by both FT-IR spectroscopy and TGA measurements to conclude that no silica microparticles remain in the porous NIPA gel. These analytical methods presented here can be used to check the residual silica microparticles in porous gel films. By utilizing the expansion in surface area of polymer hydrogels in the porous structures, it would be technologically advantageous to fabricate the high-performance sensors, displays, and lasers with intrinsic features such as lightweight, low-cost, flexibility, and easy processability [24].

Acknowledgments

All of the authors express sincere thanks to Messrs. T. Kawa and T. Kaneda for their kind supports and fruitful discussions. This research was financially supported in part by the JSPS Grant-in-Aid for Scientific Research (B) (Grant Nos. 17H03848 and 21H02261), NEXCO Group Companies' Support Fund for Disaster Prevention Measures on Expressways, and Precise Measurement Technology Promotion Foundation.

References

1. P. Pieranski, *Contemp. Phys*., **24** (1983) 25.
2. Y. Xia, B. Gates, Y. Yin, and Y. Lu, *Adv. Mater*., **12** (2000) 693.
3. H. Fudouzi and Y. Xia, *Langmuir*, **19** (2003) 9653.
4. S. Furumi, H. Fudouzi, and T. Sawada, *Laser & Photon. Rev.*, **4** (2010) 205.
5. T. Kaneda, Y. Seki, N. Iwata, and S. Furumi, *J. Photopolym. Sci. Technol.*, **34** (2021) 543.
6. Y. Seki, Y. Shibata, and S. Furumi, *J. Photopolym. Sci. Technol.*, **33** (2020) 473.
7. J. D. Joannopoulos, P. R. Villeneuve, and S. Fan, *Nature*, **386** (1997) 143.
8. Y. Zhao, L. Shang, Y. Cheng, and Z.-Z. Gu, *Acc. Chem. Res*., **47** (2014) 3632.
9. J. Hou, M. Li, and Y. Song, *Angew. Chem. Int. Ed.*, **57** (2018) 2544.
10. Y. Takeoka and T. Seki, *Langmuir*, **22** (2006) 10223.
11. H. Li, L. Chang, J. Wang, and Y. Song, *J. Mater. Chem*., **18** (2008) 5098.
12. F. Xue, Z. Meng, F. Qi, M. Xue, F. Wang, W. Chen, and Z. Yan, *Analyst*, **139** (2014) 6192.
13. M. Kohri, A. Kobayashi, T. Okoshi, H. Shirasawa, K. Hirai, K. Ujiie, T. Kojima, and K. Kishikawa, *Chem. Lett*., **50** (2021) 106.
14. M. Xiong, Y. Sheng, Y. Di, F. Xing, L. Yu, J. Zhang, W. Zhou, C. Liu, L. Dong, and Z. Gan, *ACS Appl. Mater. Interfaces,* **13** (2021) 33566.
15. M. Kumoda, M. Watanabe, and Y. Takeoka, *Langmuir*, **22** (2006) 4403.
16. P. A. Rundquist, P. Photinos, S. Jagannathan, and S. A. Asher, *J. Chem. Phys.*, **91** (1989) 4932.
17. K. Otake, H. Inomata, M. Konno, and S. Saito, *Macromolecules*, **23** (1990) 283.
18. Y. Ohtsuka, T. Seki, and Y. Takeoka, *Angew. Chem. Int. Ed.*, **54** (2015) 15368.
19. Y. Hirokawa and T. Tanaka, *J. Chem. Phys.*, **81** (1984) 6379.
20. S. Musić, N. Filipović-Vinceković, and L. Sekovanić, *Braz. J. Chem. Eng.*, **28** (2011) 89.
21. Y. Maeda, T. Higuchi, and I. Ikeda, *Langmuir*, **16** (2000) 7503.
22. K. Ohno and Y. Mizuta, *ACS Appl. Polym. Mater.*, **2** (2020) 368.
23. K. Ohno, T. Akashi, Y. Huang, and Y. Tsujii, *Macromolecules*, **43** (2010) 8805.
24. N. Iwata, T. Koike, K. Tokuhiro, R. Sato, and S. Furumi, *ACS Appl. Mater. Interfaces,* **13** (2021) 57893.

The synthesis of the high resolution i line novolak resist

Atsushi Sekiguchi[1*, 3, 4], Makoto Hanabata[1, 4], Hiroko Minami[1], Yoko Matsumoto[1], Yosuke Ohta[1], Fucheng Wang[2], Martin Z Ma[2], and Zhiqiang Su[5]

[1] Litho Tech Japan corporation
2-6-6 Namiki, Kawaguchi, Saitama 332-0034, Japan
[2] Shaoxing Shangyu Ziqiang Polymer Chemical Material Co., Ltd.
No.338 Baixie Rd,, Shangyu 312300, P. R. China
[3] Osaka Prefecture University, Department of Physics and Electronics
11-1 Gakuen-cho, Naka-ku, Sakai, Osaka 599-8531, Japan
[4] Osaka City University, Department of Physics and Electronics
3-3-138 Sugimoto-cho, Sumiyoshi-ku, Osaka 558-8585, Japan
[5] Beijing University of Chemical Technology
15 Beisanhun East Road, Chaoyang District, Beijing 100029, P. R. China
**sekiguchi-pdg@ltj.co.jp*

Semiconductors have continued to grow smaller alongside the development of shorter wavelength exposure sources and the development of photoresists optimized for such exposure wavelengths. For the g-line (436 nm) and i-line (365 nm) exposure wavelengths, novolak resists made of novolak resin have been used for patterning at pattern sizes of 0.5 μm-1 μm. For the exposure wavelength of 248 nm (KrF excimer laser), polyhydroxystyrene (PHS) has been used for patterning at pattern sizes of 0.2 μm-0.35 μm. For the exposure wavelength of 193 nm (ArF excimer laser), acrylic-based resin has been used for patterning at pattern sizes of 30 nm-0.2 μm. With the most advanced current lithography technologies, patterning at pattern sizes finer than 20 nm can be performed using exposure wavelengths of 13.5 nm (EUV). Apparently, then, lithography using novolak resists made of novolak resins is an outdated technology. However, it continues to be employed in LCD processes that involve TFT technology, where the development of higher definition LCDs continues to drive miniaturization. We studied the novolak resist, from synthesis to formulation and to evaluation of its resolution, to reexamine which factors are key to achieving high resolution in novolak resists.

Keywords: novolak resin, novolak resist, solution method, low molecular weight fractionation, phenol addition, resist development analyzer, GPC, ICP-MS, lithography simulation

1. Introduction

Semiconductors have continued to grow smaller alongside the development of shorter wavelength exposure sources and the development of photoresists optimized for such exposure wavelengths. For the g-line (436 nm) and i-line (365 nm) exposure wavelength, novolak resists made of novolak resin have been used for patterning at pattern sizes of 0.5 μm-1 μm [1-2]. For the exposure wavelength of 248 nm (KrF excimer laser), polyhydroxystyrene (PHS) has been used for patterning at pattern sizes of 0.2 μm-0.35 μm [3-4]. For the exposure wavelength of 193 nm (ArF excimer laser), acrylic-based resin has been used for patterning at pattern sizes of 30 nm-0.2 μm [5-6]. With the most advanced current lithography technologies, patterning at pattern sizes finer than 20 nm can be performed using exposure wavelengths of 13.5 nm (EUV) [7-8].

Apparently, then, lithography using novolak resists made of novolak resins is an outdated technology. However, it continues to be employed

Received March 31, 2022
Accepted June 20, 2022

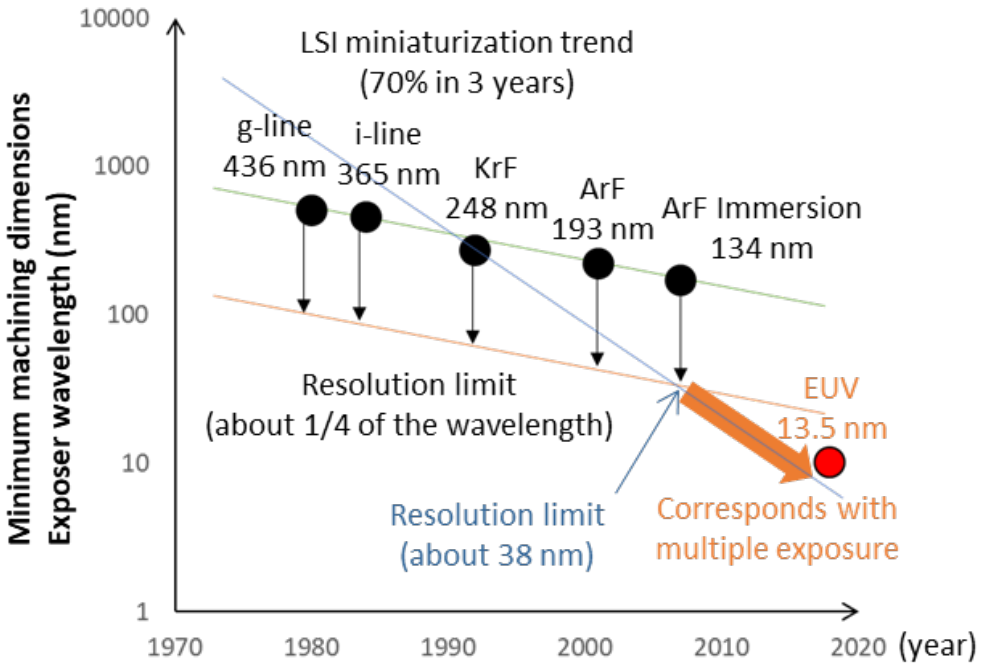

Fig. 1. History of miniaturization in lithography.

in many applications related to LCD processes that involve TFT technology, where the development of higher definition LCDs continues to drive miniaturization. We studied the novolak resist, from synthesis to formulation and to evaluations of its resolution, to reexamine which factors are key to achieving high resolution in novolak resists. This report presents the results.

2. Synthesis and low molecular weight fractionation of novolak resin

2.1. Synthesis of novolak resin

We began by synthesizing novolak resin.

We placed 54 g (0.5 mol) of m-cresol, 54 g (0.5 mol) of p-cresol, 0.284 g (0.012 mol) of oxalic acid, and pure water in a reaction flask, to which we gradually added 73 g (0.9 mol) of 37 wt.% formalin heated to 90°C over a period of 40 minutes. At this point, the ratio of cresol to formalin is 0.75. The mixture was stirred slowly for 3 hours at 90°C to allow the methylolation reaction to proceed in the presence of oxalic acid, a catalyst (Fig. 2).

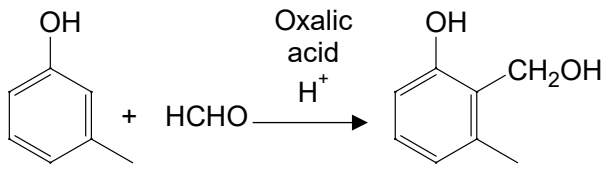

Fig. 2. Methylolation reaction.

We then added PGMEA and 5 % oxalic acid solution to the solution and heated the solution to promote a condensation reaction (Fig. 3) and subsequent polymerization reaction (Fig. 4).

We maintained and stirred the mixture at 90°C for 10 hours for the polymerization reaction [9-12].

We neutralized the polymer solution thus obtained with 5 % sodium hydroxide solution and washed with water to remove the oxalic acid that had served as the catalyst. We used an evaporator to remove water from the resin.

2.2. Low molecular weight fractionation

We performed fractionation to increase the molecular weight of the resin. (Fractionation is the process whereby the resin is washed with solvent to dissolve and remove low molecular weight components by liquid-liquid extraction.) The novolak resin solution obtained was transferred to a separatory funnel, to which PGMEA and n-heptane were added at a resin:PGMEA:n-heptane ratio of 1:5:6. When the funnel is agitated for 3 minutes and left to stand, the funnel contents separate into two liquid layers. The upper layer is the n-heptane layer with the low molecular weight component dissolved, while the bottom layer is the PGMEA layer with medium to high molecular weight components dissolved. By separating the bottom layer and by removing the n-heptane from the upper layer by evaporation, we obtain the fractionation 1 resin solution. By repeating the fractionation process two more times while altering the ratio of

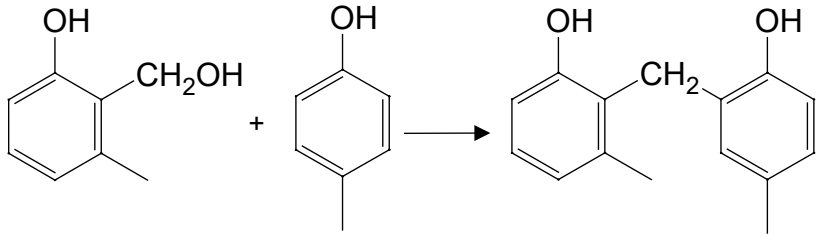

Fig. 3. Condensation reaction

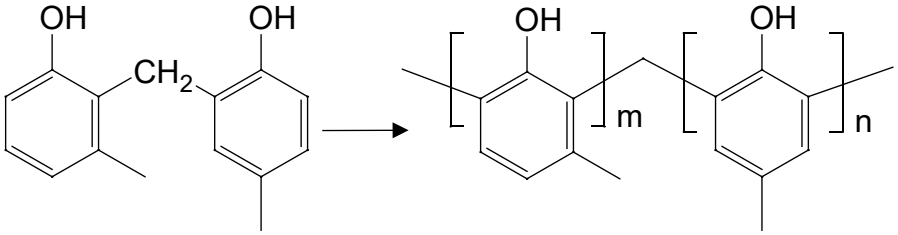

Fig. 4. Polymerization reaction.

PGMEA and n-heptane, we remove the medium molecular weight component and ultimately obtain resin consisting only of the high molecular weight component. We will refer to this as the fractionation 2 resin solution.

3. Evaluation of resin characteristics (GPC/ADR/ICP-MS)

We took GPC measurements for resins before fractionation, fractionation 1, and fractionation 2 using a Prominence LC-20AD GPC analyzer (manufactured by Shimadzu Corporation). The column and separation solvent used were TSKgel GMHHR-N (manufactured by Tosoh Corporation) and tetrahydrofuran (THF), respectively. Figure 5 shows GPC measurement results for each resin type.

The fractionation process removes the low

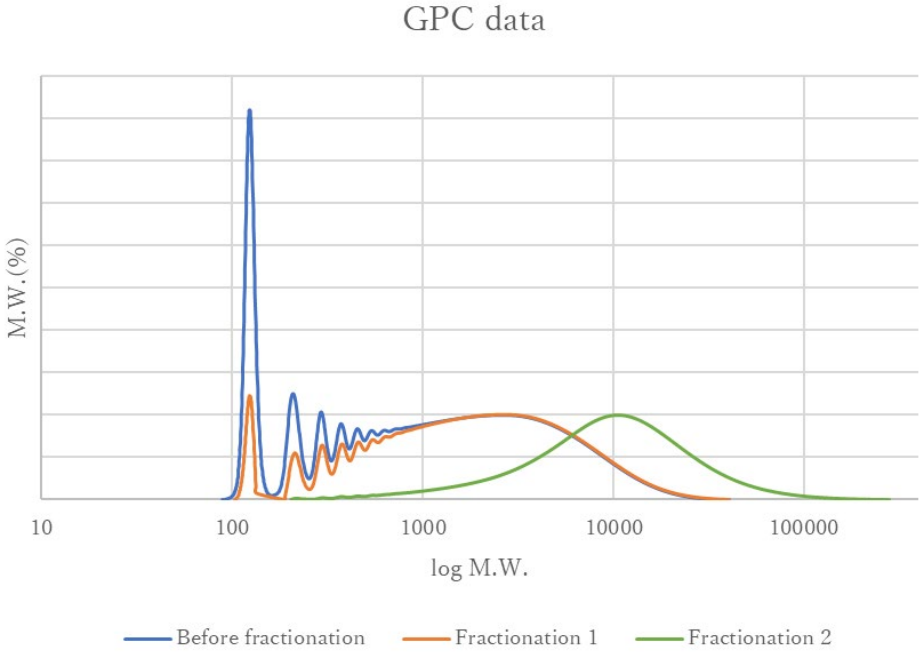

Fig. 5. Comparison of GPC measurement results for before fractionation, fractionation 1, and fractionation 2.

Table 1. Results of GPC measurement for before fractionation, fractionation 1, and fractionation 2.

	Before Fractionation	Fractionation 1	Fractionation 2
Number average molecular weight Mn	361	682	4356
Weight average molecular weight Mw	2071	2772	13562
Z average-molecular-weight Mz	6677	7099	32521
Mw/Mn	5.74	4.06	3.11

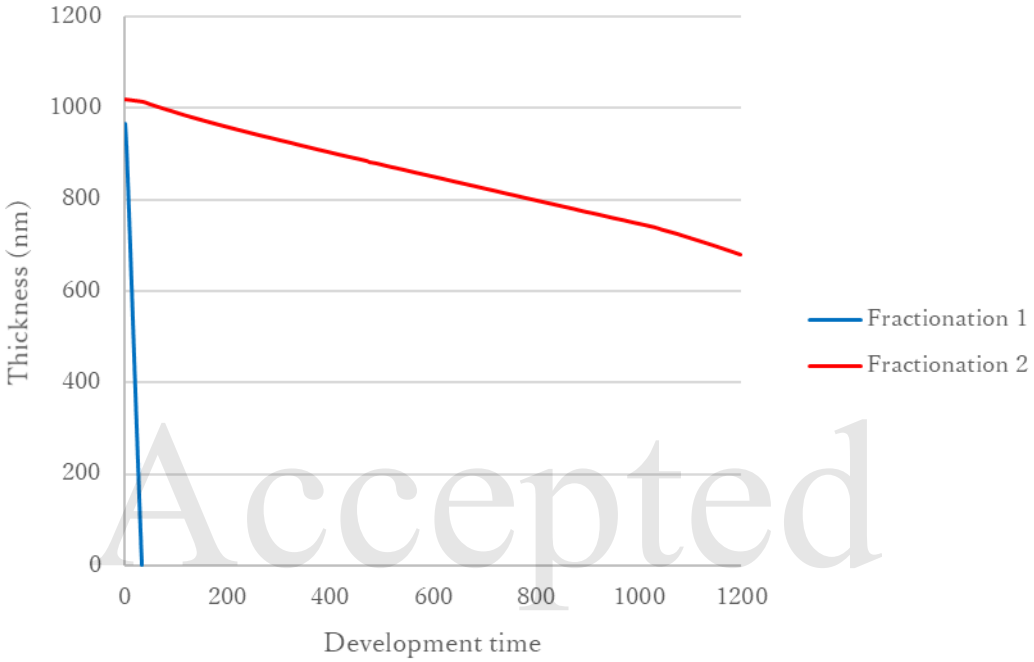

Fig. 6. Comparison of ADR results for fractionation 1 and fractionation 2.

Table 2. Result of ICP-MS analysis.

Metal	Before Fractionation	Fractionation 1	Fractionation 2
Na	1000	850	200
K	190	0.61	0.85
Ca	480	0.87	0.05
Fe	210	0.95	<0.05
Cu	20	0.02	<0.02
Zn	1900	0.11	<0.02

molecular weight component; thus, the average molecular weight increases, while the Mw/Mn ratio decreases.

We compared the results of ADR measurements between the fractionation 1 and fractionation 2 resins (Fig. 6). Resin viscosity is adjusted by

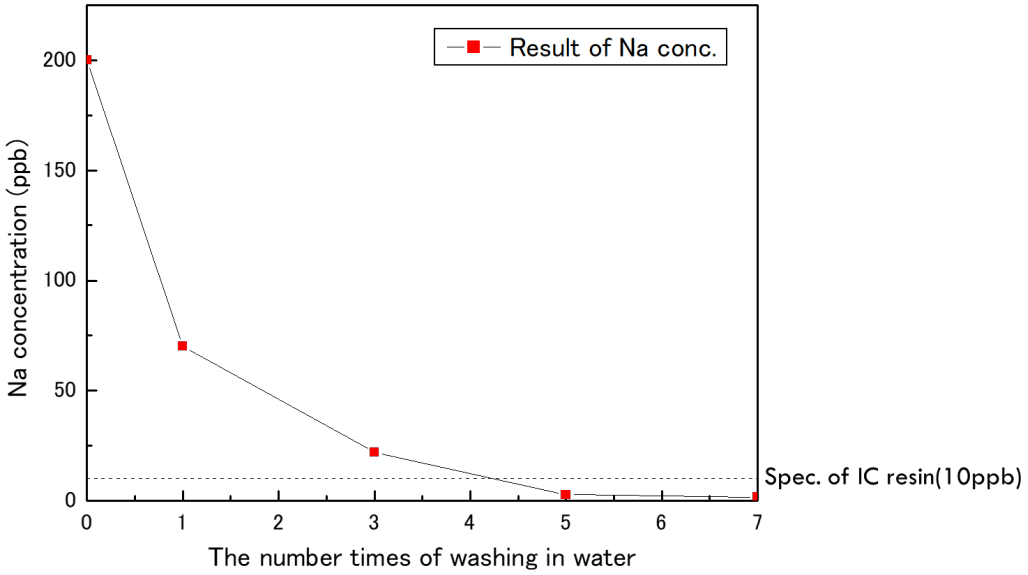

Fig. 7. Relationship between number of times of washing in water and Na contamination

adding PGMEA to the fractionation 1 and fractionation 2 resin solutions before application to a Si substrate at a thickness of 1 μm. We used the RDA-760 Resist Development Analyzer [14] for ADR measurements. The developer was 2.38 % TMAH solution adjusted to 23°C. The ADR was smaller for the fractionation 2 resin than for the fractionation 1 resin, a result attributable to the increase in molecular weight.

Table 2 shows the results of ICP-MS analysis.

The specifications require all metal concentrations in the novolak resin for IC to be 10 ppb or lower. The results indicate all metal concentrations meet the specifications, except for Na. To determine how we might reduce the Na contamination, we reviewed the washing process with water carried out before the fractionation step. The resin was placed in washing water set to 40°C inside a separatory funnel and agitated for 3 minutes, left to stand for 3 minutes to allow the resin to settle, then separated.

Figure 7 shows the relationship between Na contamination and the number of times the resin was washed with water.

Based on the results, we concluded that washing with water for 5 or more times reduced Na contamination to within the range required by the specifications.

4. Resist preparation and evaluation

After producing a novolak resin meeting the specifications for semiconductors, we proceeded to

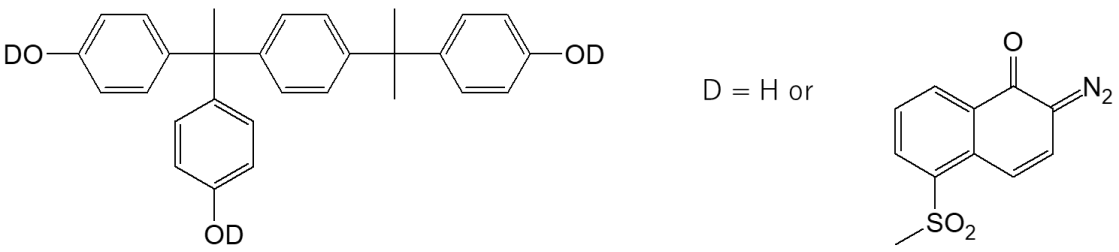

Structure of the added PAC

PAC	Disubstituted	Trisubstituted
TPPA-200	42.21	41.31
TPPA-250	28.89	66.29

(Area%)

Fig. 8. Structure and esterification ratio of PAC

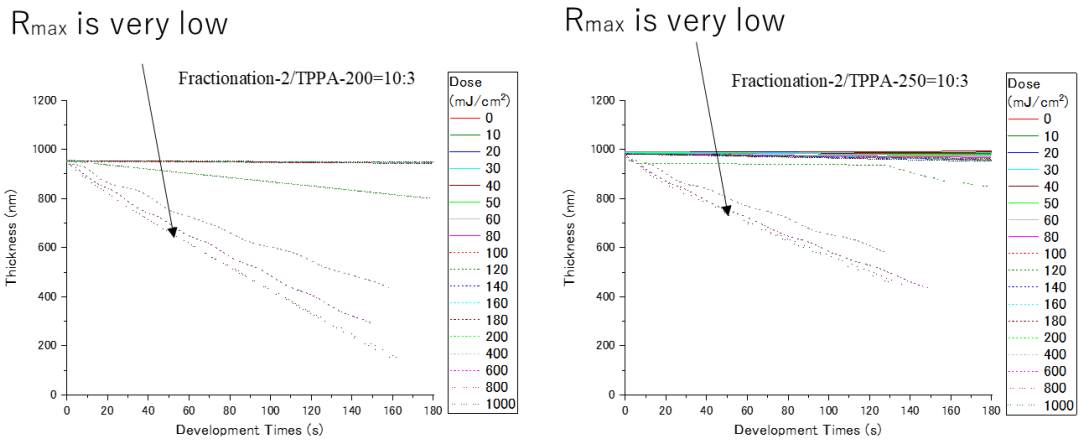

(a) Fractionation 1/TPPA-200=10:3 (b) Fractionation 1/TPPA-250=10:3

Fig. 9. Comparison of development rate curves measured with RDA.

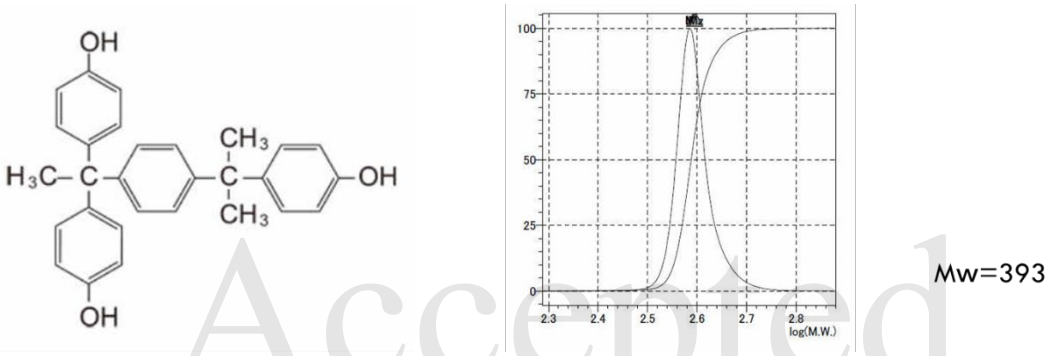

Fig. 10. Structure and molecular weight of the dissolution promoting agent TrisP-PA.

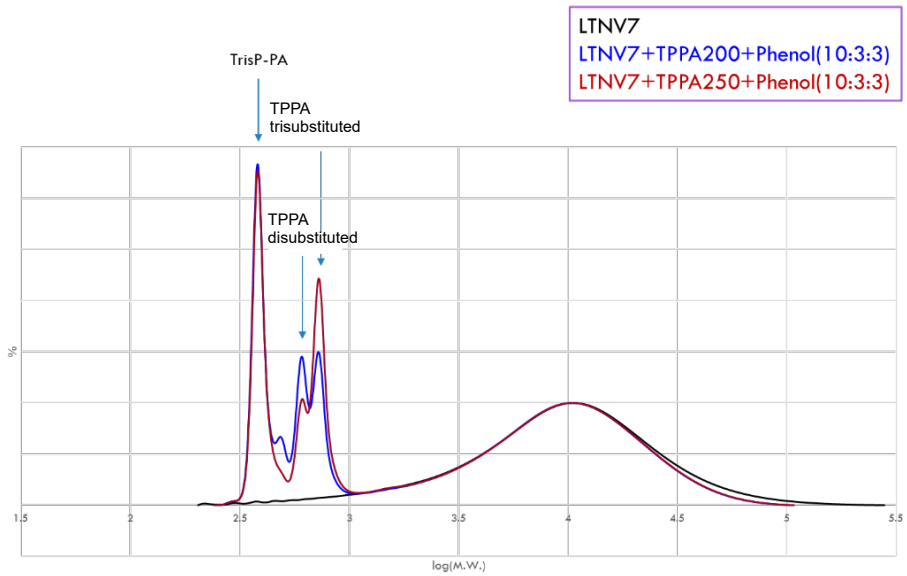

Fig. 11. Comparison of GPC measurement results of resists with dissolution promoting agent TrisP-PA added.

prepare photoresists [15]. We used fractionation 2 resin to prepare the photoresists, as the higher molecular weight can be expected to achieve higher resolution than the fractionation 1 resin. We used

two types of photoactive compounds (PAC) of differing esterification ratios (TPPA-200 and TPPA-250, Toyo Gosei Co, Ltd.).

The amount of PAC added was 30 % of the resin by weight. The solvent was PGMEA.

Figure 9 shows the development rate curves measured using the RDA-800 Resist Development Analyzer (manufactured by Litho Tech Japan Corporation). The film thickness of the photoresist was 1,000 nm. PAB was carried out for 60 sec. at 100°C and PEB for 60 sec. at 110°C.

The results showed that the dissolution rate at maximum exposure dose (Rmax) was too low in this state for the formula to function as a photoresist.

5. To achieve higher resolution

To overcome this issue, we added a dissolution promoting agent to the present photoresist to improve the dissolution rate at maximum exposure dose (Rmax).

Figure 10 shows the structure and GPC measurement data of the dissolution promoting agent used, TrisP-PA(α,α-Bis(4-hydroxyphenyl)-4-(4-hydroxy-α,α-dimethylben-zyl)-ethylbenzene) (manufactured by Honshu Chemical Industry Co., Ltd.).

The amount of the dissolution promoting agent added was 30 wt.% of the resin. Figure 11 shows the comparison of GPC measurement results of the present photoresist.

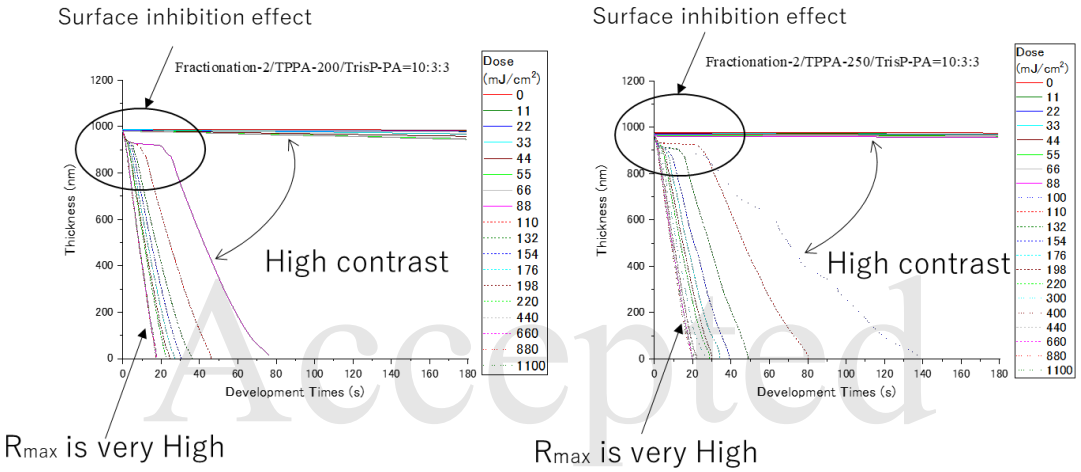

(a) Fractionation 1/TPPA-200=10:3 (b) Fractionation 1/TPPA-250=10:3

Fig. 12. Comparison of development rate curves measured with RDA (with dissolution promoting agent added).

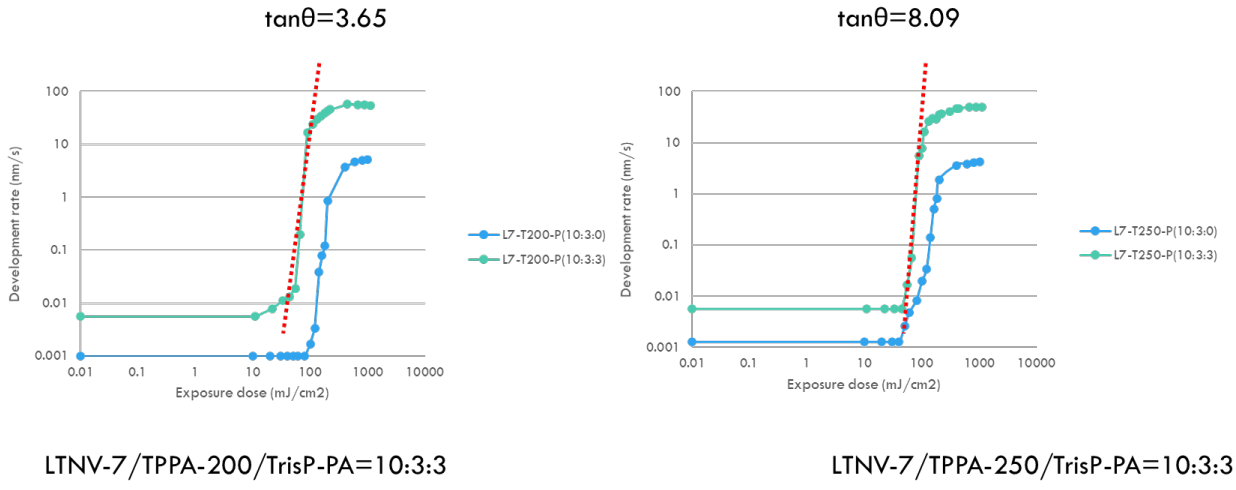

Fig. 13. Comparison of development rate curves with and without the addition of dissolution promoting agent.

Table 3. Comparison of simulation parameters.

	NV-7/T200NV-7/P	NV-7/T250/P	THMR-iP3000
A(μm^{-1})	0.591	0.649	0.444
B(μm^{-1})	0.072	0.059	0.249
C(cm^2/mJ)	0.014	0.014	0.015
Eth60(cm^2/mJ)	112.3	124.3	179.7
Gamma60	6.4	7.37	2.93
tanθ	3.65	8.09	3.47
Rmax(nm/s)	55.7	53.5	46.6
Rmin(nm/s)	0.006	0.006	0.03
Mth	0.254	0.195	0.13
n	8.84	12.53	5.82
RSR	0.58	0.52	0.52
ID(nm)	104	350	33.3

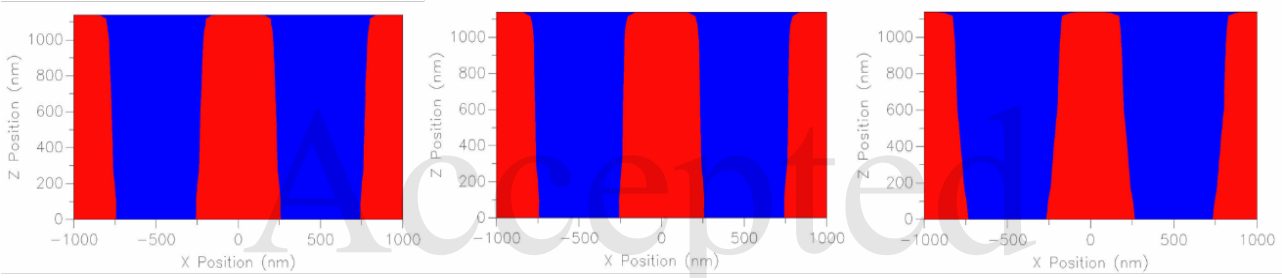

(a) Comparison of results for 0.5 μm pattern

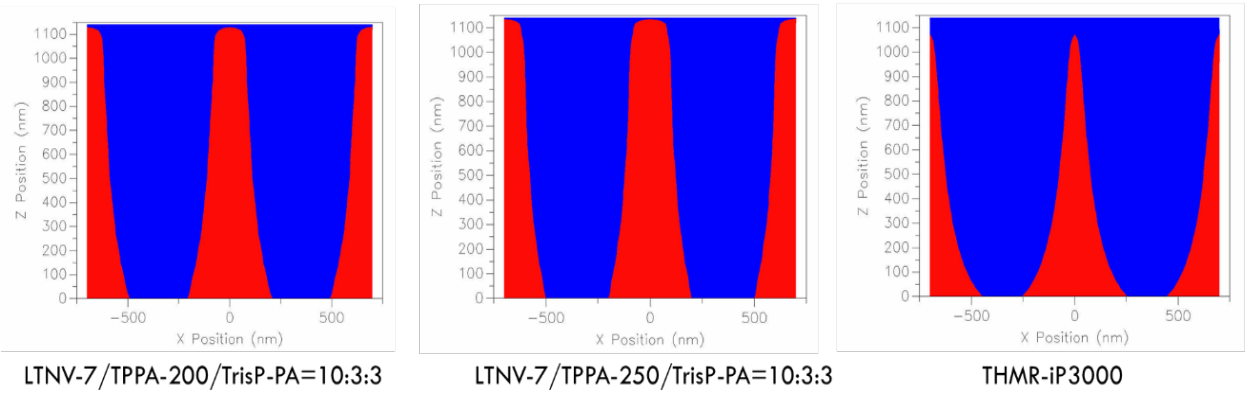

(b) Comparison of results for 0.35 μm pattern

Fig. 14. Results of simulations.

The peaks for TrisP-PA, PAC, and resin can be confirmed, indicating that the so-called tandem type resin structure [16-17] had been created.

Figure 12 shows the development rate curves

measured using the Resist Development Analyzer RDA-800 (manufactured by Litho Tech Japan Corporation) [14]. The film thickness of the photoresist was 1,000 nm. PAB was carried out for 60 sec. at 100°C and PEB for 60 sec. at 110°C. The results indicated the contrast required for producing a high-resolution photoresist had been achieved. Figure 13 compares development rate curves for photoresist with and without the addition of a dissolution promoting agent.

By adding the dissolution promoting agent, we were able to obtain the Rmax necessary for resolving photoresists. Comparisons of the results for the two types of PAC indicated contrast up to $\tan\theta = 8.09$ with TPPA-250.

We performed pattern simulation using PROLITH. For comparison, we also carried out calculations for an i-line photoresist widely available on the current market.

The simulation conditions are given below.

Pattern dimensions:	0.50 μm and 0.35 μm, line and space pattern
Exposure wavelength:	365 nm
Illumination coherence σ:	0.5
NA:	0.5
Development time:	60 sec.

Figure 14 shows the results of simulations for 0.5 μm and 0.35 μm line-and-space patterns.

The results suggest that good pattern resolution can be achieved, even compared to the i-line photoresists widely available on the current market. Comparisons of the results for the two types of PACs indicate TPPA-250 offers better pattern resolution than TPPA-200, perhaps because the concentration of trisubstituted derivatives is higher in TPPA-250, which would promote azo coupling reactions, thereby generating higher development contrast for the photoresist.

6. Summary

To achieve higher resolution, we performed fractionation of novolak resin to synthesize a resin of higher molecular weight. Additionally, we identified the optimal number of times the resin should be washed with water to suppress metal contamination to within the range required by specifications for use with semiconductors. We prepared the photoresists by adding PAC to the resin obtained. Measurements of their development rates indicated poor dissolution rates. We added a dissolution promoting agent to prepare a so-called tandem type resin. Measurement of development rates of photoresist prepared by adding two types of PAC showed high dissolution rates and suppressed dissolution. Results of lithography simulations using development parameters confirmed that the present photoresist exhibits higher resolution than the i-line photoresists widely available on the current market.

Acknowledgements

We are grateful to Mr. Chen at Shaoxing Shangyu Ziqiang Polymer Chemical Material Co., Ltd. for his skillful translations during the technical review process. We thank KLA Corporation for granting permission to use PROLITH.

References

1. Ralph Dammel: *Tutorial texts in optical engineering v. TT, SPIE*, (1993).
2. R. Dammel, *"diazonaphthoquinone based resist" SPIE TT.*, **11** (1993).
3. H. Ito and C. G. Willson, *Technical Papers of SPE Regional Technical Conference on Photopolymers, Society of Plastics Engineers*, 331 (1982): *polym. Eng. Sci.*, **23** (1983) 1012.
4. H. Ito and C. G. Wilson, *In polymers in Electronics, T. Davidson, Ed., American chemical Society*, (1984) 11.
5. R. D. Allen, G. M. Wallraff, W. D. Hinsberg, and L. L. Simpson, *J. Vac. Sci. Technol.*, **B9**, (1991) 3357.
6. N. Abe, S. Takechi, Y. Kaimoto, M. Takahashi, and K. Nozaki, *J. Photopolym. Sci. Technol.*, **8** (1995) 637.
7. T. Watanabe, H. Kinoshita, N. Sakaya, T. Shoki, and S. Y. Lee, *Jpn. J. Appl. phys.*, **44** (2005) 5556.
8. K. Hamamoto, T. Watanabe, H. Tsubakino, H. Kinoshita, T. Shoki, and M. Hosoya, "Fine Pattern Replication by EUV Lithography", *J. Photopolym. Sci. Technol.*, **14** (2001) 567.
9. M. Hanabata, A. Furuta, and Y. Uemura, *Proc. SPIE*, **631** (1986) 76.
10. M. Hanabata, A. Furuta, Y. Uemura, *Proc. of SPIE*, **771** (1987) 85.
11. M. Hanabata, Y. Uemura, A. Furuta, *Proc. of SPIE*, **920** (1988) 349.
12. M. Hanabata and A. Furuta, *Proc. SPIE*, **1262** (1990) 476.
13. M. Hanabata, F. Oi, and A. Furuta, *Proc. SPIE*, **1466** (1991) 132.
14. A. Sekiguchi, C. A. Mack, Y. Minami, and T. Matsuzawa, *Proc. SPIE*, **2725** (1996) 49.
15. M. Yamamoto, R. Kitai, H. Horibe, A. Sekiguchi,

and H. Tanaka, *J. Photopolym. Sci. Technol.*, **22** (2009) 357.
16. A. Sekiguchi, Y. Matsumoto, H. Tanaka, T. Horiuchi, and Y. Sensu, *Proc. SPIE*, **9779** (2016) 55.
17. A. Sekiguchi, Y. Matsumoto, Y. Sensu, S. Takei, and M. Hanabata, H. Tanaka, *Proc. SPIE*, **10146** (2017) 101461K-1.

Synthesis of a Dipyridyl Disulfide Cross-linking Reagent and Its Application to Photo-adhesion of Dissimilar Materials

Masahiro Furutani* and Ritsuto Senkyo

Department of Chemistry and Biology, National Institute of Technology, Fukui College, Geshi-cho, Sabae, Fukui 916-8507, Japan
**furutani@fukui-nct.ac.jp*

Photo-adhesion of dissimilar materials was performed by using a diacrylate cross-linking reagent containing a 2,2'-dipyridyl disulfide moiety. Cross-linking reagent designed in this work was purified by recrystallization. UV-cured films were fabricated with the cross-linking reagent, 4-hydroxybutyl acrylate and a radical photo-initiator. Hydrophilicity of the film surface seemed to be changed larger than that of control samples. In photo-adhesion experiments, 0.3-2.5 MPa of shear stress was recorded after 1 J/cm^2 of UV irradiation at a wavelength of 365 nm. Remarkable improvement of adhesive strength was observed when copper adherends were used, suggesting interaction between copper surface and sulfur atoms of the dipyridyl disulfide moieties in the adhesive layer.

Keywords: Dipyridyl disulfide, Cross-linking reagent, Photo-adhesion, Dissimilar material, Recrystallization

1. Introduction

Photo-adhesive materials have been used in many industrial fields such as appliance manufacturing [1], printing [2] and dentistry [3]. Fast and local adhesion is accomplished without heating treatment, by using light source as a trigger of formation of adhesive layers. Furthermore, photo-adhesives having additional functionalities have been recently developed. Dismantlable photo-adhesives were reported where acid-degradative groups (with photo-acid generators) [4] and disulfide bonds [5,6] were used to make adhesive layers disrupt. Reversible photo-adhesives were also reported using isomerization of azobenzene [7,8], or reversible reactions of anthracene [9] and disulfide [10]. These photo-adhesives would become one of key materials for approaching sustainable development goals, SDGs.

On the other hand, photo-adhesive materials for dissimilar materials have been desired, because such adhesive materials ensure lightweight and free-designing of industrial products. Chemical structures and properties of catechol and its analogues have been in the limelight for this purpose, since adhesive proteins including these structures were found in marine organisms [11,12]. The two phenolic hydroxy groups would take part in hydrogen bonding, coordination bonding, and covalent bonding [13]. The aromatic rings would be also used for π-π stacking. Polystyrene [14], polymethacrylate [15], or polyamide [16] bearing with catechol groups have been developed as adhesive materials. Encouraged these studies, 2,2'-dipyridyl disulfide (PySSPy) moieties were tried to apply an acrylate photo-adhesive material [17,18]. PySSPy moiety has two sets of a sulfur atom and a pyridine ring, which these chemical structures would contribute to interaction with interface of metallic substrates. While a cross-linking reagent was designed and synthesized in the previous work, purification of the reagent was somewhat difficult with column chromatography. In this article, the chemical structure has been modified (Fig. 1), to improve miscibility toward other components of the photo-adhesive material, additionally resulting in simple purification by recrystallization processes.

Received March 31, 2022
Accepted May 20, 2022

The adhesive layer was formed between a glass substrate and another one (glass, metal, or plastic), through radical UV curing process without any organic solvents.

2. Experimental

2-Mercaptonicotinic acid, thionyl chloride, 4-hydroxybutyl acrylate (HBA), Omnirad651 (2,2-dimethoxy-2-phenylacetophenone, a radical photo-initiator), and concentrated nitric acid were purchased from Tokyo Chemical Industry Co., Ltd. (Tokyo, Japan). *N*,*N*-Dimethylformamide (DMF), triethylamine, and tetrahydrofuran (THF) were purchased from FUJIFILM Wako Pure Chemical Corporation (Osaka, Japan). Chloroform, ethyl acetate, *n*-hexane, and acetone were purchased from NACALAI TESQUE, Inc. (Kyoto, Japan). All chemical reagents were used without further purification.

Glass substrate (1 mm thick) was purchased from AS ONE Corporation (Osaka, Japan). Copper (Cu, 0.3 mm thick), stainless (SUS430, 0.1 mm thick) and aluminum (Al, 0.3 mm thick) substrates were purchased from HIKARI Co., Ltd. (Osaka, Japan). Calcium fluoride (CaF_2) substrate was purchased from Pier Optics Co., Ltd. (Gunma, Japan). These substrates were ultrasonicated with acetone and then chloroform for 10 min each. Treated-Cu was prepared according to the literature [19], with immersion Cu substrates into concentrated nitric acid for 1 min. After washing with distilled water, the substrates were used for photo-adhesion experiments as early as possible. Polyvinyl chloride (PVC, 1 mm thick) and polypropylene (PP, 0.2 mm thick) were purchased from Acrysunday Co., Ltd. (Tokyo, Japan), and these substrates were wiped with paper-wastes before using for photo-adhesion experiments.

^{1}H- and ^{13}C-NMR spectra were recorded using a Bruker AVANCEIII. APCI-MS measurments were performed using an AB Sciex API2000. Thermal property was measured using a Rigaku Thermo plus EVO II TG8120 (rate of temperature increase: 10 K/min, under air atmosphere). FT-IR spectral measurements were performed using a Perkin Elmer Spectrum100. Anionic UV curing and photo-adhesion experiments were performed with 3UV^{TM}-36UVLamp (Analytik Jena AG) and UIT-250/UVD-C365 ultraviolet radiometer (Ushio Inc.). Water contact angle of each substrate or UV-cured samples was measured using an SImage Entry 6 (Excimer Inc.). Shear stress was recorded using an MCT-2150 (A&D, Co., Ltd., tensile rate: 10 mm/min).

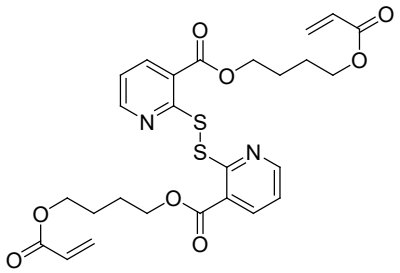

1

Fig. 1. Chemical structure of cross-linking reagent **1** containing a PySSPy moiety.

2.1 Synthesis of 1

To a dried flask were added 2-mercaptonicotinic acid (0.50 g, 3.2 mmol), thionyl chloride (2.7 mL) and DMF (0.36 g), and stirred at room temperature for 3.5 h. After removal of unreacted thionyl chloride, HBA (1.9 g, 13 mmol) and triethylamine (0.33 g, 3.2 mmol) in THF (20 mL) were added to the residue, and the mixture was stirred at room temperature for 3.7 days. After evaporating the solvent, the residue was dissolved in chloroform (50 mL), which was washed twice with brine. The organic layer was dried with magnesium sulfate, and the chloroform solution was allowed to stand at room temperature for several days, depositing a dark olive crystal. Again, the crystal was subjected to recrystallization in chloroform, followed by washing with ethyl acetate, to obtain **1** in a 6.5% yield as a white crystal. ^{1}H-NMR (400 MHz, $CDCl_3$): δ 1.94 (8H, m, -CH_2-CH_2-), 4.28 (4H, t, J = 6.0 Hz, vinyl-COO-CH_2-), 4.87 (4H, t, J = 6.0 Hz, Py-COO-CH_2-), 5.86 (2H, dd, J = 0.80, 10 Hz, -CH=C$\underline{H}_2$), 6.16 (2H, dd, J = 10, 17 Hz, -C$\underline{H}$=CH_2), 6.44 (2H, dd, J = 0.80, 10 Hz, -CH=C$\underline{H}_2$), 7.15 (2H, dd, J = 4.4, 7.6 Hz, Py-H) , 8.29 (2H, dd, J = 1.2, 7.6 Hz, Py-H) , 8.52 (2H, dd, J = 1.2, 4.4 Hz, Py-H). ^{13}C-NMR (100 MHz, $CDCl_3$): δ 25, 25, 64, 65, 120, 124, 128, 128, 131, 139, 152, 160, 166. APCI-MS $[M]^+$: *m/z* calcd for $C_{26}H_{28}O_8N_2S_2$: 560.64; found: 560.5. Melting point: 113.5°C (TG-DTA).

2.2 Fabrication of UV-cured films with 1

To HBA were mixed **1** (0 or 1.2 mol% toward HBA) and Omnirad651 (2.4 wt%), which were drop-cast on a glass substrate. UV irradiation (1.5 mW/cm^2, 1 J/cm^2) was performed at a wavelength of 365 nm under nitrogen atmosphere, obtaining UV-cured films through radical UV curing. Contact angle of a water drop (8.2 μL) on the UV-cured films or a glass substrate was

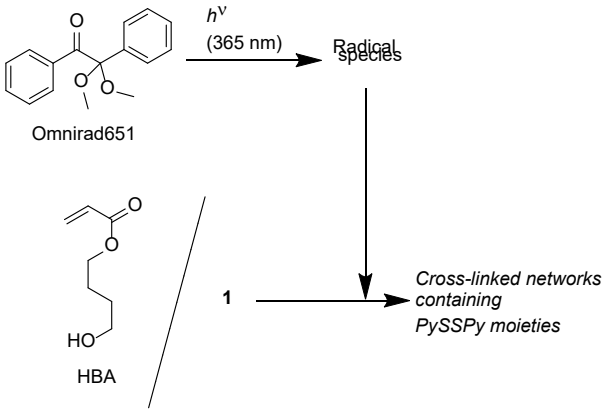

Scheme 1 Radical UV curing of HBA and **1** to form cross-linked networks containing PySSPy moieties, using Omnirad651 as a photo-initiator.

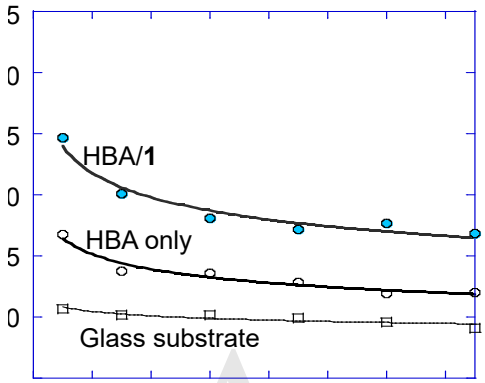

Fig. 2 Time course of decrease of water contact angles on glass substrate, or the UV-cured films fabricated with HBA, **1** (0 or 1.2 mol% toward HBA), and Omnirad651.

recorded after 0.5 min and at 1.5 min of intervals. The mixture containing **1** was also dropped between two CaF_2 substrates, followed by FT-IR spectral measurements with/without UV irradiation (3.7 mW/cm^2 at 365 nm, 1 J/cm^2).

2.3 Photo-adhesion of dissimilar materials

Mixtures described in the section 2.2 were prepared with HBA, **1** and Omnirad651. The mixtures were dropped on a substrate (glass, Cu, treated-Cu, stainless, Al, PVC or PP), and sandwiched using another substrate (glass). UV irradiation (3.7 mW/cm^2, 1 J/cm^2) was performed at a wavelength of 365 nm, obtaining photo-adhesive samples. Three samples were fabricated with each pair of substrates, and adhesion area was below 60 mm^2.

3. Results and discussion

3.1. Synthesis of 1

In the first recrystallization in chloroform, **1** seemed to be crystallized with four HBA molecules, estimated from the ^{1}H-NMR spectrum. The second recrystallization and subsequent washing with ethyl acetate removed residual HBA molecules. Compound **1** showed good solubility toward THF and chloroform as well as good miscibility toward HBA that was one of components of the photo-adhesive material.

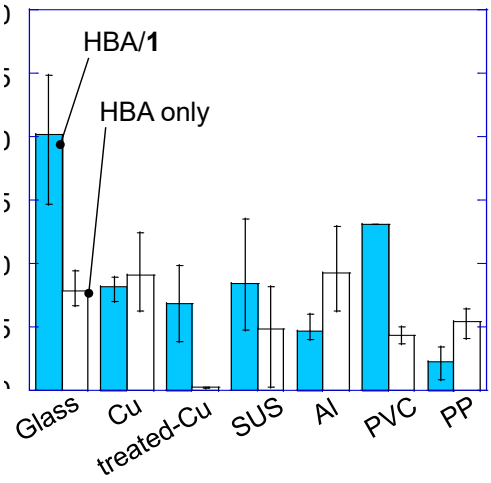

Fig. 3 Results on the shear stress test of photo-adhesive samples fabricated with HBA, **1** (0 or 1.2 mol% toward HBA), and Omnirad651, after 1 J/cm^2 of UV irradiation. Height of each bar is average value of the sample. Upper and lower parts of each error bar are the maximum and the minimum values of the sample.

3.2. Fabrication of UV-cured films with 1

The mixture consisting of HBA, **1** and Omnirad651 did not become homogeneous, although **1** or Omnirad651 dissolved individually into HBA. Nevertheless, the UV curing reactions (Scheme 1) proceeded in a radical process, confirming FT-IR spectral measurements. A peak around 1650 cm^{-1} disappeared after 1 J/cm^2 of UV irradiation, indicating the consumption of acryloyl groups of HBA and **1** (data not shown). Fig. 2 shows water contact angles on UV-cured films or a glass substrate, which hydrophilicity of a film fabricated with **1** is lower than that of a film without **1** or of a glass substrate. However, the hydrophilizing variation range (0.5 to 7.5 min) of the former (Δ = 25.2°) was larger than of the latter (Δ = 18.7°), although motion of polymer chains in the former would be suppressed by cross-linking points. In the case of a glass substrate, the water contact angle was not almost changed, implying the effect of hydrophilic functional groups from HBA and **1** on the change of contact angles.

3.3. Photo-adhesion of dissimilar materials

As shown in Fig. 3, photo-adhesion was achieved with glass-glass and glass-X (X: metals or plastics) samples. Interfacial failure on the X side was observed in all glass-X cases. The maximum value of 2.48 MPa was obtained with glass-glass samples, probably due to interfacial hydrogen bonding between the substrate and the adhesive layer. The average value of shear stress σ_{ave} became larger by using **1** ($\sigma_{ave,\ HBA/1} > \sigma_{ave,\ HBAonly}$) in the cases of glass-X (X = glass, treated Cu, SUS, and PVC), which the ratios became more than 1.0. Negative correlation between the ratios and water contact angles could be seen in Fig. 4. Shear stress of glass-X (X = Cu and treated Cu) tended to be high, probably resulting from interaction of copper atoms to sulfur (or nitrogen) atoms in PySSPy moieties [20]. The ratio of σ_{ave} of glass-treated Cu samples became about thirty.

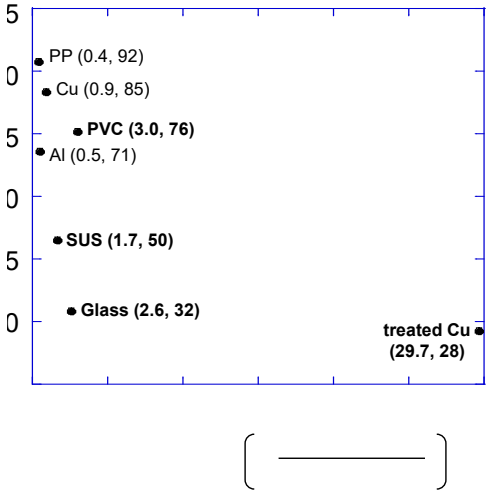

Fig. 4 Correlation between the ratios of σ_{ave} and water contact angles. Boldface means that the σ_{ave} is more than 1.0.

4. Conclusion

A diacrylate cross-linking reagent having a PySSPy moiety was synthesized, and it was purified with recrystallization. Solvent-free photo-adhesion of glass, metals and plastics was achieved with the reagent, and preparation of completely homogeneous photo-adhesive materials is now under investigation.

Acknowledgement

MF acknowledges Prof. Eiki Matsui at National Institute of Technology, Fukui College, for the use of APCI-MS instrument. This work was supported by JSPS KAKENHI Grant Number JP 21K04670.

References

1. J. H. Moon, Y. G. Shul, H. S. Han, S. Y. Hong, Y. S. Choi, and H. T. Kim, *Int. J. Adhes. Adhes.*, **25** (2005) 301.
2. R. S. Scotton, L. M. Guerrini, and M. P. Oliveira, *Prog. Org. Coat.*, **158** (2021) 106389.
3. K. Ikemura and T. Endo, *Dent. Mater. J.*, **29** (2010) 481.
4. H. Sugita, K. Itou, Y. Itou, N. Wada, T. Ueno, S. Kurita, Y. Hirose, K. Hatase, H. Matsumoto, and D. Ichinohe, *Int. J. Adhes. Adhes.*, **104** (2021) 102758.
5. M. Furutani, A. Kakinuma and K. Arimitsu, *J. Photopolym. Sci. Technol.*, **29** (2016) 607.
6. M. Furutani, A. Kakinuma and K. Arimitsu, *J. Polym. Sci. A: Polymer Chemistry*, **56** (2018) 237.
7. S. Ito, H. Akiyama, M. Mori, M. Yoshida and H. Kihara, *J. Polym. Sci.*, **58** (2020) 568.
8. Y. Zhou, M. Chen, Q. Ben, Z. Zhang, S. Shuang, K. Koynov, H. J. Butt, J. Kong and S. Wu, *ACS Macro Lett.*, **8** (2019) 968.
9. H. Akiyama, Y. Okuyama, T. Fukata, and H. Kihara, *J. Adhes.*, **94** (2018) 799.
10. M. Furutani, K. Maeno and A. Tanaka, *J. Photopolym. Sci. Technol.*, **34** (2021) 529.
11. J. H. Waite and M. L. Tanzer, *Science*, **212** (1981) 1038.
12. M. Yu, J. Hwang and T. J. Deming, *J. Am. Chem. Soc.*, **121** (1999) 5825.
13. J. Saiz-Poseu, J. Mancebo-Aracil, F. Nador, F. Busqu and D. Ruiz-Molina, *Angew. Chem. Int. Ed.*, **58** (2019) 696.
14. C. R. Matos-Pérez, J. D. White and J. J. Wilker, *J. Am. Chem. Soc.*, **134** (2012) 9498.
15. D. Payra, Y. Fujii, S. Das, J. Takaishi and M. Naito, *Polym. Chem.*, **8** (2017) 1654.
16. S. Li, N. Chen, Y. Li, J. Zhao, X. Hou and X. Yuan, *Macromol. Mater. Eng.*, (2019) 1900620.
17. M. Furutani, K. Endo and K. Arimitsu, *Mater. Technol.*, **37** (2019) 27.
18. M. Furutani, K. Nakayama, K. Okuma and K. Arimitsu, *J. Photopolym. Sci. Technol.*, **32** (2019) 619.
19. "Part twenty two: Wood, adhesives, in Annual book of ASTM standards", ed. By American Society for Testing and Materials, Philadelphia, PA, (1976) 767.
20. Ch. Zubrägel, C. Deuper, F. Schneider, M. Neumann, M. Grunze, A. Schertel and Ch. Wöll, *Chem. Phys. Lett.*, **238** (1995) 308.

Acid-responsive Emission Color Changes of Diarylaminobenzylideneanilines

Takuma Tsukada and Hideyuki Nakano*

Department of Applied Chemistry, Muroran Institute of Technology,
27-1 Mizumoto-cho, Muroran, Hokkaido 050-8585, Japan.
**nakano@mmm.muroran-it.ac.jp*

Emission color changes of 4-[bis(4-methylphenyl)amino]benzylideneaniline (BMBZA) and 4-[bis(9,9-dimethylfluoren-2-yl)amino]benzylideneaniline (BFBZA) in response to hydrochloric acid (HCl) vapor and solid organic acids, pentafluorobenzoic acid (PFBA) and benzoic acid (BA), have been investigated in their different solid states. Emission color of BMBZA crystals changed from greenish blue to reddish orange by exposure to HCl vapor, whereas the emission color of BFBZA crystals did not. However, powder sample obtained by grinding the BFBZA crystal exhibited emission color change by exposure to HCl vapor. Similar results of emission color changes of BMBZA and BFBZA crystals in response to PFBA were obtained. In the case of BMBZA–BA and BFBZA–BA systems, grinding of the crystalline mixtures allowed their emission color changes without change in their object colors.

Keywords: Diarylaminobenzylideneaniline, Hydrochloric acid, Organic acid, Emission color change

1. Introduction

Emission switching of the organic emitting films by a variety of external stimuli are the subjects of interest from not only fundamental sciences to elucidate their mechanisms but also practical applications such as optical devices and sensors. Organic electroluminescence devices are the typical examples that exhibit switching of emission controlled by applying external electric field [1]. Switching phenomena of emission color by other external stimuli e.g. photoirradiation [2,3], chemical vapors [4–6], mechanical stresses [7,8], have been attracting attentions.

We have been performing studies on the creation of stimuli-responsive emitting amorphous molecular materials. Diarylaminobenzaldehyde-based emitting amorphous molecular materials have been found to exhibit vapochromic and mechanochromic emissions [9–13]. Not only single component systems, we have been investigating hybrid systems with smart functions [14–18]. We have reported that novel hybrid films composed of diarylaminobenzaldehyde-based emitting amorphous molecular materials with *p*-toluenesulfonic acid exhibited OFF–ON fluorescence switching in response to moisture [16]. In addition, we have found very recently that hybrid amorphous films composed of emitting amorphous molecular materials, 4-[bis(4-methylphenyl)amino]benzylideneaniline (BMBZA) and 4-[bis(9,9-dimethylfluoren-2-yl)amino]benzylideneaniline (BFBZA), with organic acids, pentafluorobenzoic acid (PFBA) and benzoic acid (BA), exhibited emission color changes in response to moisture [17,18]. Chemical structures of BMBZA, BFBZA, PFBA, and BA are shown in Chart 1. In due course of the studies, we have shown that spin-coated amorphous films of BMBZA and BFBZA exhibited emission color changes by exposure to hydrochloric acid (HCl) vapor [17,18].

Like other amorphous molecular materials, BMBZA and BFBZA can form not only amorphous states but also crystalline states obtained by conventional recrystallization from solvents. Emitting properties and their

Received March 27, 2022
Accepted May 20, 2022

responsiveness to external vapors and solid molecules are expected to relate the morphology of the emitting materials. Thus, in the present study, we have investigated emission color changes of BMBZA and BFBZA in response to HCl vapor and solid organic acids, PFBA and BA, in their different solid states.

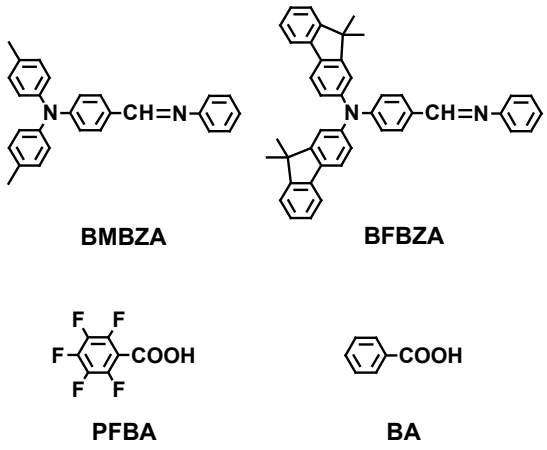

Chart 1. Chemical structures of BMBZA, BFBZA, PFBA, and BA.

2. Experimental

BMBZA and BFBZA were prepared by the procedures reported in our previous papers [13,18]. PFBA and BA were purchased commercially and used without further purification.

Crystalline samples of BMBZA and BFBZA were obtained by recrystallization from ethanol. Fluorescence spectra upon excitation with 400 nm were measured at ambient conditions (less than 50%RH at ca. 25 °C) by means of FP-8300 spectrofluorometer (JASCO Co). Cross-section of HCl-exposed BMBZA crystal was observed by means of ECLIPSE Ni-U optical microscope (Nikon). Object color changes of BMBZA–PFBA were observed by means of SMZ-2T-1 stereomicroscope (Nicon). XRD patterns of BFBZA–HCl system were acquired on a Multi Flex-120NP X-ray diffractometer (Rigaku Co.) with a scan rate of 1 deg min^{-1} upon Cu-K_α (1.542 Å) radiation.

X-Ray crystal structure analyses of BMBZA and BFBZA were performed by means of a Xta LAB Synergy-R, HyPix (Rigaku Co.). Crystallographic data can be obtained free of charge from the Cambridge Crystallographic Data Centre (CCDC 2159130 and CCDC2159131 for BMBZA and BFBZA, respectively). Some important crystallographic data were summarized in Table 1.

Table 1. Crystallographic data of BMBZA and BFBZA.

	BMBZA	BFBZA
Formula	$C_{27}N_{24}N_2$	$C_{43}H_{36}N_2$
Molecular weight	376.5	580.8
Crystal System	monoclinic	monoclinic
Space Group	$P2_1/n$	$P2_1/n$
a / Å	9.6159(3)	10.8848(4)
b / Å	12.1465(3)	8.0238(3)
c / Å	17.5141(5)	35.7936(16)
β / °	94.868(2)	91.062(4)
V / Å^3	2038.26	3125.59
Z	4	4
d_{calc} / g cm^{-3}	1.227	1.234
R / %	4.84	5.04

3. Results and discussion

3.1. Crystal Structures and Glass Formation of BMBZA and BFBZA

Single crystals of BMBZA and BFBZA were obtained by recrystallization from ethanol and their X-ray crystal structure analyses were made. Fig. 1 shows molecular and crystal structures of BMBZA and BFBZA. It was found that the

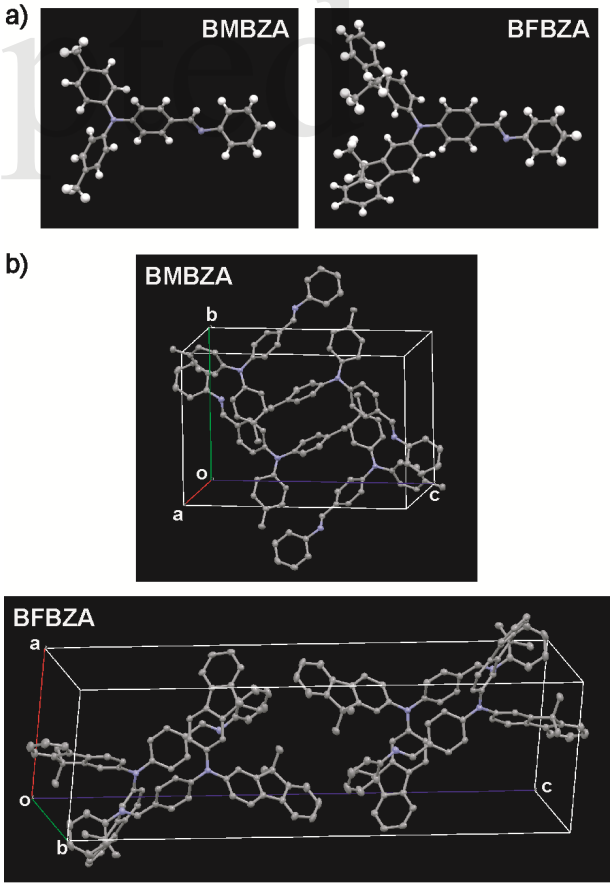

Fig. 1. a) Molecular and b) crystal structures of BMBZA and BFBZA.

triphenylamine moiety took propeller-like structures like other amorphous molecular materials possessing triarylamine moiety [19–23]. No considerably short intermolecular contacts were observed in their crystals.

When recrystallized samples of BMBZA and BFBZA were heated, they melted to give isotropic liquids at 136 °C and 198 °C, respectively. When the melt samples were cooled to room temperature, amorphous glasses were readily formed. Fig. 2 shows DSC curves of glass samples of BMBZA and BFBZA. When the BMBZA glass was heated, glass transition was observed at 25 °C. On further heating, crystallization took place at 82 °C, followed by melting at 136 °C. With regard to BFBZA glass, only glass transition at 107 °C was observed on heating process of the glass sample. The glass-transition temperature of BFBZA was higher than that of BMBZA due to existence of rigid fluorenyl moieties in the molecule.

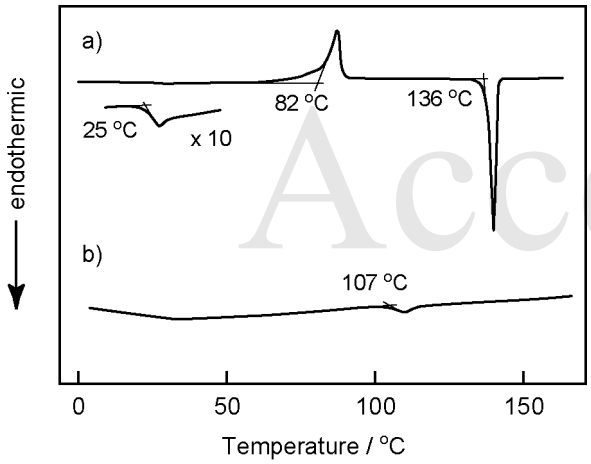

Fig. 2. DSC curves of a) BMBZA and b) BFBZA glasses obtained by cooling their melts.

3.2. Emission color changes of BMBZA and BFBZA crystals in response to HCl vapor.

We have previously reported that both greenish blue emission of amorphous BMBZA film and green emission of BFBZA film turned to reddish orange by exposure to HCl vapor [17,18]. The phenomena were suggested the protonation taking place to produce BMBZA-H$^+$ and BFBZA-H$^+$ (Chart 2) that emitted in considerably longer wavelength region than BMBZA and BFBZA. Here, emission color changes of BMBZA and BFBZA in crystalline state in response to HCl vapor were investigated.

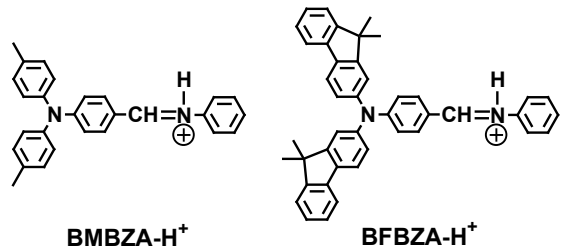

Chart 2. Chemical structures of protonated species, BMBZA-H$^+$ and BFBZA-H$^+$.

BMBZA crystal obtained by recrystallization exhibit greenish blue emission under UV lamp (365 nm). When the crystal was exposed to HCl vapor, the emission color was found to change to reddish orange. As shown in Fig. 3, emission band was shifted to longer wavelength by exposure to HCl vapor. Such spectrum shift seemed to be similar to that observed for BMBZA amorphous film [17]. Thus, the protonation to BMBZA was also suggested to take place on the crystal.

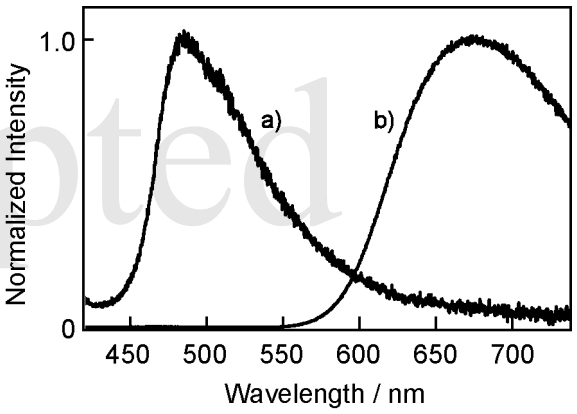

Fig. 3. Emission spectral change of BMBZA crystal a) before and b) after exposure to HCl vapor. λ_{ex}: 400 nm.

Fig. 4a shows optical microscope image of the cross section of the HCl-exposed BMBZA crystal. It was found that the object color near the surface of the crystal changed to orange due to production of BMBZA-H$^+$ while the interior of the crystal remained original green. In addition, the orange-emitting area seemed to be dark in polarized microscopy as shown in Fig. 4b, indicating that the surface area of the crystal changed to amorphous state. The results suggested that protonation to BMBZA molecules took place near the surface of the crystals upon exposure to HCl vapor, causing the area to become amorphous, and then protons penetrate into the interior of the crystal through the

amorphous region.

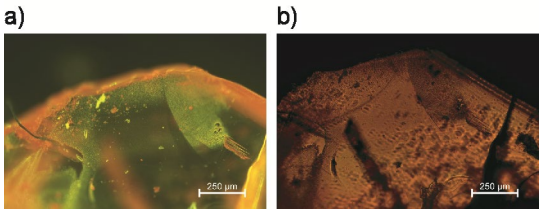

Fig. 4. a) Optical and b) polarized microphotographs of the cross section of HCl-exposed BMBZA crystal.

BFBZA crystal obtained by recrystallization also exhibited greenish blue emission under UV lamp. In contrast to BMBZA, no emission color change of BFBZA crystal was observed upon exposure to HCl vapor. However, the powder sample obtained by grinding the BFBZA crystals with a pestle in a mortar was found to exhibit emission color change to orange by exposure to HCl vapor. Fig. 5 shows emission spectral changes of BFBZA crystal. Pristine crystal showed emission spectrum with λ_{max} of 488 nm (Fig. 5a). No spectral change was observed upon exposure to HCl vapor. When the pristine crystal was ground, the resulting powder showed the somewhat broader emission band than the pristine crystal in the similar wavelength region (Fig. 5b). When the ground powder was exposed to HCl vapor, new broad emission band around 700 nm appeared. Thus, the responsiveness of BFBZA to HCl vapor was triggered by grinding.

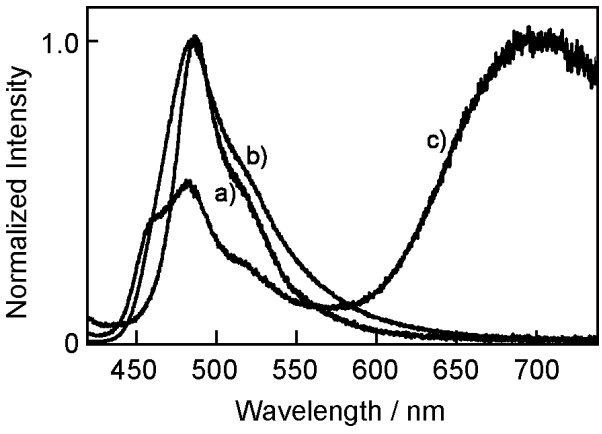

Fig. 5. Emission spectral change of BFBZA. a) Pristine crystal, b) Powder obtained by grinding the crystal, c) HCl-exposed powder sample. λ_{ex}: 400 nm.

To gain further information, X-ray diffraction (XRD) of BFBZA was performed. Pristine crystal of BFBZA shows XRD patterns with sharp diffraction peaks (Fig. 6a). Upon exposure to HCl vapor to the sample, no change in XRD pattern was observed. When the pristine crystal was ground, diffraction peaks seemed to become broader (Fig. 6b), suggesting that a part of sample turned to amorphous state by grinding. When the ground sample exposed to HCl vapor, no significant change of XRD pattern was observed (Fig. 6c). The results of emission spectra and XRD patterns suggested that protonation of BFBZA by HCl vapor could not take place in crystalline state but in amorphous state. Grinding the crystal triggered the responsiveness to HCl vapor due to formation of amorphous state. Incomplete amorphous formation by grinding might cause the remaining the emission band in the range from 450 to 550 nm in the emission spectrum of HCl-exposed ground powder sample (Fig. 5c).

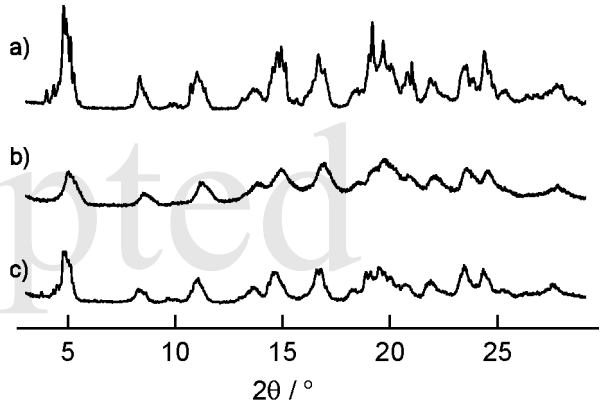

Fig. 6. XRD patterns of BFBZA. a) Pristine crystal, b) Powder obtained by grinding the crystal, c) HCl-exposed powder sample.

3.3. Emission color changes of BMBZA and BFBZA crystals in response to crystals of organic acids.

We have reported that hybrid amorphous films of BMBZA and BFBZA together with pentafluorobenzoic acid (PFBA) and benzoic acid (BA) exhibited emission color changes in response to moisture [17,18]. In case of BMBZA–PFBA and BFBZA–PFBA films, their electronic absorption spectra indicated the production of protonated species, BMBZA-H^+ and BFBZA-H^+, and then the films exhibited orange emission. BMBZA–BA and BFBZA–BA films also exhibited orange emission; however, their electronic absorption spectra were found to be almost similar

to those of single BMBZA and BFBZA films without protonated species. It was concluded that acidity levels of organic acids were the important factor for providing protonated species and that orange emissions of BMBZA–BA and BFBZA–BA films took place through excited-state intermolecular proton transfer (ESPT). As well as exposure to HCl vapor described above, protonation ability and emission color changes were expected to depend upon the morphology of the emitting materials. Then, emission color changes of BMBZA and BFBZA in crystalline state in response to PFBA and BA crystals were investigated.

It was found that the crystalline mixture of BMBZA and PFBA with a molar ratio of 1:1 obtained by shaking by hand in a sample tube exhibited orange emission. The emission spectrum as shown in Fig. 7a was almost similar to that of HCl-exposed BMBZA crystal (Fig. 3b). The result suggested that the contact of BMBZA and PFBA crystals produced BMBZA-H^+. On the other hand, the crystalline mixture of BFBZA and PFBA with a molar ratio of 1:1 obtained by shaking by hand in a sample tube exhibited green emission (Fig. 7b), suggesting that protonation did not take place. When the mixture was ground with a pestle in a mortar, however, the emission color changed to orange and the broad emission band around 700 nm appeared in the spectrum (Fig. 7c).

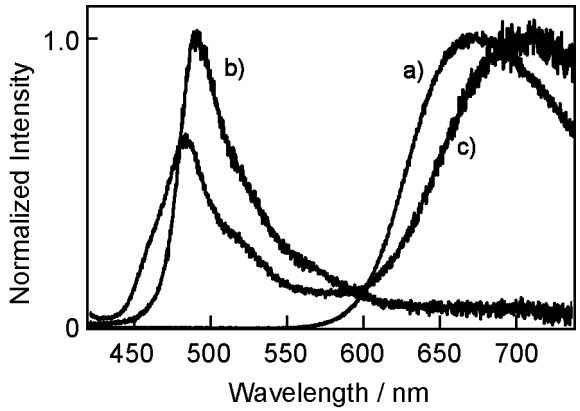

Fig. 7. Emission spectra of mixed solid samples. a) crystalline mixture of BMBZA and PFBA, b) crystalline mixture of BFBZA and PFBA, c) ground sample of the mixture of BFBZA and PFBA. λ_{ex}: 400 nm.

To gain further information, color change of an BMBZA crystal with a smaller crystal of PFBA on top was examined by means of stereomicroscope. As shown in Fig. 8, reddish orange area gradually extended from the position of contact with the PFBA crystal. The result suggested that the proton diffused from the PFBA crystal to the BMBZA crystal probably with amorphous formation. Such color change could not be observed for the BFBZA crystal with the crystal of PFBA on top.

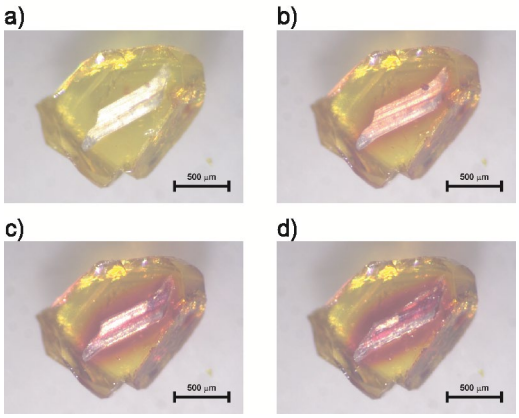

Fig. 8. Color change of an BMBZA crystal with a smaller crystal of PFBA on top. a) 0 min, b) 30 min, c) 180 min, d) 360 min.

Thus, the results of emission color changes of BMBZA and BFBZA crystals in response to PFBA crystal were consistent with those of responsiveness of BMBZA and BFBZA crystals to HCl vapor. These results were explained as follows. Protonated species, BMBZA-H^+ and BFBZA-H^+, were produced just at the area contacted with HCl and PFBA, and proton could migrate in amorphous states together with counter anion. When the BMBZA crystal was contacted with these acids, protonation caused the area to become amorphous, allowing the migration of the proton. On the other hand, protonation by acid could not induce amorphous formation for BFBZA probably due to its relatively high melting and/or glass-transition temperatures. Grinding to assist the amorphous formation allowed the migration of BFBZA-H^+, resulting in emission color change.

We also examined the emitting properties of BMBZA and BFBZA crystals in response to weaker acid, BA. In contrast to PFBA, the crystalline mixture of BMBZA and BA exhibited greenish blue emission with similar emission spectrum of single BMBZA crystal. The result indicated that the protonation did not take place due to lower acidity level of BA. Similarly, protonation did not take place for the crystalline

mixture of BFBZA and BA. When these mixtures were ground, emission colors were found to change to reddish orange with changing in emission spectra (Fig. 9), although the object color of the mixtures did not change by grinding. When BA was used as an organic acid, reddish orange emission is assumed to be produced through ESPT, as discussed above. Although protonation did not take place in the ground state, grinding the mixed samples increased the contact area between BMBZA or BFBZA and BA to allow sufficient ESPT, resulting in emission color change to reddish orange.

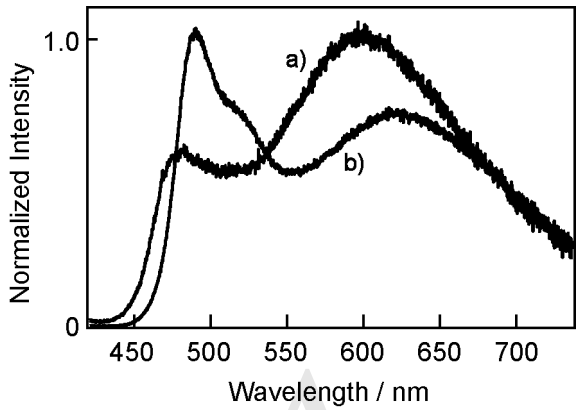

Fig. 9. Emission spectra of ground samples of mixtures. a) BMBZA–BA, b) BFBZA–BA. λ_{ex}: 400 nm.

4. Conclusion

Emitting properties of BMBZA and BFBZA in different solid states in response to HCl, PFBA, and BA have been investigated. Not only acidity level of the acid, but also morphology was suggested to be important factor in the protonation of BMBZA and BFBZA, leading to emission color change. Melting and/or glass-transition temperatures of the materials might play a role in facilitating amorphous formation and associated protonation when the crystalline sample is in contact with the acid.

Acknowledgements

X-Ray crystal structure analyses of BMBZA and BFBZA were performed by Profs. T. Nakamura and K. Kokado at Research Institute for Electronic Science, Hokkaido University. This work was partly supported by JSPS KAKENHI Grant Number JP19K05625.

References

1. U. Mitschkea and P. Bäuerle*, J. Mater. Chem.*, **10** (2000) 1471.
2. K. Matsuda and M. Irie, *Chem. Soc. Rev.*, **34** (2005) 327.
3. M. Irie and M. Morimoto, *Bull. Chem. Soc. Jpn.*, **92** (2018) 237.
4. X. Zhang, B. Li, Z.-H. Chen, and Z.-N. *Chen, J. Mater. Chem.*, **22** (2012) 11427.
5. O. S. Wenger, *Chem. Rev.*, **113** (2013) 3686.
6. E. Li, K. Jie, M. Liu, X. Sheng, W. Zhua, and F. Huang, *Chem. Soc. Rev.*, **49** (2020) 1517.
7. Z. Chi, X. Zhang, B. Xu, X. Zhou, C. Ma, Y. Zhang, S. Liu, and J. Xu, *Chem. Soc. Rev.*, **41** (2012) 3878.
8. Y. Sagara, S. Yamane, M. Mitani, C. Weder, and T. Kato, *Adv. Mater.*, **28** (2016) 1073.
9. K. Mizuguchi, H. Kageyama, and H. Nakano, *Mater. Lett.*, **65** (2011) 2658.
10. K. Mizuguchi and H. Nakano, *Dyes Pigm.*, **96** (2013) 76.
11. K. Okoshi and H. Nakano, *J. Photopolym. Sci. Technol.*, **27** (2014) 535.
12. K. Ogura and H. Nakano, *Kobunshi Ronbunshu*, **72** (2017) 199.
13. S. Manabe, E. Nagata, and H. Nakano, *Rapid Commun. Photosci.*, **3** (2014) 38.
14. R. Ichikawa, E. Nagata, and H. Nakano, *RSC Adv.*, **5** (2015) 2934.
15. Y. Kitamura, R. Ichikawa, and H. Nakano, *Mater. Chem. Front.*, **2** (2018) 90.
16. H. Nakano, T. Nishimura, E. Nagata, R. Ichikawa, *ChemistrySelect*, **1** (2016) 1737.
17. T. Tsukada, Y. Kitamura, and H. Nakano, *Asian J. Org. Chem.*, **10** (2021) 588.
18. T. Tsukada and H. Nakano, *J. Photopolym. Sci. Technol.*, **34** (2021) 525.
19. H. Inada, k. Ohnishi, S. Nomura, A. Higuchi, H. Nakano, and Y. Shirota, *J. Mater. Chem.*, **4** (1994) 171.
20. J. Sakai, H. Kageyama, S. Nomura, H. Nakano, and Y. Shirota, *Mol. Cryst. Liq. Cryst.*, **296** (1997) 445.
21. H. Nakano, E. Ueta, and Y. Shirota, *Mol. Cryst. Liq. Cryst.*, **313** (1998) 214.
22. Y. Shirota, *J. Mater. Chem.*, **10** (2000) 1.
23. H. Nakano, *ChemPhysChem*, **9** (2008) 2174.

Preparation of a polysilane-(1-pyrene)methyl methacrylate copolymer

Yukihitoi Matsuura[1]*, Yuuri Higashide[1], Yuki Takagishi[1], Masanobu Ohkita,[2] and Tomoharu Tachikawa[2]

[1]Department of Chemical Engineering, National Institute of Technology, Nara College
22 Yatacho, Yamato-koriyama, Nara 639-1080, Japan
[2]Frontier Materials Laboratories, Osaka, Gas Chemicals Co., Ltd.
5-11-61, Torishima, Konohana-ku, Osaka 554-0051, Japan
**matsuura@chem.nara-k.ac.jp*

We prepared polysilane–methacrylate copolymers using polysilane as the photoradical initiator. As polymerization is a radical reaction, the chemical structures of the arrangement of the polysilane block and methacrylate have not yet been clarified using various analytical methods. In this study, polysilane–(1-pyrene)methyl methacrylate copolymers were prepared to examine their chemical structure by photoluminescence measurements because the polysilane block and pyrene methacrylate units exhibit fluorescence. The fluorescence analysis revealed the formation of an excimer by the pyrene dimer. From the results, it was found that the pyrene methacrylate units were close to each other.

Keywords: Polysilane, (1-Pyrene)methyl methacrylate, Photopolymerization, Excimer

1. Introduction

Polysilanes are homocatenated silicon polymers, in which Si–Si bonds combine directly along the polymer main chain [1]. The continuous Si–Si bond causes the Si 3p electrons to delocalize in the main chain and express ultraviolet (UV) absorption, luminescence, and electrical conductivity. This property of polysilanes is called σ-conjugation, because it is similar to π-conjugation in unsaturated hydrocarbons [2]. Although their electronic and optical properties are fascinating for application in electronic devices, polysilanes gradually degrade in air because of reacting with O_2 and H_2O. Therefore, the functionalization of polysilanes is being developed; however, it has not yet been implemented.

Modification of polysilanes has been attempted to improve their properties [3, 4]. Our group has functionalized polysilane by adding a methacrylate unit along the polymer main chain and modifying the methacrylate using reactive functional groups [5]. For example, the insertion of an alkoxy or acrylamide allows it to react with metal alkoxides [6]. The products were polysilane–-inorganic hybrids, in which the degradation of polysilane was suppressed because of protection from air. Furthermore, nanoporous metal oxide films were successfully prepared through polysilane removal [7]. We also prepared polysilane–organic hybrid films using polysilane–methacrylate copolymers with isocyanate or allyl groups [8, 9]. As the polysilane–methacrylate copolymers were prepared via a photo-radical reaction, the

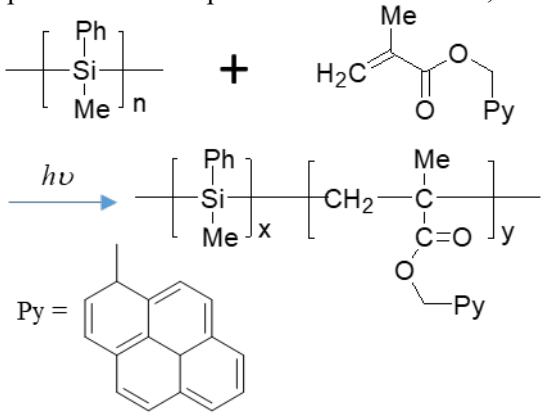

Fig. 1. Photopolymerization of PMPS and pyreneMA.

Received March 23, 2022
Accepted June 19, 2022

arrangement of the polymer units was so random that it was difficult to clarify the local chemical structure of the copolymers. As a result, the obtained copolymers were difficult to apply in nanotechnology by controlling the alignment of polymer chains on the substrate [10].

By the way, pyrene has been known as a chromophore in fundamental and applied photochemical research [11]. In paritcular, pyrene-based polymers have been synthesized because the methacrylate monomer having pyrene can be polymerized easily. Pyrene-based materials also have been remarked because of the fluorescence properties and sensitivity/selecttivity for a secific organic material in a field of organic devices [12-15]. Pyrene can form a dimer that shows excimer luminescence [16-18], and this phenomenon is possibly used to clarify the arrangement of methacrylates in the polysilane-metahcrylate copolymers. Therefore, in this study, we prepared polysilane–(1-pyrene)methyl methacrylate copolymers to examine their polymer structures.

2. Experimental

2.1 Materials

Poly(methylphenylsilane) (PMPS) was used as polysilane. PMPS (OGSOL SI-10-10) was supplied by Osaka Gas Chemicals Co. Ltd. [19]. The crude sample was purified by reprecipitation using hexane. (1-Pyrene)methyl methacrylate (pyreneMA) was purchased from FUJIFILM Wako Pure Chemical Corporation. The photoreaction of methacrylate was carried out using PMPS as a photoradical initiator [20]. A typical photoreaction was carried out using the following procedure: PMPS (0.5 g) and pyreneMA (0.5 g) were dissolved in distilled toluene (5 mL). The charged molar ratio of methylphenylsilane (MPS) unit in PMPS to pyreneMA was varied, as shown in Table 1. Degassing of the mixture was performed using the freeze–thaw method. The toluene solution was sealed in a Pyrex glass tube under N_2. The tube was then irradiated with UV light (SEN LIGHTS CORPORATION, high-pressure Hg lamp, 10 mW cm^{-2}) for 15 min. The reaction mixture was re-precipitated in hexane (300 mL) and filtered through a glass filter (pore size: 20–30 μm). Finally, the residue was dried overnight under vacuum.

Table 1. Characterization of PMPS and the photopolymerized product

Sample	Molar ratio[1)]	Mn	Mw/Mn	x/y[2)]	λ_{max}[3)]
PMPS	-	5.1×10^3	3.1	-	331.4
Product-0	0.60	-	-	-	-
Product-1	1.00	4.4×10^4	4.1	1.5×10^1	328.8
Product-2	1.67	6.1×10^3	3.2	2.5×10^2	328.8

[1)] Charged molar ratio of [MPS]/[pyreneMA].

[2)] Result of [MPS]/[pyreneMA] measured by ^{1}H-NMR.

[3)] Wavelength of UV absorption.

2.2 Measurements

The molecular weight was measured in tetrahydrofurane using a Shodex GPC-101 system. Molecular weight was analyzed using polystyrene standards. The ratio (x/y) of the number of MPS units to the number of pyreneMA units was determined by ^{1}H-NMR spectroscopy using a JEOL JNM-ECX400 spectrometer with deuterated chloroform as the solvent. Spectroscopic measurements were performed on a Shimadzu UV-3600 spectrophotometer. Photoluminescence was measured using a Shimadzu RF-5300 instrument with an excitation wavelength of 280 nm. FT-IR spectra were measured using a Shimadzu IR Affinity-ATR system equipped with a zinc selenide crystal. Raman spectroscopy was performed using a Tokyo Instruments micro-Raman spectroscopy Nanofinder 30 A with a 532 nm green laser. Differential scanning calorimetry (DSC) measurements were performed using a Seiko Instrument DSC-X5400 apparatus at a heating/cooling rate of 10 °C min^{-1} in the temperature range from −30 to 180 °C. Thermogravimetric analysis was carried out using a Seiko Instrument TG/DTA7200 apparatus at a heating/cooling rate of 10 °C min^{-1} in the temperature range from 30 to 550 °C.

3. Results and discussion

The determined molecular weight of the purified PMPS was $M_n = 5.1\times10^3$, as shown in Table 1. UV absorption at 331.4 nm was observed, indicating the existence of σ-conjugation along the polymer main chain.

The photoreaction of PMPS with pyreneMA was performed under the conditions listed in Table 1. Product-1 was obtained at a charged molar ratio of 1.0. GPC analysis showed the molecular

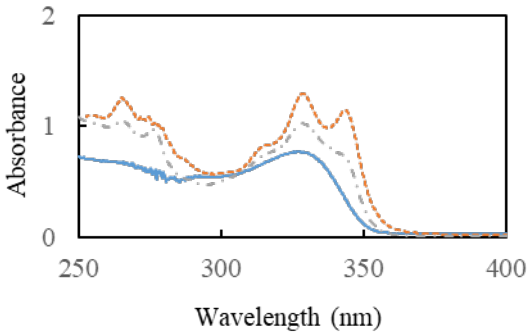

Fig. 2. UV-Vis absorption spectra of PMPS (solid line), Product-1 (dotted line), and Product-2 (hash-dotted line).

weight of M_n = 4.4×10^4 with a monodispersed molecular weight distribution. However, the dispersion of M_w/M_n = 4.1 was so large that a high molecular weight yielded a wide distribution of molecular weight. ^{1}H-NMR analysis showed that Product-1 contained pyreneMA units with a molar ratio of x/y = 1.5×10^1 [21]. Additionally, as shown in Figure 2, Product-1 showed UV absorption at 328.8 nm, which indicated that it contained polysilane blocks with σ-conjugation length shorter than that of PMPS. Furthermore, absorption was observed at 345 nm, which was assigned to pyrene.

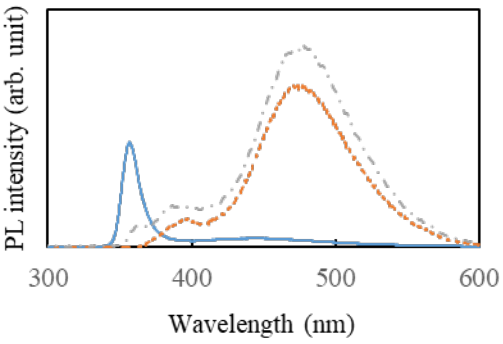

Fig. 3. Photoluminescence spectra of PMPS (solid line), Product-1 (dotted line), and Product-2 (hash-dotted line).

The charged molar ratio was varied to improve the molecular weight dispersion of Product-1. When the molar ratio of pyreneMA was increased, we obtained Product-0, which is a white solid that is insoluble in organic solvents. Conversely, when the ratio of pyreneMA decreased, Product-2 was obtained, as shown in Table 1. The GPC results indicated that the molecular weight was Mn = 6.1×10^3 with a dispersion of M_w/M_n = 3.2. Additionally, Product-2 showed UV absorption at the same wavelength as Product-1 (328.8 nm). This result indicates that Product-2 had almost the same σ-conjugation length of the polysilane block as Product-1. Therefore, photopolymerization resulted in approximately the same length of the polysilane block. Furthermore, the absorption at 345 nm assigned to pyrene decreased in comparison with that of Product-1, which also suggests a decrease in the pyreneMA content in Product-2.

Subsequently, the photoluminescence of the polysilane block and pyreneMA units was analyzed to determine their chemical structures. As shown in Figure 3, PMPS exhibited a fluorescence peak at 360 nm. Product-1 exhibited a large fluorescence peak at 485 nm, which was caused by the excimer of the pyrene dimer. In addition, there was a small fluorescence peak at 400 nm owing to the pyrene monomer. Product-1 showed no luminescence assigned to the polysilane block at 360 nm. The reason for this was unclear, but it was assumed that there was a small content of polysilane domain that emitted fluorescence strongly owing to the polymer chain orientation. Product-2 showed the same tendency in fluorescence spectrum as the pyrene dimer and pyrene monomer. In addition, the fluorescence at 360 nm was assigned to the polysilane block. The fluorescence of Product-2 at 360 nm reflected the relative content of the polysilane block. Furthermore, Product-2, which had a small content of pyreneMA units, exhibited strong fluorescence of the pyrene excimer. This result suggests that the pyreneMA units were close to each other and formed a continuous pyreneMA block.

As shown in Figure 4, the polymer structures of PMPS and its products were analyzed using DSC measurements. The PMPS exhibited a transition at 150 °C, which was assigned to the glass transition of the polysilane block. Although Product-1 had a transition at 150 °C, which was a little unclear, Product-1 and Product-2 also showed a glass transition of the polysilane block. Therefore, it was also confirmed that the products contained the polysilane block even after photopolymerization, similar to the results of UV-Vis absorption spectroscopy.

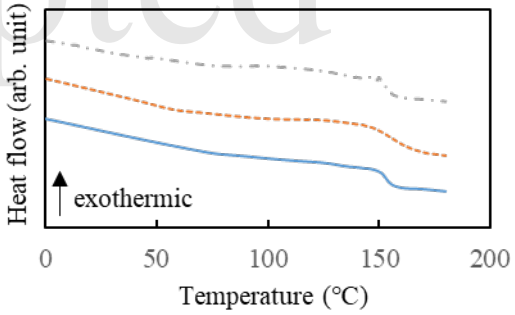

Fig. 4. DSC curves of PMPS (solid line), Product-1 (dotted line), and Product-2 (hash-dotted line). The curves were measured under an increase in temperature.

Finally, thermogravimetric analysis of PMPS and products was performed to examine the organic content, as shown in Figure 5. PMPS showed a rapid decrease in weight at approximately 400 °C to saturate the content to 35.0 %. Because the silicon content in PMPS was calculated to be 23.3 %, it was assumed that the residue contained carbon and formed a siliconcarbide-like compound. At the same time, the weight of Product-1 began to decrease at about 200 °C, and at 400 °C the weight loss rate rapidly increased. This was attributed to the presence of the pyreneMA block. The weight loss

of Product-2 began at approximately 330 °C and then showed the same tendency as that of Product-1. Furthermore, the weight loss of Product-1 was smaller than that of Product-2, which agreed with the results of ^{1}H-NMR analysis. As a result, it was found that organic content decreased the thermal resistivity of Product-1 and Product-2.

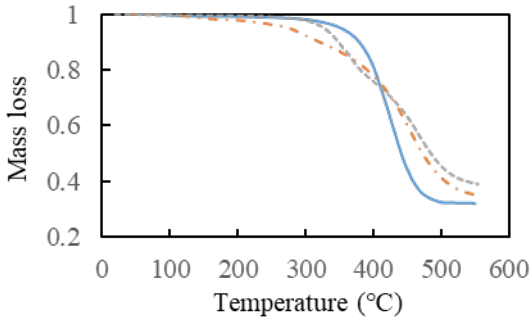

Fig. 5. TG plots of PMPS (solid line), Product-1 (dotted line), and Product-2 (hash-dotted line). The curves were measured under an increase in temperature.

We also analyzed the polymer structures using FT-IR and Raman spectroscopy. However, we did not find any new functional group peaks or peak shifts owing to a change in the electronic structure of the products.

4. Conclusion

Polysilane–pyrene methacrylate copolymers were successfully prepared using polysilane as the photoradical initiator. The copolymers exhibited fluorescence owing to the excimer of the pyrene dimer. This suggests that the pyrene methacrylate units were close to each other. The results obtained provide valuable insight into the photopolymerization mechanism with polysilane as a photopolymerization initiator. Furthermore, using these results, we can challenge the arrangement of polysilane–methacrylate copolymers on substrates in the field of nanotechnology in the future.

Acknowledgement

This work was supported by JSPS KAKENHI Grant Number 19K05638.

References

1. R. D. Miller and J. Michl, *Chem. Rev.*, **89** (1989) 1359.
2. K. Takeda, H. Teramae, and N. Matsumoto, *J. Am. Chem. Soc.*, **108** (1986) 8186.
3. T. Sanji, K. Takase, and H. Sakurai, J. Am. Chem. Soc., 123 (2001) 12690.
4. K. Furukawa, K. Ebata, H. Nakashima, Y. Kashimura, and K. Torimitsu, *Macromolecules*, 36 (2003) 9.
5. Y. Matsuura, K. Matsukawa, and H. Inoue, *Chem. Lett*, 30 (2001) 244.
6. Y. Matsuura, H. Inoue, K. Mastukawa, Macromol. Rapid Commun., 25 (2004) 623.
7. Y. Matsuura, S. Miura, H. Naito, H. Inoue, K. Matsukawa, *J. Organomet. Chem.*, 685 (2003) 230.
8. Y. Matsuura, T. Sakatani, Y. Kado, Y. Takahashi, Y. Muramoto, S. Fukunishi, S. Minami, *Euro. Polym. J.*, 108 (2018) 219.
9. F. Kato, Y. Matsuura, M. Ohikita, T. Tachikawa, *J. Photopolym. Sci. Tech.*, 34 (2021) 255.
10. K. Matsukawa,Y. Matsuura, *Mater. Res. Soc. Symp. Proc.*, 847 (2005) EE10.1.1.
11. F. M. Winnik, *Chem. Rev.*, 93 (1993) 587.
12. J. Kim, M. Choi, K. Song, K. No, S. Ahn, S. Chang, *Org. Lett.*, 9 (2007) 1129.
13. J. Kollár, P. Hrdlovič, Š. Chmela, *J. Photochem. Photobio.* A, 214 (2010) 33.
14. T. M. Figueira-Duarte, K. Müllen, Chem. Rev., 111 (2011) 7260.
15. X. Zhang, Z. Gou, Y. Zuo, W. Lin, *J. Photochem. Photobio.* A, 410 (2021) 113183.
16. T. Füorster, K. Z. Kasper, *Elektrochem*., 59 (1955) 976.
17. J. B. Birks, *Photophysics of Aromatic Molecules*, Wiley-Interscience: London, 1970.
18. K. Kalyanasundaram, J. K. Thomas, *J. Am. Chem. Soc.*, 99 (1977) 2039.
19. H. Murase, M. Sugimoto, H. Nishimura, and K. Yamada, *Mater. Sci. Appl.*, 6 (2015)576.
20. Y. Matsuura, K. Matsukawa, R. Kawabata, N. Higashi, M. Niwa, H. Inoue, *Polymer*, 43 (2002) 1549.
21. Results of photoreaction of PMPS and pyreneMA as follows: ^{1}H-NMR ($CDCl_3$, 400 MHz, δ) –1.0–0.7 (-SiMe 3H), 0.9–1.2 (-C(Me)-$\underline{CH_2}$ 2H), 1.8–2.1 (-C-$\underline{Me}$ in methacrylate 3H), 5.0-5.2 (-$\underline{CH_2}$-Py 2H), 6.5–7.8 (-Si-$\underline{Ph}$ 5H), 8.0-8.3 (pyrene, 9H).

Surface Cleaning and Modification of Oxide Films by Atomic Hydrogen Annealing

Akira Heya[1*], Koji Sumitomo[1]

[1] *Department of Materials and Synchrotron Radiation Engineering, University of Hyogo, 2167 Shosha, Himeji, Hyogo 671-2280, Japan*
**heya@eng.u-hyogo.ac.jp*

To suppress degradation of the electrical property of field-effect transistors, the removal of C contamination without damaging oxide films is important in the semiconductor industry. In addition, to reduce bonding failure, it is necessary to remove native oxide films from metal films. To achieve this, atomic hydrogen was generated by the decomposition of H_2 gas on a heated tungsten mesh. This surface treatment is referred to as atomic hydrogen annealing (AHA). The reaction of atomic hydrogen with various oxide films, such as AlO_x, TiO_x, CrO_x, NiO_x, CuO_x, and SiO_x, was investigated. The O concentrations in Al, Ti, and Cr slightly decreased by AHA. The thermal oxide films prepared at 400 °C were not changed by AHA, except for CuO_x. The reduction in the reactivity of the oxide film due to atomic hydrogen depends on the metal–oxygen bond strength. In addition, although the thermal oxide film of the Si substrate prepared at 1000 °C was not etched, AHA resulted in the etching of the Si-rich SiO_x. These findings are useful for the removal of C contamination and native oxide films and for controlling the surface properties of oxide films.

Keywords: Atomic hydrogen annealing, Surface cleaning, Modification, Oxide film, Native oxide, Metal

1. Introduction

Surface cleaning, which is the removal of C contamination and native oxides on the metal surface, is important. In the semiconductor industry, C contamination and native oxide films occur due to air exposure immediately before film formation and wire bonding. These films degrade the electrical property and interface properties, and weaken joint strength. In general, alkali solutions are used for the removal of processing and rust-preventing oils, whereas acid solutions are used for the removal of native oxide films from the metal surfaces. However, these solutions are often not suitable for use on fragile surfaces such as semiconductor devices.

Various metal oxides are removed by atomic hydrogen (hydrogen radicals) [1]. We have previously investigated the surface treatment method using atomic hydrogen, named atomic hydrogen annealing (AHA) [2-11]. In AHA, the hydrogen molecules are decomposed by the catalytic cracking reaction on a heated W mesh placed near the sample. The atomic hydrogens arrive at the sample surface, and chemical reactions such as hydrogenation and reduction (native oxide removal) take place. In addition, the sample surface is locally heated via a recombination reaction. Compared with other surface treatment methods, AHA can easily treat large areas by increasing the area over which the catalyst (W-mesh) is placed. This technique can be applied to nanographene synthesis on Cu catalyst films [2], low-temperature crystallization of a-Si [3], dry etching of single crystalline Si (c-Si) [12], vacuum chamber cleaning, and removal of photoresist residue after ashing [13-16]. The outcomes can be extended to surface modification and controlling surface properties of plastic substrates containing C and O [4,6,17].

In the semiconductor industry, native oxides on Cu wiring interfere with bonding; as a result, they are often removed by atomic hydrogen treatment [18,19]. Although the cleaning of C contamination and native oxide on metal surfaces is important, the key factor for the easy removal of the native oxide for various metals is unclear. In this study, various

Received March 30, 2022
Accepted May 20, 2022

metal films with native and thermal oxide films and Si-rich SiO_x films were subjected to AHA to clarify the reaction between metal oxides and atomic hydrogen. Here, the reduction was discussed based on the metal–oxygen bond strength.

2. Experimental

First, a Ni/Cr/c-Si substrate was used to evaluate the cleaning of the C contamination and native oxide film. Ni and Cr films were deposited via electron beam (EB) evaporation. Second, various metal films, such as Al, Cr, Cu, Ni, and Ti were prepared. The Al and Cu films were deposited on quartz substrates by vacuum evaporation, and the Cr and Ni films were deposited on quartz substrates by EB evaporation. A Ti film was prepared on a c-Si substrate by DC magnetron sputtering using a Ti target (purity 99.5%). The applied power and Ar pressure were 40 W and 0.5 Pa, respectively. The deposition rate of the Ti film was 0.083 nm s^{-1} and the film thickness was approximately 20 nm. The native oxide film was prepared by exposing the surface to air. Thick oxide films were fabricated by the thermal oxidation of the metal film at 400 °C for 600 s in air. Third, SiO_2 and Si-rich SiO_x films were used to clarify the influence of chemical composition on the reduction of SiO_x. A SiO_2 film was generated on a c-Si substrate by thermal oxidation at 1000 °C for 1800 s in a mixture of O_2 and H_2O moisture. The Si-rich SiO_x film was prepared by DC magnetron sputtering using a SiO_x target made by sintering powders of Si and SiO (21 mass% SiO powder). The applied power and Ar pressure were 15 W and 0.3 Pa, respectively. The deposition rate of the Si-rich SiO_x film is 0.067 nm s^{-1}. The thickness of the films was 100 nm.

A schematic illustration of the AHA apparatus and an optical image of the inside of the vacuum chamber are shown in Fig. 1(a) and (b), respectively. To generate atomic hydrogens, a 55×55 mm^2 W-mesh with a wire diameter of 0.03 mm and 50 holes/inch was typically heated to 1700 °C in a H_2 atmosphere by electrical heating using an alternating current power supply. In this case, the applied voltage and current of W-mesh was 14.0 V and 28.8 A, respectively. The flow rate of H_2 and gas pressure were 150 sccm and 30 Pa, respectively. The distance between the W-mesh and sample was 80 mm and the AHA treatment time was 3600 s. The saturated temperature of the c-Si substrate was measured to be 170 °C using a K-type thermocouple attached to the c-Si substrate.

The surface roughness of the Ni/Cr/Si substrates with and without AHA was measured using a tapping-mode atomic force microscope (AFM, Veeco, Dimension 3100). For AFM observation, a Si cantilever was used and the resonant frequency during the measurement was 320 kHz. The surface properties were evaluated using X-ray photoelectron spectroscopy (XPS, ULVAC-PHI, PHI 5000 VersaProbe). For XPS, an energy step of 0.2 or 0.5 eV, pass energy of 117.4 and 23.5 eV, dwell time of 20 and 100 ms were applied for wide and narrow scan spectra, respectively. For XPS measurements, a neutralizer gun was used to suppress the charge. To evaluate the effect of AHA on the interior of the oxide films, the sample surface

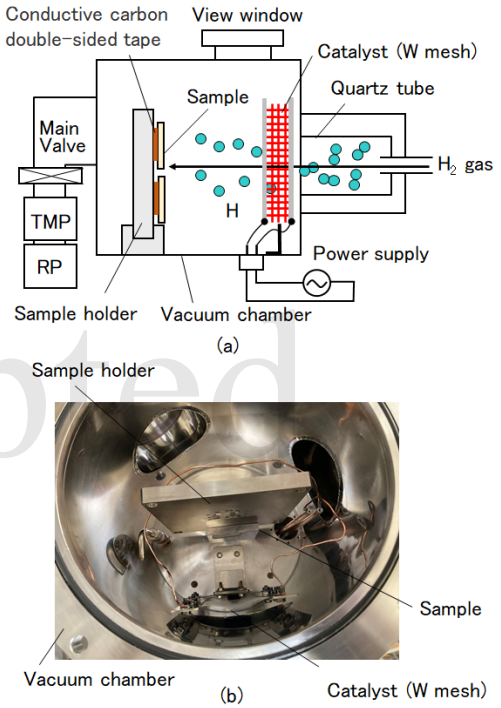

Fig. 1. (a) Schematic diagram of the AHA apparatus. (b) Optical image of inside of vacuum chamber.

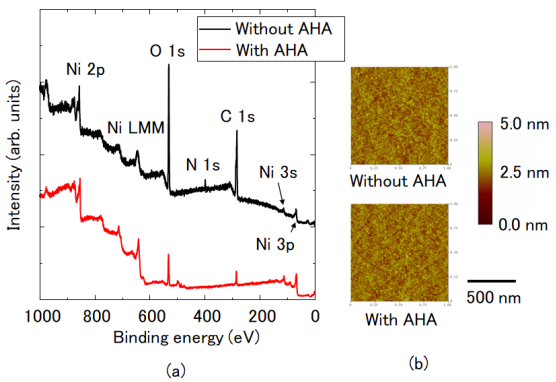

Fig. 2. XPS wide scan spectra (a) and AFM images (b) of the Ni/Cr/Si substrate with and without AHA.

was sputtered with Ar^+ during XPS measurements. For Ar^+ sputtering, the acceleration voltages were 1 kV and 2 kV.

3. Results and discussion

3.1 Surface cleaning of Ni film covered with C contamination and native oxide

The surface cleaning of Ni film was investigated by collecting XPS wide scan spectra and AFM images of the Ni/Cr/c-Si substrates with and without AHA, as shown in Fig. 2(a) and (b), respectively. In general, the metal surface is covered by native oxides and C (hydrocarbon, C_xH_y) contaminants. The C 1s peak at 284.6 eV was decreased by AHA. The mean surface roughness (average of root-mean-square roughness) of the Ni surface in AFM images were 0.32 and 0.33 nm before and after AHA. Therefore, surface cleaning without any surface damage was realized as the roughness was almost the same before and after addition of AHA.

The Ni 2p, O 1s, and C 1s spectra for various Ar^+ sputtering times (t_s) are shown in Fig. 3. The Ni 2p peak comprises metal Ni (852.6 eV), NiO (854.5 eV), Ni_2O_3 (855.8 eV), and $Ni(OH)_2$ (856.6 eV) [20]. The O 1s peak comprises NiO (529.9 eV), Ni_2O_3 (531.9 eV), $Ni(OH)_2$ (531.9 eV), and adsorbed O or H_2O (532.5 eV) [20]. A Ni-O peak was observed in the spectrum without AHA. The Ni-O peak remained even at t_s = 18 s. Conversely, the top surface of the Ni film (t_s = 0 s) with AHA had no NiO_x peak in the Ni 2p spectrum. Thus, the removal of C contamination and native oxides on the Ni film was confirmed. The reflectance of the Ni mirror at approximately 280 and 540 eV, corresponding to C and O, was improved by the removal of C contamination and native oxide after AHA [11].

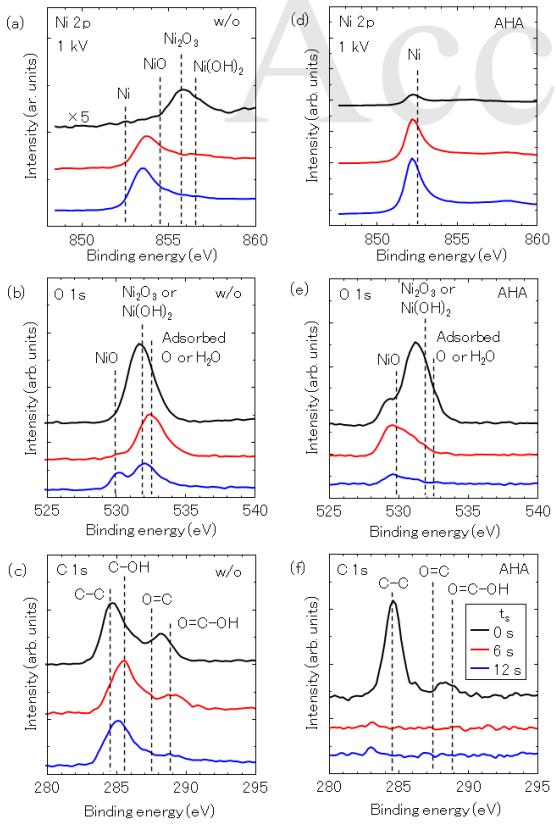

Fig. 3. Ni 2p, O 1s, and C 1s spectra of the Ni/Cr/c-Si substrate with and without AHA at various Ar^+ sputter time. (a)-(c) without AHA. (d)-(f) with AHA.

3.2. Surface modification of AlO_x film by AHA

The XPS depth profiles of the native oxide and thermal oxide Al films, with and without AHA, are shown in Fig. 4. In the native Al oxide, the C concentration decreased from 34 to 7 at.% and the area ratio of O to Al (O/Al) on the top surface decreased from 2.1 to 1.8 on addition of AHA. Conversely, in the thermal Al oxide, the C and O concentrations and O/Al ratios were not changed by AHA. This indicated that the thermal oxide was stronger than the native oxide in the Al film.

3.3. Surface modification of TiO_x by AHA

The depth profiles of the native and thermal oxide films of Ti are shown in Fig. 5. The thickness of the native oxide layer was estimated to be approximately 10 nm. In general, the native oxide on the Ti film was 10 nm thick, which is thicker than the other metals [21]. Native oxide films comprise TiO_2, Ti_2O_3, and TiO layers, in this order, from the surface [22]. In the native oxide of Ti, the thickness was slightly decreased by AHA. The area ratio of O to Ti (O/Ti) gradually decreased from the sample surface to the inside of the film. In contrast, in the thermal oxide, half of the Ti film was oxidized, and the total film thickness increased from 25 to 40 nm. The O and Ti depth profiles were not changed by the

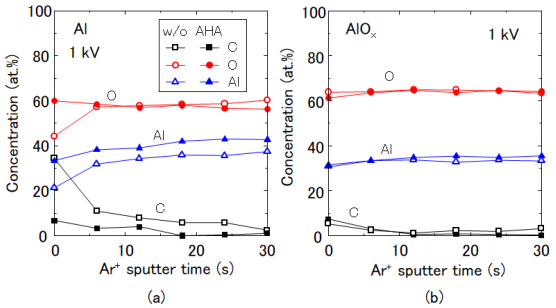

Fig. 4. Depth profiles of the native (a) and thermal oxide films (b) of Al with and without AHA.

AHA.

The change in the O/Ti ratios due to AHA is shown in Fig. 6. As the depth increased to 15 nm, the O/Ti ratio of the native oxide decreased gradually and that of the thermal oxide remain constant. The native oxide was changed by the AHA but the surface of the thermal oxide did not change. However, the thermal oxide at the interface between Ti and the c-Si substrate was changed. It was shown that the ratio changes as the composition deviates from the stoichiometric composition.

The O 1s spectra of the native oxide at a depth of 7.5 nm with and without AHA, are shown in Fig. 7. In the O 1s spectra of TiO_2, the Ti-O, Ti-OH, and O; the chemisorbed or adsorbed H_2O peaks were positioned at 530.0, 531.5, and 533 eV, respectively [23]. The area ratio of Ti-OH was increased from 38 to 56% by AHA.

In the case of plasma treatment, TiO_x is reduced by atomic hydrogen [24]. From the plasma reduction, the reaction of atomic hydrogen with the native Ti oxide is considered as follows:

$TiO_2 + 2H \rightarrow TiOH + H_2O$ (1)

$Ti_2O_3 + 4H \rightarrow Ti_2(OH)_2 + H_2O$ (2)

$TiO + H \rightarrow TiOH$ (3)

In AHA, it is considered that the Ti-O bond is transformed to Ti-OH bonds as shown in Fig. 7 was realized by these reactions.

3.4. Surface modification of CrO_x film by AHA

The XPS depth profiles of the native and thermal oxide films of Cr, with and without AHA, are shown in Fig. 8. In both the native and thermal oxide films, the C concentration was decreased by the AHA. The O/Cr of the native oxide and the thermal oxide films were decreased from 2.0 to 1.8 and from 2.2 to 2.1, respectively. This indicated that the thermal oxide was stronger than the native oxide for Cr, similar to AlO_x.

3.5. Surface modification of NiO_x film by AHA

The XPS depth profiles of the native and thermal oxide films of Ni, with and without AHA, are shown in Fig. 9. The C and O concentrations of the native oxide film of Ni were decreased by the AHA. The C concentration before AHA decreased by thermal oxidation. The C contamination and native oxide on the Ni surface were removed by AHA at t_s = 30 s. In the case of the thermal oxide, the C concentration was not decreased by AHA. This implies that C contamination changed to NiC_x because of the reaction with the Ni film. The O/Ni ratio in the native oxidized film decreased from 14.4 to 0.8 by AHA. The high O concentration before AHA may be attributed to contamination consisting of O-containing hydrocarbons on the Ni film. The O/Ni value in the XPS spectrum at t_s = 6 s, which is considered to remove the contamination, was 1.8. However, the O/Ni ratio of the thermal oxidized

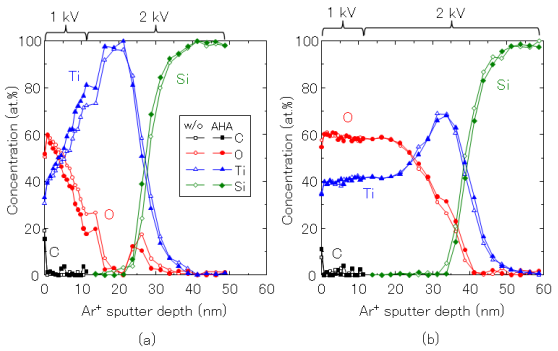

Fig. 5 Depth profiles of native oxide (a) and thermal Ti oxide (b) of Ti/Si substrate.

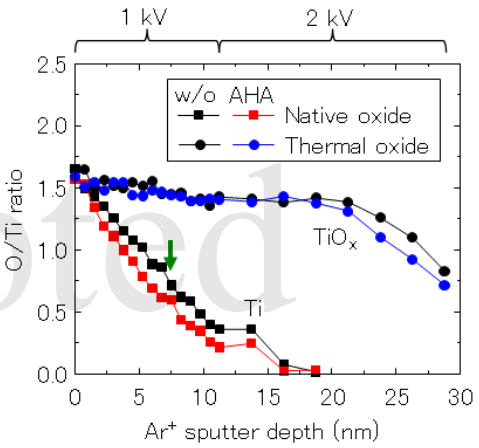

Fig. 6. O/Ti ratio of the native and thermal oxide of Ti as a function of Ar^+ sputter depth. Green arrow indicates the position for curve fitting of O 1s spectra shown in Fig. 7.

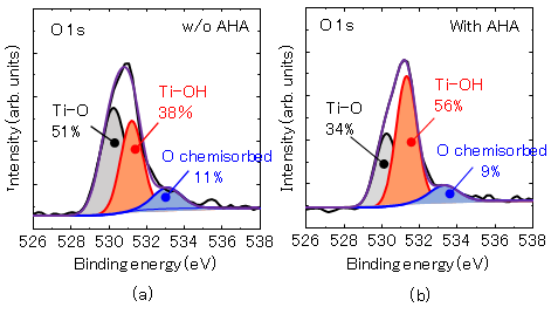

Fig. 7. Curve fitting of O 1s peak at a depth of 7.5 nm of native oxide film of Ti with and without AHA. The peak area ratios of Ti-O, Ti-OH, and O indicates chemisorbed or adsorbed H_2O on native oxide films with and without AHA at depth of 7.5 nm.

film with and without AHA did not significantly change between 2.3 and 2.2.

3.6. Surface modification of CuO_x by AHA

In the XPS profile, the Cu and Cu_2O peaks of Cu 2p were not distinguished. The Cu LMM spectra of Cu film/quartz substrates with and without AHA are shown in Fig. 10. The spectrum after Ar^+ sputtering is shown in Fig. 10 as a reference of the cleaned Cu surface. For the Cu LMM spectra, the Cu, CuO, and Cu_2O peaks have been reported to be positioned at 568.0, 568.8, and 569.9 eV, respectively [25], so dotted lines are also shown for each binding energy in Fig. 10. The Cu surface cleaned by Ar^+ sputtering showed a peak corresponding to Cu. CuO and Cu_2O were observed in the spectra of native Cu oxide without AHA. The peak due to Cu increased after AHA. This indicated that CuO_x was reduced by AHA. Although the Cu_2O and CuO peaks remained after AHA, the Cu surface was oxidized by air exposure before the XPS measurements.

The O depth profiles of the Cu film/quartz substrates with and without AHA are shown in Fig. 11. The native oxide of the Cu film was removed by AHA at t_s = 12 s. In the thermal oxide film of Cu, the O concentration decreased, and the thermal oxide film was removed by AHA at t_s = 60 s. It was observed that CuO_x is weak toward atomic hydrogen in contrast with AlO_x, TiO_x, CrO_x, and NiO_x in the case of thermal oxide.

3.7. Surface modification of SiO_2 and Si-rich SiO_x by AHA

The Si 2p and O 1s XPS spectra of the SiO_2 film on the c-Si substrate with and without AHA are shown in Fig. 12. In this case, AHA was carried out at T_{mesh} values of 1500 and 1800 °C. The Si-O (Si^{4+}) peak was observed at 103 eV and was not changed by AHA. Thus, the thermally oxidized Si (SiO_2) film was not reduced by AHA under present conditions.

To investigate the influence of the chemical composition on the reaction of Si-O with atomic hydrogen, Si-rich SiO_x (x=0.25) was used. The Si 2p XPS spectra of the Si-rich SiO_x film on the c-Si substrate, with and without AHA, are shown in Fig. 13. The Si 2p peaks due to Si-Si and Si-O were observed at 99.4 and 103.2 eV before AHA. However, the Si-O peak disappeared after AHA. The Si-O bond on the Si-rich SiO_x surface was reduced by AHA. The peaks due to the suboxide of Si^+, Si^{2+}, and Si^{3+} remained after AHA. The peak of the Si-Si bond was shifted to a higher binding

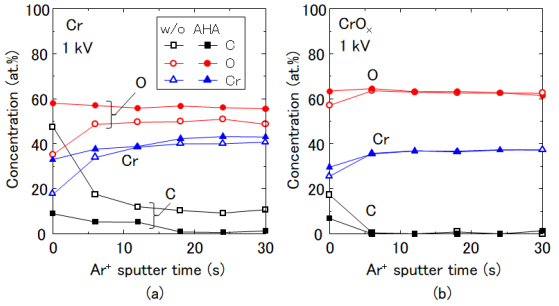

Fig. 8. XPS depth profiles of native (a) and thermal oxide Cr films (b) with and without AHA.

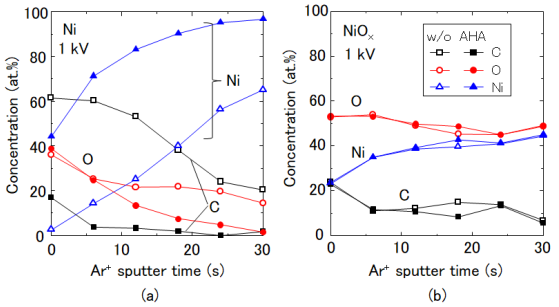

Fig. 9. XPS depth profiles of native (a) and thermal oxide Ni films (b) with and without AHA.

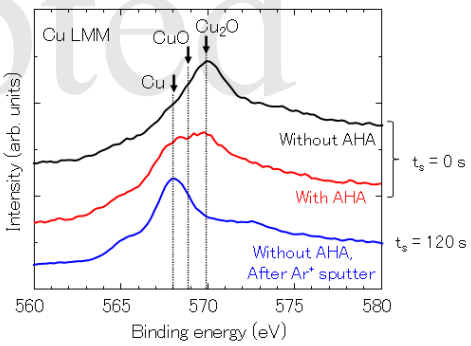

Fig. 10. Cu LMM XPS spectra of Cu film with and without AHA at t_s of 0s, and after Ar^+ sputtering at t_s of 120 s.

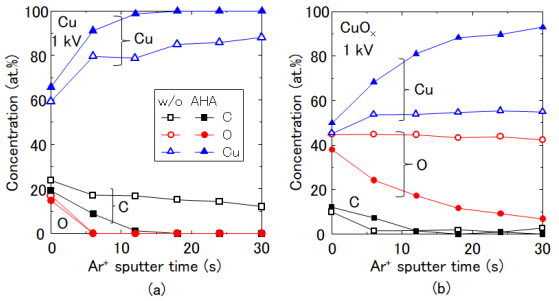

Fig. 11. XPS depth profiles of native (a) and thermal oxide Cu films (b) with and without AHA.

energy by AHA. This shift occurred because of the removal of negative charges on the sample surface.

The depth profiles of the O/Si ratio for the Si-rich SiO_x films with and without AHA are shown in Fig. 14. The interface between the Si-rich SiO_x film and Si wafer is indicated by dotted lines. The thickness of the SiO_x film decreased from 100 to 38 nm by AHA, and the etching rate due to AHA was

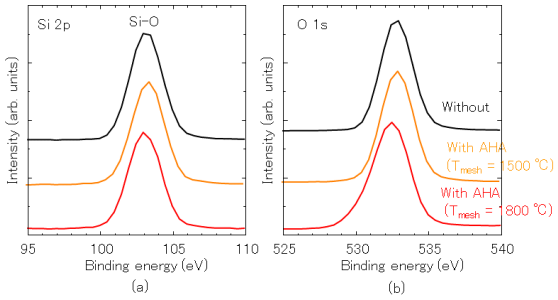

Fig. 12. Si 2p (a) and O 1s (b) spectra of the SiO_2 film on Si substrate with and without AHA. The values of T_{mesh} were 1500 and 1800 °C.

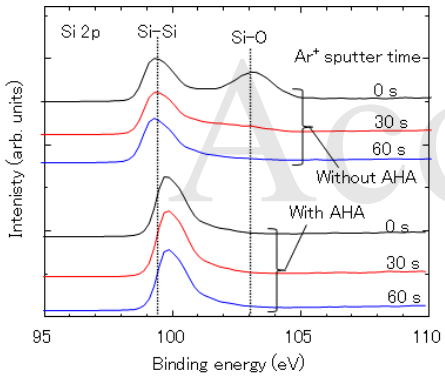

Fig. 13. Si 2p spectra of Si-rich SiO_x film with and without AHA. The T_{mesh} was 1700 °C.

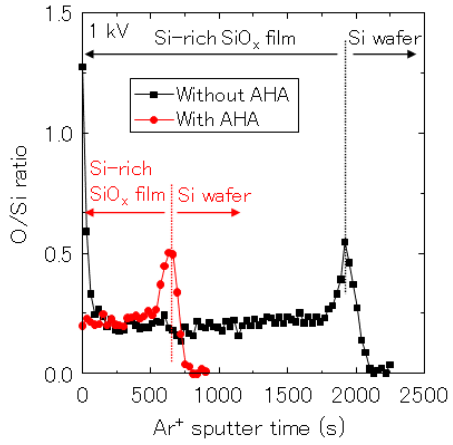

Fig. 14. Depth profiles of O/Si ratio for the Si-rich SiO_x film with and without AHA.

estimated to be 0.017 nm s^{-1}. This indicates that C contamination on the Si-rich SiO_x film was removed and the reduction of the Si-rich SiO_x occurred by the reaction with atomic hydrogen or local heating by the recombination of atomic hydrogen. The thermal SiO_2 film was not reduced by atomic hydrogen. It is considered that the reduction and etching occurred in the Si-rich region because the Si-Si bond strength (3.2 eV) is lower than the Si-O bond strength (8.3 eV). It is considered that the disordered bond network owing to the Si-rich region is sensitive to atomic hydrogen.

3.8. Reaction of atomic hydrogen with oxide films

The reduction of metal oxides is discussed based on the chemical bond strength between the metal and O. The reduction reactivities and strengths of the chemical bonds are summarized in Table 1. The native oxides of Ni and Cu were easily reduced by AHA. The native oxides of Al, Ti, and Cr were slightly reduced by the AHA. The difference between reducing and non-reducing is thought to be related to the magnitude of the chemical bond strength.

Conversely, for the thermal oxide films, the reduction due to atomic hydrogen on the metal surface was suppressed by thermal oxidation. It was shown that the oxidation process of the metal surface promotes effective bond strength by approaching a stable stoichiometric composition when O is supplied to the metal-oxide network. However, the thermal Cu oxide films were reduced by AHA. The bond strengths of Ni-O and Cu-O were below 3.8 eV and were lower than Al-O (5.2 eV), Cr-O (4.7 eV), and Ti-O (6.9 eV). The thermal oxide film of Cu, with a small bond strength of 3.0 eV, was only reduced by AHA. Moreover, for thermally oxidized films, the magnitude of the bond strength can determine whether reduction occurs.

From the comparison between SiO_2 and Si-rich SiO_x films, it was shown that the number of bonds, strongly influenced the reduction.

4. Conclusions

The removal of C contamination and native oxide films without damage using AHA was investigated. The C contamination and native oxides on the Cu and Ni films were removed by AHA; however, the thermally oxidized metals (AlO_x, TiO_x, CrO_x, and NiO_x) were not reduced by AHA. Thermal treatment improves resistance to atomic hydrogen. It is observed that the reduction depends on the bond strength. Further, the thermal

Table 1. Reduction reactivity of oxide films by atomic hydrogen and chemical bond strength.

Material	Native oxide	Thermal oxide	Bond	Strength (eV) [26]
Al	▲	×	Al-O	5.2
Ti	▲	×	Ti-O	6.9
Cr	▲	×	Cr-O	4.7
Ni	○	×	Ni-O	3.8
Cu	○	○	Cu-O	3.0
Si	-	×	Si-O	8.3
Si-rich	○	-	Si-O, Si-Si	8.3, 3.2

Reduction (○), reduction only top surface (▲), nonreduction (×), and without evaluation (-).

SiO_2 is hydrogen resistant. However, Si-rich SiO_x, reduction and/or etching occurs by AHA. These findings are useful for the removal of C contamination and the native oxide film without damage, and for controlling the surface properties of the oxide films by thermal treatment and AHA. AHA is expected as next-generation surface cleaning process in semiconductor industry.

Acknowledgements

We would like to thank to Assistant Professor M. Niibe, Professor S. Inoue, and Assistant Professor Y. Haruyama of the University of Hyogo for their useful suggestions. This work was supported in part by the Tanikawa Foundation for the Promotion of Thermal Technology, Himeji City Academic-Industry Cooperation Grant, and a research grant from the Mazda Foundation.

References

1. A. A. Bergh, *Bell Syst. Tech. J.*, **44** (1965) 261.
2. A. Heya, N. Matsuo, *Thin Solid Films,* **675** (2019) 143.
3. A. Heya, A. Masuda, and H. Matsumura, *Appl. Phys. Lett*., **74** (1999) 2143.
4. A. Heya and N. Matsuo, *Jpn. J. Appl. Phys.,* **46** (2007) 3545.
5. A. Heya and N. Matsuo, *Jpn. J. Appl. Phys.,* **46** (2007) L709.
6. A. Heya and N. Matsuo, *Jpn. J. Appl. Phys.,* **47** (2008) 266.
7. A. Heya and N. Matsuo, *IEICE Trans. Electron*, **E93-C** (2010) 1516.
8. A. Heya and N. Matsuo, *Jpn. J. Appl. Phys.*, **53** (2014) 058002.
9. A. Heya and N. Matsuo, *Thin Solid Films*, **625** (2017) 93.
10. A. Heya, S. Hirano, and N. Matsuo, *Jpn. J. Appl. Phys.*, **58** (2019) 068006.
11. A. Heya, T. Harada, M. Niibe, K. Sumitomo, T. Watanabe, *J. Photopolym. Sci. Technol.*, **33** (2020) 419.
12. K. Uchida, S. Hashioka, A. Izumi, and H. Matsumura, *2000 Dry Process Symp.*, 2000, p. 231.
13. A. Izumi and H. Matsumura, *Jpn. J. Appl. Phys.,* **41** (2002) 4639.
14. M. Yamamoto, H. Umemoto, K. Ohdaira, S. Nagaoka, T. Shikama, T. Nishiyama and, H. Horibe, *J. Photopolym. Sci. Technol.,* **28** (2015) 303.
15. T. Maruoka, Y. Goto, M. Yamamoto, H. Horibe, E. Kusano, K. Takao, and S. Tagawa, *J. Photopolym. Sci. Technol.*, **22** (2009) 325.
16. M. Yamamoto, H. Horibe, H. Umemoto, K. Takao, E. Kusano, M. Kase, and S. Tagawa, *Jpn. J. Appl. Phys.*, **48** (2009) 026503.
17. A. Heya, T. Harada, M. Niibe, K. Sumitomo, T. Watanabe, *J. Photopolym. Sci. Technol.,* **33** (2020) 419.
18. K. Abe and A. Izumi, *Solid state Phenom.,* **145-146** (2009) 389.
19. E. Kondoh, M. Fukasawa, and T. Ojimi, *J. Vac. Sci. Technol.*, **A 25** (2007) 415.
20. S. Oswald and W. Brückner, *Surf. Interface Anal.*, **36** (2004) 17.
21. J. Pouilleau, D. Devilliers, F. Garrido, S. Durand-Vidal, E. Mahé, *Mater. Sci. Eng. B*, **47** (1997) 235.
22. A. Takemura, *J. Vac. Soc. Jpn*., **49** (2006) 339. (in Japanese)
23. C. Fan, C. Chen, J. Wang, X. Fu, Z. Ren, G. Qian, and Z. Wang, *Sci. Rep.*, **5** (2015) 11712.
24. R. A. Palmer, T. M. Doan, P. G. Lloyd, B. L. Jarvis, and N.U. Ahmed, *Plasma Chem. Plasma Process*, **22** (2002) 335.
25. M. M. Sung, K. Sung, C. G. Kim, S. S. Lee, and Y. Kim, *J. Phys. Chem. B*, **104** (2000) 2273.
26. J-P. Cheng, "*CRC Handbook of Chemistry and Physics"*, eds. J. R. Rumble, CRC Press, Boca Raton London New York (2021-2022) 102nd ed., p.9-73.

Three-dimensional Numerical Simulation of Liquid Film Formation and the Distribution of Cleaning Solutions on a Rotating Disk

Yoshinori Jinbo[1*], Yuki Mizushima[1], and Toshiyuki Sanada[1]

[1] *Department of Mechanical Engineering, Shizuoka University, 3-5-1 Johoku, Naka-ku, Hamamatsu, Shizuoka 432-8561, Japan*

* *jimbo.yoshinori@shizuoka.ac.jp*

In a single wafer processing, it is crucial to predict and control liquid film flow flowing over the rotating disk and the chemical solution concentration distribution to achieve efficient cleaning. This study numerically obtained the distribution of liquid film and cleaning solution concentration on a rotating disk using the open-source program, OpenFOAM. We prevented numerical diffusion from liquid to gas by incorporating a conservative scheme into the mass transport equation. The obtained liquid film distribution and surface etching amount agreed with the literature.

Keywords: Cleaning, Single wafer processing, Liquid film distribution, Etching, Numerical simulation, OpenFOAM

1. Introduction

One of the important manufacturing processes supporting recent semiconductor developments based on precise surface profile controls is wafer surface cleaning, such as removing contaminants and organic residues. For example, we must remove the photopolymer resist after printing circuit patterns. Environmentally and economically effective removal procedures are required while preventing the surface's fine structure from collapsing [1–9]. One of the main approaches to remove contaminants and residues is using a single wafer spin processor. Injecting a liquid jet or a solution into a rotating disk causes mechanical or chemical effects to remove contaminants or residues.

In the single wafer process, it is crucial to predict and control liquid film flow flowing over the rotating disk and chemical solution concentration distributed on the disk to achieve efficient removal. When the solution injected from the nozzle and spreading over the rotating disk distributes ununiformly, the progress of chemical reactions differs location by location. Therefore, the solution must be distributed uniformly to achieve precise surface quality. Especially when the chemical reaction rate is faster than the transport speed of the dissolved reactant convected following the fluid flow, as seen in the process of wet chemical etching using HNO3, how many the chemical reaction occurs directly depends on how many the reactant reaches the reaction surface [10]. Thus, it is important to investigate the distribution of the solution concentration in the vicinity of the reacting surface for estimating the chemical reaction amount. Recent industrial processes try to control the concentration distribution by various ways, e.g., swinging motion of the nozzle supplying the solution, multiple and non-axisymmetric arrangements of the nozzles, and installing a rotor, such as a brush, which disturbs the film flow. However, a method that makes the concentration distribution uniform over the rotating disk has not yet been established. Therefore, we need to construct a numerical method to predict the liquid film formation and the following solution distribution on the rotating disk under a three-dimensional condition.

In the present paper, we investigate the applicability of OpenFOAM [11] to the three-dimensional numerical simulation of the formation

Received April 2, 2022
Accepted June 20, 2022

of the thin-film flow and the distribution of the solution on the rotating disk. Until now, some numerical simulations on the solution convection and diffusion following a film flow on a rotating disk have been carried out using various ways, such as a home-made code [10], ANSYS FLUENT [12], an integral boundary layer method [13], and a thin film approximation with OpenFOAM [14]. One of advantages of using OpenFOAM, an open-source code, is that the implementation cost is not expensive, which is important when considering industrial applications of the proposed method. Moreover, OpenFOAM is based on the finite volume method, which allows us to handle unstructured meshes, which can represent complex boundary shapes, with relative ease. Thus, we can comparatively easily prepare and compute complex structures, such as nozzle, rotating disk, and brush. Furthermore, OpenFOAM provides methods to treat moving boundaries, which enables us to straightforwardly extend the present method to more advanced simulations such as swinging movement of a nozzle and rotating motion of a brush over a rotating disk.

In the present paper, we construct a computational method on the fundamental phenomena in which a liquid jet injected from the nozzle impinges a rotating disk perpendicularly, which follows the formation of thin-film flows spreading over the disk surface, which conveys solutes included in the liquid. Then, we consider the validity and applicability of the method.

2. Methods

OpenFOAM solves the thin-film flow formed over the rotating disk by the liquid jet ejected from a nozzle in this study. Moreover, a method for computing the convection (explicitly determined by the fluid flow) and diffusion of the solution accompanied by the liquid jet is introduced into OpenFOAM. These methods are explained below.

The film flow formed by the injected liquid jet is solved by interFoam, an incompressible gas–liquid two-phase flow solver in OpenFOAM. In interFoam, the motion of the gas–liquid interface is captured by a modified volume-of-fluid method, in which the volume fraction of the first phase of gas–liquid two phases, α, is developed by the following equation containing a compressive velocity, which works for preventing the interface from being smeared.

$$\frac{\partial \alpha}{\partial t} + \nabla \cdot (\alpha \boldsymbol{u}) + \nabla \cdot \{\boldsymbol{u}_r \alpha(1-\alpha)\} = 0 \qquad (1)$$

where t is the time, $\boldsymbol{u}$ is the fluid velocity, and $\boldsymbol{u}_r$ is the relative velocity between gas and liquid phases. Since $\alpha(1-\alpha)$ is included, the third term in Eq. (1) is zero except for the computational cells at the interface. The term works such that the interface is maintained sharp. The mass and momentum conservation equations are coupled by the PIMPLE algorithm, which combines the PISO [15] and SIMPLE [16] algorithms. The surface tension is taken into account as a body force in the computational cells containing the interface by the continuous surface force method [17]. The details of the algorithm and validity of interFoam are mentioned in the reference [18].

In this study, chemical species are assumed to exist only in the liquid. The distribution of the solute concentration obeys the advective–diffusive equation in which the advection velocity is explicitly determined by the fluid velocity field. When the advection–diffusion equation is simply solved, some amount of the solute passes through the interface and leaks into the gas phase in the transport process. Thus, in the present paper, the following conservation equation is solved.

$$\frac{\partial \alpha C}{\partial t} + \nabla \cdot (\alpha C \boldsymbol{u}) = \nabla \cdot (\alpha D_{ls} \nabla C) \qquad (2)$$

where C is the solution concentration and D_{ls} is the diffusivity of the solute in the liquid. For the diffusion term in Eq. (2), we neglect an internal exchange term, corresponding to the third term on the r.h.s of Eq. (25) in the paper of Marchall et al. [19]. This corresponds to making the amount of the solute passing through the interface in each computational cell zero. By implementing this equation in interFoam, we can compute the advection and diffusion of the solute only in the liquid. The implementation was accomplished according to a multi-phase CFD solver shown by Li [20].

In the present paper, two problems are numerically solved. One is the damBreak problem [11], which OpenFOAM provides as a tutorial problem. We demonstrate the validity of the present method. The other is the main computation in which the formation of thin-film flows on a rotating disk is followed by the advection and diffusion of a solute.

3. Results and discussion

3.1. DamBreak problem

First, we evaluate the mass conservation of chemicals in the liquid phase when using the present method, in which the conservation equation (Eq.

(2)) is solved for the chemical concentration in the liquid phase, αC. We apply the present interFoam, implementing Eq. (2), to the damBreak problem. For comparison, we also compute the damBreak problem by a method in which the advection–diffusion equation for the concentration C is solved instead of Eq. (2). In the method, the diffusion coefficient is defined as αD_{ls}, which results in no diffusion of the concentration in the gas phase. The computational conditions are the same as those of the tutorial damBreak problem, except that the rigid wall boundary conditions are applied to the top surface of the domain and that a static chemical concentration distribution is initially given in a static liquid. The initial concentration distribution is given as $C = 100$ in a circle of radius 0.1 centered at $(x, y, z) = (0, 0.146, 0)$, such as not to overlap the gas–liquid interface. The diffusion coefficient, D_{ls}, is 2×10^{-3} m^2/s.

Figure 1 shows a comparison of mass conservation performances between the aforementioned two methods. The horizontal and vertical axes represent the time and the relative error of the total mass of the solute from the initial total mass, $E_{\alpha C}$, respectively. $E_{\alpha C}$ is defined as follows:

$$E_{\alpha C} = \frac{\left(\Sigma_i^N \alpha_i C_i \delta V_i\right)^n - \left(\Sigma_i^N \alpha_i C_i \delta V_i\right)^0}{\left(\Sigma_i^N \alpha_i C_i \delta V_i\right)^0} \quad (3)$$

where i is the computational cell number, N is the number of the computational cells, δV is the volume of the computational cell, superscript n is the time step number in unsteady computation, and superscript 0 represents the value at the initial time step. In the figure, the solid line represents the case where Eq. (2) is solved, and the broken line represents the case where the advection–diffusion

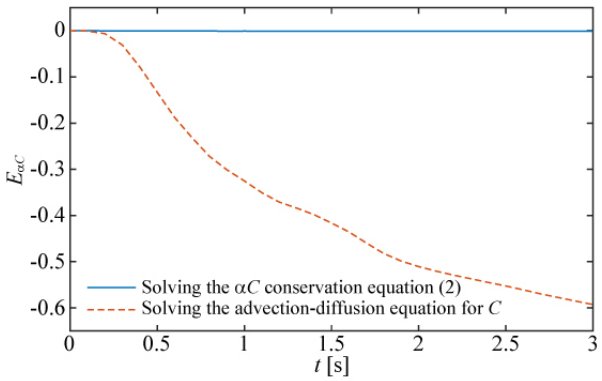

Fig. 1. Time histories of the relative total mass error of the solute in the liquid from the initial total mass.

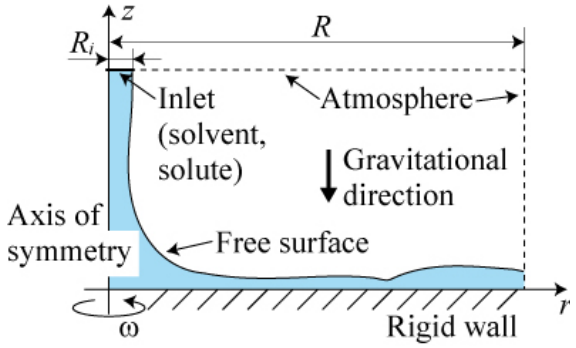

Fig. 2. Schematic of the computational domain for the axisymmetric two-dimensional computation.

equation for the concentration C is solved. The total mass of the solute in the liquid is conserved when solving Eq. (2), while the value decreases when solving the advection–diffusion equation for C. The total mass summing up the solute masses in both phases is conserved, although the result is not shown in the figure. This represents that the mass decrease (broken line) corresponds to the leak of the solute from the liquid to gas. Simply defining the diffusion coefficient as αD_{ls} is not sufficient to prevent the solute from unphysically passing through the gas–liquid interface.

3.2. Film formation on a rotating disk

Figure 2 shows the computational domain of the axisymmetric two-dimensional computation of the liquid film flow. A liquid jet is ejected from a nozzle exit of radius R_i. The jet impacts a flat plate vertically, and a liquid film spreads over the flat plate. The liquid phase supplied from the nozzle is assumed to contain a chemical solution, and the advection–diffusion process due to the liquid film flow on the flat plate is also calculated simultaneously. The flat plate is of radius R and rotates at a rotational speed ω.

The velocity and pressure boundary conditions for the rigid wall, which is the top surface of a rotating disk, are given using “rotatingWallVelocity” and “fixedFluxPressure” of the OpenFOAM function, respectively. The boundary conditions for the atmospheric release section are given by “pressureInletOutletVelocity” and constant total pressure. The flow rate is given for the inflow condition at the nozzle exit. The velocity distribution is assumed to be uniform within the nozzle.

The computational conditions are determined according to the experimental study [21]. The inlet radius, R_i is 2 mm, the flow rate of the inlet liquid,

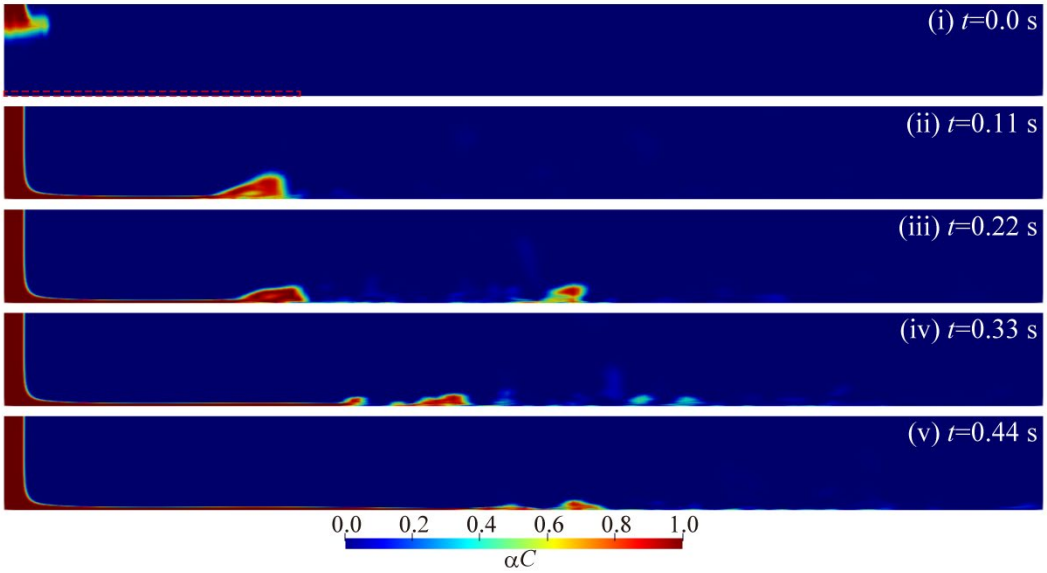

Fig. 3. Successive distributions of the solute concentration formed by the thin-film flow injected from the inlet patch (top left of each panel) and spreading over the top surface of the rotating disk (bottom of each panel). The rectangle drawn by the red broken line at the lower left in panel (i) is shown for the reference of the characteristic length used in Fig. 4. The size of the rectangle is $2h_c \times r_c$, where r_c and h_c are defined by Eqs. (4) and (5), respectively.

Q, is 1.25 L/min, the surface tension coefficient is 0.07 N/m, and the kinematic viscosity, ν, is 2.87×10^{-6} m^2/s. The Reynolds number of the inlet flow is 2311. Turbulent effects are neglected. The radius of the rotating disk R is 100 mm, and the rotational speed ω is 500 rpm. The concentration diffusivity is determined such that the Schmidt number is 1200. The concentration at the inlet is 1. The number of computational cells is 13200.

Figure 3 shows the successive distributions of the solution concentrations following the liquid jet injection and the liquid film flow obtained by the axisymmetric two-dimensional computation. The solution, accompanied by the liquid jet injected from the upper left inlet, flows into the domain, impinges on the rotating disk (bottom of each panel of Fig. 3), and spreads over the disk. As shown by the motion of the tip of the spreading liquid film (rim), the part moves largely along the disk due to the inertia of the liquid jet (from (i) to (ii)). Then, the speed decelerates largely (from (ii) to (iii)). Then, the rim moves largely again in the radial direction (from (iii) to (iv) and (v)). This is because the dominant physics acting on the spreading lamella varies depending on the radial location r along with the rotating disk. As r increases, the spreading speed of the film decelerates due to the decrease of the amount of liquid supplied from the liquid jet as well as due to the influence of the wall viscosity. On the other hand, the centrifugal force because of the disk rotational motion increases with the radial location. Thus, the thin film moves largely in the radial direction while extended. Then, the almost steady flow is achieved after the rim exits from the domain. (Unsteadiness appears around the right end of the domain.) The film thickness varies depending on the variation of the dominant forces, which can result in a change in the concentration boundary layer thickness and a change in the amount of chemical reactions on the disk surface [13].

Figure 4 shows the spatial distribution of the film thickness along with the rotating disk at the almost steady state. The vertical and horizontal axes are normalized by r_c and h_c, respectively, which are determined according to the reference [13] as follows:

$$r_c = \left(\frac{9Q^2}{4\pi^2\nu\omega}\right)^{1/4} \tag{4}$$

$$h_c = \left(\frac{\nu}{\omega}\right)^{\frac{1}{2}} \tag{5}$$

The rectangle drawn by the red broken line at the lower left in Fig.3(i) is a scale reference and the size is $2h_c \times r_c$. The liquid jet impinges on the rotating disk and spreads over the disk. The liquid film thickness increases, and the local maximum appears around $r/r_c = 0.9$ due to the deceleration of the film flow aforementioned in Fig. 3. Then, because the centrifugal force increases with the radial position, the liquid film on the disk stretches, and

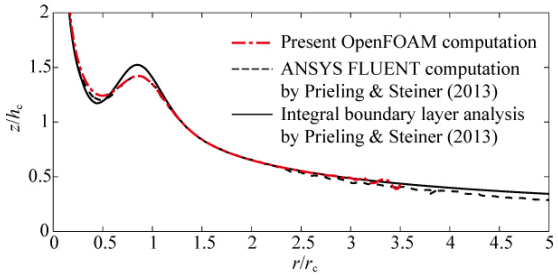

Fig. 4. Comparison of the thickness of the film flow spreading over the rotating disk obtained by the present computation with those by the ANSYS FLUENT computation and by the integral boundary layer analysis [13].

the thickness decreases. Comparing with the FLUENT computation and the integral boundary layer analysis [13], we successfully capture the variation of the liquid film thickness. Note that the thickness by the FLUENT computation [13] is a time-averaged thickness of partly unsteady film flow.

3.3. Etching rate

Figure 5 shows the distribution of etching rates R_{etch} in the almost steady state. According to the reference [10], the R_{etch} is determined as the following equations:

$$j_{HNO_3} = \rho D_{ls} \frac{\partial C}{\partial z}\Big|_{z=0} \tag{6}$$

$$R_{etch} = \beta \frac{j_{HNO_3}}{\rho_{Si}} \frac{M_{Si}}{4M_{HNO_3}} \tag{7}$$

where ρ is the density of the liquid, β is an empirical proportionality constant, ρ_{Si} is the silicon density, M_{Si} is the molar mass of silicon, and M_{HNO_3} is the molar mass of nitric acid. As shown in Fig. 5, etching primarily occurs just around the jet impact point, and the etching rate decreases with r increases. Then, the etching rate reaches the local minimum. After that, the rate turns to increase and reaches the local maximum. Then, the rate decreases monotonically as r increases. Connecting the etching rate with the thickness of the concentration boundary layer, Prieling & Steiner explained the reason for the appearance of the local minimum of the etching rate on the disk [13]. The concentration boundary layer thickness increases with the thickness of the liquid film, which leads the concentration gradient to be gradual, resulting in a decrease in the etching rate. The results of the

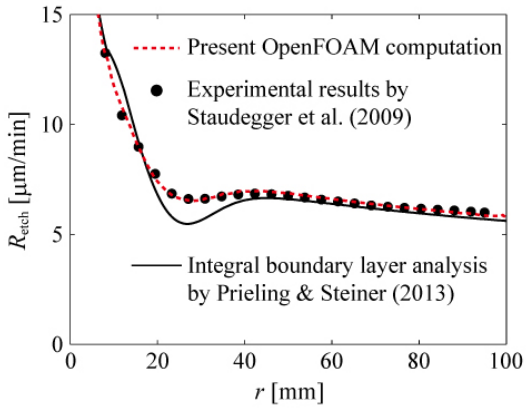

Fig. 5. The distribution of the etching rate R_{etch} along with the rotating disk at the rotating speed of 500 rpm when etchant of 1.25 L/min is injected. The characteristic length in the horizontal direction, r_c, which is defined by Eq. (4) is around 28.5 mm.

present computation agree well with the experimental results [21]. The present computation can capture the distribution of the etching rate along with the rotating disk.

3.4. Three-dimensional computation of a non-axisymmetric jet injection on a rotating disk

Finally, we demonstrate the three-dimensional simulation with a non-axisymmetric computational condition. Figure 6 shows a result of a computation in which the nozzle location has an offset, δr, from the axis of symmetry. Here, $\delta r = 0.43R_3$, where R_3 is the disk radius and the value is 75 mm. The radius of the nozzle is 2.15 mm, and the flow rate of the liquid flow at the nozzle exit is 7 L/min. The rotational speed of the spinning disk is 100 rpm, and the direction is counterclockwise in the direction from the nozzle to the rotating disk. The number of computational cells is 1284063.

In Fig. 6, the shape of the free surface of the liquid film flow spreading over the rotating disk and the fluid velocity distribution are shown. The liquid jet is injected from the upper right in each panel of the figure. The jet impinges the top surface of the rotating disk perpendicularly. Then, the jet turns into the liquid film flow spreading over the rotating disk. The non-axisymmetric liquid film flow can be successfully computed. The amount of the flow reaching each location differs location by location. This result suggests that the present three-dimensional computation can be applied to prediction tools or engineering design tools by estimating the spatial deviation of the flow rate and evaluating the cleaning efficiency.

4. Conclusion

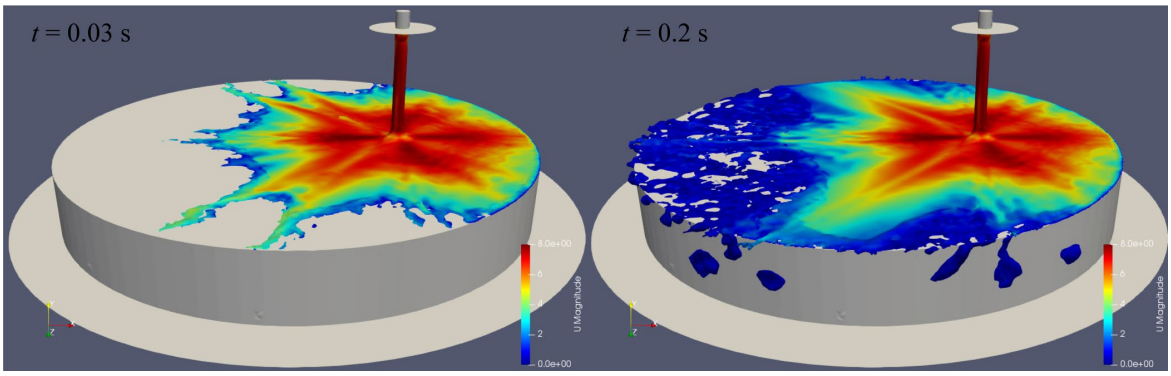

Fig. 6. Liquid film flow and the distribution of the velocity magnitude over the rotating disk at the non-axisymmetric computational condition in which the nozzle location has an offset of $0.43R_3$ where R_3 is the disk radius.

The liquid film flow spreading over a rotating disk and the following convection and diffusion of the solute are computed by using OpenFOAM. By implementing a solving method of the conservation equation for αC in OpenFOAM, we were able to compute the advection and diffusion of the solute in the liquid phase while preventing the solute from leaking into the gas phase. We confirmed the concentration conservation of the present method by computing the damBreak problem. We applied the method to the axisymmetric computation of the liquid film flow spreading over a rotating disk. Comparing the liquid film thickness and etching rate computed by the present method with those obtained by the previous computation [13] and experiment [21], we demonstrated the validity of the present computation. Furthermore, we carried out a three-dimensional computation with a non-axisymmetric computational condition. We demonstrated that the present computation was able to estimate the spatial deviation of the liquid flow rate on the rotating disk, which relates to a cleaning performance.

References

1. H. Horibe, M. Yamamoto, E. Kusano, T. Ichikawa, and S. Tagawa, *J. Photopolym. Sci. Technol*., **21** (2008) 293.
2. T. Mashiko, T. Sanada, I. Nishiyama, and H. Horibe, *Jpn. J. Appl. Phys*., **51** (2012) 067101.
3. J. Ishimoto, and H. Horibe, *J. Photopolym. Sci. Technol*., **28** (2015) 285.
4. M. Takahashi, H. Horibe, K. Matsuura, and K. Tatera, *J. Photopolym. Sci. Technol*., **28** (2015) 293.
5. T. Sanada and M. Watanabe, *J. Photopolym. Sci. Technol*., **28** (2015) 289.
6. M. Yamamoto, T. Shiroi, T. Shikama, S. Nagaoka, H. Umemoto, and H. Horibe, *J. Photopolym. Sci. Technol*., **32** (2019) 609.
7. M. Yamamoto, K. Akita, S. Nagaoka, H. Umemoto, and H. Horibe, *J. Photopolym. Sci. Technol*., **33** (2020) 433.
8. A. Hosaka, T. Miyaki, Y. Mizushima, S. Hamada, R. Koshino, A. Fukunaga, and T. Sanada, *J. Photopolym. Sci. Technol*., **34** (2021) 505.
9. K. Tsujimoto and H. Horibe, *J. Photopolym. Sci. Technol*., **34** (2021) 485.
10. K. Kaneko, A. Tamenori, N. Alleborn, and F. Durst, *ECS Trans.*, **2** (2007) 295.
11. C. J. Greenshields, OpenFOAM User Guide version 9, OpenFOAM Foundation Ltd, (2021).
12. H. Habuka, K. Mizuno, S. Ohashi, and T. Kinoshita, *ECS J. Solid State Sci. Technol.*, **2** (2013) P264.
13. D. Prieling and H. Steiner, *Chem. Eng. Sci.*, **101** (2013) 109.
14. P. Víta, Dissertation of Montan University, (2016).
15. R. I. Issa, A. D. Gosman, and A . P. Watkins, *J. Comp. Phys.*, **62** (1986) 66.
16. S. V. Patankar and D. B. Spalding, *Int. J. Heat Mass Transfer,* **15** (1972) 1787.
17. J. U. Brackbill, D. B. Kothe, and C. Zemach, *J. Comp. Phys*., **100** (1992) 335.
18. S. S. Deshpande, L. Anumolu, and M. F. Trujillo, *Comput. Sci. Discov.*, **5** (2012) 014016.
19. H. Marschall, K. Hinterberger, C. Schüler, F. Habla, and O. Hinrichsen, *Chem. Eng. Sci.*, **78** (2012) 111–127.
20. H. Li, (2021) interAdsFoam, https://github.com/ Rdfing/interAdsFoam.
21. F. Staudegger, M. W. Hofbaur, and H. J. Kruwinus, *J. Electrochem. Soc.*, **156** (2009) H340.

High Speed Ashing of Ion Implanted Photoresist by Microwave Excited Water Vapor Plasma with Powered Substrate

Takeshi Aizawa[1,2*], Tasuku Sakurai[1], Khant Nyar Paing[1], Yusuke Kayamori[1], Yusuke Nakano[1], Yasunori Tanaka[1], and Tatsuo Ishijima[1]

[1] Electrical Engineering and Computer Science, Graduate School of Natural Science & Technology, Kanazawa University, Kakuma-machi, Kanazawa, Ishikawa 920-1192, Japan
[2] Yonekura Mfg. Co., Ltd. 2-11-5 Shin-yokohama, Kohoku, Yokohama 222-0033, Japan
**t-aizawa@stu.kanazawa-u.ac.jp, ishijima@ec.t.kanazawa-u.ac.jp*

This study examined a substrate bias voltage introduced into a microwave excited water vapor plasma to enable fast ashing of photoresist implanted with high-dose ions without occurring popping. The ashing rate at the center of the ashing distribution for the photoresist implanted with boron with an implantation dose of 1×10^{16} atoms/cm^2 was estimated as 1.0 μm/min. Results of plasma emission diagnostics suggest that rf bias application effects generated a plasma rich in excited hydrogen and oxygen atom near the substrate surface. This plasma is presumed to assist the removal of the hardened layer of ion implanted photoresist and to affect hydrogen gas addition. A self-bias voltage during bias application was sufficiently low, approximately −30 V, at a peak-to-peak voltage of 1 kV at 1 MHz.
Keywords: Ion implantation, Microwave-excited plasma, Optical emission spectroscopy, Substrate rf bias, Water vapor

1. Introduction

Photoresists serve to mask a substrate surface when ion implanting or etching during semiconductor manufacturing. Through these processes, ions are implanted into the photoresist surface and the substrate surface. The ion-implanted photoresist then forms a hardened layer that is very difficult to remove [1]. For photoresist removal, chemical solution treatment (sulfuric acid hydrogen peroxide mixture, SPM) [2] or oxygen plasma treatment [3−5] is generally used. However, removing the photoresist implanted with high-dose ions by SPM treatment alone is impossible. Therefore, generally, oxygen plasma is applied to remove ion implanted photoresist films. In the case of oxygen plasma, the substrate must be heated to realize a high rate of removal. However, if the implanted photoresist with high doses ions is heated, then the photoresist will rupture [6,7]. This phenomenon, called popping, leads to much residue on a wafer. Therefore, various techniques have been developed to remove high-dose ion implanted photoresists to suppress popping phenomena.

One removal method uses highly concentrated ozone gas, with treatment conducted at 400°C for various ion implantation doses [8]. Results show that the amount of popping depends on the ion implantation dose and ion species. Removal methods using mixtures of multiple chemicals [9], and using water/carbon dioxide mixtures at elevated temperature and pressure have also been studied [10]. In the removal method using atomic hydrogen, photoresists implanted with an implantation dose of 5×10^{15} atoms/cm^2 can be removed without increasing the substrate temperature, although the ashing rate was not high [11]. In general, chemical reactions are enhanced when the substrate temperature is high. It is therefore difficult to achieve a high ashing rate at a low substrate temperature [12]. It is necessary to develop a removal method that suppresses the occurrence of popping with a high ashing rate. A water-plasma

Received March 25, 2022
Accepted June 19, 2022

asher (WPA) we have been developing provides a direct substrate cooling effect by introduction of ultrapure water into the chamber interior and a high ashing rate for ion-implanted photoresists [13].

For this study, we introduced an rf bias voltage application on a substrate holder in the WPA to achieve a high ashing rate at a low substrate temperature. The rf bias voltage system is used conventionally in etching processes because the ion energy distribution function can be controlled by adjusting the applied the substrate bias voltage and frequency. It has been reported that increasing ion flux with bias increases the ashing rate [14]. However, its application to ashing processes for ion-implanted photoresist film has been reported for ICP plasma [15], but a few reported for microwave-excited plasma or water vapor plasmas. As described herein, the ashing rates of photoresist films with boron or arsenic ion at a high dose density were investigated. Differences in optical emission distributions using a band pass filter were examined with application of rf bias voltage on the substrate holder.

2. Experiment Setup

2.1. Water vapor ashing for an ion implanted photoresist with bias voltage on a substrate holder

Fig. 1 presents a schematic diagram of the experimental apparatus for WPA. 10 ml of ultrapure water was introduced to a groove made in a chamber. The chamber pressure was reduced and fixed at about 2.5 kPa using a scroll pump. Consequently, the chamber was filled with saturated vapor of ultrapure water. Microwaves of 2.45 GHz were propagated in a quartz-filled rectangular waveguide with TE_{10} mode, and were propagated to an antenna installed at the waveguide end. In that study, an H-shaped antenna made of Si was used [16]. The input microwaves were modulated using a 100 Hz square wave, as presented in Fig. 2. The peak power was 200 W. The on-time duty factor was 30%. The averaged input power (P_{avg}) was 60 W. A copper circular substrate holder was placed along a cylindrical chamber axis. 1 MHz sine wave generated using a function generator (WF1943A; NF Corp.) was amplified using a voltage amplifier (T145-5016A; Thamway Corp.) and was applied to the substrate holder via an impedance converter (T013-5016A; Thamway Corp.), and a capacitor of 300 pF. The substrate holder and chamber were insulated a polytetrafluoroethylene insulator. The chamber was grounded. The sine wave was synchronized with the excited microwave

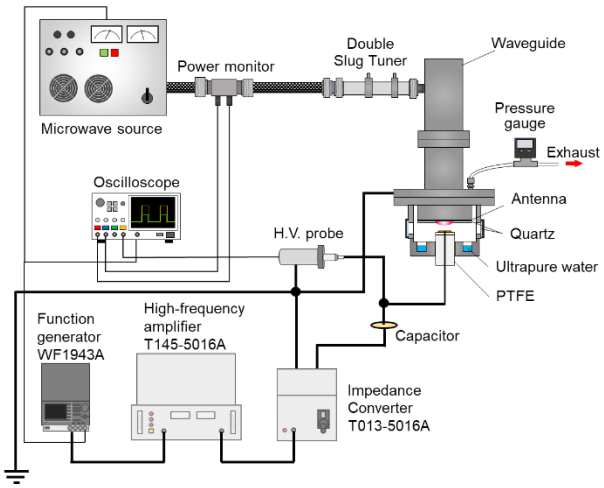

Fig. 1 Schematic of the ashing experiment setup.

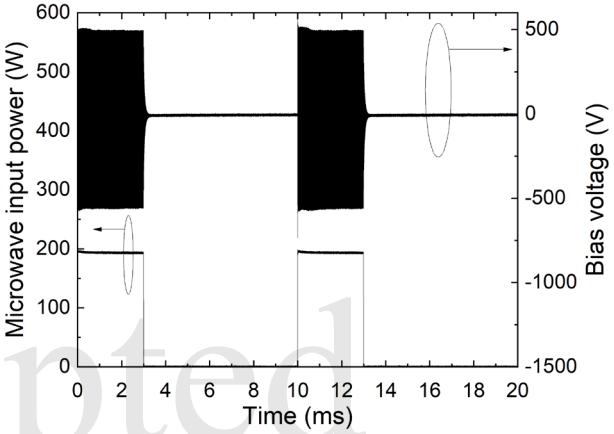

Fig. 2 Microwave input power and applied bias voltage modulated at 100 Hz as a function of time.

modulation signal. The rf bias voltage was applied only when the microwave was excited. A high voltage probe (P6015A; Tektronix Inc.) was used to measure the voltage between the capacitor and the substrate holder. The measured peak-to-peak of the rf bias voltage (V_{pp}) was approximately 1 kV. The ashing target had a base polymer of poly-hydroxystyrene (PHS), which was a photoresist for KrF (248 nm) laser. The photoresist was coated to a 300 mm wafer. Then, the photoresist was implanted with boron ion with an implantation dose of 1×10^{16} atoms/cm^2 at acceleration energy of 55 keV or arsenic ion with an implantation dose of 1×10^{15} atoms/cm^2 at an acceleration energy of 50 keV. Subsequently, the Si wafer with the ion implanted photoresist was cut into 20 mm square pieces. The photoresists were marked with three scratches horizontally and vertically to correct the measurement profile. The wafer was placed on a substrate holder at 9 mm below the antenna. Then plasma was generated for 20 s. The photoresist film thickness was measured using a probe type step

profiler (ET200A; Kosaka Laboratory Ltd.) before and after ashing.

2.2. Optical emission spectroscopy

Fig. 3 presents details of the experimental apparatus for optical emission spectroscopy. The spectrometer with ICCD (PI-MAX4; Teledyne Princeton Instruments) was placed on the side of the chamber window. After the plasma emission was injected into the spectrometer through the lens, the emission image was acquired by ICCD as 0th order light. A bandpass filter was placed between the lens and the spectrometer so that only emissions of a specific wavelength were observed. The characteristics of the three installed filters are 10 nm FWHM and center wavelength, with 310 nm, 656 nm, and 780 nm, respectively corresponding to the OH (*A*-*X*), H_α, and O emissions. The exposure time was set to 10 ms. The accumulation number was set to one. The gain of the image intensifier was set as 0% for OH (*A*-*X*) and H_α, and as 100% for O because the emissions of O are much weaker than those of either OH (*A*-*X*) or H_α. In this experiment, a two-inch (approx. 5 cm) Si wafer without a photoresist coating was set on the substrate holder. The other conditions for plasma generation are the same as the experiment conditions described in chapter 2.1.

3. Experiment Results and Discussion

3.1. Plasma emissions with and without rf bias and appearance of wafers after ashing

Fig. 4 presents emission images of the water vapor plasma taken using a digital camera. The plasma was observed through the quartz window on the side of the chamber. For the case without rf bias voltage, plasma generated by the microwave was observed near the antenna. However, for the case with rf bias voltage, plasma was generated simultaneously both near the antenna and near the wafer surface by the application of high voltage due to rf bias. Fig. 5 shows the photoresist on the wafer after water vapor plasma ashing. In the condition without rf bias voltage, the photoresist was removed only slightly. In contrast, in the condition with rf bias voltage, the photoresist removal proceeded for both B and As. The surface of the photoresist film was smooth without clear holes, suggesting popping was negligibly suppressed. The shape of the photoresist removal was circular. The removal speed near the wafer center appeared to be the highest.

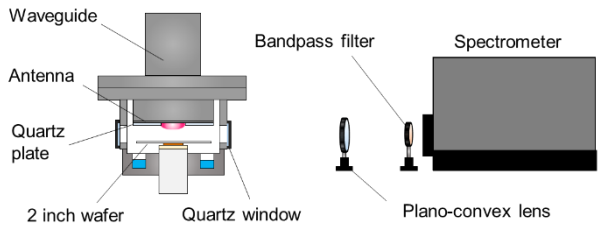

Fig. 3 Schematic of the experiment setup for optical emission spectroscopy.

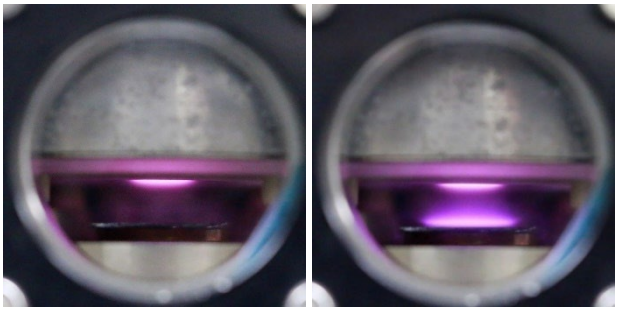

(a) (b)

Fig. 4 Emission images of the microwave excited plasma at P_{avg} = 60 W and p = 2.5 kPa: (a) without bias voltage and (b) with bias voltage at V_{pp} = 1 kV.

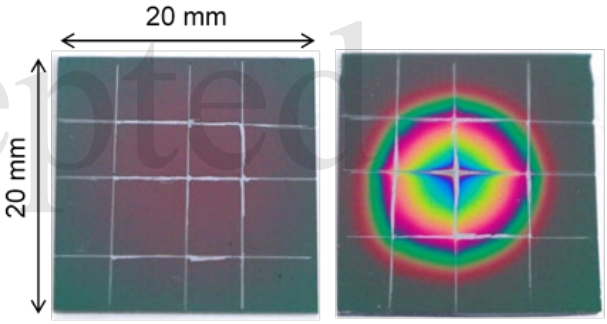

(a) (b)

Fig. 5 Images of the ion-implanted photoresist with boron with an implantation dose of 1×10^{16} atoms/cm^2 after 20 s ashing at P_{avg} = 60 W (a) without bias voltage and (b) with bias voltage at V_{pp} = 1 kV.

3.2. Film thickness after ashing

Fig. 6 portrays the photoresist thickness after ashing, as measured by the step profiler. Wafers without rf bias were measured four times radially from the wafer center; those with rf bias were measured eight times radially from the ashing distribution center. The average film thickness in the radial direction is shown with the measurement center at 0 mm. Error bars represent the maximum and minimum thicknesses. The initial thicknesses of the photoresist film were 0.57 μm for B and 0.76 μm for As. For the case without bias voltage, results show little change from the initial film thickness for both B and As. For the case with rf bias voltage,

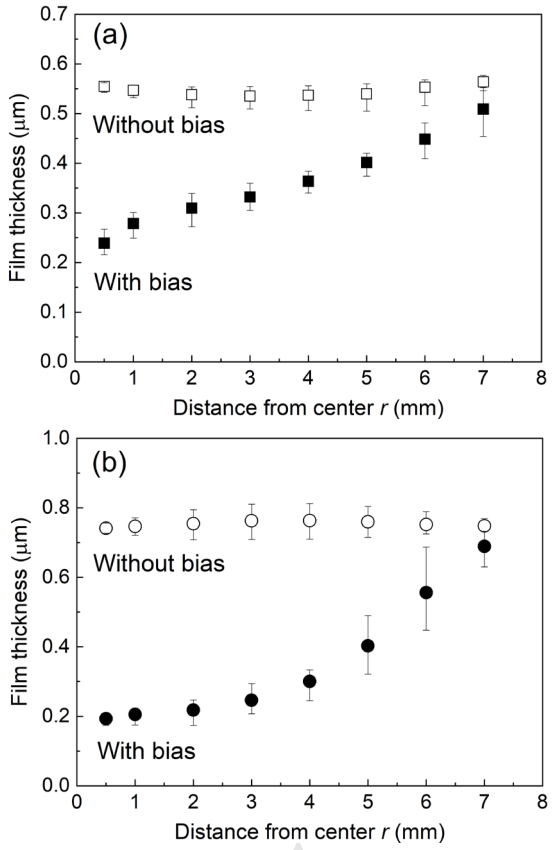

Fig. 6 Remaining photoresist film thickness after 20 s ashing with or without bias voltage as a function of distance from ashing distribution center. The photoresist was implanted ion (a) with boron and an implantation dose of 1×10^{16} atoms/cm^2 and (b) with arsenic and an implantation dose of 1×10^{15} atoms/cm^2.

results show that the photoresist implanted high-doses of ions for both B and As can be removed, despite the short irradiation time. The averaged ashing rate for r = 0.5 mm was estimated as 1.0 μm/min for B and 1.7 μm/min for As. The ashing rate of B was lower than that of As because of the higher ion implantation dose. Of course, the ashing rate differs between the upper hardened layer and the lower normal layer. The ashing rate decreases during removal of the hardened layer. Therefore, the ashing rate is presumed to be faster than the present value when the irradiation time is extended.

3.3. Plasma spectroscopic observation with or without rf bias

Fig. 7 portrays a color map of the 2D emission spectra obtained with each bandpass filter. The circle in the figure represents the quartz window on the side of the chamber. Among the two black lines in the figure, the upper represents the antenna position. The lower one represents the two-inch wafer position. Fig. 7 (a) and (b) demonstrate that OH (*A*-*X*) are most intense not on the antenna surface but slightly below it, and that they are diffused widely around there. However, Fig. 7 (c), (d), (e), and (f) demonstrate that the excited states of O and H_α were strong near the antenna surface. The emission area was narrow. This difference is probably attributable to the fact that the dissociation reaction of water differs depending on the electron impact energy. According to Itikawa et al., the dissociation reaction in eq. (1) occurs when water collides with electrons with energy greater than 9.15 eV [17]. However, when the electron energy is higher than 17.19 eV, the dissociation reaction of eq. (2) occurs. In other words, at high electron energies, OH is produced in the ground state, not in the excited state.

$$H_2O + e\ (e > 9.15\ \text{eV}) \rightarrow OH^*\ (A) + H\ (n = 1) \quad (1)$$

$$H_2O + e\ (e > 17.19\ \text{eV}) \rightarrow OH\ (X) + H^*\ (n = 3) \quad (2)$$

For this reason, H_α and O were strong, whereas OH (*A*-*X*) was weak near the antenna surface in our experiment. However, OH* (*A*) is produced instead of OH (*X*) because the electron energy decreases with distance from the antenna. It is therefore assumed that emissions of OH (*A*-*X*) were observed over a wide area in Fig. (a) and (b). Another reason for the OH (*A*-*X*) expansion might be the long lifetime of OH* (*A*). Bruggeman et al. described the radiative lifetime of OH (*A*-*X*), H_α, and O [18]. They presented their radiative lifetime at 700-1100 ns, 27 ns, and 15 ns. Because of this long OH* (*A*) lifetime, OH* (*A*) can spread by diffusion. Specifically examining the difference between cases with and without rf bias voltage, it becomes readily apparent that the intensity of H_α and O increases near the wafer surface. However, there is not much change in the trend of OH (*A*-*X*) intensity distribution. Therefore, the plasma observed on the wafer in Fig. 2 might contain mainly H_α and O. Based on this idea, it is assumed that the fast ashing of the ion implanted photoresist is attributable to these reactive species. In general, the addition of hydrogen gas readily breaks the cross-links in the hardening layer and increases the ashing rate in the removal of ion implanted photoresist [19]. Therefore, we inferred that the plasma generated by application of rf bias voltage might have the same effect as adding hydrogen gas because hydrogen radicals are predominant in the plasma.

Plasma on the wafer surface is also considered to provide damage to the substrate because of rf bias

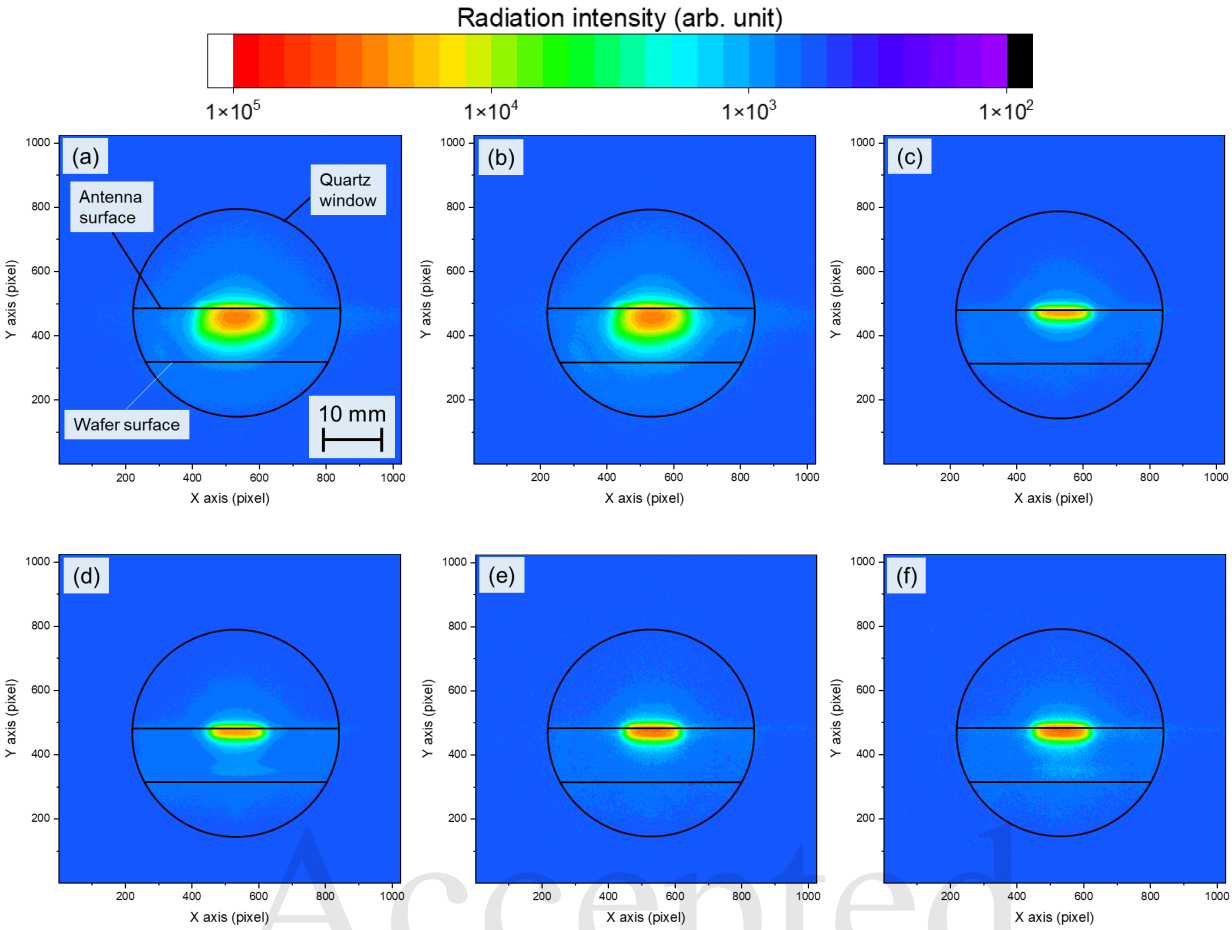

Fig. 7 Results of the optical emission spectroscopy for the microwave excited plasma at P_{avg} = 60 W using various bandpass filters without or with bias voltage at V_{pp} = 1 kV: (a) OH without bias voltage, (b) OH with bias voltage, (c) H_α without bias voltage, (d) H_α with bias voltage, (e) O without bias voltage, and (f) O with bias voltage.

application. When rf bias is applied, ions flow into the substrate accelerating by generated self-bias voltage. Yokoyama et al. observed extensive damage to Si at self-bias voltages higher than −80 V in Ar plasma [20]. The self-bias voltage in this study was −29.9 V at V_{pp} of 1 kV, which was less than −80 V. Therefore, generation of plasma by rf bias voltage can be expected not only to have a high ashing rate, but also to minimize damage to the substrate.

4. Conclusion

To increase ashing rates at low temperatures, the effects of rf bias application on water plasma ashing were investigated. Plasma different from the microwave excited plasma was generated on the wafer by applying the bias voltage. The plasma improved the ashing rate of the ion implanted photoresist considerably without any occurrence of popping. The reason for the ashing rate improvement is that the hydrogen radicals increasing near the wafer had the same effect as hydrogen gas addition. The plasma by rf bias is effective for photoresists with a high dose of boron implanted of the 1×10^{16} atoms/cm^2. The ashing rate was 1.0 μm/min. Damage to the substrate caused by bias voltage is expected to be negligible because the self-bias voltage was sufficiently low when plasma was generated on the wafer surface.

Acknowledgments

The authors are grateful to Prof. Tetsuya Taima of Kanazawa Univ. for supporting film thickness measurement.

References

1. K. K. Ong, M. H. Liang, L. H. Chan, and C. P. Soo, *J. Vac. Sci. Technol. A*, **17** (1999) 1479.
2. W. Kern, *J. Electrochem. Soc.*, **137** (1990) 1887.
3. S. Fujimura, J. Konno, K. Hikazutani, and H. Yano, *Jpn. J. Appl. Phys.*, **28** (1989) 2130.
4. S. Fujimura, K. Shinagawa, M. T. Suzuki, and M. Nakamura, *J. Vac. Sci. Technol. B*, **9** (1991)

357.
5. K. Taniguchi, K. Tanaka, T. Inomata, and M. Kogoma, *J. Photopolym. Sci. Technol.*, **10** (1997) 113.
6. G. K. Vinogradov, V. M. Menagarishvili, and S. Yoneyama, *J. Photopolym. Sci. Technol.*, **11** (1998) 125.
7. M. Kikuchi, and R. Bersin, *Jpn. J. Appl. Phys.*, **31** (1992) 2035.
8. T. Miura, M. Kekura, H. Horibe, and M. Yamamoto, *J. Photopolym. Sci. Technol.*, **21** (2008) 311.
9. E. Oh, and S. Lim, *J. Ind. Eng. Chem.*, **77** (2019) 230.
10. K. L. Chavez, G. L. Bakker, and D. W. Hess, *J. Vac. Sci. Technol. B*, **19** (2001) 2144.
11. H. Horibe, M. Yamamoto, T. Maruoka, Y. Goto, A. Kono, I. Nishiyama, and S. Tagawa, *Thin Solid Films*, **519** (2011) 4578.
12. C. K. Huynh, and J. C. Mitchener, *J. Vac. Sci. Technol. B*, **9** (1991) 353.
13. T. Ishijima, K. Nosaka, Y. Tanaka, Y. Uesugi, Y. Goto, and H. Horibe, *Appl. Phys. Lett.*, **103** (2013) 142101.
14. W. Lee, H. Kim, W. Park, W. S. Kim, D. Kim, J. W. Kim, H. W. Cheong, and K. W. Whang, *J. Appl. Phys.*, **117** (2015) 173302.
15. M. N. Kawaguchi, J. S. Papanu, and E. G. Pavel, *J. Vac. Sci. Technol. B*, **24** (2006) 651.
16. T. Aizawa, T. Shimada, T. Sakurai, Y. Nakano, Y. Tanaka, Y. Uesugi, and T. Ishijima, *J. Photopolym. Sci. Technol.*, **34** (2021) 479.
17. Y. Itikawa, and N. Mason, *J. Phys. Chem. Ref. Data*, **34** (2005) 1.
18. P. Bruggeman, J. L. Walsh, D. C. Schram, C. Leys, and M. G. Kong, *Plasma Sources Sci. Technol.*, **18** (2009).
19. K. Hirose, H. Shimada, S. Shimomura, M. Onodera, and T. Ohmi, *J. Electrochem. Soc.*, **141** (1994) 192.
20. S. Yokoyama, Z. J. Radzimski, K. Ishibashi, S. Miyazaki, and M. Hirose, *Jpn. J. Appl. Phys.*, **33** (1994) 2179.

Investigation of Pressure Dependence in Photoresist Ashing Process using Microwave Excited Water Vapor Plasma

Khant Nyar Paing[1*], Takeshi AIZAWA[1], Hiroto NISHIOKA[2], Masashi YAMAMOTO[2], Tasuku SAKURAI[1], BAT-ORGIL Erdenezaya[1], Yusuke KAYAMORI[1], Yusuke NAKANO[1], Yasunori TANAKA[1] and Tatsuo ISHIJIMA[1]

[1] Electrical Engineering and Computer Science, Graduate School of Natural Science & Technology, Kanazawa University, Kakuma-machi, Kanazawa, Ishikawa 920-1192, Japan
[2] Department of Electrical and Computer Engineering, National Institute of Technology Kagawa College, Chokushi-cho, Takamatsu, Kagawa 761-8058, Japan
**khantnyarpaing@stu.kanazawa-u.ac.jp, ishijima@ec.t.kanazawa-u.ac.jp*

Microwave-excited water plasma asher (WPA) is our laboratory's new technology for the photoresist (PR) ashing process in semiconductor manufacturing which uses water vapor as process gas. It has the potential to solve many problems of conventional PR ashing technologies including high temperature, oxidation of metal structure, low ashing rate for ion-implanted PR, and high costs of chemicals. In this study, the pressure dependence of various aspects of plasma in water plasma asher, including light emission area, emission intensity, and substrate temperature was investigated. The ashing rate of the novolak PR film on the silicon wafer at the various condition of process pressure was also investigated. Average emission intensity and emission area of plasma significantly increased as process pressure in the chamber were decreased, and they were the highest when the process pressure was 0.3 kPa. The average ashing rate of PR film was only 0.42 μm/min when process pressure was 2.14 kPa, and it gradually increased as process pressure was decreased. It is also found that the ashing rate was improved after reducing the temperature of the water. The ashing rate when using air-rich condition of plasma was observed to be higher than when only water vapor is used as process gas.

Keywords: Microwave-excited plasma, Semiconductor, Photoresist, Pressure, Ashing rate, Water vapor, H-shaped antenna

1. Introduction

In modern life, semiconductor products are used in all fields such as automobiles, smartphones, medical devices, and industrial robots. With the development of AI and 5G technology, the trend toward multi-functionalization of these products will accelerate and the types of semiconductor devices will also diversify. Photoresist (PR), a photosensitive polymer material, is used as a mask in the lithography process in semiconductor device manufacturing. Removal of PR is an important step in the semiconductor manufacturing process. Conventional technologies for PR removal are (1) Chemical treatment using SPM solution (H_2SO_4 + H_2O_2) [1] and (2) Oxygen plasma treatment [2–4]. Chemical treatment method uses dangerous, costly, and toxic chemicals that are environmentally damaging. It is necessary to continue flowing the chemical solution because the instance of mixing sulfuric acid and hydrogen peroxide is the most effective in removing PR. Oxygen plasma treatment increases the temperature of the substrate to 250-300 ^{0}C. It can cause damage to the substrate and deterioration of the metal interconnects on the substrate due to oxidation. When ashing PR with ion implantation, the PR can be blown off by an

Received March 31, 2022
Accepted June 20, 2022

increase in internal pressure due to heating and nanosized particle are generated which can cause problems [5]. A novel method for ion-implanted photoresist removal using atomic hydrogen generated by a heated tungsten catalyzer is also being developed. Although the temperature is low in this process (85 ^{0}C), the ashing rate using this method is in the order of 90 nm per minute even for PR without ion implantation, which is not a practical speed for the semiconductor manufacturing process. A higher ashing rate using the atomic hydrogen method was achieved when the substrate temperature is increased to 280 ^{0}C [6,7]. A new technology that can remove photoresists at a high speed while keeping the substrate temperature low is in need.

Microwave-excited water plasma asher (WPA) method is a new technology of our laboratory. This method is relatively simple because it uses a slot antenna for plasma generation, and it does not require an external mechanism for electrodes. It is environmentally friendly because it uses water vapor as the process gas instead of chemicals [8]. The substrate temperature is low due to the direct cooling of the substrate by water vapor. PR is removed by the radicals generated from water vapor plasma and the removal rate of polymer materials has been investigated [9]. Using this method, the PR ashing rate is high even on the PR surface that was hardened by ion implantation [10].

Water vapor plasma can also be generated using a slot antenna submerged underwater [11]. Studies were done to investigate this plasma using optical emission spectroscopy [12]. In this study, water vapor is evaporated by reducing the process pressure p in the chamber using a dry scroll pump. The process pressure p can affect the generation of OH radicals and the ashing rate of PR. A better understanding of the dependence of various parameters of WPA on process pressure p is essential to improve the PR ashing process of this new technology. In this study, we investigated the effect of pressure inside the chamber on the various aspects of microwave-excited water vapor plasma, including light emission intensity, light emission area, and substrate temperature. We have also evaluated the average ashing rate of PR on silicon wafers by WPA and investigated the dependence of the ashing rate on process pressure.

2. Experiment Setup

2.1. Microwave power

Figure 1 shows the experimental setup that was used in this study. The microwave power supply consists of a 2.45 GHz microwave oscillator with adjustable power from 0 W to 200 W, an isolator, a tuner (ADS-2450200-01, Plasma Applications), a directional coupler, and a power monitor (MMO-020HP, Ota Electronics). The isolator has a built-in dummy load that absorbs the reflected MW power. A directional coupler, power monitor and oscilloscope (DSOX2004A, Keysight Technologies) were used to monitor the forward and reflected microwave power. The double slug tuner was used for impedance matching to maximize the difference between forward and reflected microwave power. Function generator from the oscilloscope was used to transmit pulse wave signal for pulse wave modulation of the microwave power. The peak power of the microwave P_{peak} was 200 W. The square wave modulation frequency was 100 Hz and the on-time duty factor DF was 30% (P_{avg} = 60 W).

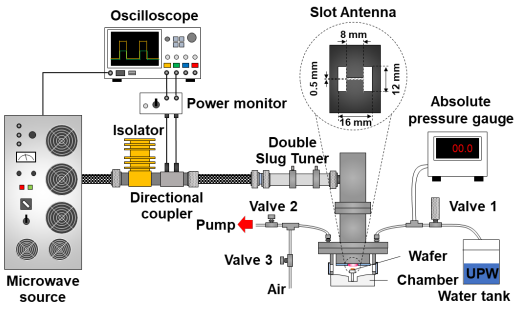

Fig. 1 Experimental setup of microwave excited WPA

2.2. Process gas and process pressure

A container with ultrapure water (UPW) is connected to the chamber through a tube. The temperature of UPW (T_w) can be adjusted by putting UPW in the freezer before the experiment. A dry scroll pump (XDS10, Edwards Vacuum) was used to reduce the pressure inside the chamber p until it reached saturated water vapor pressure (2.3 kPa), at which UPW evaporated and filled the chamber with water vapor. Process pressure p can be controlled by adjusting Valve 1. Outside air can also be allowed into the chamber through valve 3 to generate air-rich condition of plasma. The pressure inside the chamber (p) was measured using a pressure transducer (PT-L9, PSI-TRONIX) and a digital manometer (PEN-33-A, SOKKEN).

2.3. Plasma generation

Microwave power was propagated through a rectangular quart waveguide (κ = 3.75). The waveguide dimension was 56 mm × 28 mm and

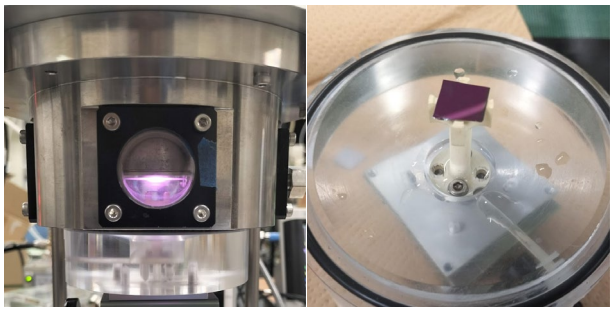

(a) (b)

Fig. 2 (a) Microwave-excited water vapor plasma generation and (b) 10 mm × 10 mm silicon wafer with PR film

microwave propagated inside the waveguide in TE_{10} mode. Different types of slot antenna designs have been developed for microwave-excited plasma [13]. In this study, microwave power was irradiated into the chamber via an H-shaped silicon slot antenna [14,15] instead of a conventional single-slot antenna to improve the area and uniformity of PR ashing. A strong electric field was generated in the gap of the slot antenna. Electrons in the gas were accelerated and collided with neutral atoms and molecules to ionize them and generate microwave plasma as shown in Figure 2.

2.4. Photoresist ashing

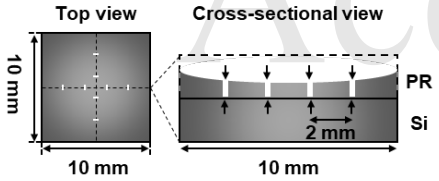

Fig. 3 Average ashing rate of PR film on Si wafer

A rectangular silicon wafer (10 mm × 10 mm, Kagawa NCT) with novolak-type positive-tone PR film (1 μm thickness) was put downstream of the microwave-excited plasma and the antenna-to-substrate distance d was 9.3 mm. OH radicals created from the water vapor inside the chamber reacted and removed PR. Even in air-rich condition of plasma without UPW, OH radicals were still observed due to leftover water droplets in the chamber. The thickness of PR film after ashing was measured using a stylus-type microfigure measuring instrument (SURFCORDER ET200, Kosaka Research Institute). In this study, the average ashing rate was defined as the removed PR thickness in μm divided by per duration of ashing in minute averaged at 8 positions across the wafer as shown in Figure 3.

2.5. Light emission and temperature measurement

A DSRL camera (CANON EOS 70D) was used to capture the emission aspect of plasma directly from below. The camera setting was configured as Exposure time: 1/1000 second, Aperture setting: *f*-10, ISO: 1000. Captured image was converted into a grayscale value (0-255). Average emission intensity was evaluated by averaging the grayscale level over 26.3 mm × 17.2 mm area centered at the slot antenna. The emission area was also evaluated by calculating the area with the grayscale threshold value of 60.

K-type thermocouple and a datalogger (midi GL900, GRAPHTEC) can also be equipped instead of the Si wafer to measure the temperature rise due to plasma. In this measurement, the pressure is swept from 0.6 kPa to 4.8 kPa at a step of 0.6 kPa and a duration of 60 seconds is allowed after each step before taking the temperature measurement.

3. Experiment Results and Discussion

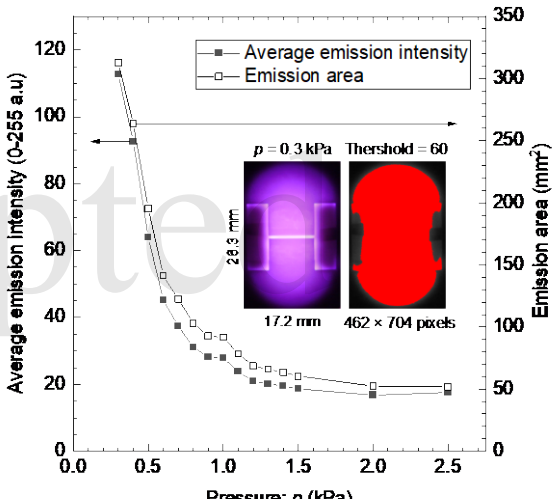

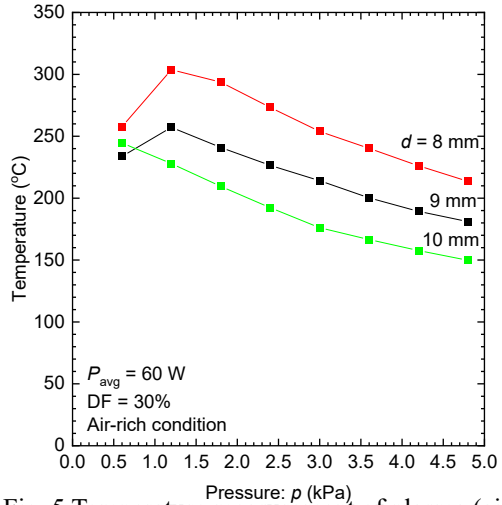

Fig. 5 Temperature measurement of plasma (air-rich condition) with respect to chamber pressure p and distance d

Figure 4 shows that average emission intensity was the highest when the chamber pressure p is the lowest at 0.3 kPa, and it significantly decreased as p was increased to 2.5 kPa. A similar relation between emission area and chamber pressure p was also observed.

Figure 5 shows the pressure dependence of the substrate temperature measured at d = 8 mm, 9 mm, and 10 mm away from the antenna downstream of the plasma. It is found that the temperature of the substrate decreases when the process pressure p is increased and when the distance d is decreased. However, the temperature was also found to decrease when the p is very low at 0.6 kPa.

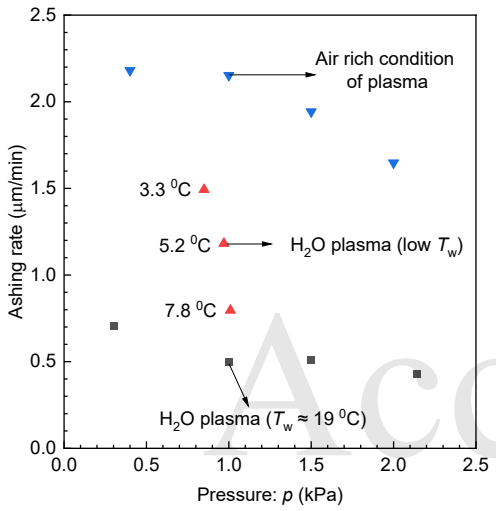

Fig. 6 Ashing rate of PR film on Si wafer at various conditions

In Figure 6, the ashing rate of PR film on the Si wafer is evaluated and compared at various conditions of chamber pressure p and water temperature T_w. When p = 2.14 kPa, the ashing rate of water plasma is evaluated as 0.42 μm/min and it gradually increases as the pressure is reduced. It was also found that reducing T_w, increases the ashing rate of PR film significantly. In the case of plasma with air-rich conditions, a much higher ashing rate was observed, and it also gradually increases as the pressure is reduced.

4. Conclusion

The effect of pressure on the PR ashing rate and light emission aspect of the MW plasma generated by WPA were investigated. At low pressure, the light emission intensity and area increased significantly. This may be because the ionization rate and excitation rate are higher at lower pressure condition due to a longer free mean path. Moreover, the ashing rate of PR film on Si wafer increases gradually as the pressure decreases. Ashing rate is also improved by reducing the temperature of the water and by using air-rich condition of the plasma.

Acknowledgments

The authors are grateful to Prof. Masashi Yamamoto of National Institute of Technology Kagawa College for providing silicon wafers with photoresist film. The authors are grateful to Prof. Tetsuya Taima of Kanazawa Univ. for supporting film thickness measurement.

References

1. W. Kern, *J. Electrochem. Soc.*, **137** (1990) 1887.
2. S. Fujimura, J. Konno, K. Hikazutani, and H. Yano, *Jpn. J. Appl. Phys.*, **28** (1989) 2130.
3. K. Taniguchi, K. Tanaka, T. Inomata, and M. Kogoma, *J. Photopolym. Sci. Technol.*, **10** (1997) 113.
4. S. Fujimura, *J. Vac. Sci. Technol. B Microelectron. Nanom. Struct.*, **9** (1991) 357.
5. T. Miura, M. Kekura, H. Horibe, and M. Yamamoto, *J. Photopolym. Sci. Technol.*, **21** (2008) 311.
6. A. Izumi, and H. Matsumura, *Jpn. J. Appl. Phys.*, **41** (2002) 4639.
7. M. Yamamoto, H. Horibe, H. Umemoto, K. Takao, E. Kusano, M. Kase, and S. Tagawa, *Jpn. J. Appl. Phys.*, **48** (2009) 026503.
8. T. Ishijima, H. Sugiura, R. Saito, H. Toyoda, and H. Sugai, *Plasma Sources Sci. Technol.*, **19** (2010).
9. R. Saito, H. Sugiura, T. Ishijima, and H. Toyoda, Influence of temperature and pressure on solute decomposition efficiency by microwave-excited plasma, in: Curr. Appl. Phys., 2011.
10. T. Ishijima, K. Nosaka, Y. Tanaka, Y. Uesugi, Y. Goto, and H. Horibe, *Appl. Phys. Lett.*, **103** (2013) 142101.
11. T. Ishijima, H. Hotta, H. Sugai, and M. Sato, *Appl. Phys. Lett.*, **91** (2007).
12. T. Kitano, T. Aizawa, T. Ishijima, H. Suzuki, A. Shiota, Y. Tanaka, and Y. Uesugi, *J. Photopolym. Sci. Technol.*, **34** (2021) 469.
13. P. Veronesi, C. Leonelli, G. Poli, and M. Garuti, *Plasma Devices Oper.*, **15** (2007) 13.
14. T. Aizawa, T. Shimada, T. Sakurai, Y. Nakano, Y. Tanaka, Y. Uesugi, and T. Ishijima, *J. Photopolym. Sci. Technol.*, **34** (2021) 479.
15. I. Inoue, T. Aizawa, T. Ishijima, and R. Ono, *J. Phys. D. Appl. Phys.*, **54** (2021).